THEORY AND PRACTICE OF EVAPORATION MEASUREMENT, WITH SPECIAL FOCUS ON SLS AS AN OPERATIONAL TOOL FOR THE ESTIMATION OF SPATIALLY-AVERAGED EVAPORATION

by

MJ SAVAGE[1], CS EVERSON[2], GO ODHIAMBO[1], MG MENGISTU[1] and C JARMAIN[3]

[1]School of Environmental Sciences, University of KwaZulu-Natal,
Pietermaritzburg, South Africa
(savage@ukzn.ac.za)
[2]Environmentek, CSIR, c/o School of Environmental Sciences,
University of KwaZulu-Natal,
Pietermaritzburg
and [3]Environmentek, CSIR, Stellenbosch, South Africa

Report to the Water Research Commission on the project
"Implementation of bichromatic scintillation as an operational tool for the estimation of spatially averaged evaporation"

ISBN No 1-77005-247-X

WRC Report No 1335/1/04

November 2004

Disclaimer

Printed by Silowa Printers: 012 804 1164

Executive summary

1 Motivation

The need for increased food and timber production has led to increases in irrigated and forestry lands in South Africa. Agriculture and forestry face increased competition for water by industries, municipalities and other groups. This ever-growing demand for water makes it imperative that water resource management procedures and policies are wisely implemented and improved. The accurate assessment of evaporation is essential if this is to be done. Furthermore, the real and/or potential impact of global warming and climate change on all forms of water resources increases the imperative for a knowledge base on water use (and productivity) of commercially-managed lands and natural vegetation. In particular, what is the potential impact of these large-scale changes on evaporation? Implied in this question is the definition of a standard or a benchmark for evaporation measurement or estimation.

The 1998 Republic of South Africa National Water Act refers to the possible prescription, by the Minister, of methods for making a volumetric determination of water for purposes of water allocation and charges in the case of activities resulting in stream flow reduction. Given this scenario and the above-mentioned demand on water resources it is important to consider how evaporation, one of the main components of the water balance, is to be measured or estimated routinely with reliable accuracy and precision.

So, what is the standard or benchmark for evaporation measurement or its estimation? This important and fundamental question needs to be addressed to achieve the ideal of accurate and reliable evaporation data. This investigation focuses on one method, using a surface layer scintillometer (SLS) and other measurements, to estimate evaporation. The SLS method involves the more fundamental aspects of micrometeorological research. Advances in this field will have direct benefits to water resources assessments and management processes. Examples of areas not easily addressed using the more traditional evaporation measurement and modelling methods include amongst others: measurement of evaporation in riparian zones; determination of open water evaporation from rivers and dams (both large and small); effluent water management from saline dams in the mining environment; measurement of evaporation from slimes tailings; water use of trees and crops in agro-forestry trials; remote sensing applications; determination of baseline evaporation from natural communities (e.g., indigenous forests); irrigation research.

Since John Dalton first introduced the mass transport equation for evaporation estimation, numerous methods for estimating or measuring evaporation have been developed. In certain instances, these methods are accurate and reliable; in others, they are unsuitable or unreliable for certain surfaces or certain times or provide only rough approximations. Currently, there is no single accepted method capable of providing both good spatial and temporal measurements or estimates of evaporation that is reliable and has adequate resolution. This has been confirmed by Drexler et al. (2004) who concluded in their review that there is no single approach that is best for estimating wetland total evaporation. Similarly, Hanson et al. (2004) concluded that no single tested model (using hourly, daily or annual time steps), for capturing intra- and inter-annual forest water and carbon cycle, consistently performed best at all time steps or for all variables considered. However, they did find that inter-model comparisons showed good agreement of water cycle fluxes.

South African researchers have had good success with the heat pulse velocity (HPV) (Dye et al. 1992, Dye and Olbricht 1993) and energy balance methods (Savage et al. 1997). The energy balance is defined by the balance of energy between the net irradiance at a surface and the energy terms used for evaporating water, heating the atmosphere, heating the soil and for photosynthesis. [Net irradiance refers to the flux density of net radiant energy comprised of the incoming solar energy minus the reflected solar plus the incoming long wave energy minus the outgoing long wave. Flux density is the change in an entity, for example net radiant energy per unit time per unit area. Hence net irradiance is the net radiant energy per unit time per unit area with unit W m^{-2}].

The HPV method for estimating sap flow is based on using heat as a tracer for sap flow in plant stems. Temperature needles and a heater probe are inserted in the plant stem and a pulse of heat is applied at regular intervals of time. The rate of change in temperature as measured by the needles a known distance for the heater is related to the sap flow. However, the HPV method is suited only to mono-specific stands of trees, is problematic when scaling from single trees to whole stands and is a destructive method since the tree must be felled to calculate sapwood areas and wound size. The lack of wound size information at the time of measurement makes calculations of transpiration only possible at the end of an experiment. Another method fo determining sap flow, the stem steady state heat energy balance technique, has also received attention in South Africa (Savage et al. 1993, 2000).

Another traditional method for estimating evaporation, the Bowen ratio (BR) method, uses measurements of profile differences in air temperature and water vapour pressure above the canopy, surface net irradiance and soil heat flux density. The method assumes that the coefficients of exchange between the surface and the atmosphere for sensible heat [heat transferred from the atmosphere to a surface, or *vice versa*, that results in a temperature change] and latent energy are identical. Latent energy refers to the energy removed from a surface when water from the surface evaporates. The evaporation causes a cooling effect due to the loss of energy. The term latent is used since largely the process is invisible and results in no temperature change. The BR method, compared to the HPV method, is well suited to mixed species communities such as grassland, but is limited by constraints imposed by both fetch distances and measurement height and is essentially a point measurement. Fetch refers to the upwind distance from the instrument location across a uniformly rough surface such as a forest or a grassland until there is a discontinuous change in surface roughness. Thus, the BR method is not suited to narrow strips (e.g., riparian zones, wetlands, etc.), where fetch distances are short, or above tall vegetation where there are small gradients of air temperature and water vapour pressure (caused by the increased wind turbulence above tall canopies) or above almost any surface in the dry season typical of even the humid areas of South Africa. These gradients may be outside the measurement resolution of the sensors particularly when placed above forest canopies.

The EC method is also a traditional method for direct and point measurement of one or more of sensible heat and latent energy flux density. The method uses uses high frequency (typically 10 Hz) measurements of air temperature and vertical wind speed (for sensible heat) and air temperature and water vapour pressure (for latent energy flux density). In recent years, direct measurements of turbulent fluxes have been achieved using the eddy covariance (EC) method in KwaZulu-Natal (Monnik et al. 1995, Savage et al. 1995a, b). If only sensible heat flux density is measured using the EC method, then latent energy flux density may be estimated by also measuring net irradiance and soil heat flux density. A drawback of EC measurements is that they, like BR measurements, are point measurements although both sets of measurements are affected by fluxes from upwind source areas. However, the application of the EC method is sometimes problematic. The necessary sensors for vertical wind speed, air temperature and water vapour pressure (or equivalent) must respond very quickly (frequency of 5 Hz or greater) and at the same time must not show noticeable drift. This makes them delicate, expensive and in some cases difficult to calibrate. However, more serious is the airflow distortions by the sensor, mast, etc., as well as the horizontal misalignment measurement errors. In addition, there are technical problems because temporal co-spectra, measured at a fixed local sensor, extend to very low frequencies. To achieve acceptable significance often demands averaging periods of several tens of minutes. Such long averaging periods reduce the temporal resolution and conflict with the requirement of atmospheric stationarity within averaging periods.

Because of the above-mentioned theoretical and practical difficulties associated with the various measurement methods, alternative or complementary flux measurement methods for estimating evaporation have been sought. Recent investigations have demonstrated the potential of using a scintillometer to measure areally-averaged sensible heat flux density. A scintillometer measures the intensity fluctuations of visible or infrared radiation after propagation above the plant canopy of interest. A scintillometer is an instrument that optically measures a parameter associated with refractive index fluctuations, over atmospheric path lengths from 50 m up to at least 3 km and beyond in some cases, from which sensible heat flux density may be calculated. The refractive index fluctuations are caused by interference after the radiation has been scattered by inhomogeneities of the refractive index of air, the latter caused by turbulent fluctuations of air temperature and atmospheric humidity. The parameter is referred to as the structure parameter for refractive index fluctuations C_n^2. Once C_n^2 has been determined, the sensible heat flux density may be estimated from air temperature, atmospheric pressure, effective beam height and beam path length. In contrast to BR and EC measurements, scintillometers provide path-averaged results. Surface layer scintillometer (SLS) systems have beam paths between about 50 and 250 m and large apertures scintillometer (LAS) systems usually operate over distances of between 500 m and 3 km or even up to 10 km for boundary-layer scintillometer (BLS) systems.

The main objective of this project is to estimate areally averaged sensible heat flux density using the SLS method, previously untested in South Africa, and to compare these estimates with those obtained using the more traditional BR and EC methods. A preliminary investigation on the use of the so-called surface renewal (SR) method, also previously untested in South Africa, is also conducted. The SR method is a high frequency, typically 8 Hz, single-temperature measurement technique that also allows for the estimation of sensible heat flux density.

For most of the measurement methods used in this study, the use of the energy balance, requiring measurement of the net irradiance and soil heat flux density, is crucial. The measurements are required together with sensible heat flux density to estimate evaporation. Net irradiance and soil heat flux density measurements are made above and within the surface respectively and need to reflect the spatial variability of the surface and therefore the spatial variation of evaporation. Attention to these measurements for heterogeneous terrain is all the more crucial.

This project falls within the hydroclimatological research programme of the WRC. In this programme the project will contribute to research support for water resources assessment, management and sustainable utilisation in South Africa, by improving the methodologies for monitoring evaporation from surfaces with variable vegetation cover and water surfaces, possibly resulting in a standard for evaporation estimation by which other methods will be judged.

2 Aims

2.1 Project aims

The original aims of the project were:

1. to make recommendations on the feasibility, to provide guidelines for the use, and to specify the limitations of the SLS method for the estimation of areally averaged sensible heat flux density over heterogeneous surfaces;

2. to provide catchment researchers and consultants with a practical, accurate and operational tool to improve our understanding of comparative evaporative losses of water from land surfaces and water bodies associated with various forms of land use and a range of catchment conditions.

Once the project had commenced, it became clear that as complete a set of measurements as possible using a variety of methods over a couple of years would be more useful than obtaining an incomplete set of data for a whole range of land surfaces. To that end, all measurements were obtained from a mixed grassland site in the KwaZulu-Natal midlands near Pietermaritzburg. Furthermore, it became clear that the SLS measurements in isolation would be insufficient to determine the measurement accuracy and limitation(s) of the SLS method. It was therefore necessary to perform measurement comparisons with measurements obtained from the other methods such as the BR, EC and SR measurement methods.

2.2 Background

This project was primarily concerned with the use of the SLS method for the measurement of sensible heat flux density from which path-averaged evaporation, for distances of between 50 and 250 m, can be determined based on additional measurements of net irradiance and soil heat flux density.

2.3 Investigation of other micrometeorological methods

2.3.1 Baseline comparisons

Prior to our study, the SLS method for the estimation of evaporation had not been tested in South Africa.

It was our intention to use the SLS method for estimating evaporation and compare this method with other methods of estimating evaporation and in particular the traditional BR and EC energy balance methods reported on in a previous Water Research Commission report (Savage et al. 1997). After the research had commenced, a fourth method was used: the SR method, also previously untested in South Africa, for the determination of the sensible heat flux density from which latent energy flux density could be estimated using other terms of the energy balance.

2.3.2 Sensible heat using field measurements and estimation of evaporation

We wished to compare the SLS method with other evaporation methods that also use energy balance measurements of net irradiance and soil heat flux density and use the SLS method for estimating evaporation in a mixed grassland community for almost two years and compare the SLS estimates with:

(i) BR energy balance estimates of evaporation;

(ii) EC estimates of evaporation using EC measurements of sensible heat flux density and the net irradiance and soil heat flux density terms of the energy balance;

(iii) preliminary measurements of sensible heat flux density using the SR method for estimating evaporation. The SR method was not part of the original proposal but was subsequently researched as part of a preliminary investigation.

In the process of testing the various methods, seasonal estimates of evaporation for the grassland site using both SLS and EC methods were collected and the impact of mowing and burning investigated.

2.3.3 Laboratory investigations

Our aim was to investigate if a cooled dew point mirror, often used as part of BR equipment, could be replaced by a cheaper sensor that required much less maintenance and avoided the possibility of data loss. The dew point mirror used required a weekly service and resulted in unacceptable data whenever the mirror inexplicably iced up.

3 Products

Products include a new method for estimating areal averages of latent energy (evaporation) over large and heterogeneous surfaces, with recommendations on its use, feasibility, and limitations under various conditions. In addition, the theory and practice of a number of evaporation measurement methods is presented.

Target Water resource managers; researchers in the following sectors: agriculture, forest, mining, agroforestry; catchment management agencies or any group interested in understanding and quantifying evaporative processes.

Application To provide catchment managers with a practical means of accurately quantifying and comparing evaporative losses of water from land surfaces and water bodies associated with various forms of land use and a range of catchment conditions.

4 Structure of report

Chapter 1 introduces the study, emphasising that currently there is no single acceptable method for evaporation measurement or estimation that is capable of providing both good spatial and temporal data of evaporation that is reliable and has adequate resolution. Additional arguments are presented to justify the need for the investigation.

An introduction to turbulence and a brief introduction to scintillometry, and the Monin-Obukhov similarity theory (MOST) upon which the SLS method is based, is presented in Chapter 2. The Monin-Obukhov similarity theory is a widely-accepted body of semi-empirical theory of atmospheric turbulence, assuming similarity between fluxes, that allows the dimensionless stability factors for sensible heat flux density to be estimated from the so-called Monin-Obukhov length. In establishing the link between turbulence and energy, the various radiation and energy balance components existing at the surface is discussed first. Following this, the Kolmogorov cascade theory of turbulence is discussed. A discussion on eddy structure and stability functions leads to the Monin-Obukhov stability length and the Monin-Obukhov stability theory. Methods for the measurement or estimation of sensible heat flux density, including the scintillometer method are discussed. Most of these methods involve turbulence theory for the estimation of sensible heat flux density and application of the energy balance which in turn allows evaporation to be estimated. The theoretical basis of various methods, with special emphasis on the scintillometer method, for the estimation of sensible heat flux density, is presented.

Chapter 3 is devoted solely to the SLS method and the logistics of estimating evaporation from SLS data. The methodology associated with the use of the dual-beam SLS method is discussed in detail. The procedures associated with the crucial step of beam alignment are presented as are the procedures for error-checking the data post-data collection. The seasonal march of the percentage of error-free data is discussed. The assumption of a horizontal beam above a horizontal surface, required by MOST, is also investigated by comparison of non-horizontal beam SLS measurements with simultaneous EC measurements. Also, for a limited time, SLS measurements at a very low beam height were compared with EC measurements. An error analysis is undertaken to determine the worst-case scenario influence of the input data on the measured sensible heat flux density as well as the influence of net irradiance and soil heat flux density on the estimated evaporation. In a sense, these so-called errors reflect the spatial variability in the surface cover.

Chapter 4, the bulk of the report, presents the comparisons between the SLS, BR, EC and SR sensible heat flux density measurements and evaporation estimates at various time scales: 2-min, 20-min, and daily. Peculiarities of the collected data such as the asymmetrical nature of the diurnal sensible heat flux density curve and the so-called counter-gradient latent energy flux densities, also receive attention in this chapter. Also, a footprint [which refers to the relative contribution of upwind surface sources to the measured flux density] model is improved upon and used to calculate three key footprint parameters: the peak location of the footprint, the footprint fraction itself and the 90 % fetch to measurement height ratio, the relative contribution of upwind surface sources to the measured flux density. This chapter is also concerned with BR measurements and in particular the replacement of a cooled mirror dew point sensor by a thin film polymer capacitive sensor.

Chapter 5 is concerned with seasonal evaporation aspects of the collected data over the 18-month period. The influence of a fire and two mowings at the site on the evaporation estimations is also discussed.

Chapter 6 presents the overall findings and recommendations for future research.

5 Results and conclusions

The various methods used for the estimation of evaporation are discussed, particularly with reference to their theoretical basis and instrumentation requirements. The operational procedures for use of the surface layer scintillometer (SLS) method is discussed in detail. The procedures for checking the integrity of the data in real-time are high-lighted as are the post-data collection rejection procedures.

Surface layer scintillometer measurements were performed at the Hay Paddock site near Pietermaritzburg for most of 2003 until November 2004. The system allowed for the real-time estimation of sensible heat flux density every two minutes. For most of the study, the automatic alignment option was enabled except near the end of the study. Without the use of the automatic alignment option, measurements were sometimes possible for periods of five days and longer. Longer periods would be possible theoretically with an increased beam height and/or a decreased path length. In addition to the SLS sensible heat flux density measurements, an energy balance system was used to measure the soil heat flux density and the net irradiance from which the latent energy flux density was calculated as a residual using the energy balance.

5.1 The logistics of estimating latent energy flux densities from raw surface layer scintillometer data

The logistics of estimating latent energy flux density from SLS data was the focus of a thorough investigation.

5.2 The rejection criteria for the exclusion of out-of-range and "bad" or doubtful data

We successfully used logical rejection criteria to exclude SLS measurements where necessary. Data rejection or filtering procedures were applied in Excel to the sensible heat flux density 2-min values. Sensible heat flux density values were rejected, blanks were created or data recalculated:

- if the percentage of error-free data was less than or equal to 25 %, data were rejected;
- if the inner scale of refractive index fluctuations was less than or equal to 2 mm data were rejected;
- for missing data, designated by zeros, a blank cell was used for sensible heat flux density;
- the sign of sensible heat flux density was assigned depending on the measured vertical air temperature gradients.

5.3 Error considerations of the surface scintillometer method

The percentage of "acceptable" 2-min SLS sensible heat flux density measurements for the daytime hours (taken as 06h00 to 18h00) showed little seasonal variation and was consistently high - between 86.7 % and 94.8 % for the 22-month period. The nighttime variation in the percentage had a more pronounced seasonal pattern with the lowest percentage acceptable measurements occurring between January and March of each year. The lower nighttime percentage values were due to the effects of dew and mist. Included in these percentages are the times for which the electrical power was interrupted. At worst, this period was no longer than a day or so. Other minor interruptions, usually less than two days in duration, were due to an accidental fire and accidental cutting of the cables. The average percentage error-free data varied between 62 and 85 % for the 06h00 to 18h00 period and 33 to 73 % for the nighttime. The lowest percentages were during the summer rainfall period (September to March), presumably due to the influence of rain events on beam transmission.

For the SLS measurements, a sensitivity analysis was used to determine the relative importance of the data inputs of air temperature, atmospheric pressure, beam path length and beam height on sensible heat flux density estimates. Beam height was the height of beam above the level $d + z_o$ at which the wind speed is assumed to be 0 m s^{-1}. In addition, errors in the measurement of soil heat flux density and net irradiance also affected the estimated latent energy flux density.

The influence of surface slope on sensible heat flux density measurements was investigated by altering the height of the receiver relative to the transmitter. Theoretically, a non-horizontal beam relative to a horizontal surface, or *vice versa*, invalidates MOST. A receiver to transmitter vertical height difference of 1.0 m was used to alter the effective slope. For measurements performed over five days, there was no significant consistent difference between 2-min SLS and EC sensible heat flux density measurements in spite of the fact that MOST is invalid for a non-horizontal beam.

The influence of beam height was investigated by also altering the height of the transmitter and receiver units. For most of the study, the beam was about 1.68 m above the soil surface with vegetation height varying between virtually 0.0 m and a maximum of 1.13 m. The effective beam height therefore varied between 0.82 m and 1.68 m. The lowest beam height used was a height of 0.5 m. The comparison between sensible heat flux density measured using the EC and SLS methods showed that the SLS measurements were not significantly influenced by even this low beam height.

Worst-case errors in atmospheric pressure, air temperature, beam path length and beam height resulted in fractional errors in sensible heat flux density of ± 0.013, ∓ 0.015, ∓ 0.03 and ± 0.04 respectively. Clearly, the beam height above $d + z_o$ needs to be accurately known as the error in beam height contributes the most to the overall error. Overall, the worst-case total fractional error in sensible heat flux density was ± 0.054 and the typical fractional error amounted to ± 0.032.

The error in estimated latent energy flux density from independent measurements of the energy balance components depended on the error in the SLS sensible heat flux density and errors in measured net irradiance and soil heat flux density. Most-often however, the error in SLS sensible heat flux density was smaller than the error in net irradiance and soil heat flux density measurements. Using four to five soil heat flux plates and averaging thermocouples, we investigated the actual variation in soil heat flux density over an area of about a square metre. Using this information as well as other error values from the literature, including measurement error in net irradiance, we estimated the error in latent energy flux density. The seasonal variation in the error in latent energy is generally less than 0.2 mm day^{-1} (0.49 MJ m^{-2}) in winter when the daily evaporation rate was around 1 mm day^{-1} (2.45 MJ m^{-2}) and typically less than 0.4 mm day^{-1} (0.98 MJ m^{-2}) when the evaporation rate exceeded 4 mm day^{-1} (9.8 MJ m^{-2}). The measurement with the greatest contributing error is the soil heat flux density measurement. Care therefore needs to be exercised to ensure that soil heat flux density measurement procedures do not compromise the estimates of latent energy flux density using SLS sensible heat measurements. The same caution would apply to BR estimates of latent energy flux density and the EC method when only sensible heat flux density is measured and latent energy flux density is estimated using the net irradiance and soil heat flux density energy balance components.

5.4 Field comparison of evaporation measurements using surface layer scintillometry, eddy covariance, Bowen ratio, and surface renewal methods

The main aim of this research is to investigate dual-beam surface layer scintillometer (SLS) estimates of sensible heat flux density also obtained using the following methods: Bowen ratio (BR), eddy covariance (EC), reference evaporation, and surface renewal (SR). These measurements and measurements of net irradiance and soil heat flux density allowed evaporation to be be estimated as a residual using the energy balance. The influence of wind direction, in particular winds perpendicular and parallel to the SLS beam, on these measurement comparisons is examined. Since the measurement height of the various instrumentation was necessarily different, the relative contribution of upwind surface sources to the sensible heat flux density measured at a height above the canopy surface was investigated using a footprint analysis.

In order to obtain accurate comparisons using the BR method, we also investigated the possibility of replacing the often problematic Dew-10 cooled dew point mirror usually used with such systems with a thin film polymer capacitive sensor such as a Vaisala sensor. The main disadvantage of the use of a Vaisala sensor is that two measurements, relative humidity and temperature, from two different sensors was required for the estimation of the airstream water vapour pressure. A laboratory experiment showed that potentially, a Vaisala CS500 and the predecessor of the Vaisala HMP45C could replace the Dew-10 sensor. A four-month field-comparison between 20-min latent energy flux density obtained using the HMP45C and a Dew-10 sensor (6002 data points) yielded a slope of 0.9938 and y-intercept of -0.095 W m^{-2}. This excellent agreement shows that the HMP45C would be a cheaper and adequate replacement for the Dew-10 cooled mirror sensor. Furthermore, the HMP45C requires no servicing compared to the Dew-10 which requires a bias adjustment and mirror cleaning each week. The water vapour pressure measurement noise for the HMP45C sensor was greater than that for the Dew-10 but the average water vapour pressure profile difference for the two sensors was highly correlated (slope of 0.9334, r^2 = 0.9899, n = 12965). The HMP45C sensor used was not as accurate as the Dew-10 but the resolution of the HMP45C profile difference measurements was better than the minimum resolution of 0.01 kPa required for BR measurements when averaged over 20 min. The even cheaper Vaisala CS500 sensor was also used for field measurements. Comparison of the HMP45C with the CS500 yielded a slope of 1.0236 (r^2 = 0.9956, n = 213). The CS500 sensor exhibited greater variation in measured water vapour pressure mainly as a consequence of greater variation in temperature using the CS500 temperature sensor even when compared to the HMP45C temperature sensor. In spite of this, the resolution in the CS500 water vapour pressure was better than 0.01 kPa. The water vapour pressure variation could be reduced by replacing the temperature sensor with a thermocouple. These findings will make BR measurements of evaporation considerably cheaper, more reliable than in the past and easier to assemble.

Polar diagrams were used to show that during daytime hours, the wind vector wind direction is generally from the SE (180 to 270°) but sometimes from the NW (0 to 90°). The SLS beam was aligned from 20° east of S to 15° W of north - almost from S to N. The largest SLS and EC differences in the daily sensible heat density occurred for the 0 to 60° wind direction. These winds were from residential areas and the fetch more limited than the other wind directions. However, there were many days when the wind direction was almost perpendicular to the beam and seldom parallel.

The footprint model of Hsieh et al. (2000) was corrected and extended to include a surface with a zero plane displacement height. The more unstable the atmospheric conditions, the closer was the peak location of the footprint to the measurement position. For convectively unstable conditions, the peak location was within metres of the measurement position. Generally, during the daytime hours, the 100:1 fetch to measurement height ratio is too stringent for the atmospheric conditions experienced. The general stability condition for the 9 am to noon hours is not the same as that for the noon to 3 pm period. Surprisingly, the morning hours are generally more unstable than are the afternoon hours. This asymmetry in stability often results in asymmetrical diurnal sensible heat flux density curves.

The general agreement between the 2-min SLS and EC measurements was very good. The EC measurements showed greater variability since they are point estimates. The SLS measurements represent a line-average and were much less variable. The correspondence between the two measurement techniques improved when there was reduced turbulence, particularly for uniformly cloudless days and before 10 am and after 2 pm. There did not appear to be a consistent bias between the two measurement methods. This implies that the correct value for the zero plane displacement height, based on two-thirds of the canopy height, was chosen. The 2-min SR sensible heat flux density was more variable than the other methods (error mean square of 2299.1 W m^{-2} when compared with SLS measurements). Averaging SR measurements over 20 min is recommended.

Latent energy flux density is estimated as a residual from the energy balance equation. Negative latent energy values correspond to normal evaporation but cases were found when the latent energy flux density was positive for brief periods. Positive latent energy flux density values correspond to the magnitude of the sensible heat flux density exceeding the available heat flux density. Counter-gradient fluxes of sensible heat were detected. Some of the selected data displayed show that counter-gradient fluxes may be associated with large reductions in solar irradiance but were short-lived.

The BR 20-min measurements of sensible heat and latent energy flux density were in good agreement with the corresponding SLS, EC and SR estimates. Examples of this correspondence were selected from the large data set collected. There was no consistent under- or overestimate in the SLS sensible heat flux density measurements compared to the sensible heat flux density measurements from the three other methods. The magnitude of the SR sensible heat flux density measurements, if anything, tended to be less than the sensible heat flux density measured using the other measurement methods and therefore tended to overestimate the latent energy flux density. The SR method is the least expensive in terms of instrumentation and datalogging requirements. The good agreement between the different measurements is remarkable considering the different underlying theory of each method, the different measurement heights, different footprints, differing spatial scales of measurement (i.e., point measurements *vs* path averaging) and differing measurement frequencies. Furthermore, it would appear that the EC sensible heat flux density measurements do not underestimate as stated in the literature.

Comparisons of the daily estimates of sensible heat density for EC and SLS techniques showed good agreement (error mean square of 0.188 MJ m^{-2} which is equivalent to 0.077 mm). These comparisons were separated out according to wind direction which showed that best comparisons between EC and SLS measurements were obtained for the 180 to 270° wind directions (error mean square of 0.171 MJ m^{-2} compared to 0.229 MJ m^{-2} for the 0 to 90° wind directions). The 0 to 90° wind directions corresponded to wind from residential areas and relatively limited fetch.

Measurement comparisons over a period in excess of 55 days showed that the ECopen system daily latent energy density measurements had a variable relationship with daily latent energy density estimated using SLS measurements, net irradiance and soil heat (error mean square of 0.632 MJ m^{-2}, $r^2 = 0.239$). Daily estimates of latent energy density for the SLS and EC techniques were compared for a period of about 250 days during 2003. The 95 % confidence bands for a single predicted value were within 0.5 mm of the regression line and the error mean square was 0.295 MJ m^{-2} or about 0.12 mm. There was no statistical difference between daily latent energy density estimates obtained using the EC method based on point measurements and the line-averaged estimates obtained using the SLS method.

5.5 Estimation of seasonal evaporation using surface layer scintillometer and eddy covariance measurements

The main aim of this research is to investigate the application of the dual-beam surface layer scintillometer (SLS) and eddy covariance (EC) methods for estimating evaporation in an open and mixed grassland community in a summer rainfall area. Evaporative water loss is often the largest component of the hydrological cycle and is usually calculated as the remainder term of the soil water mass balance. Quantifying the total evaporative loss is difficult but necessary for an informed, objective long-term management plan of catchment areas. Determination of total evaporation from a grassland site in the midlands of KwaZulu-Natal, South Africa (-29.617° S, 30.417° E, altitude of 706 m with a very slight slope) was carried out over eighteen months (mid January 2003 to June 2004). The measured sensible heat flux density, net irradiance and soil heat flux density were used to estimate latent energy flux density every two minutes. The 2-min estimates were then totalled for each day for the 6 am to 6 pm period. The estimates from the SLS and EC methods were averaged for each day. The daily values were totalled to form a monthly total. The seasonal trend in latent energy density (evaporation) and the impact of the mowing and fire treatments over the 18-month period is discussed. After the 2004 mowing, the Bowen ratio increased significantly. Following the removal of vegetation, the sensible heat daily total increased and the latent energy daily total decreased. The levels were maintained for nearly two months, except for rain days.

Priestley-Taylor evaporation was a poor estimate of evaporation amounts during this period with below-average expected rainfall, overestimating the measured evaporation. The evaporation total of 673 mm for 2003 and 306 mm for the first six months of 2004 exceeded the rainfall totals of 532 and 248 mm respectively. The magnitude of the daily total latent energy density typically varied from a summer maximum of about 12 MJ m^{-2} (4 mm) to a winter season minimum of 2 MJ m^{-2} (less than 1 mm). The SLS and EC methods were shown to be suitable for long-term monitoring of daily total evaporation and capable of detecting the effects of management fires and mowing.

6 Extent to which contract objectives have been met

Our research has taken the contract objectives further than was originally envisioned. We have:

- investigated evaporation measurement using two methods not previously tested in South Africa: the SLS method and the low-cost SR method;
- thoroughly investigated the SLS method and identified the sources of error(s) in the estimation of surface evaporation using this method including the influence of beam angle and beam height on sensible heat flux density measurements;
- made extensive comparisons between SLS and EC methods of estimating evaporation using the energy balance as well as performed comparisons with direct measurements of EC evaporation that do not involve use of the energy balance;
- identified the practical limitations of the BR method and presented data using a replacement sensor for the commonly-used dew point mirror system;
- made comparisons between SLS, BR and EC energy balance estimates of evaporation for a period of ten months;
- investigated footprint aspects of the SLS measurements. An improved footprint analysis framework was applied to the SLS measurements;
- made preliminary comparisons of sensible heat flux density between the SR and SLS methods;

- obtained a set of evaporation data using SLS and/or EC measurements for an open and mixed grassland community in a summer rainfall area for a period of 22 months.

7 Future research

7.1 General comments

One of the major limitations to real economic growth of South Africa is the limitation imposed by inadequate water resources to support the given human population and their activities. Evaporation is a process whereby water is used consumptively. The measurement and/or the estimation of evaporation is key to quantifying this consumption in relation to the productive or beneficial use of water. Also, the quantification of water use can assist management in shifting from less to more productive consumptive water use and therefore research into evaporation measurement or its estimation is crucial to South Africa.

7.2 Large aperture scintillometer and surface layer scintillometer comparisons

Our research has concentrated on the use of the SLS method. There was insufficient time to extend the focus to comparisons with a large aperture scintillometer (LAS). Such a comparison would prove useful and allow evaporation measurements to be scaled to pixel size with greater confidence.

7.3 Bowen ratio methodology

Our research has concentrated on energy and water movement exclusively and therefore has ignored the important aspect of plant productivity in terms of the amount of water used. We believe that the BR research needs to be extended to research on a BR carbon dioxide and water vapour system. This research would allow such a BR CO_2 system to determine water use efficiency in real-time.

7.4 Surface renewal methodology

Preliminary but important work on the SR method is reported on in this report (Chapter 4). Given the simplicity of the method theoretically and practically, the results found and that it is relatively inexpensive, the method certainly deserves further investigation.

7.5 Soil heat flux density and net irradiance influences

This report has shown the importance of the energy balance components net irradiance and soil heat flux density measurements for estimating latent energy flux density from a measured sensible heat flux density measurement. Since these measurements are required for both SLS and LAS measurements, future research would need to consider these two measurements in more detail. In particular, for short vegetation and for heterogeneous terrain, the measurement of soil heat flux density closer to the surface requires attention.

7.6 Collected data not used in the report

It appears possible to use canopy temperature and remote sensing techniques for the determination of sensible heat flux density if measures of aerodynamic resistance are also possible using the SLS or LAS methods. In view of the possibility of "areal" measures of sensible heat flux density, it may then be possible to also calculate surface evaporation from estimates of net irradiance and soil heat flux density. Furthermore, the temperature variance method, used together with measurements or estimates of the friction velocity, needs to be investigated as a possible method for the estimation of sensible heat flux density.

7.7 Technology transfer

In a sense, this project has already resulted in technology transfer. The results produced early on were valuable and resulted in much greater confidence in the use of the EC method for the measurement of sensible heat flux density. This confidence did not previously exist. Furthermore, the results of 2004 have confirmed the suspicion that BR measurements would be made more reliable by introducing a sensor replacement for the cooled dew point mirror sensor. Furthermore, preliminary investigations involving the use of the SR method, indicated that this technique can be implemented at locations where data logging capability currently exists as is the case for automatic weather stations.

It is proposed that a variety of methods be used to transfer some of the technology of the research investigated here: small workshops, conference workshops and e-mail interest groups. A cooperative effort is needed. The WRC has been proactive in this regard through a call for solicited research proposals on evaporation measurement or estimation. Technology transfer forums should encourage young scientists as much as possible. These processes would quickly permit the transfer of the technology described in this report.

Much of the research described here has already benefited students, researchers and technical staff at the University of KwaZulu-Natal and the CSIR.

It is the intention to publish parts of this report in scientific journals and present the results at conferences. Specifically, the error analysis of Chapter 3, the role of wind direction on the SLS and EC comparisons in Chapter 4, the comparisons between BR measurements for the various sensors used, the footprint analysis and the sensible heat measurement comparisons between the various methods used in this report could be published and/or presented at scientific conferences. Furthermore, it is envisaged that at least two PhD theses will stem from this project.

8 Capacity building

The SLS results produced early on in this project were extremely valuable and resulted in much greater confidence in the use of the EC method and also confidence in the SLS method for the measurement of sensible heat. So these methodologies can be used by researchers and students with confidence.

Mr Rasool (ex CSIR) and Mr Xaba (both previously disadvantaged individuals) have furthered their technical training by completing the course on: Environmental Instrumentation for the Life and Earth Sciences in 2002. Both technicians are now capable of servicing the micrometeorological instrumentation associated with this project.

Ms Jarmain and Dr Everson attended a course on the Linux operating system used for the open path EC system.

Ms Jarmain has been trained to use the open path EC instrumentation and the LAS system.

In 2003, Dr Everson visited the Meteorology and Air Quality Group, Wageningen University, Wageningen, The Netherlands.

A PhD student (Mr George O. Odhiambo) is using the experiment as the subject for a PhD thesis on SLS. Mr Michael G. Mengistu is also using the SLS and SR methods for a PhD registration as part of his research. A third student will use the method as part of his PhD research. Two other students from Zimbabwe are making plans to undertake postgraduate study starting next year on the use of one or more of these evaporation methods for irrigation research (one masters student and one PhD student). Another student from outside South Africa, that has been accepted for PhD study in the area of energy and water relations, would be involved in these techniques. He is in the process of applying for a study permit.

Students from various undergraduate courses have visited the site for practical demonstrations on the various methods for evaporation estimation.

In addition, students and researchers from Swaziland and Mozambique spent a morning visiting the research site and receiving instruction on the use of scintillometers.

Scintillometry is a new technology to Africa - we have confirmed that there are no other SLS units available in Africa. There are however some LAS units in operation. With any new technology, a great deal of effort is needed first to understand it and apply it. Capacity has therefore been built in terms of this new technology in all the members of the project team. The success in the use and application of the methodologies has been encouraging and advantage should be taken of this.

9 Acknowledgements

The research in this report emanated from a project funded by the Water Research Commission entitled:

- "Implementation of bichromatic scintillation as an operational tool for the estimation of spatially averaged evaporation".

The Steering Committee responsible for this project consisted of the following persons:

Dr G.C. Green (Water Research Commission), Chairman;

Ms F. Ballim, Department of Water Affairs;

Professor R. Bharuthram, Research Office, University of KwaZulu-Natal;

Dr A. Singels (South African Sugar Association);

Mr J. Bosch (CSIR).

Their time, interest and effort in this project is greatly appreciated.

The financing of the project by the Water Research Commission and the contribution of the members of the Steering Committee is gratefully acknowledged. The project was only possible with the cooperation of the following:

University of KwaZulu-Natal (ex University of Natal) and the CSIR for use of eddy covariance, and Bowen ratio equipment and to the University of KwaZulu-Natal for part-payment of the surface layer scintillometer equipment;

owner, staff (and in particular Hamish and Jaapie) and workers of the Bellevue farm used for this research. Without their cooperation, this research would not have been possible;

neighbours and occupants of 70 Crestview Road next to the site for putting up with the phantom nighttime site visits and research team visits during the day;

Ms Jothi (Jody) Moodley (Agrometeorology) of the School of Applied Environmental Sciences, University of KwaZulu-Natal for her assistance, Mr Peter N. Dovey for part of the technical support required for this project and Mr Vivek Naiken (CSIR) for assistance with Fig. 1.2;

Meryl A. Savage for her support and encouragement;

Dr Volker Thiermann for his comments on the SLS data for cloudless days and other staff of Scintec, Atmosphärenmesstechnik AG, Germany;

Dr Rick L. Snyder (Department of Land, Air and Water Resources, University of California, Davis, California, USA) for his assistance with aspects of this work;

Dr Monique Y. Leclerc (Environmental Physics, University of Georgia, Griffin, Georgia, USA) for reinforcing the importance of footprints.

"In the beginning God created the heavens and the earth" (Genesis 1:1, The Bible).

10 Statement regarding the archiving of material

The raw data has been archived to one DVD (SLS_DATA1) and to a second as a backup (SLS_BUDATA1). The subdirectory structure for the raw data is contained in the file read_me.txt contained in the root subdirectory. All of the SLS data is space delimited. The EC, BR, SR, energy balance and automatic weather station data are comma delimited. The worked data (that is, Excel spreadsheets, files for the graphics created including Plotit and Origin graphics files) has also been archived to one DVD (SLS_DATA2) and to a second as a backup (SLS_BUDATA1). The report itself has been converted to a number of pdf files.

11 Information about this report and data handling

Initially the Microsoft Word (2000) word processing software package was used for entering text for this report. In the final report stages, the desktop publishing program Corel Ventura 10 was used. Virtually all of the computer graphics were generated using Plotit 3.1 and version 3.20k (Scientific Programming Enterprises, Haslett, Michigan). TextPad 4.6.2 was used for combining SLS and data logger files. The data required to generate the graphics was copied from Excel to Plotit using the Windows clipboard and saved in Plotit as txt files. The Plotit graphics were either copied to the Windows clipboard and pasted individually directly into Ventura frames or exported from Plotit as wmf files and then imported into Ventura. Some of the scientific graphics were generated using Origin, version 7.5 from OriginLab Corperation and copied to the Windows clipboard and pasted directly in Ventura frames. The report was printed using a Hewlett Packard LaserJet 4 printer at the 600 dpi by 600 dpi resolution. Most of the calculations for this report were performed using MicroSoft Excel (version 2002).

A List of Figures

B List of Tables

C List of abbreviations and symbols

Abbreviations

ABL	atmospheric boundary layer - same as PBL
BLS	boundary layer scintillometer that uses an extra-large aperture for measurement of C_n^2 over distances between 500 m and 10 km
BR	Bowen ratio method
BREB	Bowen ratio method energy balance method
EC	eddy covariance
ECAT	Applied Technologies eddy covariance system
ECopen	open path eddy covariance system
HPV	heat pulse velocity
IBL	inner or internal boundary layer - region of atmosphere affected by a step change in surface conditions
IRT	infrared thermometer
LAS	large aperture scintillometer for measurement of C_n^2 over distances between 500 m and 3.5 km
LIDAR	light detection and ranging system

MWS	microwave scintillometer (- see RWS)
MOST	Monin-Obukhov similarity theory, a semi-empirical theory of atmospheric turbulence
PBL	atmospheric or planetary boundary layer
RWS	radio wave scintillometer
SBL	surface boundary layer - lowest 10 to 15 % of the PBL
SLS	surface layer scintillometer for measurement of C_n^2 over distances between 50 m and 250 m
SPU	signal processing unit for SLS system
SR	surface renewal, a method for determining sensible heat flux density from high frequency measurements of air temperature at a single atmospheric level
TKE	turbulent kinetic energy
XLAS	extra-large aperture scintillometer for measurement of C_n^2 over distances between 500 m and 10 km

Roman symbols

$\%EFD$	percentage error free SLS data	%
a	air temperature amplitude for the SR method	°C
a	constant in the relationship between C_T^2 and C_n^2 (= 7.89 × 10^{-5} K hPa^{-1})	
a	regression coefficient	
a_1	proportionality constant	
a_2	proportionality constant	
$a_{buoyancy}$	buoyant acceleration of a parcel of air	m s^{-2}
A	area	m^2
A	available energy flux density $A = I_{net} + F_{soil}$	W m^{-2}
$A_{lysimeter}$	cross-sectional surface area of a lysimeter	m^2
B_1	variance of the logarithm of the amplitude of SLS beam 1 signal	
B_{12}	covariance of the logarithm of the amplitude of the received SLS beam radiation	
c	energy balance closure	W m^{-2}
c_{dsoil}	specific heat capacity of dry soil	J kg^{-1} K^{-1}
c_p	specific heat capacity of air at constant pressure (≈ 1004 J kg^{-1} K^{-1})	J kg^{-1} K^{-1}
c_w	specific heat capacity of water	J kg^{-1} K^{-1}
c_{soil}	specific heat capacity of soil	J kg^{-1} K^{-1}
C	Bowen's definition of the sum of conductive and convective heat energy flux densities $C = R(L_v F_w)$	W m^{-2}
C	concentration of scalar quantity	kg m^{-3}
C	constant used in Eq. 2.55 - vegetation type dependent	
C_n^2	structure parameter of refractive index	
C_T^2	structure parameter of air temperature	
d	SLS detector separation distance	m
d	zero-plane displacement height	m
de	actual profile water vapour pressure difference	kPa

dP	change in pressure due to a change in heat added to a thermodynamic system	kPa
dQ	heat energy added to a parcel of air	J
dt	time interval	s
dT	actual profile air temperature difference	°C or K
D	similarity parameter used in the Hsieh et al. (2000) footprint model	
D	SLS detector diameter	m
D	separation distance of surface roughness elements	m
DOY	day of year	
$D_T(r)$	air temperature structure function	°C
e_*	water vapour pressure scale of turbulence	kPa
$\overline{e}_o$	surface boundary water vapour pressure	kPa
$\overline{e}_1$	average water vapour pressure (usually over 20 min) at height z_1	kPa
$\overline{e}_2$	average water vapour pressure (usually over 20 min) at height z_2	kPa
$e_{air\ stream}$	BR air stream water vapour pressure	kPa
e_s	saturation water vapour pressure	kPa
$e_s(T_{Vaisala})$	saturation water vapour pressure at the Vaisala temperature	kPa
E'	fluctuation in entity E	various
E	turbulent kinetic energy per unit mass	J kg^{-1}
EC	eddy covariance	
$E(\kappa)$	energy spectrum as a function of wave number κ	J m^{-3}
f	uniform upwind fetch	m
f	frequency	Hz
f_B	a function that describes the decrease of B_{12} with increasing l_o, d and D	
$f_\Phi(l_o, 2\pi/\lambda)$	a function that describes the decay of refractive index fluctuations in the dissipation range of turbulence	
$f(x, z_m - d)$	footprint function at distance x from the source and a measurement height z_m for a surface with a zero plane displacement height d	unitless
F	viscous force	N
F	flux density at measurement height	W m^{-2}
F_c	carbon dioxide flux density	kg s^{-1} m^{-2}
F_E	flux density of entity E	various
F_h	sensible heat flux density (sometimes H is used)	W m^{-2}
$F_{h(correct)}$	correct sensible heat flux density	W m^{-2}
$\overline{F}_{plate}$	average plate-measured heat flux density (20-min average)	W m^{-2}
F_{soil}	soil heat flux density	W m^{-2}
$\overline{F}_{soil}$	average soil heat flux density (20-min average)	W m^{-2}
$\overline{F}_{stored}$	average soil-stored heat flux density (20-min average)	W m^{-2}
F_v	water vapour flux density	kg s^{-1} m^{-2}
$F(x, z_m - d)$	scalar flux density at distance x from the source and a measurement height z_m for a surface with a zero plane displacement height d	W m^{-2}
F_{zone}	Fresnel zone size	m
$F_{zone\ small\ aperture}$	small aperture Fresnel zone size	m
g	acceleration due to gravity	m s^{-2}

h_{beam}	SLS beam height	m
h	canopy height	m
h	height of roughness elements	m
h_{beam}	SLS beam height	m
$h_{beam\,correct}$	correct SLS beam height	m
H	sensible heat flux density	W m^{-2}
$\bar{I}_1$	mean intensity for SLS beam 1	
I_{net}	net irradiance $I_{net} = I_s - rI_s + L_d - L_u$ (sometimes R_{net} is used)	W m^{-2}
I_s	solar irradiance	W m^{-2}
j	sample lag between data points for the SR method	unitless
k	von Karman's constant ($k \approx 0.41$)	
K	general turbulent exchange coefficient	m^2 s^{-1}
K	optical wave number ($=2\pi / \lambda_{beam}$)	m^{-1}
K_h	turbulent exchange coefficient for sensible heat transfer	m^2 s^{-1}
K_m	turbulent exchange coefficient for momentum transfer	m^2 s^{-1}
K_q	turbulent exchange coefficient for quantity q	m^2 s^{-1}
K_w	turbulent exchange coefficient for latent heat transfer (water vapour)	m^2 s^{-1}
K_z	eddy diffusivity at height z	m^2 s^{-1}
KE_b	kinetic energy associated with buoyancy	J
KE_i	initial turbulent kinetic energy	J
l	breadth of surface roughness element	m
l	characteristic length	m
l	ramping period used in the SR method	s
l_o	inner scale of turbulence	mm
L or $\mathcal{L}$	Monin-Obukhov length	m
L_{beam}	transmitter to receiver beam distance	m
$L_{beam\,correct}$	correct SLS beam distance	m
LAI	leaf area index	m^2 m^{-2}
LE	latent energy flux density	W m^{-2}
L_d	long wave irradiance in the downward direction	W m^{-2}
L_o	outer scale of turbulence	m
L_u	long wave irradiance in the upward direction	W m^{-2}
L_v	specific latent heat of vapourisation	MJ kg^{-1}
$L_v F_w$	evaporation of water (latent energy flux density) - sometimes LE is used	W m^{-2}
$L_v F_{w\,lysimeter}$	lysimeter latent energy flux density	W m^{-2}
$L_v F_{w\,reference}$	reference latent energy flux density	W m^{-2}
m	number of data points collected, using the SR method, in a certain time interval	
M_{air}	mass of air	kg
n	eddy frequency	Hz
n	number of acceptable two-minute wind speed measurements between 06h00 and 18h00	
n	refractive index	

n	stability factor	
p	coefficient of a third order polynomial used to solve for the amplitude of the air temperature ramp of the SR method	$°C^2$
p	period ($= 2\pi / \omega$)	s
P	similarity parameter used in the Hsieh *et al.* (2000) footprint model	
P	atmospheric pressure	kPa
$P_{correct}$	correct atmospheric pressure	kPa
q	coefficient of a third order polynomial used to solve for the amplitude of the air temperature ramp of the SR method	$°C^3$
Q	flux density of the entity q	$s^{-1}\ m^2$
r	eddy size	mm
r	correlation coefficient	unitless
r	reflection coefficient	unitless or %
r_a	aerodynamic resistance	$s\ m^{-1}$
r^2	coefficient of determination	unitless
r_{ah}	aerodynamic resistance for sensible heat	$s\ m^{-1}$
r_{am}	aerodynamic resistance for momentum	
r_{av}	aerodynamic resistance for latent energy (water vapour transport)	$s\ m^{-1}$
r_s	canopy resistance (also referred to as the bulk stomatal resistance)	$s\ m^{-1}$
Ri	Richardson number: $Ri = \frac{g}{T}\frac{\partial\theta / \partial z}{\partial u^2 / \partial z^2}$	unitless
Re	Reynolds number	
RH	relative humidity	%
$RH_{Vaisala}$	relative humidity measured by a Vaisala sensor	%
R_{net}	net irradiance	$W\ m^{-2}$
$R(0)$	correlation function defined as the time-averaged correlation between $w'(t)$ and $w'(t)$ for a zero time lag	$m^2\ s^{-2}$
$R(\delta\tau)$	correlation function defined as the time-averaged correlation between $w'(t)$ and $w'(\delta t)$ for time lag δt	$m^2\ s^{-2}$
s	quiescent period used in the SR method	s
s	static stability parameter	
S	soil heat flux density	$W\ m^{-2}$
$S(n)$	eddy spectral density as a function of frequency n	
$S^n(r)$	the air temperature structure parameter to the n th exponent corresponding to a time lag r	$°C^n$
S_o	surface source flux density	$W\ m^{-2}$
t	time	s
$\bar{T}$	average air temperature	°C
T_1	air temperature at height z_1	°C
T_2	air temperature at height z_2	°C
$T_{correct}$	correct air temperature measurement	°C
T_{IRT}	infrared thermometer measurement of canopy surface temperature	°C
T'	air temperature fluctuation	°C
T'_{sonic}	fluctuation in the measured sonic temperature	°C

$\overline{T}$	average air temperature	°C
$\overline{T}_2, \overline{T}_1$	time-averaged air temperatures at heights z_2 and z_1 respectively	°C or K
T_*	temperature scale of turbulence	K
TKE	turbulent kinetic energy - often per unit mass	$m^2 s^{-2}$
$\overline{T}_o$	average surface temperature	K
T_{lower}	lower BR thermocouple air temperature	K
T_{upper}	upper BR thermocouple air temperature	K
$T_{Vaisala}$	temperature of the Vaisala temperature chip	°C
T_o	surface temperature	K
$T(r,t)$	air temperature at position r and time t	°C or K
T_v	virtual temperature	°C or K
T_z	air temperature at height z	°C
$T(z)$	air temperature at atmospheric level z	°C
$\overline{T}_z$	mean air temperature at atmospheric level z	°C or K
$T_{v\ parcel}$	virtual temperature of an air parcel	K
$T_{v\ surrounds}$	virtual temperature of the surrounds	K
U	horizontal wind speed	$m\ s^{-1}$
u'	fluctuation of the resolved component of the horizontal wind speed in the x direction	$m\ s^{-1}$
u_1	wind speed in the x direction	$m\ s^{-1}$
v'	fluctuation of the resolved component of the horizontal wind speed in the y direction	$m\ s^{-1}$
u_2	horizontal wind speed in the y direction	$m\ s^{-1}$
U'	fluctuation of the horizontal wind speed	$m\ s^{-1}$
u_*	friction velocity	$m\ s^{-1}$
U_a	average wind speed between height $z_o + d$ and measurement height z_m	$m\ s^{-1}$
u	horizontal wind speed in the x direction	$m\ s^{-1}$
$\overline{u}$	mean horizontal wind speed	$m\ s^{-1}$
$\overline{u}_1$	mean of the horizontal wind speed in the x direction	$m\ s^{-1}$
$\overline{u}_2$	mean of the horizontal wind speed in the y direction	$m\ s^{-1}$
v	horizontal wind speed in the y direction	$m\ s^{-1}$
vpd	water vapour pressure deficit	kPa
V	volume of air	m^3
V_{soil}	volume of soil	m^3
w	vertical wind speed	$m\ s^{-1}$
w'	vertical wind speed fluctuation	$m\ s^{-1}$
$w'(t)$	vertical wind speed fluctuation at time t	$m\ s^{-1}$
$\overline{w}$	average vertical wind speed	$m\ s^{-1}$
x	fetch distance	m
x	distance in the x-direction	m
<X>	average of SLS signal for beam 1	
x_{peak}	peak location of the footprint for sensible heat flux density	m
y	distance in the y-direction	m
<Y>	average of SLS signal for beam 2	

z	distance in the z-direction	m
z	height above ground	m
z	height above ground	m
z'	substitution for $(z-d)/z_o$	
z_1	placement height at level 1 above canopy	m
z_2	placement height at level 2 above canopy	m
z_m	measurement height	m
z_o	roughness length	m
z_{om}	roughness length for momentum	m

Greek symbols

α	weighting factor used in the SR method	
α_1	Kolmogorov constant - between 0.5 and 0.6	
β	Bowen ratio	
β	empirical function of LAI (Eq. 2.60)	
β_1	Obukhov-Corrsin constant (= 0.86)	unitless
δ	thickness of internal boundary layer	m
δe	measured water vapour pressure profile difference	kPa
δe_{CS500}	Vaisala CS500 measured water vapour pressure profile difference	kPa
δe_{HMP45C}	Vaisala HMP45C measured water vapour pressure profile difference	kPa
δ'	thickness of equilibrium sub layer	m
δT	measured air temperature profile difference	^oC
δT	finite difference in air temperature	^oC
δT_{air}	profile air temperature difference	K
δW	change in weight of a weighing lysimeter between two known times	kg
δz	depth increment	m
Δ	slope of the saturation water vapour pressure *vs* temperature relationship	Pa ^oC
Δt	time difference	s
$\overline{\Delta T}_{soil}$	average soil temperature difference from one time interval to the next	^oC
Δz	depth increment	m
ε	energy dissipation rate	W kg^{-1} or $m^2\ s^{-3}$
ε_{F_h}	fractional error in sensible heat flux density measurements	unitless
$\varepsilon_{T_{air}}$	fractional error in air temperature measurements	unitless
ε_p	fractional error in atmospheric pressure estimate	unitless
$\varepsilon_{L_{beam}}$	fractional error in beam path length measurements	unitless
$\varepsilon_{h_{beam}}$	fractional error in beam height measurements	unitless
Φ_{CT}	stability parameter for the structure parameter for temperature	
Φ_h	dimensionless stability function for sensible heat	
Φ_m	dimensionless stability function for momentum	
Φ_n	three-dimensional spectrum of refractive index inhomogeneities	
Φ_w	dimensionless stability function for latent energy	
Φ_ε	normalised dissipation rate of turbulent kinetic energy	

$\Phi_n(\kappa)$	spatial power spectrum for refractive index as a function of wave number κ	
$\Phi(w)$	energy spectrum density	
γ	psychrometric constant	Pa °C^{-1}
Γ	dry adiabatic lapse rate	°C m^{-1}
η	coefficient used to correct sensible heat flux density for stability (Eq. 2.57)	
κ	spatial wave number associated with eddy size	m^{-1}
λ	specific latent heat of vapourisation	J kg^{-1}
λ_{beam}	transmitter beam wave length	nm
λ	spectral wave length	nm
μ	dynamic viscosity of air	Pa s
θ	wind direction	degrees anti-clock-wise from N
θ_w	gravimetric soil water content	kg kg^{-1}
Θ	potential temperature	K
Θ_v	virtual potential temperature	K
ρ_a	air density	kg m^{-3}
ρ_{air}	density of air	kg m^{-3}
ρ_{parcel}	density of a parcel of air	kg m^{-3}
$\rho_{surrounds}$	density of the surrounding air	kg m^{-3}
ρ_w	density of water	kg m^{-3}
σ_1^2	variance of the intensity of SLS beam 1	
σ_{F_h}	standard deviation of a sensible heat flux density measurement	W m^{-2}
$\sigma_{F_{h,SLS40-A}}$	standard deviation of a sensible heat flux density measurement from the SLS40-A	W m^{-2}
$\sigma_{F_{soil}}$	standard deviation of a soil heat flux density estimate	W m^{-2}
$\sigma_{I_{net}}$	standard deviation of a net irradiance measurement	W m^{-2}
$\sigma_{L_v F_w}$	standard deviation of a latent energy flux density measurement	W m^{-2}
σ^2	variance of TKE	
σ_I^2	variance of the amplitude of the scintillometer beam intensity	relative units
τ	momentum flux density	Pa
υ	kinematic viscosity of air	m^2 s^{-1}
ξ	quantum yield	J kg^{-1}
ζ	dimensionless stability parameter proposed by Monin-Obukhov $(z-d)/L$	

Mathematical symbols

∂	partial derivative

D Table of contents

Chapter 1

Introduction

1.1 Abstract

The theory, use and application of the dual-beam SLS method for estimating evaporation in an open and mixed grassland community in a summer rainfall area is investigated. One of the justifications for this work is the reference, in the 1998 Republic of South Africa Water Act, to the possible prescription by the Minister, of methods for making a volumetric determination of water for purposes of water allocation and charges in the case of activities that result in stream flow reduction. Also, given the demand on water resources and the potential and/or real impact of global warming and/or climate change, it is important to consider how evaporation is to be measured or estimated with reliable accuracy and precision.

Currently there is no single accepted method that is reliable and results in adequate resolution that can provide accurate temporal and spatial evaporation measurements or modelling estimates of evaporation. The focus of this work is on evaporation estimation using micrometeorological measurement methods.

The specific objective is the use of the surface layer scintillometer (SLS) method, previously untested in South Africa, to estimate areally averaged sensible heat flux density over a mixed-community grassland canopy and comparison with measurements obtained using an eddy covariance (EC) method. The SLS methodology for evaporation estimation relies on the energy balance and in particular relies on the measurement of the net irradiance, defined by net short wave and net long wave irradiances, and the soil heat flux density and depends on the Monin-Obukhov similarity theory (MOST) for determining sensible heat flux density. Other evaporation methods used for comparison purposes also include the traditional Bowen ratio (BR) and the surface renewal (SR) method, the latter also previously untested in South Africa.

This project falls within the hydroclimatological research programme of the Water Research Commission (WRC). In this programme the project will contribute to research support for water resources assessment, management and sustainable utilisation in South Africa, by improving the methodologies for monitoring evaporation from both land and water surfaces, possibly resulting in a standard for evaporation measurement by which other methods will be judged.

A summary structure of the report on a chapter-by-chapter basis is outlined.

1.2 Motivation for this study

The 1998 Republic of South Africa National Water Act states that the Minister may make regulations: "requiring that any water use be registered" (p 19). Furthermore, the Minister may also prescribe "...methods for making a volumetric determination of water to be ascribed to a stream flow reduction activity for purposes of water use allocation and the imposition of charges" (p 20).

The Water Research Commission (2004) has called for solicited research project proposals refining tools for evaporation monitoring in support of water resource management, stating that: "This (the Act) makes it important to know (a) the degree of accuracy/precision that can be achieved when measuring or estimating evaporation using currently available methods, including those computational methods built into hydrological and agrohydrological models, and (b) how closely these values come to meeting requirements of IWRM (integrated water resource management) within the context of the Water Act. There are also other compelling water-resource related reasons for being able to monitor evaporation with sufficient confidence in the accuracy and precision of the measurements/estimates." Given the reference in the Water Act to the possible prescription, by the Minister, of methods for making a volumetric determination of water for purposes of water allocation and charges in the case of activities that result in stream flow reduction and given the demand on water resources and the potential and/or real impact of global warming and/or climate change, it is important to consider how evaporation, one of the main components of the water balance, is to be measured or estimated routinely with reliable accuracy and precision.

The need for increased food and timber production has led to dramatic increases in irrigated and forestry lands in South Africa. Agriculture and forestry faces increased competition for water by industries, municipalities and other groups. This ever-growing demand for water makes it imperative that water resource management procedures and policies are wisely implemented and improved. The accurate assessment of evaporation is essential if this is to be done.

So, what is the standard or benchmark for evaporation measurement or estimation? This important and fundamental question needs to be addressed to achieve the ideal of accurate and reliable evaporation data. Although this investigation on the SLS method for estimating evaporation will also necessarily focus on the more fundamental aspects of micrometeorological research, advances in this field will ultimately have direct benefits to water resources assessments and management processes. Examples of areas not easily addressed using the more traditional evaporation measurement techniques include amongst others: measurement of evaporation in riparian zones; determination of open water evaporation from rivers and dams (both large and small); effluent water management from saline dams in the mining environment; measurement of evaporation from slimes tailings; water use of trees and crops in agro-forestry trials; remote sensing applications; determination of baseline evaporation from natural communities (e.g. indigenous forests); irrigation research.

Since John Dalton first introduced the mass transport equation for evaporation estimation, and Penman researched the potential evaporation formulation, numerous methods for estimating or measuring evaporation have been developed. Currently, there is no single accepted method capable of providing both good spatial and temporal measurements or estimates of evaporation that is reliable and has adequate resolution.

South African researchers have had good success with the heat pulse velocity (HPV) (Dye et al. 1992, Dye and Olbricht 1993) and energy balance techniques (Savage et al. 1997). The HPV technique for estimating sap flow is based on using heat as a tracer for the flow of sap in the stem of plants. Needles and a heater probe are inserted into the stem of the plant and a pulse of heat is applied at regular intervals of time. The rate of heat movement is related to the sap flow. However, the HPV technique is suited only to mono-specific stands of trees, is problematic when scaling from single trees to whole stands and is a destructive technique - trees must be felled to calculate sapwood areas and wound size. The lack of wound size information at the time of measurement makes calculations of transpiration only possible at the end of an experiment. The stem steady state heat energy balance technique for determining sap flow has also received attention in South Africa (Savage et al. 1993, 2000).

The Bowen ratio energy balance (BREB or simply BR) method on the other hand, is well-suited to mixed species communities such as a grassland community. The BR method is a traditional method for the estimation of evaporation using measurements of profile differences in air temperature and water vapour pressure above the canopy, surface net irradiance and soil heat flux density. The technique assumes that the coefficients of exchange between the surface and the atmosphere for sensible heat [heat transferred from the atmosphere to a surface, or *vice versa*, that results in a temperature change] and latent energy are identical. The BR method is limited by constraints imposed by both fetch distances and measurement height. Fetch refers to the upwind distance of traverse across a uniformly rough surface such as a forest or a grassland surface from the instrument location until there is a discontinuous change in surface roughness. The fetch often depends on the wind direction (unless the shape of the uniformly rough surface is circular). Thus, the BR method is not suited to narrow strips (e.g. riparian zones, wetlands etc.), where fetch distances are short, or above tall vegetation where there are small gradients of air temperature and water vapour pressure (caused by the increased wind turbulence above tall canopies). These gradients may be outside the measurement resolution of the sensors particularly when placed above forest canopies. The method is critically dependent on a cooled dew point mirror sensor that is prone to bias, requires almost weekly adjustment and periodically and inexplicably occasionally ices up resulting in unacceptable data.

In recent years, direct measurements of turbulent fluxes have been achieved by eddy covariance (EC) measurements in KwaZulu-Natal (Monnik et al. 1995, Savage et al. 1995a, b). A drawback of EC measurements is that they, like BR measurements, are point measurements although both sets of measurements may represent a fairly large upwind area depending on the atmospheric stability. However, the application of the EC method is sometimes problematic. The necessary sensors for vertical wind speed, air temperature and water vapour pressure must respond very quickly (frequency of 5 Hz or greater) and at the same time must not show noticeable drift. This makes them delicate, expensive and in some cases difficult to calibrate. However, more serious is the fact that airflow distortions by the sensor, mast, etc., as well as horizontal misalignments may cause measurement errors. In addition, there are technical problems because temporal co-spectra, measured at a fixed local sensor, extend to very low frequencies. To achieve acceptable significance often demands averaging periods of several tens of minutes. Such long averaging periods reduce the temporal resolution and conflict with the requirement of atmospheric stationarity within the averaging period.

Because of these and other theoretical and practical difficulties, alternative and/or complementary flux density measurement methods have been sought. Recent investigations have demonstrated the potential of using a scintillometer to measure areally averaged sensible heat flux densities. A scintillometer measures the intensity fluctuations of visible or infrared radiation after propagation over the plant canopy of interest. The fluctuations are caused by interference after the radiation has been scattered by inhomogeneities in the refractive index of the air, the latter caused by turbulent fluctuations of air temperature and humidity. In contrast to BR and EC measurements, scintillometers provide path-averaged results. Surface layer scintillometers (SLS) have beam path lengths between about 50 and 250 m and large apertures scintillometers (LAS) usually operate over distances of between 500 m and 3 km or even up to 10 km for BLS (boundary layer scintillometer) systems. For all three types of scintillometer systems, measurement of the net irradiance and soil heat flux density terms of the energy balance is required to estimate evaporation as a residual term using the energy balance equation.

The main objective of this project is to use the SLS method, previously untested in South Africa, to obtain measurements of areally averaged sensible heat flux density and compare with measurements using the BR and EC methods and also to estimate evaporation from the additional measurements of net irradiance and soil heat flux density. The fourth method chosen for preliminary measurement comparisons is the relatively new surface renewal (SR) method, also previously untested in South Africa, for measuring sensible heat flux density. It is the least expensive of the four methods used.

This project falls within the hydroclimatological research programme of the WRC. In this programme the project will contribute to research support for water resources assessment, management and sustainable utilisation in South Africa, by improving the methodologies for monitoring evaporation from both land and water surfaces, possibly resulting in a standard for evaporation measurement by which other methods will be judged.

1.2.1 The physical processes of evaporation and transpiration

Evaporation is a physical process for which a liquid or a solid substance is transformed to a gas. In meteorology, evaporation is usually restricted to the change of liquid to gas/vapour without a change in temperature. Sublimation is used to describe the change from solid to gas. In the case of the evaporation of water, large amounts of energy are required. The process of evaporation for the most part is invisible. However, in times of drought, for example, water managers can see the depleting water levels in dams and rivers. On the other hand, evaporation is a necessary process that provides us with an inhabitable earth.

The evaporation of water exists everywhere in the hydrological cycle, from rain, land and water surfaces and from vegetation in the form of transpiration. When water evaporates from a surface, there is a removal of energy. Thus, evaporation is a cooling process. Whilst part of this energy remains latent in the atmosphere, it is released when water vapour condenses. This is an ongoing process as the average tenure of a water vapour molecule in the atmosphere is about nine days.

Thus water vapour is an energy carrier, and energy must be available to cause the water to evaporate. That part of energy flux from a surface which produces a temperature change is often referred to as sensible heat to distinguish it from latent energy. The word "latent" is derived from the Latin word *lateo* meaning hidden and is used to describe the evaporation process since there is no temperature change during the evaporation process even though a cooling effect at the surface is evident. Also, the process of evaporation is usually invisible. At 25 °C, 1 kg of water will remove about 2.44 MJ of energy from the evaporating surface if all the water evaporates. The sources of this energy in the soil-plant-atmosphere system include:

- sun (solar energy) during the day and long wave or terrestrial radiant energy at night;
- heat energy carried into the area by wind (advected energy);
- heat energy stored by vegetation and in land masses;
- heat energy stored in water bodies.

The most important of these energy sources is usually solar energy, but advected energy may on occasion be considerable.

1.2.2 Evaporation measurement methods

Most often, a water balance approach is used for the estimation of evaporation. The disadvantages in this approach (Slatyer 1967) include the low level of measurement accuracy and the difficulties of determining total evaporation during rainy periods. However, even with careful measurements, it is difficult to detect daily soil water changes to within 2 mm of water. This magnitude of error makes it unsuited for estimating daily total evaporation for many locations and times of the year.

1.2.2.1 Lysimetry

Weighing lysimeters have been used for decades to estimate evaporative loss from large containers, filled with soil, water and other chemicals and whole plants. The containers are weighed at regular time intervals to calculate evaporation. Improved instrumentation allows water loss from such containers to be measured for very short time intervals and longer from minutes to days or longer.

Lysimeters are regarded as the standard for evaporation measurement although they may require extensive engineering logistics to ensure accurate measurement and also require adequate drainage mechanisms at their base. Also, lysimetric methods are non-portable, expensive and destructive in the sense that usually a relatively large volume of disturbed or sometimes undisturbed soil is placed in a container usually of metal construction. Their lack of spatial scale and their high cost serve as a justification for the quest for alternative accurate evaporation measurement methods.

If evaporation could be measured using above-canopy methods, they would be more portable than lysimetric methods. However, such measurement methods have not been fully researched. The height placement of sensors above surfaces, in relation to the fetch distance, is important.

1.2.2.2 Transpiration

Transpiration may be measured directly using a variety of methods. Two of these, the heat pulse velocity method (Dye et al. 1992) and a stem steady state heat energy balance method (Savage et al. 2000), formed the basis of previous WRC reports.

1.2.2.3 Micrometeorological methods

Above-surface flux measurement methods are complex. Estimates of sensible heat and latent energy exchange, for example, at the canopy surface are affected by a dynamic atmosphere changing in character in time and three-dimensional space, in turn affected by radiation and the variable gaseous constituents. Over an extensive uniform stand of level vegetation, fluxes of water vapour are constant with height in the lowest parts of the turbulent boundary layer. Exchange fluxes between the canopy and the air flowing over it can be determined by measuring vertical fluxes, representative of surface fluxes, in this part of the boundary layer provided there is adequate fetch. To measure evaporation above a grassland surface, adequate fetch would ensure that the measured evaporation is not influenced by evaporation from adjacent non-grassland areas.

Four methods of determining fluxes, above a uniform stand of vegetation, from micrometeorological measurements in the boundary layer were used in this report. Two of the methods are regarded as traditional methods and two have not previously been tested in South Africa.

The direct method, known as the eddy covariance (EC) method (Swinbank 1951, Verma et al. 1992) requires simultaneous and rapid measurements of vertical wind speed and air temperature for the determination of sensible heat flux density (Fig. 1.1a). The covariance between these two measurements is a direct measure of the sensible heat flux density at the point of measurement. Most

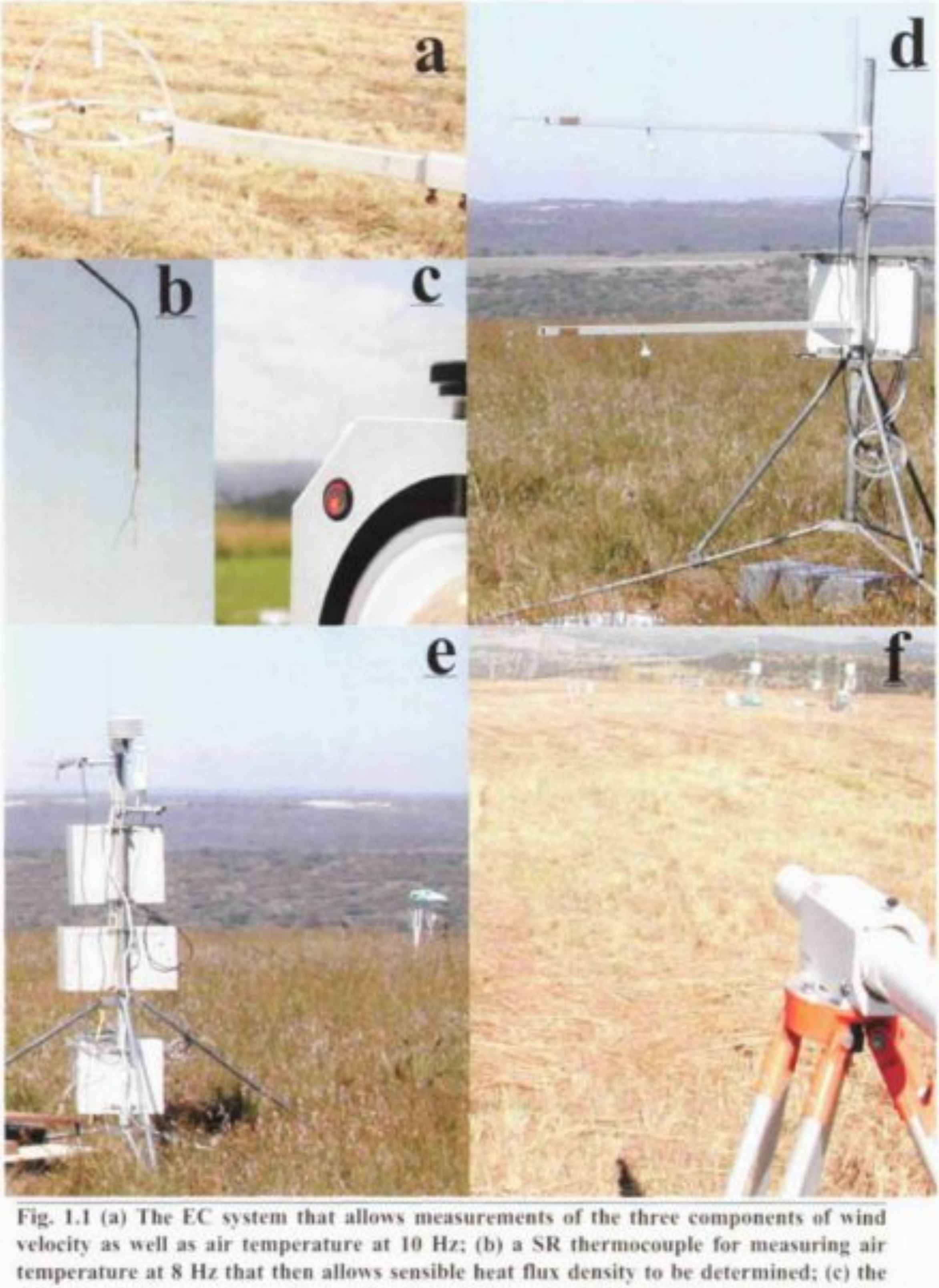

Fig. 1.1 (a) The EC system that allows measurements of the three components of wind velocity as well as air temperature at 10 Hz; (b) a SR thermocouple for measuring air temperature at 8 Hz that then allows sensible heat flux density to be determined; (c) the SLS beam when viewed at the receiver. The SLS method involves measurements of the transmission properties of a laser beam across a distance of between 50 and 250 m; (d) the BR system consists of a pair of air temperature and water vapour pressure measurements, net irradiance and soil heat flux density; (e) the EC open path system showing the open path sensor (white, upper right of the mast); (f) the SLS receiver (bottom right) and the transmitter is shown at the top left corner. Also barely in view at the top is the BR equipment as well as the EC sonic anemometer

often, a single sensor, a sonic anemometer is used for measurement of both the vertical wind speed and air temperature at high frequency and estimation of sensible heat flux density.

The BR method (Bowen 1926), an indirect method of determining fluxes (Fig. 1.1d), relies on the measurement of mean air temperatures and water vapour pressures and their gradients in the atmosphere as well as the net irradiance and soil heat flux density terms of the energy balance.

The SR method involves high frequency air temperature measurement (Fig. 1.1b) and considering air temperature ramps (positive or negative) consisting of periods during which there is no change in air temperature with time and then ramping periods for which there is an air temperature ramp. Positive ramps occur for unstable conditions and negative ramps for stable conditions. The amplitude of the ramps and the time taken for them is estimated from the high frequency record of air temperature and the sensible heat flux density calculated from the amplitude and the times.

The SLS method (Fig. 1.1c, f) is intensively investigated in this report. It is a micrometeorological method since turbulent fluctuations in air temperature affect the transmission of the scintillometer beam.

The emphasis in the research documented in this report is on the use of the SLS method for evaporation estimation largely based on measurements of sensible heat flux density and the application of the energy balance equation. These estimates however need to be compared against other methods in order that the accuracy of the SLS measurements may be ascertained.

1.2.2.4 Surface layer scintillometry

Scintillometry depends on the application of the Monin-Obukhov similarity theory (MOST). A SLS consists of a transmitter and a receiver unit separated by between 50 and 250 m with a laser beam between the transmitter and receiver. In the case of the commercially-available dual-beam SLS used in this project, two parallel and displaced beams with orthogonal polarizations are used. The receiver unit measures the radiation intensity fluctuations at 1 kHz, caused by atmospheric refractive scattering of turbulent eddies in the path of the SLS beam. The so-called inner scale of refractive index fluctuations (l_o) is calculated from the beam path length and the variances of the logarithm of the amplitude of the two beams and the structure parameter of refractive index fluctuations C_n^2 is calculated from the covariance of the logarithm of the amplitude fluctuations between the two beams. Using an iterative method, and applying MOST, sensible heat flux density may be calculated from inputs of air temperature, atmospheric pressure, beam path length and the SLS beam height above the level corresponding to a wind speed of 0 m s^{-1}. The latent energy flux density is then estimated as a residual using the energy balance equation and measurements of net irradiance and soil heat flux density.

1.2.3 Site description

Field measurements were conducted from 14 January 2003 to November 2004 above an open and mixed grassland community in the Hay Paddock area neighbouring Ashburton and close to Pietermaritzburg (Fig. 1.2), South Africa (-29.6348° S, 30.4329° E) with an altitude of 671.32 m. The average slope of the study site is 1° 15' to the SE. The fetch distances in the prevailing S-E wind direction is 135 m for the EC systems and 90 and 138 m for the SLS transmitter and receiver respectively. The fetch for the next-most dominant winds from the N-W is 117 m for the EC systems

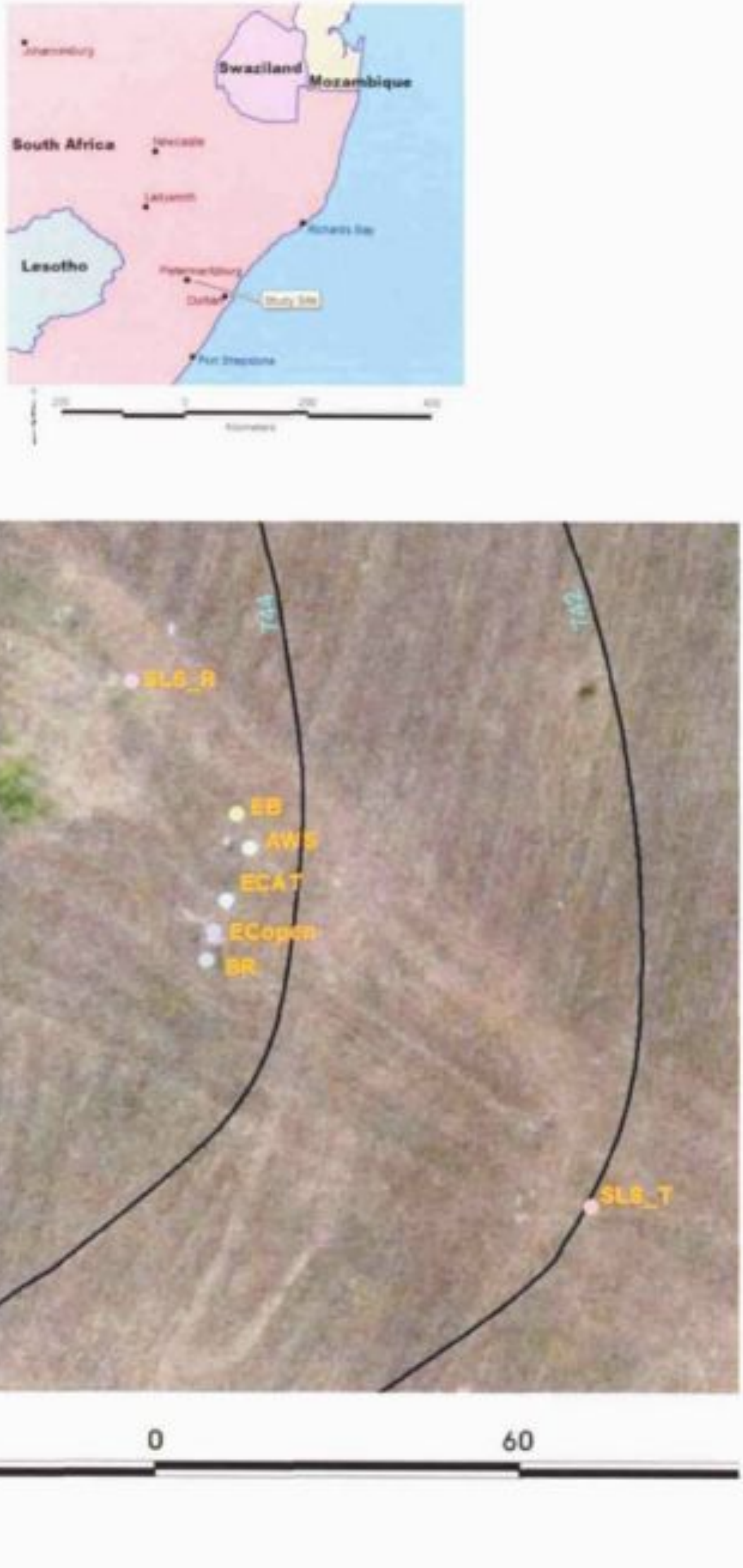

Fig. 1.2 Top: Map showing the location of the site; bottom: aerial view of the experimental site

and 146 and 114 m for the SLS transmitter (indicated by SLS_T) and SLS receiver (indicated by SLS_R) respectively. Note that the direction indicated in Fig. 1.2 is the true north direction. Magnetic north is 22° W of true N. Beyond these distances and to the south, the site is exposed and the slope increases significantly. To the north of the study area, there is a residential area and tall trees. The contours, at 2-m intervals are shown. Entry to the site is gained using the gate that is east of the light red-roofed house in the top left corner of Fig. 1.2. The SLS measurements were collected for a full 22 months apart from interruptions due to a fire, mowings, accidental damage to cables and infrequent electrical power cuts. First measurements were using a SLS beam path length of about 50 m but subsequently 100 m was used. The EC measurements commenced on 17 February 2003 using a 3-dimensional sonic anemometer although there were earlier measurements using a 1-D sonic. The SR measurements commenced in October 2003 and the first reliable measurements from the BR systems commenced in December 2003. The energy balance system, indicated by EB in Fig. 1.2, was moved to close to the BR systems after the accidental fire.

For most of the study, energy balance measurements were collected as well as routine automatic weather station and surface temperature measurements. Additional measurements included the soil water content and leaf wetness, the latter from April 2004 until August 2004.

1.3 Project aims

The original project aims were:

- to make recommendations on the feasibility, to provide guidelines for the use, and to specify the limitations of surface layer scintillometry for the estimation of areally-averaged sensible heat flux density over heterogeneous surfaces;
- to provide catchment researchers and consultants with a practical, accurate and operational tool to improve the understanding of comparative evaporative losses of water from land surfaces and water bodies associated with various forms of land use and a range of catchment conditions.

Once the project had commenced, it became clear that as complete a set of measurements as possible using a variety of methods would be more useful than obtaining an incomplete set of data for a whole range of land surfaces. To that end, all measurements were obtained from a mixed grassland site in the KwaZulu-Natal midlands. The collected data set, extending over a period of 20 months, also allowed for the influences of two mowings and a fire on the evaporation measurements to be investigated. Furthermore, it became clear that the SLS measurements in isolation would be insufficient to determine the measurement accuracy and limitation(s) of the SLS method. It was therefore necessary to perform SLS measurement comparisons with measurements obtained from the other methods such as the BR, EC and SR measurement methods.

1.4 Structure of report

There is a List of Figures, Tables and List of abbreviations and symbols following the Executive Summary. These may prove useful to the reader. The definition of a particular term may not be sufficient in the list of symbols so the reader may find a fuller definition in the body of the report. An introduction to turbulence and a brief introduction scintillometry, and the Monin-Obukhov similarity theory upon which the SLS method is based, is discussed in Chapter 2. The Monin-Obukhov similarity semi-empirical theory is a widely-accepted body of theory of atmospheric turbulence, assuming similarity between fluxes, that allows the dimensionless stability factors for sensible heat flux density to be estimated from the so-called Monin-Obukhov length. In establishing the link between turbulence and energy, the various radiation and energy balance components existing at the surface is discussed. Following this, the Kolmogorov cascade theory of turbulence is discussed. A discussion on eddy structure and stability functions leads to the Monin-Obukhov stability length and the Monin-Obukhov stability theory. Methods for the measurement or estimation of sensible heat flux density, including the scintillometer method are discussed. Most of these methods involve turbulence theory for the estimation of sensible heat flux density and application of the energy balance which in turn allows evaporation to be estimated. The theoretical basis of various methods, with special emphasis on the scintillometer method, for the estimation of sensible heat flux density, is presented.

Chapter 3 is devoted solely to the SLS method and the logistics of estimating evaporation from SLS data. The methodology associated with the use of the dual-beam SLS method is discussed in detail. The procedures associated with the crucial step of beam alignment are presented as are the procedures for the error-checking of the data post-data collection. The seasonal march of the percentage of error-free data is discussed. The assumption of a horizontal beam above a horizontal surface, a requirement of the SLS measurements, is also investigated by comparison of non-horizontal beam SLS measurements with simultaneous EC measurements. Also, for a limited time, SLS measurements at a very low beam height were compared with EC measurements. An error analysis is undertaken to determine the worst-case scenario influence of the input data on the measured sensible heat flux density as well as the influence of errors in net irradiance and soil heat flux density on the estimated evaporation.

Chapter 4, the bulk of the report, presents the comparisons between the SLS, BR, EC and SR measurements at various time scales: 2-min, 20-min, and daily estimates of sensible heat as well as evaporation estimates are compared for the various measurement methods. The influence of wind direction, in particular those perpendicular and those parallel to the beam, on the SLS and EC measurement comparisons is reported on. Also, a footprint model is improved upon and used to calculate three key footprint parameters: the peak location of the footprint, the footprint fraction itself and the 90 % fetch to measurement height ratio. This chapter is also concerned with BR measurements and in particular the possible replacement of a cooled mirror dew point sensor by a thin film polymer capacitive sensor. Measurement data from two types of polymer sensors are presented and compared with BR measurements using a cooled dew point mirror. Peculiarities of the collected SLS data such as the asymmetrical nature of the diurnal sensible heat flux density curve and the so-called counter-gradient latent energy flux densities, also receive attention in this chapter.

Chapter 5 discusses seasonal evaporation aspects of the collected data over the study period. The influence of a fire and two mowings at the site on the evaporation estimations is also discussed.

Chapter 6 presents the overall findings and recommendations for future research.

Chapter 2

Introduction to turbulence and scintillometry

2. 1 Introduction

Turbulence may be regarded as the irregular motion of air resulting in uneven currents of air. It is common, when turbulence is qualitatively described, to speak of eddies. An eddy is a rather abstract concept generally used to describe turbulence or its effects. Eddies are three-dimensional structures (i.e., that vary in x, y, and z directions) that change with time. A smoke-filled room may show turbulent flow composed of a wide range of eddy diameters, typically from millimetres to metres, referred to as length scales or the scale of turbulence. The link between turbulence and energy is often evident. For example, we can see that vertical and horizontal eddy motion is driven by energy. Unlike viscosity, turbulence is a feature of the flow of the fluid rather than a feature of the fluid itself. In establishing the link between turbulence and energy, the various radiation and energy balance components existing at the surface is discussed first. Following this, the Kolmogorov cascade theory of turbulence is discussed. A discussion on eddy structure and stability functions leads to the Monin-Obukhov stability length and the Monin-Obukhov stability theory. Methods for the measurement or estimation of sensible heat flux density, including the scintillometer method are discussed. Most of these methods involve turbulence theory for the estimation of sensible heat flux density and application of the energy balance which in turn allows evaporation to be estimated. The theoretical basis of various methods, with special emphasis on the scintillometer method, for the estimation of sensible heat flux density, is presented.

2.2 Radiation balance and components of the energy balance

Energy flux density available at the earth's surface is either sensible heat F_h (or H, in W m^{-2}), which results in a temperature change with no phase change of water, or latent energy $L_v F_w$ or LE which results in a phase change of water usually from liquid to vapour with no temperature change. The water vapour flux density (F_w in kg s^{-1} m^{-2}), multiplied by the specific latent heat of vapourization, L_v (in J kg^{-1}) is the latent energy flux density $L_v F_w$, in W m^{-2}.

For a short, horizontal and extensive surface, net irradiance I_{net} is the sum of the incoming short I_s and long wave L_d irradiances, less the reflected short wave $r \cdot I_s$ and emitted long wave L_u irradiances:

$$I_{net} = I_s - r \cdot I_s + L_d - L_u, \qquad 2.1$$

commonly referred to as the radiation balance. The net irradiance also appears as a term in the energy balance equation. For a short and flat surface, the shortened form of the energy balance equation ignores advection (both sensible and latent heat forms), the photosynthetic flux density ξF_c (W m^{-2}) [where ξ is the quantum yield (J kg^{-1}) and F_c is the flux density of carbon dioxide in kg s^{-1} m^{-2}], physically and biochemically (photosynthetically) stored heat flux densities in the canopy as they are considered negligible (Thom 1975) compared to the other energy balance components. So the important terms of the energy balance are the net irradiance and sensible heat, latent energy and soil heat flux density if advection is negligible. Rosenberg et al. (1983) used an operational definition for regional advection: that the sensible heat flux density is directed towards the surface for conditions of large positive net irradiance. Due to its complex nature, advection is usually not routinely accounted for when using methods to estimate surface sensible heat and latent energy flux densities, always in W m^{-2}.

Two sign conventions are used for energy balance terms in relating their direction to the sign assigned to their magnitude. Writing

$$I_{net} = L_v F_w + F_h + F_{soil} \qquad 2.2$$

(commonly referred to as the shortened form of the energy balance equation), the sign convention is that during the day the net irradiance (defined by Eq. 2.1) is positive with terms on the right hand side of Eq. 2.2 leaving the earth's surface being regarded as positive. The alternative convention requires that terms leaving the surface are negative:

$$I_{net} + L_v F_w + F_h + F_{soil} = 0. \qquad 2.3$$

This sign convention results in negative latent energy and sensible heat values under normal daytime conditions. This convention has been used throughout in this work. In an alternative commonly-used notation, the energy balance is given by:

$$R_{net} + LE + H + C = 0.$$

The available energy flux density A in W m^{-2} is the sum of the net irradiance above a vegetated surface and the soil heat flux density F_{soil} stored by and entering (or leaving) the soil surface:

$$\text{available energy flux density } A = I_{net} + F_{soil} = -L_v F_w - F_h, \qquad 2.4$$

where all terms are in W m^{-2}. Using the alternative energy balance sign convention and invoking the shortened form of the energy balance, viz.,

$$I_{net} = L_v F_w + F_h + F_{soil},$$

the available energy flux density is defined as follows:

$$A = I_{net} - F_{soil} = L_v F_w + F_h.$$

2.3 Closure of the shortened energy balance

If components of the energy balance are measured independently and correctly, then Eq. 2.3 should be satisfied and closure is said to be satisfied. However, the condition could still be satisfied even if two or more terms have incorrect value and that fortuitously the terms still sum to 0 W m^{-2}. It would be inconceivable however that an incorrect set would always sum to 0 W m^{-2} for each time interval. Use of the energy balance equation for independent measurements of the component terms results in:

$$I_{net} + L_v F_w + F_h + F_{soil} = c$$

where c is termed the energy balance closure (W m^{-2}). Closure is satisfied if $c = 0$ W m^{-2}. A non-zero value for c may be due to measurement errors in one or more of the component energy balance terms, although a near-zero value for c may be due to two or more of the component terms with incorrect value tending to cancel each other. As pointed out by Stannard et al. (1994), a near-zero value for c only increases confidence in the flux density measurements but does not necessarily verify them.

The spatial scales of the measurements for the component energy balance terms are different due to the nature of their measurement. For example, the source area of soil heat flux density measurements using a heat flux plate which is small in area, is very much less than 1 m^2 whereas the fraction F of the source area A_{source} measured by a net radiometer placed a distance d above the canopy is given by:

$$F = \frac{A_{source}}{A_{source} + \pi\, d^2}$$

(Savage et al. 1997). Defining $F = 0.9$, a value also used by Stannard et al. (1994) for which the net radiometer measures 90 % of the source area A_{source}, results in $A_{source} = 9\pi\, d^2$ or a source area radius of $3d$. Hence, for a net radiometer measurement height of 2 m above canopy, the source area radius is 6 m, equivalent to an area of 113 m^2. The EC measurements of sensible heat flux density are point measurements influenced by downwind source areas. The differing spatial scales of measurements tend to counter the achievement of closure especially for heterogeneous terrain (Stannard et al. 1994).

For their relatively homogeneous terrain, Savage et al. (1997) found that the mean closure value $\bar{c}$ was positive. For their heterogeneous terrain using eddy covariance (EC) measurements, Stannard et al. (1994) also found that the mean closure value $\bar{c}$ was positive. Stannard et al. (1994) listed a number of possible mechanisms associated with $\bar{c} > 0$ W m^{-2}:

the magnitude of one or both of F_h and $L_v\ F_w$ is underestimated;

the available energy flux density, $I_{net} + F_{soil}$, is overestimated;

the sensible heat or latent energy content, or both, of the air advected into the source area of the flux density measurements by the mean wind speed was less than that leaving the source area (-horizontal flux divergence);

mismatched source areas for the different measurements of the energy balance component terms.

Stannard et al. (1994) reasoned that the influence of horizontal flux divergence on $\bar{c}$ would be small. They reasoned that divergence of sensible heat flux density would tend to be opposite in sign to the divergence of latent energy flux density since wetter areas tended to be cooler and drier areas tended to be warmer. Therefore in total, these divergences would tend to be nullified. They concluded that a detailed network of air temperature, relative humidity and wind speed sensors would be required to determine the net effect of divergence at any site. They also concluded that the underestimation of sensible heat and latent energy flux densities were the major cause of the tendency for $\bar{c}$ to be positive.

If closure is not satisfied, then, for example, $I_{net} + F_{soil} > -L_v\ F_w - F_h$ (or using the alternative sign convention that $I_{net} - F_{soil} > L_v\ F_w + F_h$). Another measure of the lack of closure is the closure ratio, which using the second sign convention (Eq. 2.3) is given by:

$$\text{closure ratio} = \frac{-L_v\ F_w - F_h}{I_{net} + F_{soil}} \qquad 2.5$$

for which a closure ratio of 1 yields the shortened energy balance equation.

Han et al. (2003) found that the energy imbalance persisted in different surfaces with an average of about 20 % but that the energy balance closure was better on average in the afternoon than in the morning, possibly suggesting the underestimation of storage terms, which are usually larger in the morning.

In the case of the BR technique, for which by definition $\beta = F_h / L_v F_w$, and invoking the energy balance yields $L_v F_w = (-I_{net} - F_{soil}) / (1+\beta)$, the closure ratio is necessarily always 1. Other methods for estimating sensible heat flux density used in this report such as the EC, surface layer scintillometer (SLS) and surface renewal (SR) methods involve measurements of F_h and calculation of $L_v F_w$ by assuming a closure ratio of 1. The EC systems that measure F_h and $L_v F_w$ independently of each other make no assumption of the value of the closure ratio.

2.4 Ficks Law

A generalised statement of Fick's Law is that the flux density of an entity is proportional to the relevant concentration gradient. We assume for example that sensible heat flux density is given by:

$$F_h = \rho_{air}\ c_p\ K_h\ \partial\overline{T} / \partial z \qquad 2.6$$

where ρ_{air} (kg m^{-3}) is the density of air, c_p (J kg^{-1} K^{-1}) is the specific heat capacity of dry (unsaturated) air at constant pressure, K_h (m^2 s^{-1}) is the exchange coefficient for sensible heat flux density F_h(W m^{-2}) and $\partial\overline{T} / \partial z$ is the mean air temperature gradient (°C m^{-1}) typically averaged over a time period of 20 min and usually measured across a vertical distance of 1 m just above the canopy. The overbar for air temperature T indicates that a time period is used to obtain its average value and does not imply that it has a fixed value. In the literature, the exchange coefficient K_h is also referred to as the eddy diffusivity for sensible heat flux density. Notice in Eq. 2.6 that under normal daytime conditions, the air temperature gradient $\partial\overline{T} / \partial z < 0$ °C m^{-1} since the surface warms the air closer to the surface than air at higher elevation. Hence, under these conditions, $F_h < 0$ W m^{-2}. Similarly, we assume that the latent energy flux density is given by:

$$L_v F_w = (\rho_{air}\ c_p\ K_w / \gamma) \cdot \partial\overline{e} / \partial z \qquad 2.7$$

where K_w is the exchange coefficient for latent energy flux density $L_v F_w$ (W m^{-2}), γ (kPa K^{-1}) the psychrometric constant and $\partial\overline{e} / \partial z$ the mean water vapour pressure gradient (kPa m^{-1}) where $\overline{e}$ (kPa) is the mean water vapour pressure usually measured at the same positions as the air temperature measurements. In Eq. 2.7 under daytime evaporative demand conditions, the water vapour pressure gradient $\partial\overline{e} / \partial z < 0$ kPa m^{-1} since the water vapour pressure closer to the surface is greater than that at higher elevation. Hence, under these conditions, $L_v F_w < 0$ W m^{-2}.

In practice, $\partial\overline{T} / \partial z$ is estimated from two profile air temperature measurements and similarly for $\partial\overline{e} / \partial z$ where both gradients are negative:

$$\partial\overline{T} / \partial z \approx (\overline{T}_2 - \overline{T}_1) / (z_2 - z_1)$$

and

$$\partial\overline{e} / \partial z \approx (\overline{e}_2 - \overline{e}_1) / (z_2 - z_1).$$

For the exchange of momentum flux density τ (Pa) from the surface to the atmosphere, we assume that

$$\tau = \rho_{air}\ K_m \cdot \partial\overline{u} / \partial z \qquad 2.8$$

where K_m is the momentum exchange coefficient (m^2 s^{-1}) and $\partial\overline{u} / \partial z$ is the mean horizontal wind speed gradient in the vertical direction (m s^{-1} m^{-1}). Momentum flux density τ is an expression of drag force per unit area of level ground caused by horizontal air motion. Due to the friction that the surface offers, the wind speed gradient $\partial \bar{u} / \partial z > 0$ m s^{-1} since wind speed increases with distance away from the surface. Hence, under these conditions, $\tau > 0$ Pa.

2.5 Ohm's Law analogue to entity transport

Ohm's Law relates electrical resistance to the potential difference divided by the electrical current. Applying Ohm's Law to sensible heat flux density using $\rho_{air}\, c_p$ as a proportionality constant, for example,

aerodynamic resistance = proportionality constant × concentration difference / flux density.

Hence,

$$r_{ah} = \rho_{air}\, c_p \cdot \frac{\bar{T}_z - \bar{T}_o}{F_h}, \qquad 2.9$$

$$r_{av} = (\rho_{air}\, c_p / \gamma) \cdot (\bar{e}_z - \bar{e}_o) / L_v\, F_w,$$

and

$$r_{am} = \rho_{air} \cdot \bar{u} / \tau \qquad 2.10$$

where r_{ah}, r_{av} and r_{am} are the respective aerodynamic resistances (s m^{-1}) for sensible heat, latent energy and momentum flux density, and $\bar{T}_o$, $\bar{e}_o$ and $\bar{u} = 0$ m s^{-1} are the average surface boundary conditions for temperature, water vapour and wind speed respectively and $\bar{T}_z$, $\bar{e}_z$ and $\bar{u}$ represent the average air temperature, water vapour pressure and wind speed respectively at height z. Given that under normal daytime conditions $\bar{T}_z - \bar{T}_o < 0$ °C and since $F_h < 0$ W m^{-2} so that $r_{ah} > 0$ s m^{-1}. Similarly, under evaporative demand conditions $\bar{e}_z - \bar{e}_o < 0$ Pa and since $L_v\, F_w < 0$ W m^{-2} so that $r_{av} > 0$ s m^{-1}.

2.6 Fetch and the Similarity Principle

Vertical transport in the atmosphere is referred to as convection. Fully forced convection occurs when the associated vertical motions are generated and maintained by the surface which offers friction to the atmosphere above. In this case, we assume that a truly logarithmic vertical wind speed profile exists provided that the local effects of neighbouring trees, buildings, changes in topography, etc., on the horizontal air flow over the measurement site are insignificant. The assumption of a logarithmic vertical wind speed profile assumes that the horizontal wind speed u is related to $\ln z$ where z is the vertical height.

As a simplistic rule of thumb [often referred to as the 100:1 rule], for a canopy with height h (m), the highest measurement height should not exceed h by more than 1 % of the uniform upwind fetch:

$$\text{greatest measurement height} = h + 0.01\, f \qquad 2.11$$

where f (m) is the uniform upwind fetch (Thom 1975). This rule of thumb takes no account of atmospheric stability. So, for example for a canopy height of 2 m (h = 2 m) and a uniform upwind fetch of 50 m, the highest measurement height should be below 2.5 m. If the fetch were 250 m, then the measurement height should be below 4.5 m.

If fully forced convection is assumed to exist, the Similarity Principle is applied, viz., that

$$K_h = K_w = K_m \qquad 2.12$$

or, using Ohm's Law,

$$r_{ah}(z_1, z_2) = r_{av}(z_1, z_2) = r_{am}(z_1, z_2).$$

2.13

In other words, the aerodynamic resistance between the two levels at height z_1 and z_2 in the logarithmic wind profile region over vegetation is not related to the entity being transported (sensible heat, latent energy or momentum flux density in this case) but to the exchange coefficient (Eq. 2.12) or aerodynamic resistance (Eq. 2.13).

Since the momentum flux density (τ in Pa) is related to the momentum exchange coefficient (K_m in $m^2\ s^{-1}$) and to the wind speed gradient, $\partial u / \partial z$,

$$\tau = \rho_{air}\ K_m\ \partial \bar{u} / \partial z \text{ and } r_{am} = \rho_{air}\ \bar{u} / \tau$$

where using a unit analysis, it can be shown that

$$\tau = \rho_{air}\ u_*^2 \qquad 2.14$$

[that is, the unit of momentum flux density τ is Pa which is equal to the product of the unit of density ρ_{air} (kg m^{-3}) and the square of a wind speed (defined as the square of friction velocity) (m s^{-1})].

Hence,

$$r_{am}(z_1, z_2) = \bar{u} / u_*^2 = \int_{u_1}^{u_2} d\bar{u} / u_*^2$$

assuming that the friction velocity u_*^2 is constant with height. Hence

$$r_{am}(z_1, z_2) = \int_{z_1}^{z_2} (1/u_*^2)\cdot(\partial \bar{u} / \partial z)\cdot dz = \int_{z_1}^{z_2} (1/u_*^2)\cdot \tau / (\rho_{air}\ K_m)\cdot dz$$

$$= \int_{z_1}^{z_2} [(1/u_*^2)\cdot \rho_{air}\ u_*^2 / (\rho_{air}\ K_m)]\ dz$$

or

$$r_{am}(z_1, z_2) = \int_{z_1}^{z_2} (1/K_m)\cdot dz.$$

2.7 Neutral wind profile equation

The neutral wind profile (logarithmic) equation, applied to an extensive and flat cropped surface, is used for turbulence studies. For neutral atmospheric conditions:

$$u = (u_* / k)\cdot \ln[(z-d)/z_o] \qquad 2.15$$

where u is the horizontal wind speed (m s^{-1}), u_* is the friction velocity (m s^{-1}), k is the von Kármán constant (≈ 0.41), z the height above the soil surface (m), z_o the roughness length height (m) and d is the zero plane displacement height (m). The height at which the wind speed is 0 m s^{-1} corresponds to $\ln[(z-d)/z_o] = 0$ for which $(z-d)/z_o = 1$ or $z = d + z_o$. Typically, for neutral conditions, a graph of wind speed measured at different heights as a function of ln $(z - d)$ for a particular value of d is linear with a slope of u_*/k and a y-intercept of $-(u_*/k)\cdot\ln z_o$. Normally, an iterative procedure by choosing a range of values for d is applied, and the regression coefficient obtained for each case. In this way, the value of d corresponds to the maximum regression coefficient.

In the absence of wind profile data, assumptions are made about the approximate values for d and z_o:

$$d \approx \frac{2}{3}h \text{ and } z_{o} \approx 0.1\,h \qquad 2.16$$

(Oke 1987), based on the work by Tanner and Pelton (1960).

2.8 Boundary layers and eddy size

An understanding of boundary layers, also discussed in a previous report (Savage et al. 1998) and partly repeated here for the sake of completeness, is crucial in this report. Micrometeorology focuses on phenomena that occur in the comparatively shallow layer of influence of the earth's surface. This layer is often referred to as the planetary boundary layer (PBL) or the atmospheric boundary layer (ABL). In this layer, the friction of the earth's surface causes significant exchange of energy, mass and momentum between the surface and the atmosphere. Sharp variations in the properties of flow of variables such as wind velocity, air temperature and mass concentration ([CO_2] and water vapour pressure, for example) also occur in this boundary layer. The PBL extends upwards to a fairly sharp boundary between the irregular, turbulent motions within, and the considerably smooth laminar flow of the free atmosphere above the PBL to a height of the order of 10^3 m varying from 100 to 2000 m (Elliot 1958, Brutsaert 1982 (Fig. 2.4), Arya 1988).

The surface boundary layer (SBL), about the lowest 10 to 15 % of the PBL, has received a great deal of attention since in this layer most of our human activities take place. This layer also contains most humans, animals and vegetation. Of more interest to micrometeorologists is the inner layer or internal boundary layer (IBL) which is defined by Brutsaert (1982) as the region of the atmosphere affected by a step change in the surface conditions. In other words, it is the height up to which a disturbance (a step change in surface cover) has been propagated (Fig. 2.1), and is thus the appropriate layer in which to perform micrometeorological measurements. The IBL may extend from 1 m (in extremely stable nocturnal inversion conditions) to 500 m (in convective, unstable conditions).

A two-dimensional depiction of boundary layers including, the IBL, following a discrete step change of surface roughness (from smooth to rough), is shown in Fig. 2.1.

In the case of the Bowen ratio (BR) technique, for example, the measurement of water vapour pressure and air temperature gradients between the two levels in the atmosphere must be done in the transition zone of the IBL (Fig. 2.1), in order to correctly assess the respective flux densities. The transition zone would be above the roughness sub-layer (Fig. 2.1) and ends where the effects of the surface are no longer felt. The vertical profiles of water vapour content, wind speed and air temperature approach a new equilibrium with the active surface. Only once the boundary layer stops growing upward has the air layer become representative of the new surface. The extent of the uniform upwind fetch and the type of surface change (rough to smooth *vs* smooth to rough, and moist to dry, etc.) will determine the thickness of the IBL.

2.8.1 Inertial sub-layer

Measurement of the extent of the boundary layer is difficult as it fluctuates depending on both the atmospheric stability conditions and the stage of crop growth, via the influence of z_o, where $z_o \approx 0.1 \times h$ where h is the canopy height. Perhaps due to this fact, an intermediate layer, the inertial sub-layer, has also been defined (Raupach and Legg 1984), and further confounds an absolute definition of the outer limit of the boundary layer (Fig. 2.1).

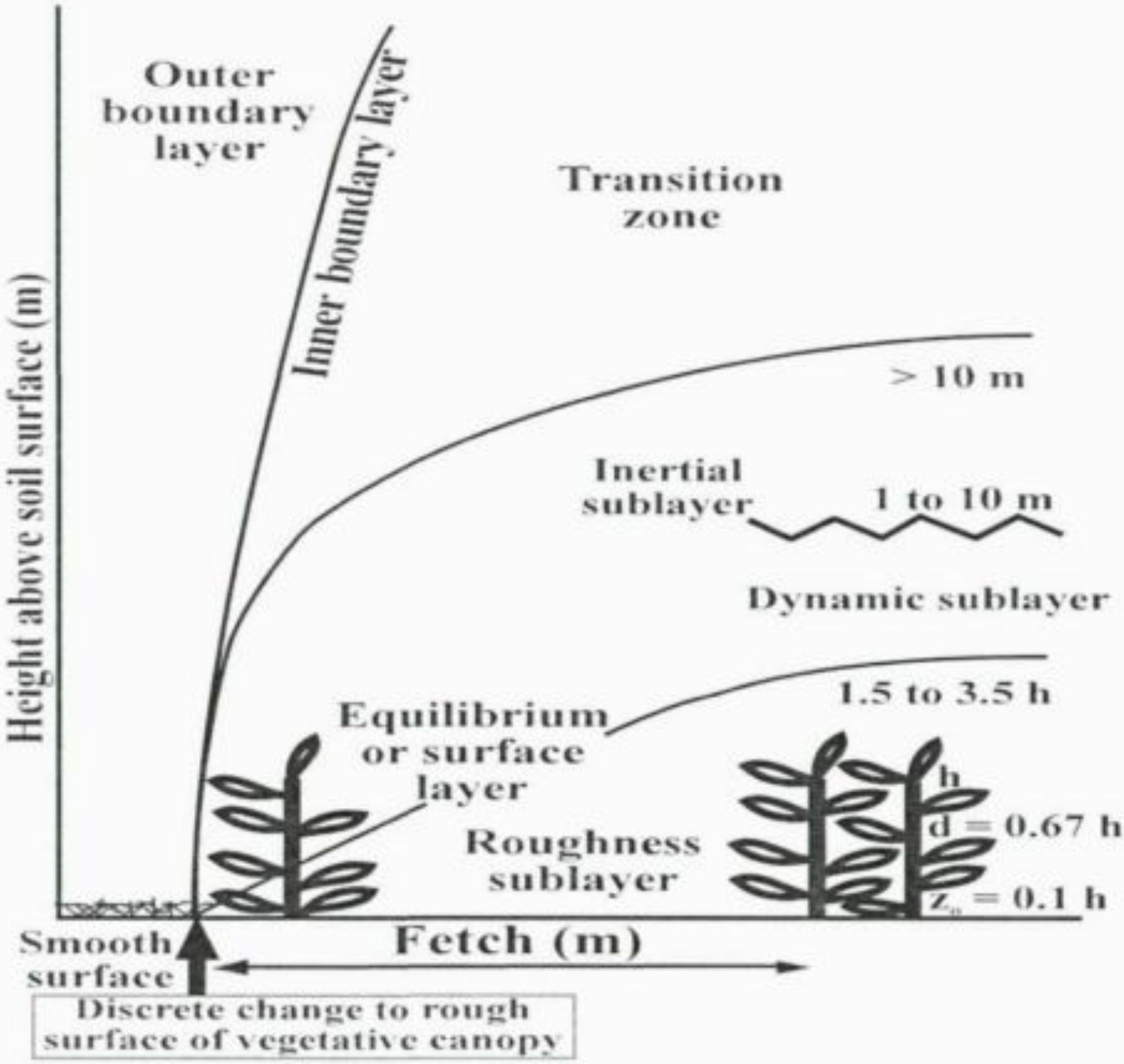

Fig. 2.1 Diagrammatic representation of the two-dimensional inner (internal) boundary layer problem (after Rosenberg 1974, Oke 1978, Brutsaert 1982, Raupach and Legg 1984, Heilman et al. 1989)

2.8.2 Internal equilibrium sub-layer

The internal equilibrium sub-layer is the lower portion of the boundary layer which has once again come into water vapour pressure, air temperature and momentum equilibrium with the surface (Fig. 2.1), defined by Brutsaert (1982) as the region where the momentum flux density is within 10 % of the value at the surface. The roughness of the surface governs the thickness of the internal equilibrium sub-layer and, thus for BR measurements, the lowest height setting of the lower measuring arm for adequate horizontal spatial homogeneity. More accurately, the minimum sensor height is governed by the vertical amplitude of the surface roughness. As a rule of thumb, five times the roughness structure may be used as the lowest measuring height (where horizontal patchiness of air temperature and humidity are smaller than the sample height) (Tanner 1963, Brutsaert 1982). The measurement of the roughness structure or elements is taken from z_o to the top of the average structure extending above z_o (Brutsaert 1982). Garratt's (1978) data indicated a minimum level of three to five times the roughness elements. Consequently, the minimum level should be set conservatively high to decrease the margin for error. This recommendation will however need to be viewed against the available fetch should this be limited.

The thickness of the internal boundary layer δ for stable conditions, may be calculated using the Munro and Oke (1975) equation:

$$\delta = x^{0.8}\, z_o^{0.2} \qquad 2.17$$

where x is the fetch (m) and z_o is the momentum roughness length of the surface (m). Instability will increase boundary layer thickness (Heilman et al. 1989).

The use of Eq. 2.17 under unstable conditions would be expected to increase boundary layer thickness (Munro and Oke 1975, Heilman et al. 1989). The momentum roughness length may be obtained from wind speed profiles, or from the approximation $z_o \approx 0.13\, h$ (Tanner and Pelton 1960) or $z_o = 0.1\, h$ where h is the canopy height. Using these values in Eq. 2.17, for a range of fetches, it can be shown that the boundary layer thickness is most dependent on the fetch and only slightly dependent on the roughness of the cover. The IBL makes up about 15 % of the total atmospheric boundary layer ABL, but of this 15 %, most is made up of a transition zone. This layer is in the process of reaching complete equilibrium with the characteristics of the new surface over which it is now flowing. In the transition zone the shear stress is expected to vary with height, which is in contrast to early theories which assumed equilibrium in the transition zone, thereby leading to the misnomer for this layer "the equilibrium sub-layer".

Air flowing from smooth to rough surfaces must decelerate from the ground upwards due to the increased shear stress caused by the greater surface roughness (as indicated by the roughness length z_o), and the wind speed profile therefore deviates from the logarithmic wind speed profile.

The extent of this equilibrium sub-layer has been found to be approximately 10 and 5 % for air flowing from relatively smooth to rough and rough to smooth transitions respectively (Brutsaert 1982), and is thus estimated from:

$$\delta' = 0.1 \cdot x^{0.8}\, z_o^{0.2}.$$

The major portion of the equilibrium layer is the upper-most inertial sub-layer where an assumption of constant stress is not too far from the truth, for the first few tens of meters (Brutsaert 1982). Flux gradient type (K-theory) models are based on assumptions of constant shear and require measurements to be made within this layer. Brutsaert (1982) pointed out that constant shear and stress imply that the wind speed profile has adjusted to be fully logarithmic, and the flux densities are therefore nearly constant with height. However, it has been found possible to successfully formulate Similarity hypotheses without this constant stress assumption (Brutsaert 1982), thereby strengthening the argument in favour of the assumption of Similarity used for example in the BR method.

In the lower portion of the inertial sub-layer under non-neutral conditions, is found the dynamic sub-layer in which water vapour and sensible heat flux density may be considered passive admixtures, and so do not affect (and are not affected by) the flow of air and momentum. Under neutral conditions, the whole equilibrium sub-layer takes on these characteristics. It follows that for other than neutral conditions, in the majority of the equilibrium layer, the movement of water vapour and sensible heat are actively strengthened or suppressed depending on the atmospheric conditions. Instability leads to eddies which are larger in their vertical than their horizontal dimension. This aids buoyancy, compared to stable conditions where vertical movements are damped by the opposite set of circumstances (e.g., Thom 1972).

In the upper portion of the inertial sub-layer, the surface-defined scales of surface roughness element height h, breadth l, and separation D, are not dynamically significant, and so the friction velocity u_* (which scales the constant momentum flux density), and the element height itself are the only factors which control the flow (e.g., Thom 1972).

Very close to the roughness elements of the surface, the turbulence structure is influenced by the wakes generated by the elements, establishing a roughness sub-layer (Raupach and Legg 1984) as illustrated diagrammatically in Fig. 2.1. This roughness sub-layer is influenced by factors such as the distribution and structure of foliage elements and the spacing between plants. Thus no simple expression for an exchange coefficient for any entity K_q is possible without including h, l, and D.

It is well known (Corsin 1974) that gradient diffusion models such as are applied in the BR method can only be justified when the length scale of turbulence is much smaller than the length scale over which mean gradients must change appreciably. In inhomogeneous turbulence such as is found in this layer, these two length scales are of the same order (Tennekes and Lumley 1972), so measurements should not be taken within this layer. In the literature, the roughness sub-layer has also been termed the canopy, interfacial, viscous or internal equilibrium sub-layer. The roughness sub-layer is the lower portion of the boundary layer where the viscosity and the molecular nature of K_h and K_w must be taken into account. Over a rough surface it extends to a height of approximately 1.5 to 3.5 h (Brutsaert 1982).

2.8.3 Atmospheric conditions and the planetary boundary layer

In laminar boundary layers, the transfer of momentum, mass and sensible heat is determined by the vertical atmospheric concentration gradient profiles, as well as by diffusivities associated with molecular agitation (- see Eqs 2.6 to 2.8). Laminar conditions are, however, almost always displaced by a turbulent boundary layer found above vegetated surfaces during the sunlight hours. In turbulent transfer theory, the same transfer principles are thought to apply, but the diffusivities are associated with turbulent eddies (which are larger by many orders of magnitude) (e.g., Arya 1988).

Most work on boundary layer theory deals with wind speed (or momentum) profiles as these are more easily measured than the entities of heat and water vapour which are then commonly assumed to follow the same rules.

The depth of the turbulent boundary layer, δ (m), is however mainly related to the extent of the uniform upwind fetch. The thickness of the internal boundary layer is dictated by wind speed profiles or momentum transfer considerations, and oftentimes the subscript m notation is used (much as the roughness length z_o should strictly be denoted z_{om}). The depth or extent of the inner layer, then, may be calculated using the Munro and Oke (1975) power equation (Eq. 2.17) for stable conditions.

2.8.4 Boundary layer limitations on the placement of sensors

Campbell (1973) pointed out that the Bowen ratio is the ratio of turbulent sensible and latent heat fluxes and the measurements must therefore be carried out only in the turbulent region of the PBL. Campbell (1973) further noted that the atmosphere is laminar close to the surface for varying thicknesses, and this may differentially affect the transfer of heat or water vapour. Thus, if the laminar layer is thin, little difference will be evident, but under windless free convection conditions, the growth of this layer may selectively hinder transport.

Since the roughness characteristic of the surface governs the thickness of the internal equilibrium sub-layer, it establishes the lowest height setting of the lowest measuring sensor used in aerodynamically based studies to obtain adequate horizontal spatial homogeneity. The minimum sensor height is governed by the vertical amplitude of surface roughness, with the implication that the rougher the surface the further removed from the surface the sensors must be. As mentioned previously, as a rule of thumb, five times the roughness structure may be used as the lowest measuring height (where horizontal patchiness of air temperature and water vapour pressure measurements are smaller than the sample height) (Tanner 1963, Brutsaert 1982).

The principle of profile-based theories, according to Brutsaert (1982), requires a uniform upwind fetch of some 50 to 100 m at the least for measurements to be taken up to 1 m above ground. This implies that to take all wind directions into account, the measurements must be done in the centre of an area of uniform cover large enough to allow the development of an internal boundary up to the measurement height. Furthermore, it is required that wind over the fetch distance has come into equilibrium with the evaporating surface and is thus representative of the energy flux density conditions at the point of measurement. A further prerequisite is that the sensors are placed within that boundary layer, and in the "safe" region of the atmosphere. Thus, it would seem that although it is desirable to measure exclusively within the equilibrium sub-layer, conditions within the entire internal boundary layer are suitable for flux gradient measurements.

2.8.5 Blending height

The blending height may be defined as the height above which there is horizontal homogeneity by turbulent mixing (- blending) of the fluxes - in other words, the signatures of the individual surface patches disappear above the blending height (Mahrt 1996). The upper limit of the individual internal boundary layers of different surface patches may be used to estimate the blending height. Above this boundary layer height, the flow is not affected by surface heterogeneity. Expressions for the blending height include the length scale of horizontal heterogeneities, friction velocity and wind speed. A way of ensuring that the measured flux is spatially representative is to use a placement height above the blending height. Schmid and Lloyd (1999) found that the blending height was considerably affected by stability. In their investigation of scalar fluxes from heterogeneous terrain, Albertson and Parlange (1999) found that the water vapour flux field blended more efficiently than the sensible heat flux field for similar surfaces.

2.8.6 Conclusion

For micrometeorological measurements, unfortunately, no visible phenomenon exists to give a clue as to what measurement level is too low or too high, and even if one did exist, it could vary continuously according to atmospheric conditions from hour to hour and day to day. The measurements required to ascertain these heights will require equipment often of greater complexity than that of the experimental equipment. A conflict exists between measuring flux profile variables too close to the surface and too far from the surface. When flux profile equipment is set up, then, these height considerations are often not given the attention they deserve, and intuitive guesses of what levels to use have to be made.

In summary, sensors for flux profile and EC measurements cannot be set too low for fear of introducing "local effects" thereby not satisfying the assumption of homogeneity of cover. At the same time, the sensors cannot be too far removed from the surface or else they will be out of the region affected by the surface conditions. These points are, in fact, the satisfaction of the fetch requirement expressed in another way.

The problem therefore remains, that due to the attenuating nature of the water vapour pressure and air temperature gradients, the points at which gradient differences are measured must be as close to the canopy surface as possible. In order to measure the very slighest gradient, and to increase precision, the greatest possible displacement between the two points is required. The topmost sensors must therefore be as high as is practical, the limits for these requirements being set by the above two constraints.

Sharma (1987) pointed out that measurement heights close to ground are desirable since this minimizes both advection, and the effect of buoyancy on the exchange coefficients.

Taller vegetation, especially forests, above which gradients are smaller, will therefore substantially increase the height requirements of the measuring sensors. These requirements may thus limit the successful use of the method to shorter crops, or, to taller vegetation with very large areas of common cover and thus extensive fetch.

2.9 Characteristics of turbulence

Webster's Dictionary defines turbulence as a "...state of disturbance, violent agitation, or great perturbation". Terms that frequently arise in so-called definitions of turbulence include chaotic, erratic, irregular, random, disordered, rotational, diffusive, dissipative, non-linear, three-dimensional. Turbulent flow may not be totally random and may in fact contain some degree of order. Furthermore, turbulence consists of a number of length scales, typically from 10^3 m to 10^{-3} m. Within the context of evaporation measurement, turbulence is responsible for transferring heat, momentum and mass (water vapour, carbon dioxide, and other gases) between the biosphere and the atmosphere. Turbulence is characterized by a number of measures. Early work showed that turbulence is associated with high Reynolds numbers. However, to define the Reynolds number, we first have to understand and define three types of forces: buoyancy forces, inertial forces and viscous forces.

2.9.1 Buoyancy forces

The Universal gas equation shows that the density of a fluid is inversely proportional to the temperature (in K) of the fluid for a constant pressure. Also variations in atmospheric humidity (and air temperature) in the planetary boundary layer therefore result in fluid density differences, referred to as density stratifications.

The consequences of these stratifications is that parcels of air moving up or down in the atmosphere may have a density different from that of their surroundings. In the presence of gravity, the difference in density between the parcel and the surrounding air leads to a buoyancy force that will either accelerate or decelerate the vertical motion of the air parcel. Following the treatment by Byers (1974) and using the Archimedes principle, the buoyant acceleration of a parcel of air is given by:

$$a_{buoyancy} = g \cdot (\rho_{surrounds} - \rho_{parcel}) / \rho_{parcel}$$

where g is the acceleration of gravity (m s^{-2}). So if the air parcel is less dense than its surrounds, it will rise and *vice versa*. Invoking the ideal gas law, it can be shown that:

$$a_{buoyancy} = -g \cdot (T_{v,surrounds} - T_{v,parcel}) / T_{v,surrounds}$$

or

$$a \approx -\frac{g}{T_{v,surrounds}} \cdot (\partial T_{v,surrounds} / \partial z - \partial T_{v,parcel} / \partial z) \cdot \Delta z.$$

Since vertical motions in the planetary boundary layer, which carry parcels of air vertically upward or downward, occur rapidly, we assume that the changes in thermodynamic properties of such parcels are adiabatic. That is, using the first law of thermodynamics the heat energy added to the parcel per unit volume is given by the work done minus the change in pressure dP:

$$dQ = \rho_{air}\ c_p\ dT - dP.$$

So if the process is adiabatic (that is $dQ = 0$ with no change in heat energy), then $dQ = \rho_{air}\ c_p dT - dP$ where from the hydrostatic equation: $\partial p / \partial z = -\rho_{air}\ g$ and hence $\rho_{air}\ c_p\ dT = -\rho_{air}\ g \cdot dz$ or $\partial T / \partial z = -g / c_p \approx$ -0.98 °C/100 m. Most often, the symbol Γ is used for $-g/c_p$. Hence, finally,

$$a_{buoyancy} = -\frac{g}{T_{v,parcel}} \cdot (\partial T_v / \partial z + \Gamma) \cdot \Delta z$$

where $\partial T_v / \partial z + \Gamma$ is defined in terms of the virtual potential temperature gradient $\Theta_v \cdot \partial \Theta_v / \partial z = \delta T_v / \delta z + \Gamma$ where Θ_v is the virtual potential temperature.

The static stability parameter s is defined as

$$s = (-g / T_v) \cdot \partial \Theta_v / \partial z,$$

where for stable conditions $\quad s > 0, \partial \Theta_v / \partial z > 0 \text{ or } \partial T_v / \delta z > -\Gamma,$

and for unstable conditions $\quad s > 0, \partial \Theta_v / \delta z > 0 \text{ or } \delta T_v / \delta z < -\Gamma,$

and for neutral conditions $\quad s < 0, \partial \Theta_v / \partial z < 0 \text{ or } \delta T_v / \delta z = -\Gamma.$

The meteorology literature also characterises an atmospheric layer as follows:

$$\text{inversion layer } \delta T_v / \partial z > 0,$$

$$\text{isothermal layer } \delta T_v / \delta z = 0,$$

$$\text{adiabatic layer } \delta T_v / \delta z = -\Gamma,$$

$$\text{superadiabatic layer } \delta T_v / \delta z < -\Gamma,$$

and

$$\text{subadiabatic layer } -\Gamma < \delta T_v / \delta z < 0.$$

2.9.2 Inertial forces

Most introductory books on physics define inertia as the tendency of any state of affairs to persist in the absence of external influences. In other words, inertia may be defined as the physical force that keeps something in the same position or moving in the same direction. Therefore, in a gas, the inertial force is proportional to the acceleration of the gas particles at any point in space and time. The faster the particle moves, the greater is the force of inertia. Not surprisingly therefore, the inertial force is related to the square of the speed of the particle. That is, it is related to the kinetic energy of the particle, viz., the product of the mass and the square of the particle speed.

2.9.3 Viscous forces

The viscosity of a fluid is a molecular property indicating a measure of the resistance of the fluid to deformation. In other words, in the case of fluid flow, viscosity is responsible for the frictional resistance between adjacent fluid layers. The resistance force per unit area is called the shearing stress τ (Pa). The shearing stress τ is directly proportional to the velocity gradient:

$$\tau = \mu\,(\partial u / \partial z)$$

where the proportionality constant μ is defined as the dynamic viscosity (Pa s). In fluids, more commonly, the kinematic viscosity υ ($m^2\ s^{-1}$) is used:

$$\upsilon = \mu / \rho$$

where ρ (kg m^{-3}) is the fluid density. The viscous force F per unit mass due to a shearing stress τ, where volume $V = A \cdot z$ for area A and depth z is given by:

$$\tau = (1/\rho)\times \partial F / \partial V = (1/\rho)\times \partial F / \partial (A \cdot z) = (1/\rho)\times \partial \tau / \partial z$$

$$= (1/\rho)\times \partial (\mu \cdot \partial u / \partial z) / \partial z = \partial (\upsilon \cdot \partial u / \partial z) / \partial z = \upsilon (\partial^2 u / \partial z^2). \qquad 2.18$$

The kinematic viscosity of air is approximately $\upsilon = 1.5 \times 10^{-5}\ m^2\ s^{-1}$.

2.9.4 Inertial and viscous forces compared: Reynolds number

The inertial force per unit mass is equal to the fluid acceleration or

$$\partial u / \partial t = (\partial u / \partial z) \cdot (\partial z / \partial t) = u \cdot (\partial u / \partial z). \qquad 2.19$$

The equations of motion for the atmosphere deal with the conservation of energy, mass and momentum. The derivation of these equations of motion are outside the scope of this work. An important issue though is that the momentum conservation equation includes inertia terms of the form $u \cdot (\partial u / \partial x)$ [from Eq. 2.19] and viscous terms which include terms of the form $\upsilon \cdot (\partial^2 u / \partial x^2)$ [based on Eq. 2.18] where u and x (also referred to as l) are characteristic velocity and length respectively and υ is the kinematic viscosity.

So the inertial forces are of the order u^2 / l and the viscous forces are of the order of $\upsilon\, u / l^2$. The Reynolds number Re is an estimate of the ratio of these two forces:

$$Re = \frac{\text{inertial forces}}{\text{viscous forces}} = \frac{u^2 / l}{\upsilon\, u / l^2} = \frac{u\, l}{\upsilon}. \qquad 2.20$$

If $Re < 1$, then viscous forces dominate and the flow will be dominated by viscosity. If $Re > 1$, then the inertial effects are more dominant than the viscous effects. It must be emphasised however that turbulent flow must be treated statistically so statements such as "for $Re > 1$, viscous forces are negligible" need to be viewed from a statistical point of view.

2.9.5 Characteristics of boundary layer spectra

Turbulence may be characterised by turbulent spectra and cospectra scales of motion that contribute to the production and dissipation of energy (Kaimal and Finnigan 1994). The spectrum of boundary layer turbulence may range from millimetres to several kilometres in spatial scale and from seconds to hours in temporal scale.

2.9.5.1 Power spectrum of turbulence

The total kinetic energy of the atmosphere is the sum of the time-averaged flow (the mean kinetic energy MKE) and the turbulent kinetic energy TKE. In this report, we are concerned with the TKE.

The spectra of an atmospheric variable indicates the spread or the spectrum distribution of the atmospheric variable over a wavelength or a period of time. So, for example, if the atmospheric variable is one of the three components of wind velocity, then the spectrum would indicate the distribution of kinetic energy over wavelengths or periods. The wave number κ (m^{-1}) is inversely proportional to the wavelength which in turn is proportional to the length scale of the eddy l:

$$\text{wave number } \kappa = 2\pi / l.$$

In the case of the EC method, for example, covariances are used to estimate the sensible heat and momentum flux density. A cospectral analysis can indicate the choice for the averaging period for covariance in order to include the contributions of all the relevant eddies.

Two types of spectra are usually considered for atmospheric turbulence: spatial spectra and temporal spectra. In the case of spatial spectra, measurements are made at differing positions and the spectrum of measurements is displayed as a function of spectral wavelength or spectral wave number. In the case of temporal spectra, used more often than spatial spectra, measurements are made at one position but at different times. The time scale between measurements may vary depending on the application. For example, in the case of EC measurements, the time scale is typically 0.1 s (equivalent to a frequency of 10 Hz) and for surface layer scintillometry, the frequency is typically 1 kHz.

Concentrating on the temporal spectrum of atmospheric variables, for example, vertical wind speed fluctuation w' measured at time t is compared, by correlation, with that measured at time $t+\tau$. Using the notation and a treatment similar to Sorbjan (1989), the correlation function $R(\tau)$ defined by:

$$R(\tau) = \overline{w'(t)\, w'(t+\tau)}$$

depends only on the lag time τ between the two measurements $w'(t)$ and $w'(t+\tau)$. For a zero lag time, $R(\tau) = R(0)$ is a measure of the kinetic energy in the vertical since kinetic energy is defined as one half the mass times the square of wind speed. For a zero time lag, $R(0)$ is also the variance σ^2 since $R(0)$ is the mean square deviation of the vertical wind speed. Using Fourier analysis the energy spectrum density $\Phi(\omega)$ is used to describe the frequency distribution of TKE, where $\omega = 2\pi / p = 2\pi\, n$ is the frequency in radians s^{-1} and where p is the period (s) and n is the frequency (Hz):

$$\Phi(\omega) = (\frac{2}{\pi}) \int_0^{\infty} R(\tau) \cos \omega\tau \, d\tau$$

where

$$R(\tau) = (\frac{2}{\pi}) \int_0^{\infty} \Phi(\omega) \cos \omega\tau \, d\omega$$

where

$$R(0) = \overline{w'^2} = \int_0^{\infty} \Phi(\omega) \, d\omega$$

Since $R(0)$ is related to TKE, the contribution by eddies with frequencies between ω and $\omega + d\omega$ is given by $\Phi(\omega)\, d\omega$ and the total contribution by eddies of all frequencies is $\int_0^{\infty} \Phi(\omega)\, d\omega$. More commonly, an eddy spectral density as a function of frequency n is used, $S(n)$, where $S(n) = 2\pi\ \Phi(\omega) = 2\pi\ \Phi(2\pi\ n)$:

$$R(0) = \int_0^{\infty} \Phi(\omega)\, d\omega = 2\pi \int_0^{\infty} \Phi(2\pi\ n)\, dn = \int_0^{\infty} S(n)\, dn$$

where $$\sigma^2 = R(0).$$

In summary, the eddy spectral density function for vertical wind speed, is defined as follows:

$$\int_0^{\infty} S(n)\, dn = \overline{w'^2} = \sigma^2.$$

Plots of the spectral density function are usually with $n\,S(n)$ as a function of $\ln n$ instead of $S(n)$ as a function of n. The reasons for this are partly due to the fact that the variance is unchanged since:

$$\sigma^2 = \int_0^{\infty} S(n)\, dn = \int_0^{\infty} n\,S(n)\, d(\ln n)$$

since from calculus $d(\ln n) = (1/n)\,dn$. Of particular note though from this last equation: since $n\,S(n) \to 0$ for $n \to 0$ correspond to a minima of the plot and that for finite variance σ^2, if $n \to \infty$ then $n\,S(n) \to 0$. In other words the plot of $n\,S(n)$ as a function of frequency n tends to 0 at both the low frequency and at the high frequency ends. Therefore the maximum of $n\,S(n)$ must occur somewhere between low and high frequencies.

Furthermore, a logarithmic plot more clearly displays eddies of high and of low frequencies compared to a linear plot. Usually, the interest is in the display of a range of frequencies that extend over several orders of magnitude and a logarithmic plot would reveal more details over this frequency range. Also, logarithmic plots presents constant powers of n as straight lines with a slope equal to the magnitude of the power (Shaw undated). The main disadvantage of the logarithmic plot however is that the frequencies are not properly weighted since equal areas under the curve no longer represent equal contributions to the total variance or covariance.

Frequently, instead of plotting $n\,S(n)$ as a function of frequency n, a plot of $E(\kappa)$ as a function of $\ln(\kappa)$ is employed, where $E(\kappa)$ represents the energy spectrum for a range of turbulence conditions and κ is the spectral wave number. A logarithmic plot is used to display the energy spectrum for a range of wave numbers over several orders of magnitude.

2.9.5.2 Spectral regions

Kaimal and Finnigan (1994) present three major spectral regions with regard to boundary layer flow, indicated by A, B and C in Fig. 2.2 where the energy spectrum is plotted as a function of the spectral wave number κ:

A. the energy-containing range which contains most of the turbulent energy and in which energy is produced by buoyancy and shear;

B. the inertial sub-range where energy is neither produced nor dissipated, cascading down to smaller and smaller scales;

C. the energy dissipation range in which TKE is converted into internal energy acting to raise the temperature of the fluid and is lost to the atmospheric boundary layer. This energy conversion occurs predominantly in the very smallest scales of motion, referred to as the dissipative scales, through the

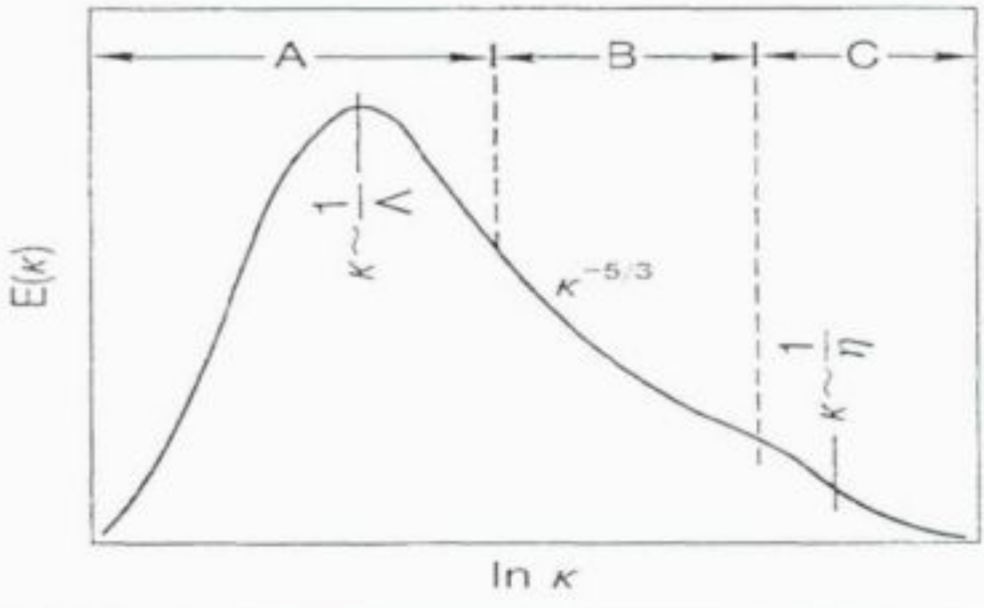

Fig. 2.2 The energy spectrum $E(\kappa)$ associated with turbulence for a range of wave numbers κ for the various boundary layer flows (taken from Kaimal and Finnigan 1994): A corresponds to regions of energy production, B to the inertial sub-range of turbulence and C to the dissipation range where kinetic energy is converted to internal energy acting to raise the temperature of the fluid. The integral length scale of turbulence is denoted Λ and η denotes the Kolmogorov microscale of length

cascading of energy through eddies of smaller and smaller sizes. By its very nature then, turbulence requires a continuous supply of kinetic energy if it is to be maintained. Turbulence can gain this energy from buoyant convection and/or the mean flow of the fluid. Notice the hump in the curve in this region of Fig. 2.2. This will be discussed in greater detail later.

The maximum of the energy spectrum, as a function of the wave number $\kappa = 2\pi / \lambda$ where λ is the wavelength, which is related to the length scale of the eddy, corresponds to the region of maximum kinetic energy (Fig. 2.2) which decreases to zero at both ends of the energy spectrum.

Special procedures are used (Shaw undated) to ensure that the spectral density is nondimensional so that different curves collapse onto a universal line in the region of the inertial sub-range B and separated well according to stability state. Also, the normalised plots allow actual frequencies to be obtained. For example, instead of plotting the spectral curves using ln n on the x-axis, a normalised logarithmic frequency ln f is used where $f = n\, z / \overline{U}$ where z is the measurement height and $\overline{U}$ is the mean horizontal wind speed. As an example, suppose that for a given stability state, the spectrum peaks at a normalised frequency $f = 3$ (no units), then for a measurement height $z = 2$ m and a mean horizontal wind speed $\overline{U} = 2$ m s^{-1}, $n = f\, \overline{u} / z = 3$ Hz, indicating that measurement frequencies of 3 Hz would capture eddies with the greatest corresponding energy.

2.9.6 Turbulent kinetic energy, energy dissipation rate and the two hypotheses of Kolmogorov

The turbulent kinetic energy per unit mass of the fluid (E in J kg^{-1}), referred to as TKE in the literature, is given by:

$$E = \frac{1}{2} \cdot (u^2 + v^2 + w^2). \qquad 2.21$$

The energy dissipation rate ε is defined as the rate of change in E due to viscous effects. Using Eq. 2.21, the units of the dissipation rate ε are J s^{-1} kg^{-1} = N m s^{-1} kg^{-1} = kg m s^{-2} m s^{-1} kg^{-1} = m^2 s^{-3}.

In the 1940s, the Russian statistician Kolmogorov hypothesized that, in the limit as the Reynolds number (Eq. 2.20) tends to infinity, the distribution of eddy sizes in the inertial and dissipation ranges should depend on only two parameters (besides wave number κ): the dissipation rate ε and the viscosity υ. That is, $E = E(\kappa, \upsilon, \varepsilon)$.

Kolmogorov also suggested that the spectrum in the inertial range (region B of Fig. 2.2) should be simpler still by virtue of being independent of viscosity. In that case $E = E(\kappa, \varepsilon)$ and he showed that the function dependence of the turbulent kinetic energy can be predicted from dimensional reasoning except for the universal constant α_1: $E(\kappa) \approx \alpha_1 \varepsilon^{2/3} \kappa^{-5/3}$. This power law spectral form indicates that motions in the inertial sub-range are self-similar.

Kolmogorov (1941a, b) introduced two hypotheses that in the atmospheric boundary layer high frequency fluctuations, because of their small size, are not influenced by the surface and have the same properties in all directions:

1. the average properties of the small-scale eddies of any turbulent flow at large Reynolds number (Eq. 2.20) are uniquely determined by the fluid kinematic viscosity υ and the average dissipation rate ε of the fluid;

2. for large Reynolds number, there is a sub-range of the equilibrium for which the average properties of the flow are determined only by the average rate of energy dissipation ε.

Using dimensional analysis (or a unit analysis) and noting that the unit of dissipation rate ε is (m s^{-1})^2 s^{-1} = m^2 s^{-3} and that of kinematic fluid viscosity υ is m^2 s^{-1}, expressions for the scales of length, time and velocity, referred to as the Kolmogorov microscales representative of the energy dissipation process, can be derived:

unit of υ / ε = s^2 and hence the scale of time is defined using υ / ε = (scale of time)^2.

Similarly, the unit of υ^3 / ε = m^4 = unit of (scale of length)^4.

Hence the scale of velocity = (scale of length^4)$^{1/4}$/(scale of time^2)$^{1/2}$

or
$$\text{scale of velocity} = \frac{\text{scale of length}}{\text{scale of time}} = \frac{(\upsilon^3 / \varepsilon)^{1/4}}{(\upsilon / \varepsilon)^{1/2}} = \upsilon^{1/4} \varepsilon^{1/4} = (\upsilon \varepsilon)^{1/4}.$$

Hence, using conventional notation:

$$\text{length } \eta = (\upsilon^3 / \varepsilon)^{1/4}, \qquad 2.22$$

$$\text{time } \tau = (\upsilon / \varepsilon)^{1/2}, \qquad 2.23$$

and
$$\text{velocity } v = (\upsilon \varepsilon)^{1/4} \qquad 2.24$$

define the Kolmogorov microscales representative of the energy dissipation process. Defining length l_o (m) as the inner-scale length beyond which energy is dissipated as viscous heat energy in the dissipation range, Hill and Clifford (1978) showed that the Kolmogorov microscale length $\eta = l_o / 7.4$. Hence, the inner-scale length is given by:

$$l_o = 7.4\ (\upsilon^3 / \varepsilon)^{1/4}. \qquad 2.25$$

For the turbulent spectral region B (Fig. 2.2), the inertial region, for which energy is neither produced nor dissipated, Kolmogorov argued that energy spectrum $E(\kappa)$ as a function of spectral wave number κ is proportional to $\varepsilon^{2/3}\ \kappa^{-5/3}$ with the proportionality constant estimated as being between 0.5 and 0.6:

$$E(\kappa) \approx \alpha_1\ \varepsilon^{2/3}\ \kappa^{-5/3} \qquad 2.26$$

where α_1 is referred to as the Kolmogorov constant. This relationship is referred to as the -5/3 power law for the inertial sub-range (Fig. 2.2, region B). Kaimal and Finnigan (1994) point out that theoretical arguments suggest that turbulence is isotropic in the inertial sub-range B. They also point out that a consequence of the local isotropy of turbulence is the vanishing of all correlations between velocity components and between velocity components and scalars with the result that there can be no turbulent fluxes in the inertial sub-range B.

For the inertial sub-range, the Kolmogorov hypothesis relies on the fact that energy is not created or destroyed within this range but that it is merely redistributed among the inertial-range wave numbers. Kolmogorov (1941b) suggested that the very large eddies will not interact directly with very small eddies, but only via eddies of an intermediate size. In other words, kinetic energy is extracted from the mean flow by the large eddies. This energy is then transferred via smaller and smaller eddies to the smallest eddies. This is called the cascade process.

2.10 Structure functions

2.10.1 Structure parameter of air temperature

Structure functions are the basis for scintillometry (Hill 1997). Structure functions can be defined for air temperature, water vapour pressure, refractive index of air, wind velocity, etc. For example, the time-average of the air temperature deviations squared, termed the air temperature structure function $D_T(r)$ at point r, can be expressed as:

$$D_T(r) = \overline{[T(r,t) - T(0,t)]^2} \qquad 2.27$$

where the overbar indicates a time average. $T(0,t)$ denotes the air temperature at position 0 at time t and $T(r,t)$ denotes the air temperature at position r from the point measurement $T(0,t)$. Therefore both $T(r,t)$ and $T(0,t)$ are measured at the same time t but are separated spatially by distance r. Structure functions are similar to the standard deviation function used in statistics. In the case of Eq. 2.27, it is the average deviation squared for two measurements of air temperature at slightly different positions with both measurements performed at the same time. Cross-structure functions can be defined between say air temperature and water vapour pressure. For spacing r in the inertial range of turbulence, millimetres to tens of millimetres, Obukhov (1949) showed that:

$$D_T(r) = C_T^2\ r^{2/3} \qquad 2.28$$

where C_T^2 is termed the structure parameter of air temperature. Some of the literature refers to C_T^2 as the structure function constant of air temperature or the structure constant of air temperature.

Another structure function, the spectral amplitude of the refractive index fluctuations is designated C_n^2 and is referred to as the structure function constant or simply the structure constant. Since the refractive index fluctuations are most often affected by air temperature fluctuations and less by fluctuations in atmospheric humidity, C_n^2 is often interpreted as a measure of the structure parameter of air temperature (Thiermann and Grassl 1992). It may also be interpreted as a measure of the strength of the refractive turbulence (Green 2001).

The standard deviation function used in statistics is just one way of expressing statistically the characteristics of fluctuations in refractive index. Other ways include: the correlation function, variance, covariance, structure functions such as that expressed by Eq. 2.27, probability density function, higher order moments, and power spectra.

Kolmogorov (1941b) showed that the structure function in the eddy range (inertial sub-range, region B of Fig. 2.2) is a measure of the total energy and can be expressed with a characteristic power spectrum. The wave number power spectrum of the refractive index fluctuations is a key parameter for investigating the propagation and scattering of optical waves in the atmospheric boundary layer. Since Kolmogorov's original work, different spectral models have been developed to describe this cascade process for the refractive index fluctuations in the atmospheric boundary layer.

The form of the three dimensional spatial power spectrum of the refractive index n, designated $\Phi_n(\kappa)$ where $\kappa = 2\pi/\lambda$, is very important for determining scintillation parameters such as the structure function constant C_n^2 and the inner scale of turbulence l_o. The influences of the random perturbations in the refractive-index on the beam propagating through a turbulent atmosphere is quantified by $\Phi_n(\kappa)$.

2.10.2 Kolmogorov cascade theory of turbulence

Statistical functions such as structure functions have been used to analyse turbulence regimes (Kolmogorov 1940). The original idea of cascading energy, by Richardson (1922), was further developed by Kolmogorov: large eddies of typical size 100 m, referred to as the outer scale of turbulence L_o, are not sustainable or stable and break up by transferring their energy to eddies of smaller and smaller size – millimetres to tens of millimetres. Typically, the inner scale of turbulence l_o is of the order 0.01 m near the surface and the outer scale of turbulence L_o increases linearly with height above surface and may approach sizes of the order of 100 m. Eddies of size r where

$$l_o << r << L_o \qquad 2.29$$

are in the inertial sub-range of turbulence (Figs 2.1 and 2.2). The inner scale of turbulence is important since it is related directly to the TKE ε via Eq. 2.25. Note that in Fig. 2.2, Λ is a measure of the outer scale of turbulence L_o and η is a measure of the inner scale of turbulence l_o.

Defining a wave number $\kappa_m = 2\pi / l_o$ and another as $\kappa_o = 2\pi / L_o$, then

$$\kappa_o << \kappa << \kappa_m$$

also defines the inertial range of turbulence (Fig. 2.3).

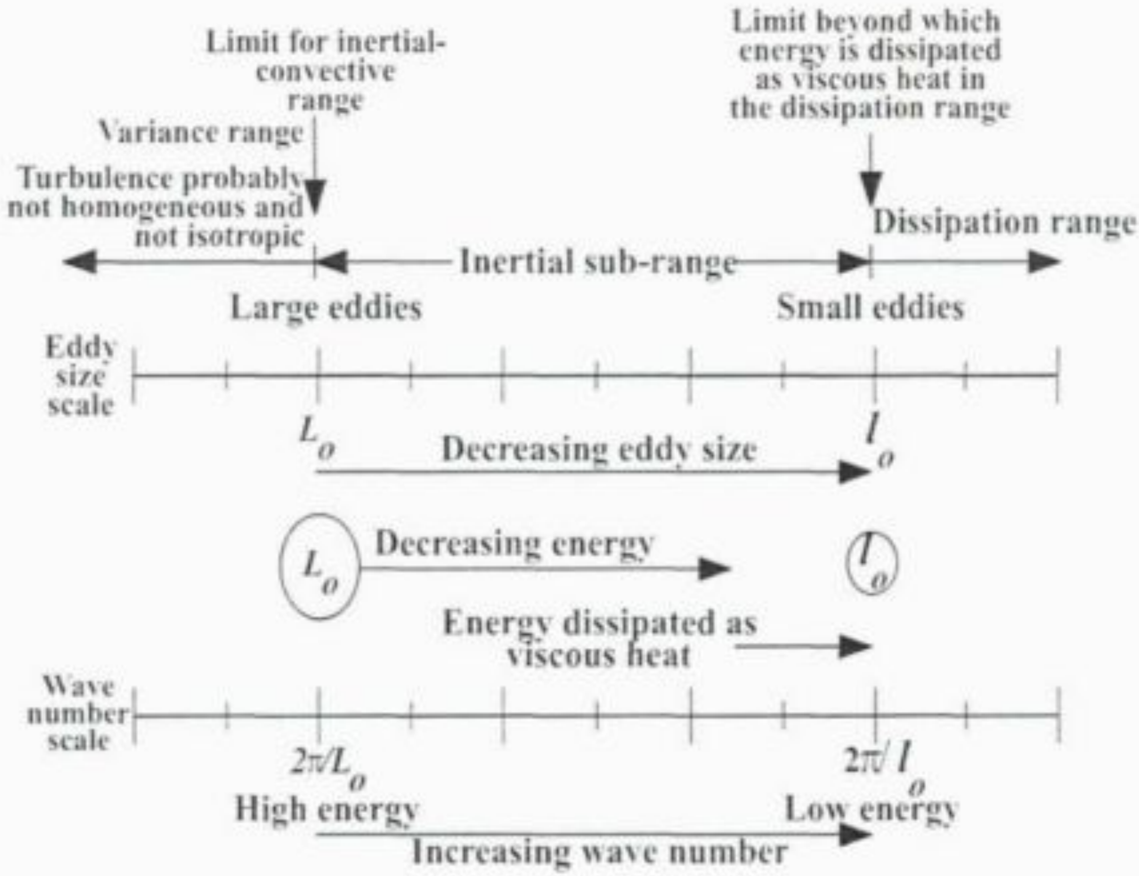

Fig. 2.3 An illustration of the range of eddy sizes, from the inner scale l_o to the outer scale L_o and the corresponding wave numbers. The different turbulent ranges, based on Fig. 2.2, are shown. The term "variance range" is taken from Green (2001). For the SLS method, the dissipation range is used

2.11 Eddy structure and stability functions

2.11.1 Introduction

Under fully-forced convection conditions, turbulent eddies are circular with no suppression in the vertical as might be the case under stable conditions. The atmosphere would then have a neutral state and the wind profile would be logarithmic. Under stable conditions, eddies are almost elliptical with the long axis in the horizontal direction. Under unstable conditions, the long axis of the elliptically-shaped eddy would be in the vertical.

Eddy structure of the atmosphere with fully forced convection conditions can be regarded as being composed of a number of circular eddies with diameters l, referred to as the mixing length (m). The mixing length is defined by $l = k\,z$ at height z where k is von Karman's constant, $k \approx 0.41$, independent of surface type. The tangential speeds of the rotating eddies are given by:

$$w' = u' = u_* = l \cdot \partial u / \partial z$$

where w' and u' are the vertical and horizontal turbulent velocity fluctuation. Under unstable conditions, w' exceeds u' by an amount generated by buoyancy where $u' = l \cdot \partial u / \partial z$ and $l > k\,z$. Under stable conditions, w' is less than u' by an amount related to damping effects. Again $u' = l \cdot \partial u / \partial z$ but $l < k\,z$.

Under unstable or stable conditions, the neutral wind profile relationship derived from Eq. 2.15, no longer applies. Generalizing this relationship:

$$\partial u / \partial z = \Phi_m \cdot u_* / [k(z-d)] \qquad 2.30$$

where the dimensionless stability function $\Phi_m = 1$ for neutral conditions, $\Phi_m > 1$ for stable conditions and $\Phi_m < 1$ for unstable conditions. The departure of Φ_m from unity would depend on the degree of stability or instability in the fluid flow. To arrive at expressions for Φ_m, the influence of vertical air temperature gradients on the nature of the turbulent boundary layer flow needs to be determined.

2.11.2 Generalised flux expression

The generalised wind profile relationship (Eq. 2.30) is extended to water vapour pressure and air temperature by defining e_* (kPa), the turbulent scale for water vapour pressure, and T_* (K), the turbulent scale of temperature:

$$\partial e / \partial z = -\Phi_w \cdot e_* / [k(z-d)] \qquad 2.31$$

and

$$\partial T / \partial z = -\Phi_h \cdot T_* / [k(z-d)] \qquad 2.32$$

where since, $\tau = \rho_{air}\ u_*^2$ (Eq. 2.14),

$$L_v F_w = -(\rho_{air}\ c_p / \gamma) \cdot e_*\ u_* \qquad 2.33$$

and

$$F_h = -\rho_{air}\ c_p \cdot u_*\ T_* . \qquad 2.34$$

The negative sign in each of Eqs 2.31 to 2.34 ensure that under normal daytime evaporative demand conditions the gradients and the fluxes are negative. The relationship between the various stability functions and the respective exchange coefficients includes height $z-d$ and the frictional velocity u_* and is easily derived from, for example, Eqs 2.8, 2.14 and 2.30 for K_m:

$$K_m = k\ u_*\ (z-d) \cdot \Phi_m^{-1} \qquad 2.35$$

$$K_h = k\ u_*\ (z-d) \cdot \Phi_h^{-1} \qquad 2.36$$

and

$$K_w = k\ u_*\ (z-d) \cdot \Phi_w^{-1} . \qquad 2.37$$

The remarkable aspect of Eqs 2.35 to 2.37 is that they provide the link between a critical element of K-theory (Eqs 2.6 to 2.8) and atmospheric stability (Eqs 2.30 to 2.32).

2.11.3 Richardson number

In order to arrive at a measure for atmospheric stability, consider a unit volume of air moving under turbulent motion in an unstable atmosphere with l exceeding $k\ z$ by an amount dependent on the buoyancy (Thom 1975). The initial turbulent kinetic energy KE_i per unit volume (J m^{-3} = Pa) is increased by an amount dependent on buoyancy KE_b and dependent on the air temperature difference between level z at temperature $T(z)$ and level $z+l$ at temperature $T(z+l)$ where:

$$T(z+l) \approx T(z) + l \cdot \partial T / \partial z.$$

Hence

$$KE_b = m\ g\ l \cdot \delta T / T$$

where m is the mass of air, or $\quad KE_b$ / volume $= \rho_{air}\ g\ l \cdot \delta T / T.$

Assuming that $T(z+l) < T(z)$,

$$\delta T = T(z) - T(z+l) \approx -l \cdot \partial T / \partial z.$$

Hence, averaging the KE_b/volume at level z (at which $\delta T = 0$) and level $z + l$ where:

$$KE_i \ / \ \text{volume} = \frac{1}{2}\rho_{air}\ g \cdot \delta T \ / \ T = -\frac{1}{2}\rho_{air}\ g \cdot l^2 \partial T / \partial z \ / \ T.$$

This is the inertial turbulent kinetic energy per unit volume of air.

To arrive at an expression for the inertial kinetic energy per unit volume of air, the inertial kinetic energy is written as $\frac{1}{2}\,m\,v^2$ or:

$$KE_i \ / \ \text{volume} = \frac{1}{2} m \cdot l^2 \cdot (\partial u / \partial z)^2 / \ \text{volume} = \frac{1}{2}\rho_{air} \cdot l^2\ (\partial u / \partial z)^2.$$

The ratio $KE_b \ / \ KE_i$ is a measure of the relative importance of free (buoyant) and forced (inertial) convection in a turbulent boundary layer.

It is conventional to define the Richardson number as:

$$Ri = -KE_b \ / \ KE_i = -[\frac{1}{2}\rho_{air}\ g\ l^2 \cdot \frac{\partial T}{\partial z} / T] / [\frac{1}{2}\rho_{air}\ l^2\ (\frac{\partial u}{\partial z})^2] = \frac{g}{T} \cdot \frac{\partial T}{\partial z} / (\frac{\partial u}{\partial z})^2$$

or

$$Ri = \frac{g}{T} \cdot \frac{\partial T}{\partial z} / (\frac{\partial u}{\partial z})^2. \qquad 2.38$$

Note that if $\partial T / \partial z < 0$ (lapse considerations), $Ri < 0$. For inversion conditions, $Ri > 0$. If air temperature and wind speed are measured at two heights, then:

$$Ri \approx \frac{g}{T}(T_2 - T_1) \cdot \frac{(z_2 - z_1)}{(u_2 - u_1)^2}.$$

Typically, for $g = 9.8$ m s^{-2}, $T = 300$ K, $|T_2 - T_1| \leq 1$ K, $z_2 - z_1 = 1$ m and $|u_2 - u_1| \leq 1$ m s^{-1}, $|Ri| \leq 0.033$.

The Richardson number is a dimensionless measure of the intensity of mixing (turbulence), and provides a simple criterion for the existence or non-existence thereof in a stable and stratified environment. A large positive value of $Ri > 0.25$ is indicative of weak and decaying turbulence and that the environment is tending towards a stable condition.

2.11.4 Monin-Obukhov similarity theory (MOST)

The disadvantage of the use of the Richardson number, as a stability measure, is that it is height dependent as shown by Eq. 2.38. Furthermore, it requires the measurement of air temperature and wind speed at two levels in the atmosphere. The ideal would be a height-independent measure that is not reliant on measurement at two levels.

Combining

$$\partial u / \partial z = \Phi_m \cdot u_* / [k(z-d)] \text{ [Eq. 2.30]},$$

$$\partial T / \partial z = -\Phi_h \cdot T_* / [k(z-d)] \text{ [Eq. 2.32]},$$

$$F_h = -\rho_{air}\, c_p \cdot u_*\, T_* \text{ [Eq. 2.34]}$$

the definition for the Richardson number (Eq. 2.38) can be written as:

$$Ri = \frac{g}{T} \cdot \frac{-\Phi_h \cdot T_* / [k(z-d)]}{\Phi_m^2 \cdot u_*^2 / [k(z-d)]^2}$$

or

$$Ri = -\frac{g}{T} \cdot \frac{\Phi_h}{\Phi_m^2} \cdot \frac{T_*}{u_*^2 / [k(z-d)]}$$

or using Eq. 2.34,

$$Ri = \frac{g}{T} \cdot \frac{\Phi_h}{\Phi_m^2} \cdot \frac{F_h}{\rho_{air}\, c_p} \cdot \frac{k(z-d)}{u_*^3}. \qquad 2.39$$

In arriving at a height-independent stability parameter, Monin and Obukhov defined the terms preceding $k(z-d)$ apart from the stability functions as the reciprocal of stability length L:

$$L = \frac{T}{k\, g} \cdot \frac{\rho_{air}\, c_p}{F_h} \cdot u_*^3. \qquad 2.40$$

In this expression, since the sensible heat flux density is negative under "normal unstable" daytime conditions, $L < 0$. Some of the literature defines sensible heat flux density as positive for these conditions and then define Eq. 2.40 using a negative sign preceding the right hand side. The Monin-Obukhov stability length L contains all of the parameters associated with free and forced convection except height z. The ratio $k(z-d)/L$ is therefore regarded as an absolute dimensionless measure of stability at height z. The Monin-Obukhov stability length L (m) has, as has been referred to, the dimensions of length and is essentially independent of height (Eq. 2.40):

$$Ri = \frac{z-d}{L} \cdot \frac{\Phi_h}{\Phi_m^2}. \qquad 2.41$$

For simplicity, if it is assumed that $\Phi_h / \Phi_m^2 = 1$, often taken to correspond to unstable conditions, then

$$Ri = \frac{z-d}{L}. \qquad 2.42$$

The magnitude of L for unstable conditions is $(z-d)/|Ri|$ where $|Ri|$ is a function of height z and in fact by definition is directly proportional to $z - d$. For unstable conditions, $|L|$ can be interpreted as the height above $z = d$ at which free convection becomes the dominant energy transfer mechanism (and at which $Ri = -1$). MOST (Monin-Obukhov Similarity Theory) relies on the assumption that $\Phi_h / \Phi_m^2 = 1$ (Eqs 2.41, 2.42).

Since the Richardson number is a non-dimensional ratio describing conditions in the surface layer over uniform terrain, it can, according to MOST, be equated directly to z / L in unstable air (Panofsky and Dutton 1984).

2.11.5 Example of Monin-Obukhov stability length assuming MOST conditions

Suppose that for unstable conditions above tall grass: $F_h = -300$ W m^{-2}, $T = 300$ K, and $u_* = 0.5$ m s^{-1}. Hence using Eq. 2.39 and assuming that $\Phi_h = \Phi_m^2$ or equivalently Eq. 2.40:

$$Ri = \frac{9.8}{300} \cdot 1 \cdot \frac{-300}{1.2 \cdot 1004} \cdot \frac{0.41(z-d)}{0.5^3}\ \mathrm{m}^{-1}$$

$$\text{or } Ri = -0.02667 \cdot (z-d) \text{ m}^{-1}$$

and

$$L = \frac{z-d}{Ri} = \frac{z-d}{-0.02667 \cdot (z-d)} \text{ m} = \text{-37.5 m.}$$

Hence, at a height of 37.5 m above the zero plane displacement level, free convection dominates. Note then that L is independent of height z.

2.11.6 The Monin-Obukhov stability length and atmospheric stability

In stratified turbulent flow any dimensionless characteristic is determined by: the height $z-d$, the shear stress at the surface τ_s, the air density ρ_{air}, and the production rate of turbulent energy resulting from the work of buoyancy forces. These four quantities can be expressed in terms of the three basic dimensions of time, length and mass, combined into one dimensionless variable, Ri proposed by Monin and Obukhov (1954), as shown by Eq. 2.42, where L is Obukhov's (1946) length (Brutsaert 1982) or "buoyancy length scale", defined by its originator Obukhov (1946) as "the characteristic height (scale) of the sub-layer of dynamic turbulence".

The relevance of this is that, in magnitude, L represents the thickness of the layer of dynamic influence near the surface in which shear or friction effects are always important. On strongly convective (windless free convective) days, $|L| \approx 10$ m (i.e. small), $|L| \approx 100$ m on windy days, and approaches infinity with purely mechanical turbulence (Brutsaert 1982). At night, or with downward heat flux, L is positive, and when turbulence ceases, $Ri >> 0$.

Closest to the surface (i.e. $z < |L|$) shear effects dominate, and buoyancy effects are insignificant, whereas the latter dominates when $z > |L|$. Thus the ratio $(z-d)/L$ is important in assessing the relative importance of buoyancy versus shear effects in the stratified surface layer, similar to the Ri number, to which it can be related (Panofsky and Dutton 1974). Under stable conditions, $(z-d)/L$ varies linearly with height showing the increasing importance of buoyancy above the surface (Arya 1988).

In the vertical direction, the atmospheric boundary layer consists of the surface layer with approximately constant turbulent fluxes and the outer layer above. The surface layer is approximately 10 % of the atmospheric boundary layer in vertical extent. It is in this lower 10 % that MOST is applied. In terms of stability, the atmospheric boundary layer can be classified as convective, unstable, neutral, stable-continuous and stable-sporadic (Deardorff 1978):

- convective: $(z-d)/L < -0.5$ for which buoyancy dominates. The vertical profiles of the mean wind speed and air temperature are almost uniform. The term "mixed layer" is therefore used to describe this state;
- unstable: $-0.05 \le (z-d)/L < -0.02$ for which there may be significant wind shear;
- neutral: $-0.02 \le (z-d)/L \le 0.02$;
- stable-continuous: $0.02 < (z-d)/L \le 0.2$ for which turbulence is mechanically driven;
- stable-sporadic: $(z-d)/L > 0.2$ for which only a very shallow layer next to the soil surface is turbulent in character.

The relationships have been extended to allow for a zero plane displacement height.

2.11.7 Semi-empirical stability functions

For stable conditions, it has been found from the so-called Kansas data (Businger et al. 1971, Wyngaard and Cote 1971) with other refinements (Dyer 1974, Högström 1988) that:

$$\Phi_h = \Phi_m = 1 + 5\frac{z-d}{L} \text{ and } \Phi_w = 1.25\cdot(1+0.2\frac{z-d}{L}) \text{ for } 0 \le \frac{z-d}{L} \le 1 \qquad 2.43$$

where the relationships have been extended to allow for a zero plane displacement height.

Similarly, for unstable conditions, it has been proposed that:

$$\Phi_h = \Phi_m^2 = (1+16\frac{z-d}{L})^{-0.5} \text{ and } \Phi_w = 1.25\cdot(1+3\frac{z-d}{L})^{1/3} \text{ for } -2 \le \frac{z-d}{L} \le 0 \qquad 2.44$$

where the relationships have again been extended to allow for a zero plane displacement height. Note that it can be shown that $\Phi_w / \Phi_h = K_h / K_w$.

A generalized stability factor F is defined as

$$F_P = (\Phi_P \cdot \Phi_m)^{-1}$$

(Thom 1975) where F_P is the stability factor for any property P.

2.11.8 Alternative methods for determining the zero plane displacement

Many of the equations involving MOST depend on the zero plane displacement (Eq. 2.15, 2.16). Various methods for determining the zero plant displacement height, based on wind profile measurements, are discussed by Wieringa (1993). A method based on single-level measurements of the standard deviation of the vertical wind speed σ_w and the sensible heat flux density F_h is described by de Bruin and Verhoef (1996) for tall vegetation. Using MOST, they show that for unstable conditions, the cube of the standard deviation of the vertical wind speed σ_w^3 is directly proportional to the product of the magnitude of the sensible heat flux density and $z-d$:

$$\sigma_w^3 = 0.019619\cdot(z-d)|F_h|/T$$

where T is the air temperature (K). This equation is different from their version through the direct use of the sensible heat flux density, as opposed to the covariance (w, T) and substitution of the various constants they used. A plot of σ_w^3 as a function of $|F_h|$ should yield a slope of $0.019619\cdot(z-d)$ from which $z-d$ and hence d may be determined. The assumptions of this approach are that the magnitude of the Monin-Obukhov stability length is very much less than $z-d$ and that free convection applies. They used sensible heat flux density magnitudes exceeding 120 W m^{-2} as indicative of free convection. This method would require EC measurements to obtain estimates of σ_w and F_h for unstable conditions. Furthermore, the regression between σ_w^3 and F_h would need to be statistical significant.

2.12 Methods for estimating surface evaporation

Evaporation measurement using a weighing lysimeter is usually regarded as the standard measurement against which all other evaporation (latent energy) measurements or estimates are compared. In spite of this standard, the use of lysimeters is often fraught with complications that may impact on measurement accuracy. The main limitation of their use is the cost and complex engineering involved and the non-portable nature of measurements that represent a small area of the experimental site.

In Chapter 1, it was pointed out that there is no single accepted method that is reliable and results in adequate resolution that can provide accurate temporal and spatial evaporation measurements or modelling estimates of evaporation. Some evidence for this statement is provided in a review, by Drexler et al. (2004), of models and micrometeorological methods used to estimate wetland total evaporation. They concluded that: 1. due to the variability and complexity of wetlands, there is no single approach that is the best for estimating wetland total evaporation; 2. there is no single foolproof method to obtain an accurate, independent measure of wetland evaporation.

Therefore, it does become important to understand the limitations, advantages, accuracy and resolution of a variety of methods for estimating surface evaporation.

Hanson et al. (2004) evaluated stand-level models varying in spatial, mechanistic, and temporal complexity for their ability to capture intra- and inter-annual components of the water and carbon cycle for an upland, oak-dominated forest of eastern Tennessee. The comparisons between model simulations and observations were conducted for hourly, daily, and annual time steps. The comparative data were obtained from a wide range of methods including: EC, sapflow, chamber-based soil respiration, biometric estimates of stand-level net primary production and growth, and soil water content by time or frequency domain reflectometry. They concluded that a single model did not consistently perform the best at all time steps or for all variables considered. Inter-model comparisons showed good agreement for water cycle fluxes.

The emphasis in the research documented in this report is on the use of SLS method for evaporation measurement. These measurements however need to be compared against other measurements using other evaporation methods in order that the accuracy of the SLS measurements may be ascertained. The other methods chosen include the BR method, EC methods, SR and the reference evaporation method, applied to a sub-daily time interval. Each of these methods will be very briefly discussed here and will receive more attention in subsequent chapters. In addition, a temperature variance and a surface temperature method for estimating sensible heat flux density is discussed.

2.12.1 Eddy covariance

Eddy covariance (EC) measurements (Swinbank 1951, Dyer and Maher 1965) allow for absolute point measurements of sensible heat and latent energy flux density at a defined height above canopy. Advances made in the cost and design of microprocessors allow for real-time calculation of flux densities. The calculation of sensible heat flux density, for example, using the EC method is based on the governing equation:

$$F_h = -\rho_{air}\, c_p\, \overline{w'T'} \qquad 2.45$$

where ρ_{air} and c_p are respectively the air density (≈ 1.17 kg m^{-3} at 25 °C and 100 kPa) and specific heat capacity of dry air (≈ 1056 J kg^{-1} K^{-1}) and where w' and T' are the vertical wind speed and air temperature fluctuations respectively and $\overline{w'T'}$ is the average covariance over a period, usually less than an hour.

The EC method may also be used to directly measure the latent energy flux density from the covariance between the vertical wind speed and the water vapour pressure. Alternatively, the latent energy flux density may be estimated as a residual from the measured sensible heat flux density

(Eq. 2.45) and measurements of net irradiance and soil heat flux density using the energy balance equation (Eq. 2.3).

2.12.2 Bowen ratio

The Bowen ratio energy balance (BREB or BR) method (Bowen 1926, Tanner 1960) is a profile method involving measurements of mean air temperature and mean water vapour pressure at two vertical heights above the canopy. The BR method also allows sensible heat and latent energy flux density to be determined. The calculation of sensible heat flux density F_h using the BR method is based on:

$$F_h = (-I_{net} - F_{soil}) / (1 + \beta^{-1}) \qquad 2.46$$

where I_{net} is the net irradiance at the canopy surface, F_{soil} the soil heat flux density and β the Bowen ratio calculated using:

$$\beta = \gamma(\overline{T}_2 - \overline{T}_1) / (\overline{e}_2 - \overline{e}_1) \qquad 2.47$$

where $\overline{T}_2$, $\overline{T}_1$, $\overline{e}_2$, $\overline{e}_1$ are the time-averaged air temperature (°C) and water vapour pressures (Pa) at profile heights z_2 and z_1 above the canopy surface, respectively. Typically, the means are performed over 20 min. The flux density of other entities, for example, carbon dioxide flux energy density ξF_c (W m^{-2}) where ξ is the quantum yield (J kg^{-1}) and F_c is the carbon dioxide mass flux density (kg s^{-1} m^{-2}), may be estimated by measuring the mean concentration of carbon dioxide at two atmospheric levels ($\overline{C}_1$ and $\overline{C}_2$ at heights z_1 and z_2 respectively) using:

$$\xi F_c = K \cdot (\overline{C}_2 - \overline{C}_1) / (z_2 - z_1)$$

where the generalised exchange coefficient (Savage et al. 1997) is determined using a rearrangement of Eq. 2.6 but expressed in finite difference form:

$$K = -\frac{F_h \rho_{air}^{-1} c_p^{-1}}{\overline{T}_2 - \overline{T}_1}(z_2 - z_1).$$

2.12.3 Surface renewal and other high frequency air temperature based methods

The surface renewal (SR) method is relatively new and quite simple (Paw et al. 1995, Snyder et al. 1996, Spano et al. 2000). Prior to the use of this method, a temperature variance method (Tillman 1972) was used. Both the SR and the temperature variance methods allow sensible heat flux density F_h to be estimated from measurements of air temperature at a single level using fine-wire thermocouples. Frequency of measurement for the SR method is typically 8 Hz and post-measurement calculations are used to estimate F_h. Measurement of net irradiance and soil heat flux density allow latent energy flux density to be estimated for both methods using the shortened energy balance equation (Eq. 2.3). The SR method is attractive because of its simplicity but also since it is relatively inexpensive:

$$F_h = \alpha \, \rho_{air} \, c_p \, z \frac{\partial T}{\partial t} \qquad 2.48$$

where z is the measurement height, $\partial T / \partial t$ is the rate of change in air temperature, and α is a weighting factor. The weighting factor α needs to be determined, for the vegetation type used, by comparison of the estimated sensible heat flux density with other sensible heat flux density measurements from other methods such as the EC method. In a sense, $\partial T / \partial t$ is a structure function (Eq. 2.27) but with measurements performed at high frequency at the same position. The method assumes that the variation in air temperature consists of a temperature quiescent period s, for which there is no change in air temperature with time, followed by a ramp period l. A ramp with a positive amplitude a occurs during unstable conditions and a negative amplitude for stable conditions. The ratio $a/(s+l)$ is therefore used as the temperature change with time in Eq. 2.48. Apart from the choice of the empirical constant α (Eq. 2.48), the disadvantage of the method is that the change in temperature following the ramp period is not quantified. For this to be quantified, the friction velocity u_* is required and MOST applied (Chen et al. 1997a, b, Castellvi 2004). The determination of friction velocity requires additional equipment such as a wind speed sensor, and MOST requires knowledge of the Monin-Obukhov stability length which in turn requires knowledge of sensible heat flux density F_h. Hence, an iterative procedure is used to determine the sensible heat flux density F_h.

Kustas et al. (1994) uses an air temperature variance method for unstable conditions based on MOST for estimating sensible heat flux density based on the work of Tillman (1972). The method involves an element of empiricism in estimating sensible heat flux density using:

$$F_h = -\rho_{air}\, c_p\, u_*\, \sigma_T / C_3 \qquad 2.49$$

where σ_T is the standard deviation of the measured air temperature (over a time period) and $C_3 = C_1 / \sqrt[3]{C_2}$ where Kustas et al. (1994) found C_1 = 1.1 and C_2 = 0.085. They cautioned that the variance method should always be calibrated with measurements from other flux measurement systems. They calculated the friction velocity u_* using MOST, either from the standard deviation of the vertical wind speed (σ_w) or from the measured wind speed:

$$u_* = \sigma_w / \{1.3 \cdot [1 - 2 \cdot (z - d_{om}) / L]^{1/3}\} \qquad 2.50$$

or

$$u_* = u \cdot k / \{\ln[(z - d_{om}) / z_{om}] - \psi_m\} \qquad 2.51$$

where from Dyer (1974) and Högström (1988):

$$\psi_m = \pi / 2 + 2 \cdot \ln[(1 + x) / 2] + \ln[(1 + x^2) / 2] - 2 \cdot \arctan x \qquad 2.52$$

where

$$x = [1 - 16 \cdot (z - d_{om}) / L]^{1/4} \qquad 2.53$$

for unstable conditions where d_{om} and z_{om} are the zero plane displacement height and roughness length for momentum respectively. Since the value of F_h needs to be known for the calculation of the Monin-Obukhov stability length L contained in the expression for u_* (Eq. 2.50), and in turn used to calculate the sensible heat flux density (Eq. 2.49), an iterative method is used by starting with L = -10^n m for determining F_h. The d_{om} and z_{om} values were estimated for unstable conditions from measurements of σ_w, u and F_h (Eqs 2.50 or 2.51).

Wang and Bras (1998) also uses an air temperature based method for estimating sensible heat flux density using K-theory. They expressed sensible heat flux density as a function of the eddy diffusivity and a weighted average (half-order derivative) of the time history of air temperature. Their expression depended on knowledge of the surface parameters and included friction velocity.

2.12.4 Determining sensible heat using a surface temperature method

Assuming a big-leaf model for the exchange of sensible heat and latent energy flux density from a surface, an expression for determining the sensible heat flux density from the surface (T_o) and air (T_z) temperatures (°C) and wind speed (m s^{-1}) may be arrived at as follows:

$$u = (u_* / k) \cdot \ln[(z-d)/z_o] \text{ [Eq. 2.15]},$$

$$r_{am} = \rho_{air}\, \bar{u} / \tau \text{ [Eq. 2.10]},$$

$$r_{ah} = \rho_{air}\, c_p \cdot \frac{\bar{T}_z - \bar{T}_o}{F_h} \text{ [Eq. 2.9]}$$

and $$\tau = \rho_{air}\, u_*^2 \text{ [Eq. 2.14]}$$

assuming that $$r_{ah}(z_1, z_2) = r_{am}(z_1, z_2) \text{ [part of Eq. 2.13]}.$$

Manipulating:

$$\rho_{air}\, c_p \cdot \frac{\bar{T}_z - \bar{T}_o}{F_h} = r_{ah} = r_{am} = \rho_{air}\, \bar{u}/\tau = \rho_{air}\, \bar{u}/\rho_{air}\, u_*^2 = \bar{u}/u_*^2 = \bar{u}/\{k\bar{u}/[\ln(z-d)/z_o]\}^2.$$

Hence, $$\rho_{air}\, c_p \cdot \frac{\bar{T}_z - \bar{T}_o}{F_h} = [\ln(z-d)/z_o]^2/(k^2\bar{u})$$

or $$F_h = \rho_{air}\, c_p \cdot \frac{\bar{T}_z - \bar{T}_o}{[\ln(z-d)/z_o]^2/(k^2\bar{u})}. \qquad 2.54$$

For neutral wind conditions, sensible heat flux density may be calculated from surface temperature estimated using infrared thermometer (IRT) measurements of canopy surface temperature, air temperature and wind speed and applying Eq. 2.15.

Applying the big-leaf model, Thom (1975) defines $\bar{T}_o$ as the mean canopy surface temperature (his Fig. 8(a)). Monteith and Unsworth (1984) however define $\bar{T}_o$ as the temperature at which wind speed is 0 m s^{-1}. The two definitions are therefore not the same since the wind speed is zero at height $d + z_o$ above the soil surface. Monteith and Unsworth (1984) define an additional boundary layer resistance r_b as follows:

$$r_b = \frac{\ln(z_o/z'_o)}{k\, u_*}$$

where $z'_o < z_o$ and $d + z'_o$ is the height at which the source of sensible heat flux density and latent energy flux density originate and $d + z_o$ is the level at which wind speed (and therefore momentum) is zero. Hence the atmospheric resistance for momentum transfer is described in terms of r_a and by $r_a + r_b$ for sensible heat and latent energy flux density. The term $u_*\, r_b$ is identical to $k\, B^{-1}$ used by other workers for investigating rough surfaces.

Using the above relationships, designating $\overline{T'_o}$ as the average temperature at the level at which wind speed is 0 m s^{-1}, then it can be shown that:

$$\overline{T_o - T'_o} = -\frac{F_h\, r_b}{\rho\, c_p}.$$

Thom (1972) obtained an empirical relationship for r_k, for smooth surfaces, as a function of friction velocity:

$$r_k = 62\ u_*^{-0.67} \text{ for } 0.1 \text{ m s}^{-1} < u_*\ 0.5 \text{ m s}^{-1}.$$

Monteith and Unsworth (1984) corrected the aerodynamic resistance r_a (s m^{-1}) for stability using:

$$F_h = \frac{\rho_{air}\ c_p \cdot (\overline{T}_z - \overline{T}_o)}{[(\ln \frac{z-d}{z_o})^2 / k^2 u] \cdot [1 - \frac{\eta g (z-d) \cdot (\overline{T}_z - \overline{T}_o)}{\overline{u}^2 \cdot [0.5 \cdot (\overline{T}_z - \overline{T}_o) + 273.15]}]} \qquad 2.55$$

For field conditions, a value of 5 for η was suggested. Different formulations of Eq. 2.55 for estimating sensible heat flux density from surface temperature have been suggested for the case of sparse cover and dry vegetation (Choudhury et al. 1986, Kustas et al. 1989, Chehbouni et al. 2000a, b). For the general case, Choudhury et al. (1986) used an analytical approach and showed that

$$F_h = \frac{\rho_{air}\ c_p \cdot (\overline{T}_z - \overline{T}_o)}{[(\ln \frac{z-d}{z_o})^2 / k^2 u] \cdot (1+\eta)^{0.75}} \qquad 2.56$$

where with sufficient accuracy

$$\eta = 5 \cdot (z-d) \cdot g (\overline{T}_z - \overline{T}_o) / (T_z\ u^2), \qquad 2.57$$

for unstable conditions where it is assumed that the roughness length for sensible heat and momentum flux density are equal. They also showed that the use of Eq. 2.55 is almost equivalent to using Eq. 2.56. The sensible heat flux density is calculated for unstable conditions by replacing the denominator of Eq. 2.54 with r_a from Eq. 2.56. For stable conditions, Choudhury et al. (1986) showed that:

$$F_h = \frac{\rho_{air}\ c_p \cdot (\overline{T}_z - \overline{T}_o)}{[(\ln \frac{z-d}{z_o})^2 / k^2 u] \cdot (1+\eta)^2} \qquad 2.58$$

For sparse cover and dry vegetation, T_o (Eqs 2.56, 2.58) is often much less than the measured infrared surface temperature. Physically, inclusion of an additional resistance term, to the denominator of Eq. 2.56, is recognition that the infrared temperature for sparse vegetation is also influenced by soil surface temperature (Kustas et al. 1989). On the other hand however, experience with the use of infrared thermometers has shown that in the case of complete cover, the sensor detects sunlit leaves as well as deep shade within the canopy. For sparse vegetation cover, Chehbouni et al. (1996, 1997) showed that:

$$\overline{T}_o - \overline{T}_z = \beta \cdot (\overline{T}_{IRT} - \overline{T}_z) \qquad 2.59$$

where β is an empirical function of leaf area index LAI and $\overline{T}_{IRT}$ is the observed infrared surface temperature. The disadvantage of this approach is that the empirical function for β would depend on vegetation type. For a grassland site, Chehbouni et al. (2000a) showed that:

$$\beta = \frac{1}{\exp(C / (C - LAI)) - 1}$$

2.60

where for their grassland site, $C = 1.5$. An alternative method involves introducing an excess resistance r_{ex} [also referred to as $k\,B^{-1}$ by Monteith and Unsworth (1990) and others], as an additional term to the denominator of Eq. 2.54, the aerodynamic resistance, to account for the differences infrared surface temperature and $\overline{T}_a$ for the case of sparse vegetation:

$$r_{ex} = k\,B^{-1} = 0.17\,U \cdot (\overline{T}_s - \overline{T}_a) \qquad 2.61$$

(Kustas et al. 1989). Moran et al. (1994) modified Eq. 2.61 by using $|\overline{T}_a - \overline{T}_s|$ instead of $\overline{T}_a - \overline{T}_s$ to only allow for positive $\overline{T}_a - \overline{T}_s$ values. Kustas et al. (1994) modified the empirical factor of Eq. 2.61 from 0.17 to 0.13, based on improvements in the estimation of the momentum roughness parameter. Moran et al. (1994) used ground-based remotely sensed data in a semi-arid grassland site to compare sensible heat flux density estimation. Their results were similar to that of Mengistu (2003), namely that the estimation of the denominator of Eq. 2.56 is sensitive to the uncertainty in estimating d and z_m. Furthermore, the excess resistance (Eq. 2.61) is also another source of uncertainty due to its empirical nature (Moran et al. 1994).

Verhoef et al. (1997) question the use of the $k\,B^{-1}$ concept that attempts to adjust the IRT-measured surface temperature for sparse canopies for which the IRT sees too much understorey or bare surface and does not yield the temperature of the top of vegetation that drives the sensible heat flux density. They recommend the use of a more physically based approach.

As is the case with other methods that use the energy balance and measurements of sensible heat flux density, net irradiance and soil heat flux density to estimate latent heat flux density as a residual, there is a cumulative effect of errors when calculating latent energy flux density that can only be reduced by reducing the errors in the individual measurements or estimates.

2.13 Scintillometry

2.13.1 Introduction

A scintillometer, depending on its type, allows determination of a number of micrometeorological parameters but in particular C_n^2. Under certain conditions, in particular under conditions of weak scattering of the scintillometer beam, and using certain measurement methods or assumptions, sensible heat flux density F_h may be derived from C_n^2. As with the other methods discussed in the previous section, knowledge of the net irradiance and soil heat flux density allows the latent energy flux density to be estimated as a residual.

A full understanding of scintillometry requires knowledge in electronics, optics, wave propagation theory, data logging and micrometeorology. Andreas (1990) presents a collection of selected key papers on wave propagation and atmospheric turbulence. A comprehensive review describing the background, recent progress and future trends in optical scintillation is described by Hill (1992). The scintillometry method is dependent on algorithms, based on MOST, for determining atmospheric surface-layer fluxes. A detailed description of these algorithms is described by Hill (1997). Green (2001) describes the practical application of scintillometers for determining sensible heat, latent energy and momentum flux density and Hartogensis (1997) describes the areal averaged sensible heat flux density using a large aperture scintillometer. de Bruin (2002) describes a resurgence of interest in the use of the scintillometer method. The assumed benefits of a path-averaged C_n^2 value when the objective is to estimate surface fluxes is discussed by Andreas et al. (2003).

Essentially, a scintillometer consists of a source of light of known wavelength usually directed over some horizontal distance to a receiver. The light beam needs to be collimated - that is, the light rays need to be parallel. For the surface layer scintillometer system (SLS), for example, the changes in the intensity and the phase of the light beam is detected at the receiver position some known horizontal distance from the transmitter. These changes result from the atmospheric perturbations caused by the variations in sensible heat and latent energy that refract the light beam. The key to the implementation of the scintillometer method is the interaction between eddy size, beam distance, beam wavelength and aperture diameter and for some of the estimates, effective beam height, air temperature and atmospheric pressure. The estimated sensible heat flux density requires the friction velocity measurement or estimate.

2.13.2 Fresnel zone

The different types of scintillometers differ in the size of the transmitter and receiver apertures (Table 2.1) when compared to what is referred to as the Fresnel (pronounced Fraenel) zone. The Fresnel zone size is the geometric mean between the wavelength λ_{beam} of the transmitter beam and the beam path length L_{beam}:

$$F_{zone} = \sqrt{\lambda_{beam} \times L_{beam}}. \qquad 2.62$$

For weak scattering of the scintillometer beam, it is the ratio of the inner scale of turbulence to F_{zone} that is important in determining which range of turbulence, shown in Fig. 2.2, is used. For a small aperture scintillometer such as a SLS that uses mainly the dissipation range of turbulence (Fig. 2.2), for a typical beam wavelength of 670 nm and a path length less than 250 m, $F_{zone\ small\ aperture}$ = 12.9 mm (Eq. 2.57, Table 2.1). Scintillometers with an aperture size less than F_{zone} are referred to as small aperture scintillometers and otherwise large aperture scintillometers (LAS). The LAS systems use mainly the inertial range of turbulence (Fig. 2.2) for which $l_o << r << L_o$ (or $\kappa_o << \kappa << \kappa_m$). The LAS systems use a typical beam wavelength of 880 nm and a path length of less than 5 km, $F_{zone\ LAS}$ = 68.6 mm (Table 2.1). The boundary layer scintillometer (BLS) systems usually use a beam wavelength of 880 nm but the beam path length can vary between 0.5 and 10 km with the result that $F_{zone\ BLS}$ is between about 21.0 and 93.8 mm.

For each category of scintillometer, viz., SLS for which 5.8 mm < $F_{zone\ SLS}$ < 12.9 mm (corresponding to 50 to 250 m beam path length) and boundary layer large aperture scintillometer (LAS) systems for which 21.0 mm < $F_{zone\ LAS}$ < 68.6 mm (corresponding to 0.25 to 5 km beam path length), and BLS systems for which 21.0 mm < $F_{zone\ BLS}$ < 93.8 mm (corresponding to 0.5 to 10 km beam path length), there are dual-beam (- in some cases multi-beam) and single-beam methods used for determining C_n^2 and from that and other measurements but in particular the friction velocity, the sensible heat flux density.

The small aperture scintillometers (or surface layer scintillometer (SLS) systems) are sensitive to eddies with diameters close to F_{zone}, corresponding to the inertial sub-range [defined by Raupach and Legg (1984) and shown in Figs 2.1 and 2.2] containing larger eddies or to the so-called dissipation sub-range of turbulence containing smaller eddies. In the case of eddies in and close to the dissipation range, the measured variances do not only depend on C_n^2 but also on the inner scale of turbulence l_o. For the SLS system employed in this study, a dual-beam laser method with two detectors is used. The inner scale l_o of refractive index fluctuations is calculated from the correlation of the light intensities at these two detectors. Only once l_o is known, can the structure parameter of refractive index fluctuations C_n^2 be calculated from the variances of the intensity from the two beams.

Table 2.1 Details of selected flux measurement systems for determining C_n^2

System type, reference	Measurement distance	Beam wavelength; F_{zone} (mm)	Aperture size	Measurement frequency/averaging period	System current	Typical measurement height	Limitations /comments
SLS, this study, Thiermann and Grassl (1992)	50 to 250 m	670 nm; $5.8 < F_{zone} < 12.9$	2.5 mm	1 kHz/2 min	< 3 A	Typically 1 m above canopy	Affected by strong turbulence - referred to as saturation; u_* determined; small footprint since measurement height typically 1 m above surface
LAS - see review by Andreas (1990)	250 m to 5 km	940 nm; $15.3 < F_{zone} < 68.6$	152 mm	Typically 1 Hz	0.1 to 1 A (transmitter) depending on path length; 0.2 A for transmitter	3 m?	u_* is required for estimation of F_h
BLS (also referred to as XLS by Andreas et al. (2002) for pathlengths around 10 km)	0.5 to 5 km for 145 mm aperture; 1 to 10 km for 265 mm aperture; < 10 km for aperture size of 310 mm	880 nm; $21.0 < F_{zone} < 66.3$; $29.7 < F_{zone} < 93.8$	145 mm; 265 mm	1 to 125 Hz/10 min	From 0.1 A for 1 Hz measurements and 145 mm aperture to 10 A for 125 Hz measurements	10 to 20 m	Current drain high for 125 Hz measurements; measurement height should be in excess of 10 m; u_* is required for estimation of F_h
MWS/RWS (Green et al. 2001) for measurement of latent energy flux density	Typically 2.2 km	> 11 mm; transmitter frequency of 27 GHz	600 mm antenna diameter	Filtered at 10 Hz and sampled at 20 Hz	Not stated	10 m	Scintillometer must be mounted sufficiently far from the surface so as to avoid signal distortion through ground reflection; u_* is required for estimation of F_h
Differential image motion (DIM) LIDAR (Gimmestad and Roberts 2003)	300 m	Laser wavelength	Not stated	Not stated	Not stated	Not stated	Measurement comparisons were made with a scintillometer

The LAS systems sense eddies close to the transmitter and receiver diameters – typically greater than 0.1 m. Eddies of this size belong to the inertial sub-range of turbulence (Fig. 2.2). In this case for LAS systems, C_n^2 is independent of l_o and hence friction velocity is required for estimating sensible heat flux density. However, measurement heights of at least 10 m may be necessary.

2.13.3 Scintillometer types

The SLS system is specifically targeted for short path lengths, compared to the BLS and LAS counterparts. The current drain of the SLS system is 1 A for the transmitter/receiver systems (if the alignment is automatic) and 1 A for the central processing unit. A computer or laptop is also required if the unit does not have data storage capability. The current drain for the BLS systems (Table 2.1) is usually greater than 1 A, depending on how the system is operated. If the system is operated at a transmitter pulse rate of 125 Hz, corresponding to maximum accuracy, the current drain varies from 3.5 to 13 A for the 0.5 to 5 km and 1 to 10 km beam path lengths respectively. The limitation of large equipment current drain however also applies to EC and BR methods although the current drain is usually less than 1 or 2 A. Routinely, it is not easy to operate the BLS systems at the high pulse rates of 125 Hz unless electrical power source is available.

There are various types of scintillometer systems in use (Table 2.1) that include:

SLS (50 to 250 m beam path length);

LAS (Kipp and Zonen LAS with a 250 to 3.5 km beam path length);

BLS (Scintec boundary layer scintillometer, with a beam path length between 0.5 and 5 km or between 1 and 10 km);

XLAS scintillometer system with a beam pathlength up to 10 km. Kohsiek et al. (2002) were the first to use a LAS with an increased diameter of 0.31 m, which they referred to as XLAS systems;

microwave scintillometer system (MWS). This type is also referred to as a radio wave scintillometer (RWS) (Meijninger et al. 2002a).

Gimmestad and Roberts (2003) used a differential image motion (DIM) LIDAR[1] concept to measure C_n^2. Their field validation was performed by testing against a conventional scintillometer for a 300 m horizontal path, for a range of turbulence conditions. Their test results supported the concept and confirmed that C_n^2 can be accurately measured with this method. The details of the work was available as an abstract. Further information on this method and in particular the cost is limited since the work was undertaken for military research reasons.

Each scintillometer type corresponds to a different range of path length sensitivity. The RWS systems use radio wavelengths that are most sensitive to humidity fluctuations (Andreas 1989, Meijninger et al. 2002). The RWS systems are not discussed further in this report. The SLS, LAS and BLS systems all operate in the visible and near-infrared wavelength range. Light with these wavelengths are affected by temperature fluctuations (Wesely 1976, Hill et al. 1980) and using MOST, makes possible the estimation of sensible heat flux density.

1 LIDAR is an acronym of light detection and ranging for describing systems that use a light beam for atmospheric monitoring, tracking and detection functions

The BLS boundary layer systems available allow measurements of C_n^2 and use two transmitters, each with hundreds of light-emitting diodes.

2.13.4 Application of weak scattering theory to scintillometry

Central to the use of scintillometers is the measurement of C_n^2, the structure parameter for refractive index. However, weak scattering of the scintillometer beam is paramount. All scintillometer units allow for the estimation of C_n^2. The first measurements of C_n^2 were obtained by Tatarskii (1961) using a relationship for weak scattering (Lawrence and Strohbehn 1970) and Wesely (1976) was the first to obtain sensible heat flux density from optical measurements.

Kolomogorov (1941) showed that within the inertial-convective sub-range of eddy sizes, the refractive index spectrum $\Phi_n(\kappa)$ is given by:

$$\Phi_n(\kappa) = 0.033\, C_n^2\, \kappa^{-11/3} \qquad 2.63$$

where

$$2\pi\, L_o^{-1} << \kappa << 2\pi\, l_o^{-1}. \qquad 2.64$$

Hill and Clifford (1978), and others, applied modifications to the Kolmogorov (1941b) relationship by describing a sub-range of the inertial-convective range, the viscous convective range and developed a theoretical spectrum for the inertial-convective through to the dissipation range:

$$\Phi_n(\kappa) = 0.033\, C_n^2\, \kappa^{-11/3}\, f(\kappa\,\eta) \qquad 2.65$$

where η, the Kolmogorov microscale length, is related to the inner scale of turbulence: $\eta = l_o / 7.4$ (Hill and Clifford 1978). Hill and Clifford (1978) described a sub-range of the inertial-convective range, referred to as the viscous convective range. They proposed a theoretical spectrum for the inertial-convective through to the dissipation range. The so-called Hill spectrum was derived from temperature fluctuations and were assumed to dominate refractive-index fluctuations at optical wavelengths.

For weak scattering of the scintillometer beam (Lawrence and Strohbehn 1970) for the inertial and dissipation turbulent regions (zones B and C of Figs 2.2 and 2.3), and integrating over the beam path length L_{beam} and wave number κ, the variance in beam intensity σ_I^2 is given by:

$$\sigma_I^2 = 0.124\, C_n^2\, K^{7/6}\, L_{beam}^{11/6}\, f_B(l_o / \sqrt{\lambda_{beam} L_{beam}}) = 0.124\, C_n^2\, K^{7/6}\, L_{beam}^{11/6}\, f_B(l_o / F_{beam}) \qquad 2.66$$

where K is the optical wave number ($= 2\pi / \lambda_{beam}$) and L_{beam} is the beam path length. Similarly, Thiermann and Grassl (1994) showed that the measured covariance in the logarithm of the amplitude of the beam intensity at the receiver position is given by:

$$B_{12}^2 = 0.124\, C_n^2\, K^{7/6}\, L_{beam}^{11/6}\, f_B(l_o / F_{beam}). \qquad 2.67$$

The function f_B describes the decrease in the measured covariance B_{12} with increasing l_o, λ_{beam} and L_{beam}. This function f_B depends on the function f_α which was determined by Hill and Clifford (1978) from the so-called Hill spectrum (Hill 1978) and is shown in Fig. 2.4. The function tails off for large values of l_o / F_{beam}. To increase the l_o / F_{beam} ratio so as not to be at the tail end of the function requires that L_{beam} be decreased. So a requirement of weak scattering is that path lengths not be too long. Another important point: to ensure that the ratio l_o / F_{beam} is not too small (and therefore in the tail

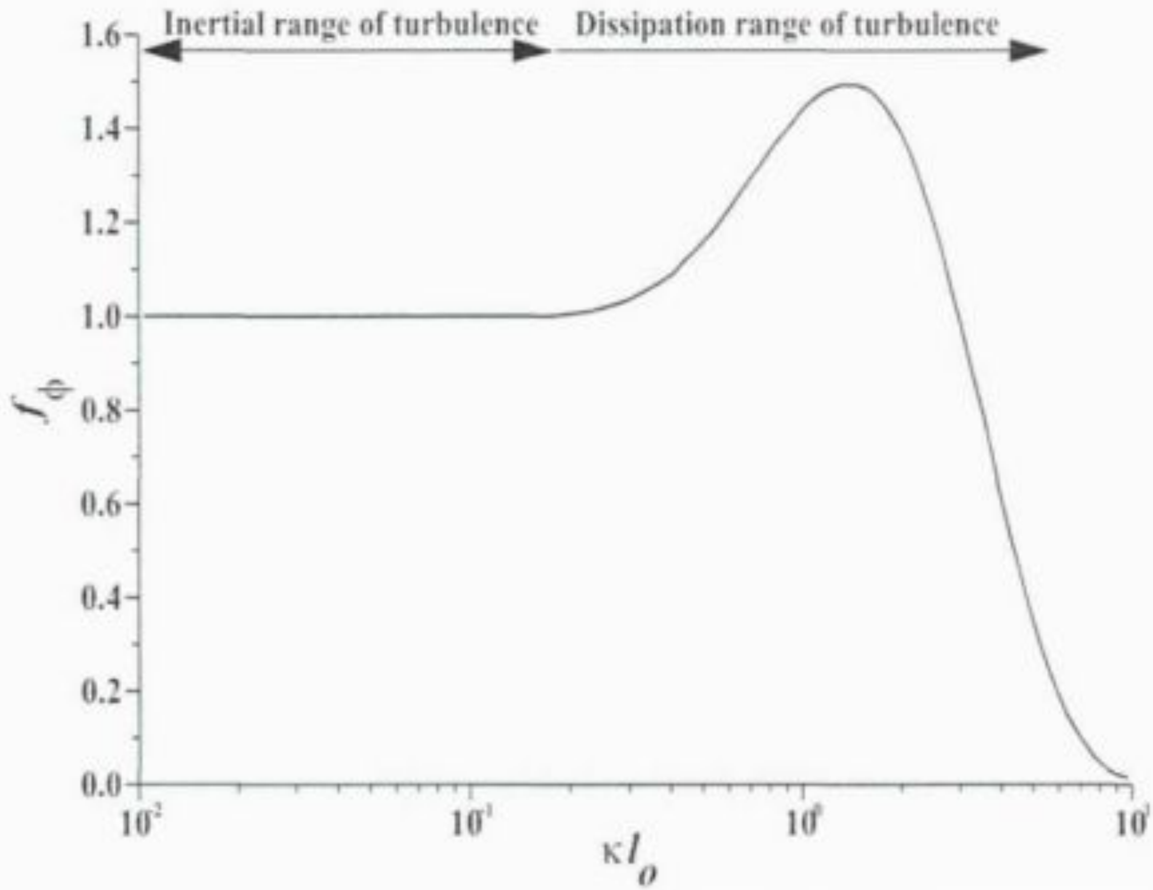

Fig. 2.4 The so-called Hill spectrum showing f_ϕ as a function of κl_o. The hump in the dissipation range of turbulence is evident. The Hill spectrum was derived from temperature fluctuations assuming they dominate refractive-index fluctuations at optical wavelengths

region of the f_ϕ function), the beam height could be increased resulting in larger eddies and larger l_o values.

In the case of the dual-beam SLS method, the function f_ϕ describes the decrease in the covariance in the logarithm of the amplitude of the radiation, measured at the scintillometer receiver position, with increasing detector separation distance d, detector diameter D and inner scale of turbulence l_o. For microwave propagation and without inner-scale dependence,

$$\sigma_\chi^2 = 0.124 C_n^2 K^{7/6} L_{beam}^{11/6}. \qquad 2.68$$

Eq. 2.68 allows C_n^2 to be determined from measurements of σ_χ^2, and knowledge of K ($= 2\pi / \lambda_{beam}$) and L_{beam}. However, to determine the sensible heat flux density, F_h, the structure parameter for temperature C_T^2 is required using the relationship for when the fluctuations in air temperature and water vapour pressure are perfectly correlated (Wesely 1976):

$$C_T^2 = (\frac{T^2}{aP})^2 C_n^2 \cdot (1 + 0.03\beta^{-1})^{-2} \qquad 2.69$$

and

$$C_T^2 = (\frac{T^2}{aP})^2 C_n^2 \cdot (1 + (\frac{0.03}{\beta})^2)^{-1}$$

when there is no correlation between the fluctuations in air temperature and water vapour pressure where T (K) is the air temperature, P the atmospheric pressure (hPa) and $a = 7.89 \times 10^{-5}$ K hPa^{-1} at $\lambda_{peak} = 680$ nm. In Eq. 2.69, the influence of humidity on C_T^2 is evident via the Bowen ratio β. Generally, the effect is regarded as small and contributing less than 3 % to C_T^2. However, the Bowen ratio would then have to exceed 2 (Fig. 2.5), corresponding to drier conditions. Hence, it may be necessary to apply a correction for when the water vapour pressure fluctuations become large compared to the air temperature fluctuations. This could be the case for measurements above water surfaces or above irrigated fields. Previous Bowen ratio measurements (Savage et al. 1997) for natural grassland showed that Bowen ratio values during summer rainfall periods were typically 0.5. Ignoring the influence of the Bowen ratio would result in an underestimation in C_T^2 of at least 10 %. Meijninger and de Bruin (2000) point out that this would in turn result in an underestimation in sensible heat flux density. They used "common-sense" values for β. They noted that other studies determined β iteratively using the measured net irradiance, soil heat flux density and the energy balance equation. For their measurements above irrigated areas, they obtained reliable estimates of sensible heat flux density that compared favourably with estimates using a temperature variance method.

The effects of water vapour on the structure parameter of the refractive index for near-infrared radiation, used mainly in LAS systems, was investigated in detail by Moene (2003) who confirmed that when C_T^2 is used to compute the sensible heat flux density, the influence of the correction for water vapour fluctuations on the measured energy balance is small. For small β, the correction is large, but the absolute value of the sensible heat flux density is small, whereas for large β, the correction is

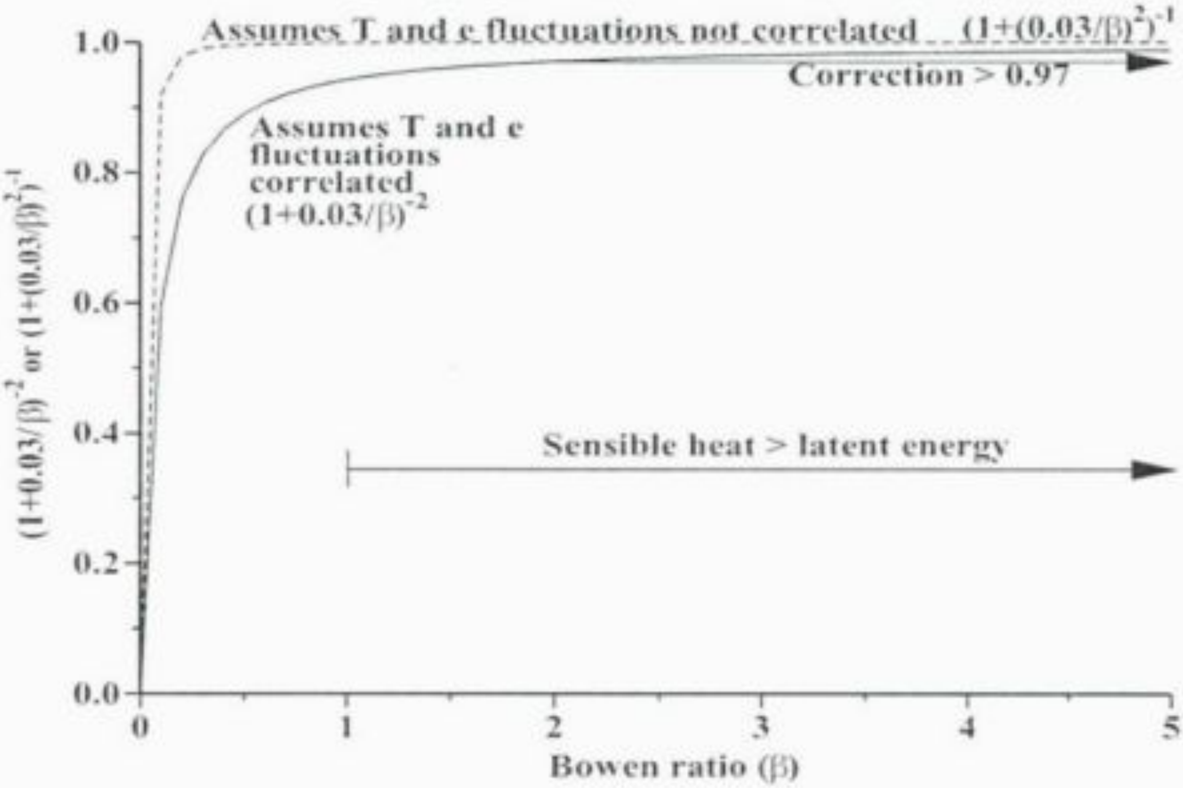

Fig. 2.5 A factor, used by Wesely (1976) for estimating C_T^2 from C_n^2 (Eq.2.59), involving the Bowen ratio β. Assuming correlation between air temperature fluctuations T' and water vapour pressure fluctuations e', for Bowen ratios greater than 1, the factor exceeds 0.942 and for factors greater than 0.97 the Bowen ratio would have to be greater than 2

insignificant. The error magnitudes shown in Fig. 2.5 were confirmed by Moene (2003) who found that estimating C_T^2 from C_n^2 using the Bowen ratio can contain errors of between 5 and 40 % for $\beta < 1$.

Some scintillometer units such as the dual-beam SLS system used in this study also allows friction velocity u_* to be determined from the SLS measurements from which sensible heat flux density F_s is estimated for stable and unstable conditions (Table 2.1). Most other scintillometer units only measure C_n^2 and hence independent measurements or estimates of u_* are required for F_s to be estimated except if the measurement height is several tens of metres and in which case, u_* is negligible. Most often, u_* is estimated, from wind speed measurements, by using Eq. 2.15 or 2.30.

2.13.5 Some disadvantages of scintillometer use

2.13.5.1 Direction of sensible heat flux density

One serious disadvantage of all scintillometers, by their very nature, is that they cannot distinguish between the upward or downward direction of the sensible heat flux density, for example. Most often, a pair of fine-wire thermocouples may be used to measure air temperature at two vertical positions to determine the direction of the sensible heat flux density. This necessitates use of a second logging system. However, frequently, an automatic weather station system is located near the centre of the beam and this could be used for the temperature differential measurement. Alternatively, EC measurements of F_s are used to ascertain the direction or assuming that unstable conditions occur between sunrise and sunset.

2.13.5.2 Saturation

The second major disadvantage of the scintillometer method is due to the fact that the method is based on the theory of weak scattering which may not always apply. Strongly turbulent conditions would invalidate the assumption of weak scattering. The expression for the variance of the log-amplitude (Eq. 2.66), which assumes weak scattering, was developed by Lawrence and Strohbehn (1970). Hence, the theory applied that allows C_n^2 to be determined from Eq. 2.66 assumes that weak scattering of the radiation beam occurs. Weak beam scattering is assumed to correspond to a variance of the log-amplitude of less than 0.3. The assumption of weak scattering is valid only when perturbations in the refractive-index are small. For weak scattering, for a spherical wave, the variance of the log-amplitude of the electromagnetic radiation at the receiver point position is a function of (Eq. 2.67):

the optical wave number $2\pi / \lambda_{beam}$,

the structure parameter of air temperature C_n^2,

and a function that describes the decay of the amplitude due to dissipation at large wave numbers (Thiermann and Grassl 1992). The function in turn depends on the inner scale of turbulence, wave number and beam path length.

As the strength of refractive turbulence increases, the scintillations saturate and any scintillometer whose performance is based on the proportionality relationship between the variance of the log-amplitude and C_n^2 (Eq. 2.66) will fail (Wang et al. 1978). This phenomenon is called saturation of scintillation and is reported by Gracheva et al. (1974). In this case, the only option is to decrease the beam path length and/or increase the beam height position.

2.13.5.3 Friction velocity requirement and free convection estimate of sensible heat flux density

A third disadvantage of many scintillometer systems is that the friction velocity needs to be known at the time C_n^2 is measured for the sensible heat flux density to be estimated. However, an estimate of sensible heat flux density can be arrived at, referred to as the free convection estimate, by performing C_n^2 measurements sufficiently far from the surface. For measurement heights of at least 10 m above the surface, for mainly unstable conditions, the importance of the friction velocity is relatively small. For these conditions the free convection method can be applied (de Bruin et al. 1995):

$$F_s = -0.57\, \rho_{air}\, c_p\, z \sqrt{\frac{g}{T}} \cdot (C_T^2)^{0.75}. \qquad 2.70$$

To summarise: large aperture scintillometers can be used to calculate the turbulent sensible heat flux from C_T^2 only in the unstable free convection layer, which for this purpose may require measurement heights in excess of 10 m. For stable and near neutral conditions, sensible heat flux density estimates using LAS measurements only are impossible. In this case, an independent estimate of the friction velocity is required. Most often, this can be estimated from wind speed. For SLS measurements, the dual-beam arrangement allows sensible heat flux density to be calculated from C_T^2 and ε for all stability conditions (unstable, stable, near neutral) and virtually any measurement height.

2.13.5.4 Influence of water vapour pressure fluctuations on C_T^2

As mentioned previously, the estimation of C_n^2 alone, is not sufficient for determining sensible heat flux density. The estimation of C_T^2 is based on C_n^2 and the Bowen ratio β (Eq. 2.69). For β > 1, the error in C_T^2 in ignoring β and hence the water vapour pressure fluctuations is less than about 6 % (Fig. 2.5). For the SLS method, this is less of a problem since an educated guess for β over a distance of less than 250 m is required. However, in the case of the LAS method, an educated guess for β over a pathlength of up to 10 km, depending on the type of scintillometer used, is more problematic. For relatively heterogeneous terrain, the choice for β is made even more difficult.

2.13.5.5 General

While encouraged by their LAS results, Chehbouni et al. (1999) list advantages and disadvantages or concerns associated with use of the method. Their concerns include the requirement for a humidity correction (Eq. 2.69) using a spatially-averaged Bowen ratio over transects that comprise several patches with significantly different Bowen ratios, the limitation of the method in being unable to distinguish between stable and unstable conditions and also the need for further investigation associated with changes in wind direction from downpath to crosspath. Overall, they found that the LAS method has several advantages over other methods such as the EC method, also mentioned by McAneney et al. (1995), for measuring sensible heat flux density: the method is not sensitive to flow distortions near the instrument; it is easy to operate and maintain; it can provide a reliable tool for estimating sensible heat flux density at spatial scales compatible with meteorological models and remote-sensing satellites.

2.13.6 Application of scintillometry

2.13.6.1 Large aperture scintillometry applications

The MOST requires homogeneous and horizontal terrain. However, such conditions almost never apply. Remotely-sensed surface temperature and use of the LAS method to estimate the area-averaged sensible heat flux density over heterogeneous has been investigated (Chehbouni et al. 2000a, b).

Meijninger et al. (2002b) used LAS measurements over heterogeneous terrain above the blending height (Section 2.8.5), for which MOST is applicable, provided the LAS beam is still in the surface layer. Their work was performed above a flat heterogeneous terrain of rectangular agricultural fields with different crops. A study using LAS measurements for an area comprising forest, grassland and lakes was undertaken by Beyrich et al. (2002a). Hartogensis et al. (2003) investigated using a slanted path over flat terrain, structured terrain, and varied the path height due to the curvature of the earth's surface. The resulting sensible heat flux densities were compared with EC measurements and showed satisfactory results.

The other aspect of scintillometry that deserved attention relates to the assumption that the influence of humidity on C_T^2, used to estimate F_h, could be neglected (Eq. 2.69). The implication is that scintillometer measurements would require knowledge of the Bowen ratio when used above irrigated areas, for example. Hoedjes et al. (2002) discuss the use of the LAS method above irrigated areas. In the former study, the role of regional advection was investigated. In another study, on a spatial scale of a watershed and water basin, Meijninger et al. (2002a) applied two methods to determine the area-averaged latent energy flux density: a two-wavelength method in which both a LAS and a RWS were used. Hemakumara et al. (2003) and Chandrapala and Wimalasuriya (2003) performed routine measurements of spatially-averaged surface fluxes of sensible heat density in river basins using LAS measurements and compared these with estimates obtained from a remote sensing based surface energy balance algorithm for land using NOAA satellite images without any *a priori* calibration. The average deviation of total evaporation estimates for a 10-day period was with 17 % and 1 % when monthly estimates were considered. They suggested that the LAS method is a low-cost alternative to other methods of estimating heat fluxes for use in basin scale water use studies. In another study above semiarid grassland, sensible heat flux density estimates obtained using LAS and NOAA radiometers on orbiting satellites compared well (Watts et al. 2000).

Lagouarde et al. (2002a, b) compared LAS measurements against EC measurements, finding that LAS-measured sensible heat flux density systematically overestimated by approximately 10 %. Their measurements were for a composite surface of wheat and bare soil. In a previous study however, Lagouarde et al. (2000) found that LAS-derived fluxes provide consistent measurements but underestimate by 15 % the flux obtained using the EC method. They attributed the over-estimation to spatial non-homogeneities of the experimental site.

One important application of the use of scintillometry is the ability to provide crosswind data (Andreas 2000, Poggio et al. 2000 and Furger et al. 2001, for example). Crosswind scintillometers use two light detectors separated horizontally by a small distance. The detectors would measure intensities that are highly correlated if one detector is time-lagged. The time lag can be related to the mean wind speed perpendicular to the scintillometer beam. The wind speed measurements represent a weighted average of the wind speed over the full beam pathlength with the winds near the centre of the path carrying greater weight. Commercial crosswind scintillometers are available for SLS and LAS systems.

In a study using a microwave scintillometer and a large-aperture infrared scintillometer, Green et al. (2001) found that the simultaneous use of both scintillometer types allows sensible heat and latent energy flux density at large scales to be measured - over 3 km in their case. Independent EC measurements showed that the LAS (infrared) F_h measurements were within 4 % and that the MWS $L_v F_w$ measurements were within 12 % of their EC counterparts.

Some of the published literature indicates that the scintillometer method is being used as a standard by which other methods are judged. For example:

a non-scintillometer method using a passive optical monitor for atmospheric turbulence and wind speed was used (Stell et al. 2003) to estimate C_n^2 and comparisons were then made against estimates using a commercial scintillometer. The passive optical monitor uses existing lights at various locations as point sources for determining light angle-of-arrival fluctuations. The real time analysis of the fluctuations enabled determination of the power spectrum of the fluctuations every few seconds. The additional power spectrum information yielded more understanding of atmospheric conditions which included average wind speed estimation based on frequency shifts in the power spectrum distribution;

Vilcheck et al. (2002) used microphones and a thermocouple to measure a pressure and temperature differential at two points separated by a specific distance. The microphone/thermocouple system performed measurements over land alongside the scintillometer which was used as the reference method for C_n^2. They presented their comparative results;

in a study of pixel-scale aerodynamic surface temperatures, LAS measurements and meteorological observations by Min et al. (2004) were used to calculate surface temperature for comparison with the hilly radiometric surface temperatures retrieved from satellite data;

Bange et al. (2002) used tower, scintillometer, and averaged ground-station sensible heat and latent energy measurements for various surface types to compare with airborne measurements of turbulent fluxes;

a model for the estimation of C_n^2 from profile measurements (at two levels) of conventional wind speed, air temperature, and humidity as input was proposed by Tunick (2003). The model is based on the structure function formulations of Tatarskii (1961) and invokes MOST for the surface layer. The model algorithm was validated by comparison with estimates from scintillometer data collected at 2 m above ground level over a 450 m path.

2.13.6.2 Surface layer scintillometry

A SLS consists of a number of components (Thiermann 1992, Thiermann and Grassl 1992) but chiefly a transmitter and a receiver unit separated by between 50 and 250 m with a laser beam (low power class 3a, 670 nm) emitted by the transmitter and directed at the receiver. In the case of dual-beam scintillometer systems, a laser beam is split into two parallel, displaced (2.7 mm separation) beams with orthogonal polarizations. The receiver unit measures the radiation intensity fluctuations at a very high frequency, typically 1 kHz, caused by refractive scattering of turbulent eddies in the scintillometer path, emitted by the transmitter. The inner scale of refractive index fluctuations (l_o) and the structure parameter of refractive index fluctuations C_n^2 are calculated from the variances of the logarithm of the amplitude of the two beams, and the covariance of the logarithm of the amplitude fluctuations between the two beams. Using an iterative technique, and applying MOST, turbulent fluxes may be calculated.

de Bruin and Meijninger (2002) compared friction velocity and the sensible heat flux density determined using the SLS method and a hot-film EC system. They found that the random errors in the SLS method were relatively small compared to the scatter found with the two EC systems used. The SLS method overestimated friction velocity for u_* values less than 0.2 m s^{-1} and underestimated for high wind speeds. This would imply that the SLS measurements of l_o are biased. They discussed causes for their results and presented a correction procedure to account for effects of random noise and of so-called inactive turbulence or sensor vibrations. Of particular note is that they also report that the estimated sensible heat flux density is less sensitive to errors in l_o and C_T^2, because of a cancelling of errors.

Hartogensis et al. (2002) investigated the performance of the SLS method in the stable boundary layer and found the method to be superior to the EC method in determining vertical flux densities of sensible heat and momentum close to the ground and/or over short (less than 1 min) averaging intervals. The systematic errors in the SLS measurements reported by de Bruin and Meijninger (2002) relating to friction velocity measurements were overcome by adjusting the beam displacement distance from 2.7 mm to 2.6 mm in the calculations. They stress that this adjustment is presented as a working hypothesis, not a general solution. However, Thiermann (personal communication, 2003) noted that unavoidable uncertainties of the beam displacement of the commercially available unit cause some errors in the absolute values of the friction velocity measurements. He maintains though that overall this error is not larger than typical errors of conventional measurements of friction velocity, considering problems of flow distortion and directional cross-talk of the sensors, instrumental rotation, spectral filtering, necessity of a cut-off at low wave numbers due to the limited averaging time, and conventional sensor calibration.

In a study under unstable conditions and for a clover-ryegrass pasture for which LAS and SLS measurements were compared with EC measurements, Green et al. (1997) found that although the scintillometers respond to eddies 150 and 10 mm respectively, the data scatter for crosspath winds was similar. There was a tighter regression for downpath winds.

Sensible heat flux density over a wheat canopy was measured by Anandakumar (1999) using the SLS, EC and SR methods for one month in order to compare the methods and to investigate the influence of cloud shadows on the 1 min temporal SLS data collected. He found that the sensible heat flux density, averaged over 20 min for the various methods, were in good correspondence with the SLS measurements showing a smoother variation.

Weiss (2001) used the SLS method in various field experiments conducted under different atmospheric conditions. The experimental sites varied from homogeneous and flat terrain to flat, non-homogeneous terrain to slanted, non-homogeneous terrain in an alpine valley. For comparison, the EC method was used. Window periods were used for measurements at the various sites. There was satisfactory accuracy of the estimated sensible heat flux density even for non-homogeneous terrain. Further, the SLS method demonstrated good temporal resolution. In general, this work demonstrated that the SLS method gives accurate values under many atmospheric conditions even over non-homogeneous terrain.

This brief review of the literature shows that there have been more measurement studies using the LAS method than using the SLS method. The reason is probably due to the desire for flux measurements at the scale of a catchment. These measurements can then be used to validate or at least compare with satellite or aircraft-derived fluxes or estimates of the surface temperature. Furthermore, the review has shown there have not been many extended studies that have used SLS, EC, SR and BR methods for estimating sensible heat flux density. In part, this is due to costs but also due to the difficult logistics involved in obtaining quality measurements over long periods. Indeed, many of the studies using the SLS methods have been very short in duration - in some cases for just a few days and in other cases for a couple of months. The same applies to LAS measurements. For example Daoo et al. (2004) compared scintillometer and energy balance methods for two periods of two days each. Beyrich et al. (2002b) used EC and profile methods over a three-week period as well as estimates of the area-integrated sensible heat flux density during daytime were obtained from continuous measurements using a LAS along a 4.7 km path. Liu et al. (2003) used LAS, BR and EC methods for one month for a bare soil surface. Most of the studies used the method for estimating sensible heat flux density but not for then estimating the latent energy flux density using net irradiance and soil heat flux density measurements and invoking the energy balance. In general however, most of the studies agree that the SLS method is a useful, robust and accurate method for obtaining a path-averaged estimate for sensible heat flux density for beam pathlengths between 50 and 250 m. The major limitation is that of saturation under conditions of strong turbulence, necessitating shorter beam pathlengths and high beam heights than that used when saturation occurs. The major advantage, compared to the LAS method, is that many of the micrometeorological parameters, for example, u_*, ε, L_* are also estimated without the need for additional instrumentation. Furthermore, the power requirements are usually not as demanding as with the LAS method. However, the SLS and the LAS methods should be seen as complimentary since their pathlengths are virtually non-overlapping. Furthermore, most-often they scale different regions of the scale of turbulence, namely region B for the LAS method and region C for the SLS method, Fig. 2.2.

To summarise, scintillometry involves the high frequency measurement of the modulation of transmitted light over large distances. The modulation of the light beam is turbulence-induced due to atmospheric temperature fluctuations causing changes in the refractive index. In the case of dual-beam SLS systems, the covariances and variances in the transmitted radiation intensities allow the so-called inner scale of turbulence l_o and the structure parameter of refractive index referred to as C_n^2 to be estimated. Using MOST, the sensible heat flux density F_h and other micrometeorological measures are estimated.

2.13.6.3 Path length details

The Scintec (2000) SLS40-A manual provides a number of useful pointers with respect to beam path length details for the SLS system. These are listed here.

(a) The calculation of the turbulent fluxes, for example sensible heat and momentum flux density, and the Monin-Obukhov length is based on MOST. MOST requires the beam height z of the scintillometer to be significantly larger than the height of the roughness elements z_o where typically, $z_o \approx 0.1\,h$ where h is the canopy height.

(b) MOST also requires site homogeneity (fetch) in the upwind direction of several tens of times the scintillometer beam height. Therefore poor site homogeneity necessitates using a lower beam height but at the same time ensuring that the beam height is much greater than z_o.

(c) For long beam propagation paths, saturation may occur under strong turbulence conditions. This results in signals that are too large to be measured, even by altering the voltage range. Saturation is avoided by using a sufficiently short propagation path or a high beam height. In other words, longer path lengths may require higher beam heights. The same restriction applies to BLS systems.

(d) The path length changes the surface scintillometer measurement range and sensitivity. For typical turbulence conditions, a 100 to 200 m path length provides an optimum sensitivity to the inner scale and all derived quantities.

(e) With short path lengths the intensity fluctuations are small. For longer paths, the average received intensity is small. Both path lengths affect the signal-to-noise ratio. Most often, a 100 to 200 m path length usually provides an optimum.

(f) The propagation path should be horizontal and the soil surface should be as even as possible. A well-defined beam height is required for application of MOST. The primarily measured quantities C_n^2, i.e. the structure parameter for refractive index fluctuations, and l_o, i.e. the inner scale of refractive index fluctuations, strongly depend on beam height and a slant path would lead to an undesired averaging.

Chapter 3

Logistics of estimating evaporation from surface layer scintillometer data

3.1 Abstract

The various methods used for the estimation of evaporation are discussed, particularly with reference to their theoretical basis and instrumentation requirements. The operational procedures for use of the surface layer scintillometer (SLS) method is discussed in detail. The procedures for checking the integrity of the data in real-time are high-lighted as are the post-data collection rejection procedures.

Surface layer scintillometer measurements were performed at the Hay Paddock site near Pietermaritzburg for most of 2003 until November 2004. The system allowed for the real-time estimation of sensible heat flux density every two minutes. For most of the study, the automatic alignment option was enabled except near the end of the study. Without the use of the automatic alignment option, measurements were possible for periods of five days and longer. Longer periods would be possible theoretically with an increased beam height and/or a decreased path length. In addition to the SLS sensible heat flux density measurements, an energy balance system was used to measure the soil heat flux density and the net irradiance from which the latent energy flux density was calculated as a residual using the energy balance.

The percentage of "acceptable" 2-min SLS sensible heat flux density measurements for the daytime hours (taken as 06h00 to 18h00) showed little seasonal variation and was consistently high - between 86.7 % and 94.8 % for the 18-month period. The nighttime variation in the percentage had a more pronounced seasonal pattern with the lowest percentage acceptable measurements occurring between January and March of each year. The lower nighttime percentage values were due to the effects of dew and mist. Included in these percentages are the times for which the electrical power was interrupted. At worst, this period was no longer than a day or so. Other minor interruptions, usually less than two days in duration, were due to an accidental fire and accidental cutting of the cables. The average percentage error-free data varied between 62 and 85 % for the 06h00 to 18h00 period and 33 to 73 % for the nighttime. The lowest percentages were during the summer rainfall period (September to March), presumably due to the influence of rain events on beam transmission.

For the SLS measurements, a sensitivity analysis was used to determine the relative importance of the data inputs of air temperature, atmospheric pressure, beam path length and beam height on sensible heat flux density estimates. Beam height was the height of beam above the level $d + z_o$ at which the wind speed is assumed to be 0 m s^{-1}. In addition, errors in the measurement of soil heat flux density and net irradiance also affected the estimated latent energy flux density.

The influence of surface slope on sensible heat flux density measurements was investigated by altering the height of the receiver relative to the transmitter. Theoretically, a non-horizontal beam relative to a horizontal surface, or *vice versa*, invalidates MOST. The receiver to transmitter vertical height difference used was 1.0 m. For measurements performed over five days, there was no significant consistent difference between 2-min SLS and EC sensible heat flux density measurements in spite of the fact that MOST is invalid for a non-horizontal beam.

The influence of beam height was investigated by also altering the height of the transmitter and receiver units. For most of the study, the beam was about 1.68 m above the soil surface with

vegetation height varying between virtually 0.0 m and a maximum of 1.13 m. The effective beam height therefore varied between 0.82 m and 1.68 m. The lowest beam height used was a height of 0.5 m. The comparison between sensible heat flux density measured using the EC and SLS methods showed that the SLS measurements were not significantly influenced by even this low beam height.

Worst-case errors in atmospheric pressure, air temperature, beam path length and beam height resulted in fractional errors in sensible heat flux density of ± 0.013, ∓ 0.015, ∓ 0.03 and ± 0.04 respectively. Clearly, the beam height above $d + z_o$ needs to be accurately known as the error in beam height contributes the most to the overall error. Overall, the worst-case total fractional error in sensible heat flux density was ± 0.054 and the typical fractional error amounted to ± 0.032.

The error in estimated latent energy flux density from independent measurements of the energy balance components depended on the error in the SLS sensible heat flux density and errors in measured net irradiance and soil heat flux density. Most-often however, the error in SLS sensible heat flux density was smaller than the error in net irradiance and soil heat flux density measurements. Using four to five soil heat flux plates and averaging thermocouples, we investigated the actual variation in soil heat flux density over an area of about a square metre. Using this information as well as other error values from the literature, including measurement error in net irradiance, we estimated the error in latent energy flux density. The seasonal variation in the error in latent energy is generally less than 0.2 mm day^{-1} (0.49 MJ m^{-2}) in winter when the daily evaporation rate was around 1 mm day^{-1} (2.45 MJ m^{-2}) and typically less than 0.4 mm day^{-1} (0.98 MJ m^{-2}) when the evaporation rate exceeded 4 mm day^{-1} (9.8 MJ m^{-2}). The measurement with the greatest contributing error is the soil heat flux density measurement. Care therefore needs to be exercised to ensure that soil heat flux density measurement procedures do not compromise the estimates of latent energy flux density using SLS sensible heat measurements. The same caution would apply to BR estimates of latent energy flux density and the EC method when only sensible heat flux density is measured and latent energy flux density is estimated using the net irradiance and soil heat flux density energy balance components.

3.2 Introduction

There are many methods used for estimating evaporation (Table 3.1). As mentioned by Drexler et al. (2004) in their recent review, very few of the evaporation estimation methods work well for an hourly time-step, and in some cases, do not work well even for a daily time-step. There is perhaps only one method that allows for the direct measurement of the total water loss from a vegetated surface (soil evaporation plus transpiration). Virtually all of the methods rely on a theoretical framework, for arriving at an expression for the latent energy flux density in terms of other measurable quantities, based on certain assumptions or approximations. Some methods, such as the EC method, involve the measurement of two atmospheric variables and a theoretical framework and assumptions that allow for the direct calculation of the latent energy flux density. Other methods, such as the BR method, involve up to eight measurements and a theoretical framework and assumptions to estimate sensible heat and latent energy flux density. There are a whole host of empirical methods, not listed in Table 3.1, used to estimate the grass reference evaporation which use the crop factor approach to calculate evaporation.

The weighing lysimetric method is often regarded as the standard for evaporation measurement (Table 3.1). Weighing lysimeters are large containers, filled with soil, water, other chemicals and entire plant(s). Weight measurements are made at regular time intervals. The weight difference per unit time difference (in s, min, h or day) divided by the density of water (1000 kg m^{-3}) and divided by the cross-sectional area (m^2) of the lysimeter yields the evaporation rate in mm s^{-1}, mm min^{-1}, mm h^{-1}

Table 3.1 Selected methods used for measurement or estimation of sensible heat F_h and/or latent energy flux density $L_v F_w$ terms of the surface energy balance where $I_{net} + L_v F_w + F_h + F_{soil} = 0$

Method	Measurement distance or area	Averaging period	Theoretical basis	Closure statement/comment
Class A-pan/ Symon's tank	$< 5\ m^2$	Usually daily	$L_v F_{w\ pan} = L_v \rho_w (\delta W / \delta t) / A_{pan}$	Only pan evaporation measured (historical merit only)
Lysimetry	$< 10\ m^2$	Usually 20 to 60 min	$L_v F_{w\ lysimeter} = L_v \rho_w (\delta W / \delta t) / A_{lysimeter}$	By definition, $F_h = -L_v F_w - I_{net} - F_{soil}$ (Eq. 2.46, 2.47)
Microlysimeter	$< 1\ m^2$	Usually daily	$L_v F_{w\ lysimeter} = L_v \rho_w (\delta W / \delta t) / A_{lysimeter}$	By definition, $F_h = -L_v F_w - I_{net} - F_{soil}$ (Eq. 2.46, 2.47). Most-often used for measuring soil evaporation
BR energy balance	Vertical measurement distance of 1 m (grassland) to 2 m for forests	Usually 20 to 30 min	$L_v F_w = \dfrac{-I_{net} - F_{soil}}{1 + \beta}$ $F_h = \beta L_v F_w$; assumes $K_h = K_w$	By definition, $-L_v F_w - F_h = I_{net} + F_{soil}$
EC (2 sensors)	Sensor path length of 100 to 150 mm	Usually between 20 and 60 min	$L_v F_w = -\rho c_p \overline{w'e'}$ $F_h = -\rho c_p \overline{w'T'}$	Generally, $-L_v F_w - F_h < I_{net} + F_{soil}$
EC (1 sensor)	Sonic path length of 100 to 150 mm	Usually between 20 and 60 min	$F_h = -\rho c_p \overline{w'T'}$ $L_v F_w = -F_h - I_{net} - F_{soil}$	By definition, $-L_v F_w - F_h = I_{net} + F_{soil}$ (Eq. 2.45)
SLS	Beam length between 50 and 250 m	2 min (possibly) and 60 min	MOST to estimate F_h and measurements of I_{net} and F_{soil} to estimate $L_v F_w$ using $L_v F_w = -F_h - I_{net} - F_{soil}$	By definition, $-L_v F_w - F_h = I_{net} + F_{soil}$
LAS	Generally 500 m < beam length < 3.5 km (up to 10 km for BLS)	2 min (possibly) to 60 min	Measures C_n^2, the structure parameter for refractive index fluctuations; MOST is assumed	By definition, $-L_v F_w - F_h = I_{net} + F_{soil}$
SR	Point measurement at a defined height above the surface	2 min (possibly) and 60 min	$F_h \propto$ amplitude of the air temperature ramps/(ramp period)	By definition, $-L_v F_w - F_h = I_{net} + F_{soil}$ (Eq. 2.48)

Table 3.1 Selected methods used for measurement or estimation of sensible heat F_h and/or latent energy flux density $L_v F_w$ terms of the surface energy balance where $I_{net} + L_v F_w + F_h + F_{soil} = 0$ (continued)

Method	Measurement distance or area	Averag-ing period	Theoretical basis	Closure statement/comment
Temperature variance	Point measurement of the friction velocity and the standard deviation in air temperature at a defined height above the surface	30 min	$F_h \propto \sigma_T$ and u_*; MOST is assumed	By definition, $-L_v F_w - F_h = I_{net} + F_{soil}$
Temperature method	Point measurement of the friction velocity and the air temperature at a defined height above the surface	30 min	F_h is related to the weighted average of the time history of air temperature and u_*	By definition, $-L_v F_w - F_h = I_{net} + F_{soil}$ K theory is assumed
Reference evapora-tion	Point measurements of solar irradiance, T_z, e_z, and U	Hourly/ daily	Penman-Monteith method for estimating reference evaporation (FAO 56), and use of a crop factor	Only reference evaporation and estimated crop evaporation estimated
Infrared technique	Areal measurement (< 25 m²) of T_{canopy} and wind speed	Hourly	Fick's Law to estimate sensible heat flux density	By definition, $-L_v F_w - F_h = I_{net} + F_{soil}$ (Eq. 2.49)
Atmometer (e.g., ET-gage)	Point measurement at 1-m height above soil surface	Hourly	Empirical, with material cover of known pore size or known material	Only reference evaporation measured
Heat pulse /sap flow	Measurements made in or surrounding the stem of plants (< 200 mm)	Hourly	Rate of movement of heat pulse in stem; stem energy balance with continuous heat applied	Transpiration measurements only

or mm day^{-1}. Lysimeters allow the water loss from such containers to be measured for very short time intervals and longer from hours to days or longer. The main component of water loss from a lysimeter is due to transpiration by plants and evaporation from the exposed soil surface. The disadvantages of the lysimetric method include: cost, destructive nature of the measurements in the sense that a relatively large volume of disturbed or sometimes undisturbed soil is placed in a container usually of metal construction and the non-portable nature of the measurement method. Also, the representation or the so-called footprint of the evaporation measurement is localised to the cross-sectional area of the lysimeter. Much less expensive is the microlysimetric method but the surface area is an order of magnitude less than a large weighing lysimeter and it is still a destructive method and not designed to contain whole plants. The more portable and much less invasive EC and BR methods used for the estimation of sensible heat and latent energy flux density by measurements above the surface are more popular research methods for the estimation of evaporation (Table 3.1). They are both portable systems that can be used to collect unattended measurements for extended periods of time. These methods were the focus of a previous report (Savage et al. 1997).

Given the previously-mentioned limitations of the lysimetric method, the search for an alternative standard for evaporation estimation has been the focus of many studies for several decades. The EC and BR methods essentially yield point estimates of sensible and latent energy flux density although these estimates are influenced by events upwind from the point of measurement. The extent of the footprint area of influence on the measurement using both EC and BR methods has received attention. For example, Savage et al. (1996, 1997) investigated the footprints of EC measurements and Stannard (1997) investigated the footprints of BR measurements. The literature reports on the inadequacy of the EC technique for the direct estimation of latent energy flux density (Wilson et al. 2002, Ham and Heilman 2003) with the result that the magnitude of the sum of sensible heat and latent energy flux density may be less than the sum of the net irradiance and soil heat flux density (Table 3.1) resulting in a closure ratio less than 1 (Eq. 2.5). This situation is referred to as a lack of closure. As an alternative therefore, the EC method could be used to measure the sensible heat flux density from which the latent energy flux density may be estimated from simultaneous measurements of soil heat flux density, net irradiance and the measured EC sensible heat flux density using Eq. 2.3.

Each of the methods presented in Table 3.1 result in measurements with different footprints. The footprint of the lysimetric measurements is the area of the lysimeter. In the case of the EC method, the footprint is defined as the relative contribution of upwind surface sources to the measured sensible heat flux density.

By theoretical definition and making certain assumptions, the BR measurements always produce exact closure (Table 3.1). Due to a number of theoretical and practical problems we investigated the use of a SLS for the spatially-averaged measurement of sensible heat flux density and the estimation of latent energy flux density using soil heat flux density and net irradiance measurements. Problems associated with EC and BR methods include the following:

- that EC measurements of latent energy flux density are often underestimated, as claimed by a number of authors (for example, Twine et al. 2000);
- that both the EC and the BR estimates of latent energy are based on point measurements;
- that due to the theoretical assumptions made using the BR technique, exact measurement comparisons between the BR and EC measurement techniques have been frustrated by differing assumptions, differing footprint areas, measurement limitations and often-times poor agreement;
- a comparison of two methods does not indicate which method is correct especially if the methods disagree or disagree some of the time.

The SLS measurement method would remove the limitation of point estimates. The use of the SLS is the only method that supposedly allows for the estimation of sensible heat flux density over distances between 50 and 250 m. The frequency of SLS measurements is typically 1 kHz compared to 10 Hz for EC measurements, 1 Hz for BR measurements and 125 Hz for BLS measurements if the crosswind measurements are included. Because of the high frequency of the SLS measurements, the averaging period for SLS measurements can be as low as 1 or 2 min compared to the commonly used 20 min for EC and BR averaging periods.

The objective of this chapter is to present the technical aspects of the SLS method for the estimation of evaporation for a mixed grassland community for an extended period of time. The methodology for the measurement of sensible heat flux density and the subsequent estimation of latent energy flux density is presented. A sensitivity analysis is used to determine the order of importance of the input parameters for the SLS method as well as the importance of beam angle and the effective beam height. Also, the procedures and definition for the rejection of out-of-range and bad or "doubtful" data are presented.

3.3 Theory

Surface layer scintillometry, with the use of Monin-Obukhov similarity theory (MOST) allows for the estimation of sensible heat flux density. The technique relies on the determination of the structure parameter of the refractive index fluctuations, C_T^2 (Eq. 2.28), from the covariance of the logarithm of the beam signal amplitude (B_{12}) measured using the two detectors. In addition, the inner scale of turbulence l_o (Eq. 2.25) is determined from a correlation coefficient r that relates the single detector beam signal amplitude variances B_1 and B_2 to the covariance B_{12}: $r = B_{12} / (B_1 B_2)^{1/2}$. The term B_1 refers to the variance of the logarithm of the amplitude of the beam signal. Application of MOST and an iterative procedure allow the following to be determined:

Monin-Obukhov length L (Eq. 2.40);

friction velocity u_* (Eqs 2.30, 2.33, 2.34);

temperature T_* (Eq. 2.34);

sensible heat flux density F_s (Eq. 2.34).

3.4 Material and methods

3.4.1 General

Surface layer scintillometry, allows for the determination of sensible heat flux density using MOST, and relying on the determination of the structure parameter for refractive index as well as the inner scale of refractive index fluctuations.

Different measurement systems were used for measuring sensible heat flux density: two EC systems and a dual-beam SLS system, two BR systems as well as an energy balance system for the measurement of net irradiance and soil heat flux density. The one EC system was also used to measure latent energy flux density directly and the BR systems used to measure sensible and latent energy flux densities for ten months. Data from a weather station system was used to calculate grass reference evaporation. Daily data from a South African Weather Service automatic weather station, about 5 km away by line of sight, but excluding solar irradiance were used to patch missing data. The clocks of all systems were set according to a USA atomic clock (www.precision-time.com) once a week. The clock used in the SLS computer tended to drift off by approximately 15 seconds per week. This drift would affect the two-minute sensible heat flux density measurement comparisons between systems but would have little effect on daily estimates.

Field measurements were conducted from 14 January 2003 to November 2004 (Table 3.2) above an open and mixed grassland community in the Hay Paddock area neighbouring Ashburton and close to Pietermaritzburg, South Africa (-29.6348° S, 30.4329° E) with an altitude of 671.32 m. The average slope of the study site (Fig. 3.1) is 1° 15' to the SE. The fetch distances in the prevailing S-E wind direction is 135 m for the EC systems and 90 and 138 m for the SLS transmitter and receiver respectively. The fetch for the next-most dominant winds from the N-W is 117 m for the EC systems and 146 and 114 m for the SLS transmitter and SLS receiver respectively. Beyond these distances and to the south, the site is exposed and the slope increases significantly. To the north of the study

Table 3.2 Details of operations at the Hay Paddock research site

Date	DOY	System	Comment
11 to 26 Jan 2003	11 to 26	SLS40-A	Installed SLS system - beam path length of 51 m, beam height of 1.58 m
13 Jan	13	EB	Installed system to measure soil heat flux density, net irradiance, soil water content, solar irradiance, fine wire thermocouples for direction of sensible heat
19 Jan	19	ECAT	Calibrated the EC system for temperature and zero wind speed using a zero air box
19 Jan to 13 Feb	19 to 44	ECCSI	Used EC system (uses 1-D sonic) that is not water-proof
26 Jan	26	SLS40-A	Removed system
28 Jan	28	SLS40-A	Moved SLS transmitter and receiver to increase the beam path length to 101 m, beam height of 1.68 m
31 Jan	31	AWS	Installed an AWS system (2 m)
17 Feb	46	ECAT	Commenced EC measurements (1.5 m height)
8 April	96	EB	Installed pyranometer to measure surface reflection coefficient
7 to 16 May	126 to 135	All	Mowing of site: On 7 to 10 May, net radiometers, soil heat sensors were still in long grass; on 16 May the grass cast of SLS40-A beam was cut
19 May	138	AWS	Removed the AWS system
5 June	155	EB	Installed ETgage and rain gauges
17 June	167	ECAT	Calibrated EC system for temperature and zero wind speed using a box covering the 3D sonic anemometer
15 Aug	227	All	Accidental fire - all measurements suspended
17 Aug	229	SLS40-A	Measurements resumed
18 Aug	230	BR	Reconnected all sensors used for energy balance to a replacement data logger
	237	BR	Installed wind speed and direction sensor
31 Aug	243	ECAT	Measurements resumed after fire and replacement of analogue to digital system
1 Sept	244	ECAT	Calibrated the EC system for temperature, relative humidity and zero wind speed using a zero air box
20 Oct	294	SR	Commenced SR measurements
23 Nov to 8 Dec	328 to 344	ECAT, SR	Power problems
27 Dec	361	BR11	Installed first BR system (Vaisala HMP45C sensor)
28 Dec	362	ECAT	Increased sensor height from 1.45 m to 2.12 m above soil surface
9 Jan 2004	9	BR15	Installed second BR system (Vaisala CS500 sensor)
13 Jan	13	BRDew-10	Installed third BR system (Dew-10 sensor)
24 to 27 Jan	24 to 27	SLS40-A	Switched off SLS system due to disconnection of power while fence was installed
28 Jan	28	BR3	Installed fourth BR system BR3 (Vaisala HMP45C sensor)
29 to 30 Jan	29 to 30	ECAT/SR	ECAT/SR battery charger problem

Table 3.2 Details of operations at the Hay Paddock research site (continued)

Date	DOY	System	Comment
2 Feb	33	BR11	Reduced flow rate (07h30) of BR11 system to 0.4 L min^{-1}
3 to 10 May	124 to 129	All	Mowing of site: grass was cut around the instruments on 4 May; the bales of hay remained on the site for three weeks; on 10 May the grass area east of SLS40-A beam was cut
25 July	207	SLS	Switched off the automatic alignment system
11 Aug	224	BR11	Increased BR11 equilibrium time before measurement from 40 s to 60 s
14 Aug	227	BR11	Replaced CS500 temperature sensor with a type E thermocouple
17 Aug	230	SLS	Decreased height of receiver to 0.68 m with transmitter height maintained at 1.68 m - effective beam height set to 1.08 m above $d + z_{\_}$ to investigate the effect of a non-horizontal beam
29 Aug	242	SLS	Decreased height of transmitter to 0.68 m with receiver height maintained at 0.68 m - effective beam height set to 0.5 m above $d + z_{\_}$ to investigate the effect of a low beam height on SLS measurements

area, there is a residential area and tall trees (cf Figs 1.2 and 3.1 but note that Fig. 1.2 refers to true north and Fig. 3.1 to magnetic north - magnetic north is 22° W of true north).

3.4.2 Climate

The long-term annual rainfall for Pietermaritzburg (South African Weather Service data) is 928 mm (58 years of data) and the mean maximum and minimum air temperatures are 24.8 and 12.3 °C respectively. During winter, there is frequent dewfall but frost hardly ever occurs. Management practices include mowing (normally in April each year) and burning (in August when firebreaks are established and in October). Due to the low rainfall in 2004, no burning was carried out prior to November 2004.

3.4.3 Surface layer scintillometer

A dual-beam surface layer scintillometer (model SLS40-A, Scintec Atmospärenmessetechnik, Tübingen, Germany), referred to as the SLS system in this report (Fig. 3.1), was used to measure the sensible heat flux density every 2 min for a beam distance of 101 m. The beam path was adjacent the automatic weather station. The SLS40-A receiver has four detectors with two of the detectors used for automatic identification of and correction for transmitter vibration by the software used for analysis. In other words, the SLS40-A dual-beam system and its four detectors enable the separation and correction for the intensity fluctuations caused by beam movement. There are two detectors per beam with the separation distance between the detectors being 2.7 mm. The dual-beam scintillometer was positioned at a height of between 1.5 and 1.65 metres above the soil surface and the path length between the receiver and transmitter units was 101 metres except at the beginning of the study a path length of 50 m was used. Towards the end of the study, various beam heights were used from an effective height of 0.5 m to a height of 1.5 m.

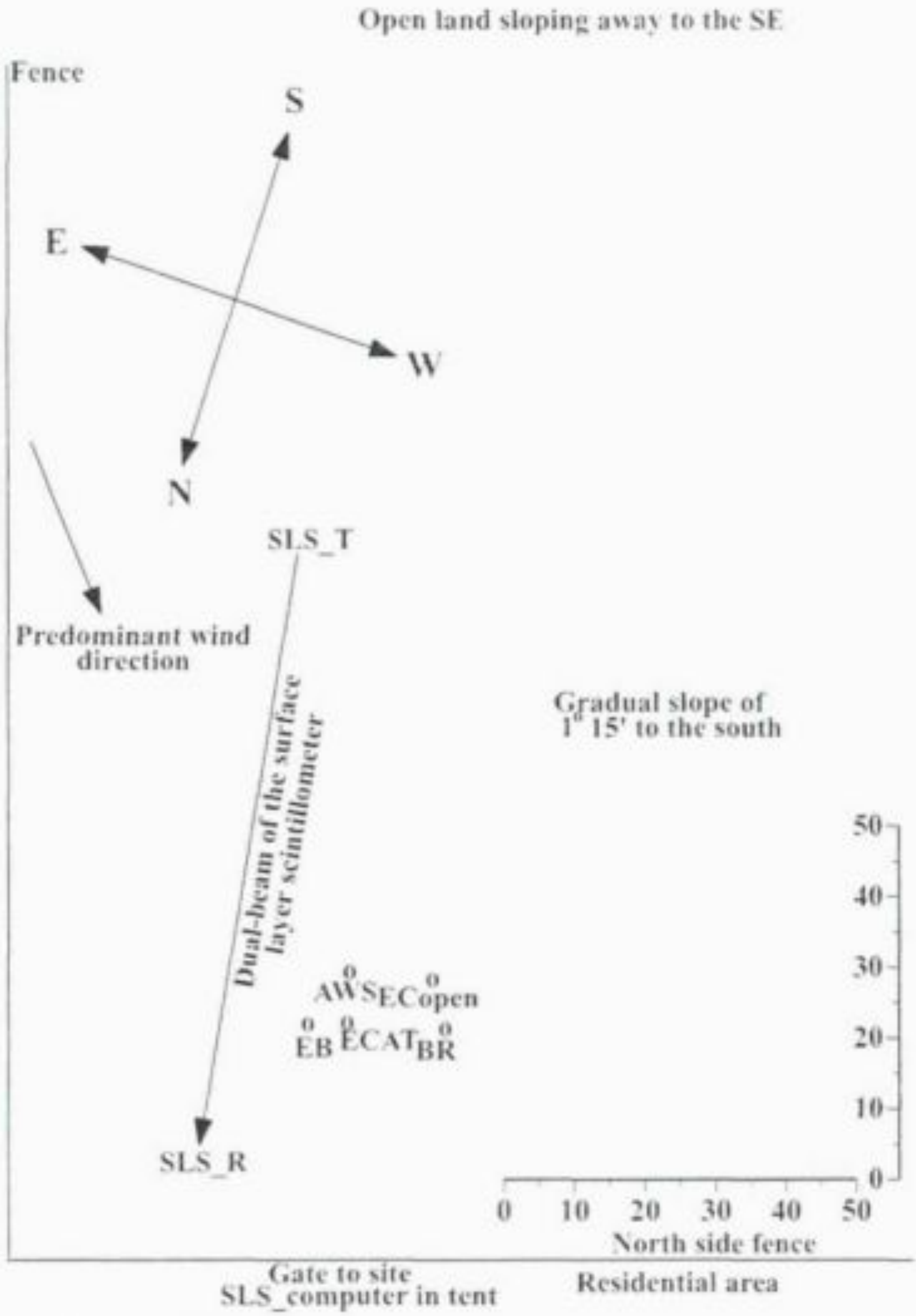

Fig. 3.1 Schematic of the research site and sensor placement. The diagram is to scale (- scale shown at bottom right in metres). The SLS transmitter and receiver positions are indicated by SLS_T, SLS_R (*generally with the dual-beam 1.5 m above canopy in 2002 winter and 0.8 m in 2001/2 summer*); the two EC systems are indicated by ECAT (100-mm sonic path at a height of 1.5 m above the soil surface) and ECopen (150-mm sonic path at a height of 2.67 m above the soil surface) indicates the open path LI-7500 water vapour pressure and carbon dioxide concentration sensor; the energy balance system (net irradiance, soil heat flux density, soil water content, soil temperature, canopy temperature, fine wire thermocouples for air temperature profile measurements) before the 2003 accidental fire is indicated by EB; the BR system is indicated by BR which was subsequently used as an energy balance and weather station system after the accidental fire; the automatic weather station system is indicated by AWS (in operation for day of year 31 to 138, 2003); the two SR thermocouple positions, not shown, were adjacent the ECAT position

A computer was connected to the signal processing unit (SPU) through the computer serial port (Fig. 3.2). The computer, the SPU and the SLS switch-box were housed in a tent. The cables to the receiver and transmitter were separately connected between the swich-box and the receiver (50 m) and transmitter (150 m) units. The transmitter (Fig. 3.3) and receiver units were mounted on tripods that could be raised to a maximum beam height of 2 m. The vegetation height during the year of study varied but was always less than 1.13 m for most of the study.

The SLS beam height was referenced to the height at which wind speed was estimated to be 0 m s^{-1}. Using Eq. 2.15, the neutral wind profile equation, this height corresponds to height $d + z_o$ above soil surface where $d \approx 0.67\,h$ where h is the canopy height and $z_o \approx 0.1\,h$ is the roughness length (Eq. 2.16). Approximately therefore, the beam height input value was the height of the beam above the soil surface minus 0.77 h. The average beam height above the soil surface during winter when the grass height was short was about 1.6 m. In the first quarter of 2003 during which the grass height was much taller, the beam height input value when the canopy height was about 1.12 m was 1.6 m - 0.77 h $\approx$ 0.82 m. The SLS manual refers to the beam height as the height of the beam above ground instead of the height above the soil surface minus $d + z_o$.

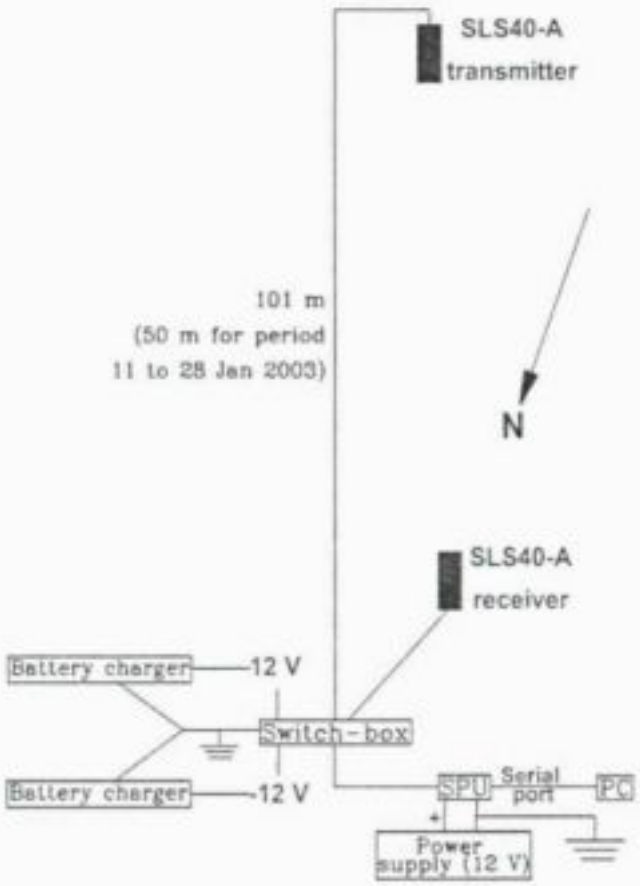

Fig. 3.2 A schematic of the SLS system: the switch-box, the signal processing unit (SPU) and the personal computer (PC) and associated batteries, battery chargers and mains power supply were all housed in a tent to prevent water damage. The power requirements of the switch-box are typical for a transmitter to receiver distance of 101 m and a receiver to switch-box distance of 50 m. The transmitter and receiver SLS units also require tripod stands

Fig. 3.3 A side-view schematic of the SLS40-A transmitter. Of particular note for alignment purposes is the embedded alignment hole and the three positioning screws - one is obscured

The SLS employs a diode laser source with an output of 670 nm wavelength and 1 mW (2 mW peak) mean output power. The beam displacement and detector separation distances are 2.5 mm each, with a detector diameter of 2.7 mm. Software together with the instrument allows on-line measurements at a frequency of 1 kHz and subsequent calculation of the structure parameter for refractive index (C_n^2, $m^{-2/3}$), structure parameter for temperature (C_T^2, $K^2\ m^{-2/3}$), the inner scale of turbulence as indicated by the inner scale of refractive index fluctuations (l_o, mm), kinetic energy dissipation rate (ε, $m^2\ s^{-3}$), sensible heat flux density (F_s, W m^{-2}), momentum flux density (τ, Pa) and the Monin-Obukhov length (L, m). The input requirements for these calculations include air temperature T_{air}, atmospheric pressure P, beam path length L_{beam} and the beam height h_{beam} relative to the reference height at which the wind speed is zero. A profile air temperature difference measurement is required for determining the direction of the sensible heat flux density. Calculations are performed for both directions at for each 2-min interval.

Two-minute averages of all SLS-calculated parameters were stored on a computer hard drive for further analysis. The sign (direction) of the sensible heat flux density was determined using the BR profile air temperature measurements and a second pair of fine-wire thermocouple measurements for the period prior to the accidental 2003 fire. For each two-minute period, only data for which the inner scale of refractive index fluctuations l_o was greater than 2 mm and the percentage of error free data (%*EFD*) was greater than 25 % were accepted for further analysis. In general, the %*EFD* was close to 100 % for much of the time during the day except during wet conditions. An analysis of the 2003 data for day of year 180 to 270 showed that the average of the daytime (06h00 to 18h00) 2-min %*EFD* data was 90 % and the nighttime average was 78 %, nighttime SLS measurements were often not possible due to condensation or mist affecting the passage of the laser beam through the boundary layer.

3.4.4 Scintillometer components and power requirements

There are a number of components to the SLS40-A scintillometer system (Fig. 3.2) used in this work:

1. the transmitter mounted on a tripod stand and firmly secured;

2. the receiver mounted on a tripod stand and firmly secured;

3. a signal processing unit (SPU) as a stand-alone unit housed in a tent. The SPU contains a microprocessor that performs the required analogue signal processing and statistical analysis and communicates the results to the PC *via* the serial port at 9600 baud. The SPU allows for the connection of a number of external sensors (air temperature, atmospheric pressure sensors and the like). The SPU also contains a stepper motor encoder card for the SLS40-A for purposes of automatic alignment. The SPU requires 12 V for operation;

4. a switch-box, housed in a tent, which connects to the transmitter and receiver units, to the SPU and to the batteries. The switch-box supplies the voltages required for the transmitter and receiver;

5. a computer with a 386 processor (20 MHz) or better operating under Windows 95/98/NT/2000/XP is sufficient, housed in a tent, to execute the MS-DOS software to capture the signals from the SPU;

6. three 12 V (7 A h) batteries, housed in a tent, to power the SPU and separate batteries to power the transmitter and receiver units *via* the switch-box;

7. for the SLS40-A unit used, cables for connecting the transmitter to the switch-box and to the SPU in turn. Alternatively, if the automatic alignment is not being used as is the case for the SLS20 and the SLS40 units, then the transmitter needs to be powered by a separate battery placed in close proximity. In this case, the SPU needs to be connected to the switch-box and the receiver to the switch-box with no direct wire connection between SPU and the transmitter.

Since the SPU is not water-proof, it does require protection from rain and dew. The laser diodes of the transmitter have a typical lifetime of 20 000 hours, are fairly weather proof but both units were partly covered with insulation to reduce radiation load. The operational temperature for the transmitter should not exceed 50 °C and 60 °C for the receiver. Both units need to be checked during routine visits for dirt, insects or cobwebs that would decrease beam transmission. A clue that the beam is obscured is often indicated by reduced $<X>$ and $<Y>$ average voltage signals as well as differences in the $<X>$ and $<Y>$ voltages indicated by the diagnostic screen discussed in more detail later.

The SPU current drain and power requirements are as follows: 12 V, 0.7 A with a peak of 1.5 A. Routinely however, the current drain of the SPU was just under 1.05 A, which may increase to 1.35 A when centering the beam and 1.15 A during alignment of the transmitter and receiver. Typically, the power requirements of the transmitter was -12 V to 12 V for cable lengths less than 150 m and for the receiver the power requirement is -12 V to 12 V for cable lengths less than 50 m. We used two 12 V batteries (7 A h) as the ± 12 V power supply connected to a common centre-tap ground such that the one battery supplied 12 V and the other -12 V. A battery charger was permanently connected to each of the two batteries of the -12 to 12 V power supply (Fig. 3.2). The current drain for both the transmitter and the receiver is 0.2 A and the maximum voltage that may be supplied is 13.5 V. For transmitter cable lengths between 150 and 350 m and receiver cable lengths less than 50 m, the power requirement is -16 V to 16 V (with a maximum of 17.6 V).

The switch at the switch-box must be set to 'int' if the transmitter and receiver are powered by the SPU. With the switch in the middle position, the transmitter and receiver are disconnected.

3.4.5 Switching beam on

For the beam of the SLS transmitter to be on, it has to be supplied with the correct voltage, there has to be a computer connected *via* the computer serial port to the scintillometer SPU, and the SLSRUN software correctly executed. Furthermore, the receiver and the SPU have to be supplied with the correct voltages. The system has no on or off switch - it is switched on using software, assuming everything else has been correctly set up. The switch-box has a red LED to indicate when the SLS transmitter laser beam is transmitting. However, even with the transmitter beam on, measurements may not be valid due to incorrect beam alignment, beam obstruction or incorrect data inputs.

3.4.6 Procedures prior to alignment

Since the rotational positions of the transmitter and receiver tubes (Fig. 3.3) can be easily altered using any one of the three positioning screws, it is important to verify that the rotational positions around their main axes are correct. This is important since each beam is identified at the receiver by its beam polarization. When standing at the rear of the transmitter, the top positioning screw will move the tube vertically up or down. The left screw will move the tube to the left or to the right and the right screw will move the tube to the right or to the left. With the top positioning screw not securing the position of the tube, simultaneously rotating the left and right screws can cause upward or downward movement of the tube. It is advisable that the operator practice altering the tube rotational position prior to a field alignment. The two beams of the scintillometer transmitter are identified at the receiver by differences in their beam polarization. An incorrect orientation will produce considerable crosstalk in the measured signals. For the same reason, it is best that both the transmitter and receiver units are correctly mounted in the horizontal.

3.4.7 Beam alignment

Crucial to the use of the SLS is correct beam alignment. Although not absolutely essential, the use of two people for beam alignment would reduce the time taken. Two-way radios also allow for easier communication between transmitter and receiver locations for the initial alignment procedures and between receiver and PC locations for subsequent software alignment. The beam alignment procedure requires that power be supplied to the SPU, the transmitter and the receiver. Furthermore, the SLSRUN software needs to be running and proper communication between the computer and the SPU established. The SLS transmitter and receiver need to be correctly mounted on tripod stands with both units roughly at the same height above surface with both units facing each other. It is not necessary for the correct data inputs to be used for beam alignment. For a path length of about 50 m, it is advisable that the operator not look directly at the beam. For distances greater than this, one may look at the beam but only for a few seconds at a time. The laser beam is a type 3a beam, similar to that used in laser pointers. As such, the equipment has to carry warning notices of this hazard. Notices were placed at the transmitter and at the receiver.

Before alignment, it is important to inspect the transmitter and receiver windows for dirt or cobwebs that may reduce the voltage signals.

The alignment procedure is best undertaken at the receiver rather than at the transmitter due to the larger field of view of the receiver. Experience has shown that the alignment procedure is also possible at night since the horizontal and vertical positions at which the beam has the greatest intensity is most easily visible to the eye at night. Nighttime alignment also meant that special equipment such as a theodolite or other survey equipment for alignment is not required. Nighttime alignment also meant that there was no need for noting the voltage signals directly at the receiver at the time of alignment. The magnitude of the voltage signals could be confirmed adequate at a later time. The only difficulty with nighttime alignment is that it is more difficult to ensure that the beam is perpendicular to the receiver window. This can however be easily done during the day.

The receiver should be as horizontal as possible on its tripod stand. It is important to note that the field of view of the receiver is much larger than the beam's divergence. Therefore, the stability of the tripod supporting the receiver is much less critical than that used for the transmitter.

Then, at the transmitter position, ensure that the transmitter tube is central to its housing. The transmitter unit should at this stage be attached firmly to the tripod stand and the stand firmly secured using guys or bungee cords. Ideally, there should be at least three such attachments. Also, the beam should be as horizontal as possible. Ideally too, MOST requires that the surface is horizontal. This requirement is impossible to satisfy for many sites. We used a level to ensure that the transmitter was horizontal. A ladder was used for easy viewing of the bubble indicators of the level placed on the transmitter. Also, viewing through the alignment hole of the transmitter allowed for identifying the initial placement position of the receiver (Fig. 3.3). If the receiver cannot be seen in the alignment hole, the transmitter position can be raised or lowered by altering the tripod stand support positions. Alternatively, the receiver position, typically 101 m from the transmitter, can be lowered or raised until the receiver appears at the centre of the alignment hole of the transmitter.

Once the beam is on, alignment is most easily achieved from the position of the receiver. A five-step procedure, also possible at night, may be used to align the beam and perform measurements:

1. the operator may walk slowly from left to right of the receiver position and back again while viewing the beam, mentally noting the strength of the beam. Three or four or more traverses may be required to identify the exact horizontal position at which the beam has the greatest intensity. Initially, this horizontal position may not coincide with the location of the receiver. The receiver on its tripod stand should then be moved to that position. It may be necessary to again walk from left to right to carefully identify again the position of maximum beam strength in the horizontal;

2. once the correct horizontal position has been identified, it remains to identify the correct vertical position for the receiver. For determining this correct vertical position, a small ladder may be required. Locate the ladder at the best horizontal position. Then walk slowly up and down the ladder to locate the position at which the beam intensity is the strongest in the vertical. If the maximum beam intensity is at the highest position of the ladder, the beam may overfly the transmitter position. Similarly, if the maximum beam intensity appears to be at a position near the bottom of the ladder, the beam position may be too low. If this is the case, this position needs to be lowered or raised, as the case may be, at the transmitter side and the procedure restarted afresh. If however, there is a horizontal position at which the beam is strongest, then the receiver needs to be lowered or raised to that height. Small horizontal and or vertical adjustments to the tripod stand of the receiver or positional adjustments to the receiver itself may be necessary to obtain maximum beam strength. These adjustments necessitate viewing the beam through the alignment hole of the receiver. This procedure is much easier to perform during the day but it is also possible to perform during the night with the aid of torch light at the far end of the alignment hole. Caution is necessary with this procedure for two reasons. Firstly, the receiver must be more than 50 m from the transmitter when viewing the beam. Secondly, an error of parallax can result in beam misalignment. The error of parallax is demonstrated in Fig. 3.4. In each of the three cases, the centre dot represents the beam, the inner circle represents the end of the receiver alignment hole furtherest from the operator and the outer circle represents the alignment hole closest to the eye. For the left and right pair of circles, the beam is in the centre of the inner circle but misalignment would still occur since the beam is not also central to the outer circle. To avoid the error of parallax, the two circles should be concentric as is the case for the middle pair of circles. The error

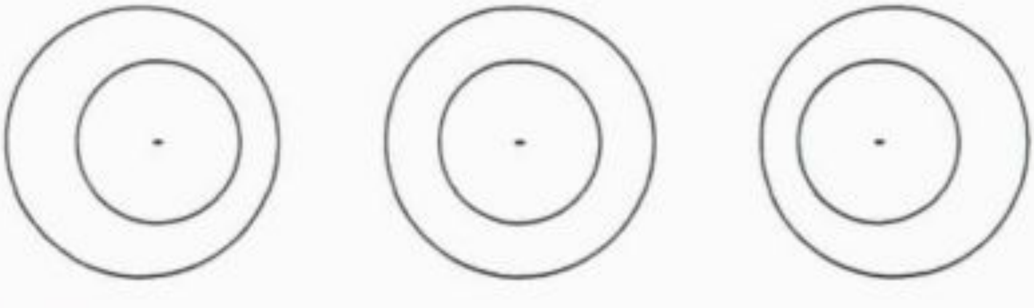

Fig. 3.4 An illustration of the error of parallax problem when viewing the distant laser at the receiver alignment hole. The problem is avoided by standing back some five or more metres from the receiver so that the two circles converge or ensuring that the two circles are concentric as is the case shown for the middle set of circles

of parallax is reduced by viewing through the alignment hole at a distance of five or more meters behind the receiver;

3. once the receiver has been positioned at the position at which the beam intensity is strongest in the horizontal and in the vertical, the stand of the receiver unit need to be made secure using bungee cords. As in the case with securing the transmitter, at least three such attachments are required. Care is needed at this stage to ensure that the receiver unit is not moved and the alignment disrupted;

4. once the best position has been determined, the central position of the beam can be improved by only viewing the beam from the receiver position through the receiver alignment hole. A beam high and to the left when viewed from the receiver positions can be better aligned by lowering it and moving it to the right from the transmitter position. This can be done by carefully adjusting the three positioning screws (Fig. 3.3) at the transmitter position. Very small incremental adjustments to the positioning screws at the transmitter should be performed and the beam strength examined using the SLSRUN software. Two-way radio communication between the transmitter and computer locations at this stage is essential. By altering the transmitter position screws, the transmitter should be carefully and incrementally moved from left to right and the position corresponding to maximum beam intensity located. Following this, the transmitter position screws should be used to incrementally move the beam upward and downward until the position corresponding to maximum beam intensity located;

5. If not already done so in step 4, the beam then needs to be centered in the window of the receiver using the SLSRUN software. Executing the software SLSRUN at the MS-DOS command line displays the screen shown in Fig. 3.5. At this stage, it is advisable to enter the correct path length (normally 101 m in this case), the beam height (which is the beam height above the soil surface minus $d + z_m$, shown here as 1.62 m), the air temperature (°C) and the atmospheric pressure (hPa) [top left and top middle of Fig. 3.5]. It is also advisable to specify the periods for the output data files (top right of Fig. 3.5): 2 min for the main data and 12 s for the diagnostic data files. Other information required is the specification of an automatic file naming convention, a data subdirectory path and the types of data to be collected (bottom left of Fig. 3.6). This is discussed in more detail later. Once these choices have been made, it remains to align the beam using the software. Clicking on the **Alignment** pull-down menu (Fig. 3.6) displays two choices - either the **Level Screen** option or the **Automatic** option. Normally, the **Automatic** option is chosen (Fig. 3.7). At this point, the beam can be centred a

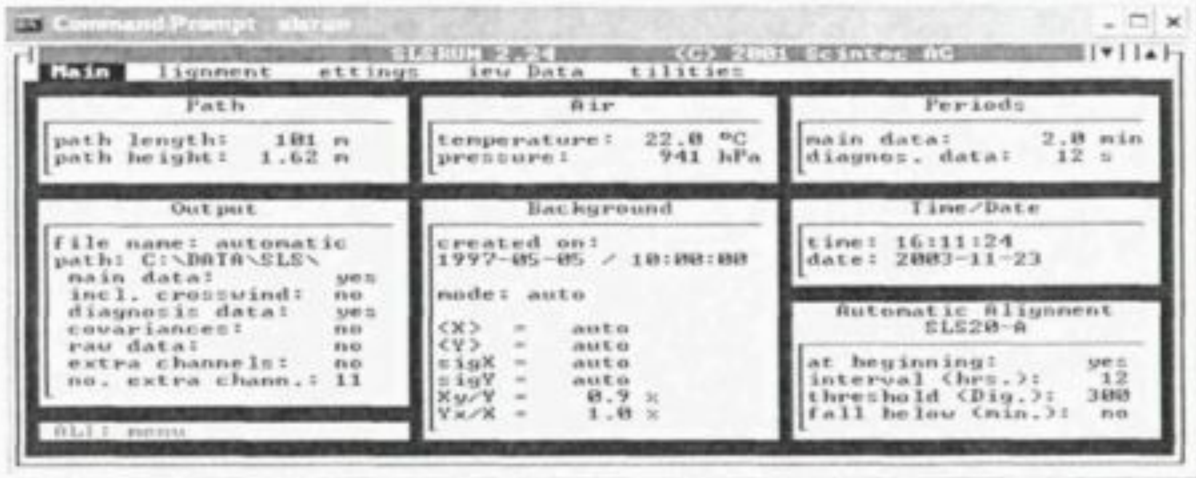

Fig. 3.5 The SLSRUN version 2.24 start-up screen showing the five different menus used as well as some of the input data and options specified

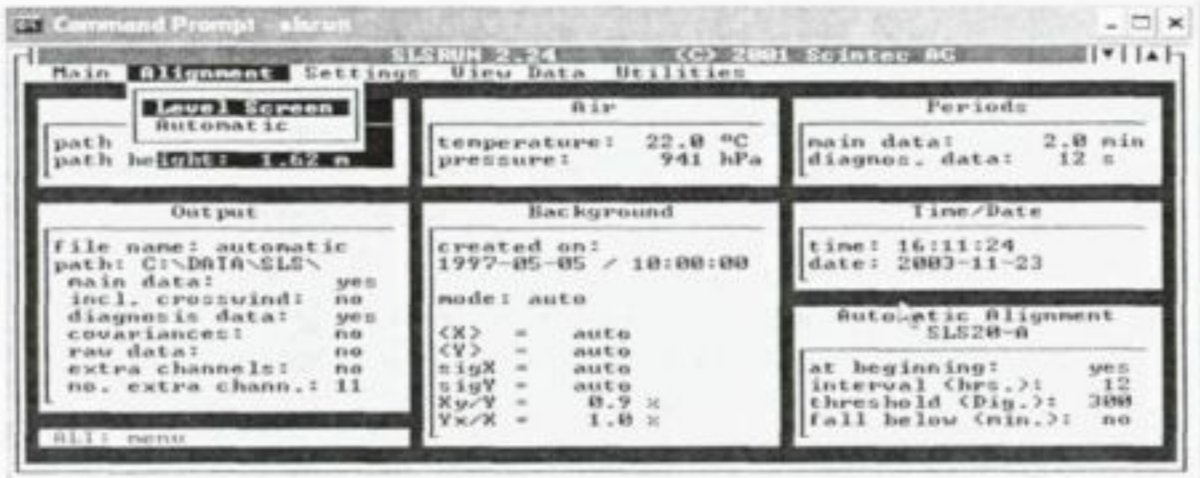

Fig. 3.6 The SLSRUN start up screen showing the selection of the Alignment option and the two sub-options: Level Screen or Automatic alignment

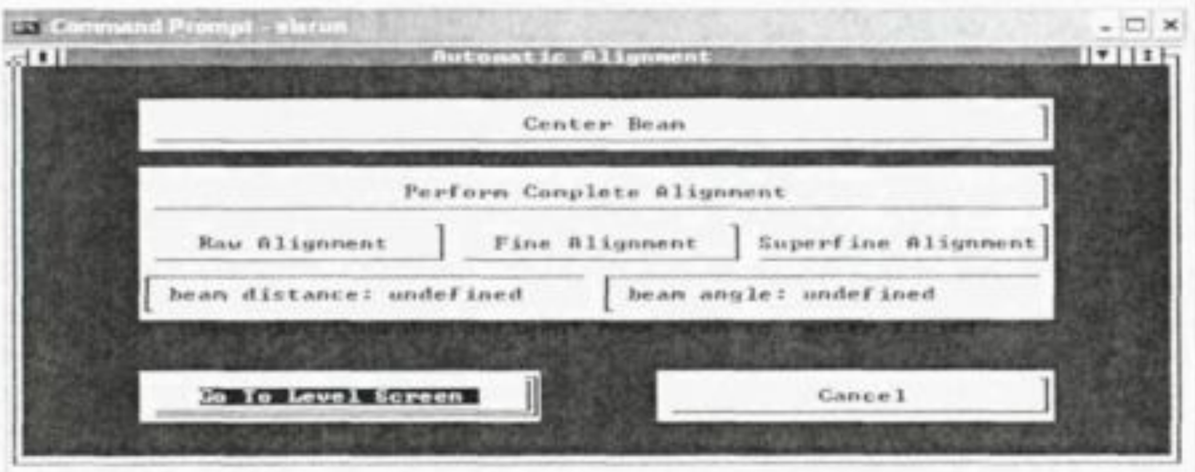

Fig. 3.7 The options for automatic beam alignment. Routinely, the beam is first centred five or more times

number of times. Any procedure may be aborted by pressing the ESC key. It is not necessary to perform a complete alignment since one of the options under the **Settings** menu and **Automatic Alignment** sub-option (Fig. 3.7) allows one to specify that a complete alignment be performed prior to the start of measurements (bottom right of Fig. 3.5). This option also allows one to specify a complete alignment on a regular time basis. We routinely used two automatic alignments per day (at 6 am and 6 pm). Each automatic alignment procedure takes about 6 min and no measurements are stored during that time. Towards the end of the study, the automatic alignment option was switched off to investigate how often the beam alignment procedure is required.

At this point, measurements may be initiated by selecting Main and Start measurements. However, following movement of the transmitter and/or receiver units, background and crosstalk measurements should be performed.

Confirmation of the strength of the voltage signals is possible by clicking on **Go To Level Screen**. This displays the voltage signals for channels A1, A2 and channels B1, B2. Ideally, the optimum range of the voltages is between 700 and 1400 relative units, is indicated by two horizontal lines. For paths shorter than 100 m or longer than 200 m, the voltage levels should be as close as possible to the optimum range. For a path length less than 100 m the voltage levels can exceed the optimum range (since the intensity fluctuations are likely to be small). For path lengths greater than 200 m, the voltages can be below the optimum range since large intensity fluctuations will improve (increase) the signal-to-noise ratio.

3.4.8 Background and crosstalk measurement

The SLSRUN software corrects for background signals and crosstalk between the two scintillometer channels (Fig. 3.5, bottom middle). The background values and crosstalk coefficients determined during this procedure are used to correct the data during measurements. It is advisable to measure both the background and crosstalk values whenever the instruments are moved and before measurements. The measurement of background and crosstalk are initiated by first selecting the **Settings** pull-down menu and then specifying **Background** to invoke the background and crosstalk measurement procedures (Fig. 3.8). In the first dialogue box, one has to first allow measurement of the undisturbed signal, then cover the whole beam to allow measurement of the background and then cover each beam

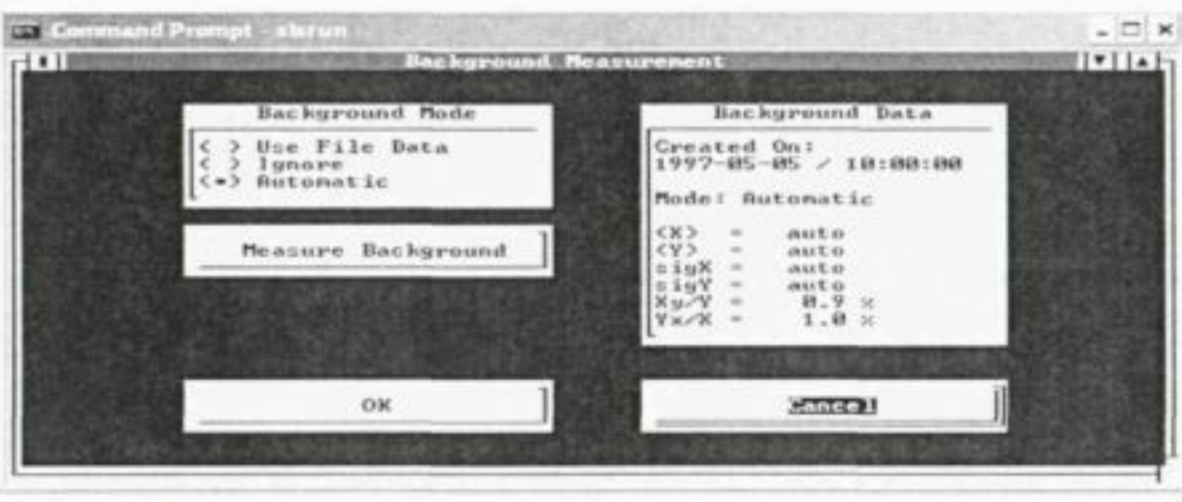

Fig. 3.8 For measurement of the background and crosstalk values, click on Settings and then Background Measure Background. Prompts are displayed on the screen for when to block both beams, the one beam and then the other beam

separately using a small piece of thin paper to allow measurement of the crosstalk. The use of thin paper allows the beam position to be revealed when covered. Covering of the beams must be done where the beam exits the transmitter. Care must be taken to ensure that only the one beam is covered and not both and that the tripod stand and transmitter position is not disturbed. A message will follow if there was incorrect procedure in covering each beam and then both beams. The measured coefficients are then displayed on the computer screen.

The mean values <X> and <Y> should be in the range 5 to 25. If not, the background measurement procedure should be repeated. The standard deviations sigX and sigY should be less than 10 and if not, the **Background Measurement** procedure would need to be repeated.

The crosstalk coefficient should be less than or equal to 5 % and if not, the **Background Measurement** procedure would need to be repeated. If one or both crosstalk coefficients are still greater than 5 %, the transmitter and receiver units should be re-aligned to the correct horizontal position and the **Background Measurement** procedure repeated.

Once the procedure has been completed, the necessary background and crosstalk coefficients are stored in a file for use by SLSRUN for automatic correction of the data during real-time measurements.

3.4.9 Beam misalignment and beam saturation

Beam misalignment results in reduced voltages, and often zeros for the various output parameters. The manual of the SLS40-A provides a five-point check procedure for possible causes of low voltage signals:

- 1. check if there is dirt, dew or ice deposit on the transmitter and/or receiver windows;
- 2. check the alignment of the transmitter;
- 3. check the alignment of the receiver;
- 4. check the pinhole adjustment at the transmitter;
- 5. check the dip switch setting, corresponding to the voltage range setting, in the receiver.

Most often, it is cobwebs or dirt that covers the windows that reduces the voltage signal. Cleaning is achieved using a cotton bud to remove the cobwebs and distilled water to remove dirt on the actual window. Next most common, it is the receiver that goes out of alignment relative to the transmitter position. This often occurs after high wind or rain. Rain events loosen the soil with the result that the tripod stands may move their positions. Saturation of the voltage signals results in low voltages under conditions of strong turbulence (Section 2.13.5.2). Such conditions invalidate the assumption of weak scattering upon which the SLS method depends. Should saturation occur frequently, then the effective beam height needs to be increased and or the beam path length decreased. In the unlikely event that all of these procedures have been followed but the voltage signals are still too low, then the voltage range setting needs to be altered. This can be done without having to switch the beam off or disconnect cables. Remove the three metal screws from the back circular plate of the receiver. Carefully remove the plate ensuring support to the plate to prevent tension on the attached wires. Two rows of switches should be visible (Fig. 3.9). The ON position corresponds to the switch being flipped vertically downwards and OFF vertically upward. The settings for the different voltage ranges are shown in Table 3.3. When securing the metal plate back in position, care is needed to ensure that the wires are moved to the side of the vero boards to avoid them being severed by the boards.

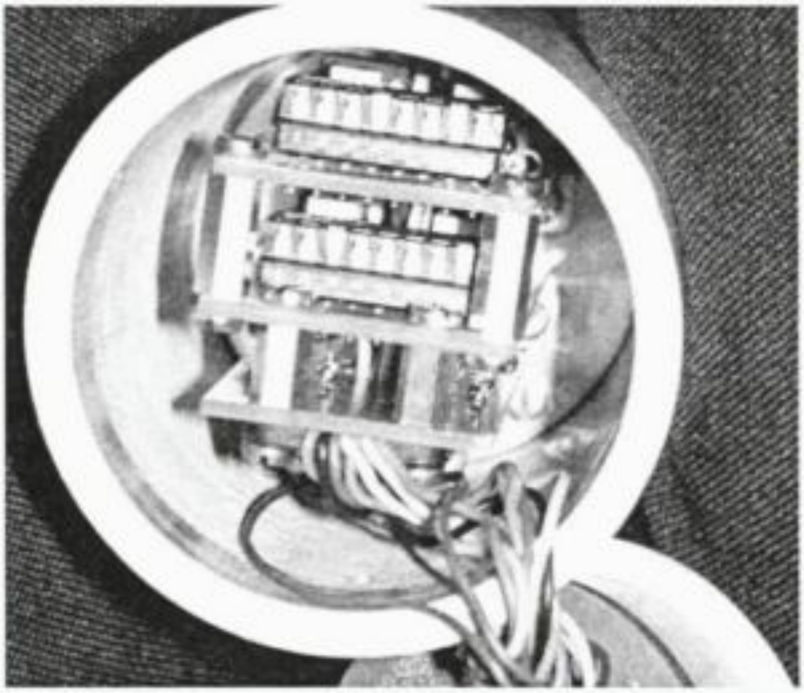

Fig. 3.9 The rear of the SLS40-A receiver with the back metal plate removed. The two rows of dip switch settings shown are used to set different voltage settings for each of the two SLS40-A beams (Table 3.3)

Table 3.3 The receiver switch settings that define the voltage range used. A "1" corresponds to ON or the down position and a "0" corresponds to OFF or an up position. Increasing the switch setting number would increase the voltages measured

Switch setting number	Switch number (from left) 1 2 3 4 5 6 7 8	Path length (m)
1	0 0 0 1 0 0 0 1	< 100
2	1 1 1 0 1 1 1 0	90 to 120
3	0 0 1 0 0 0 1 0	110 to 150
4	1 1 0 0 1 1 0 0	140 to 190
5	0 1 0 0 0 1 0 0	170 to 220
6	1 0 0 0 1 0 0 0	210 to 250

Pin hole adjustment involves maximising the beam intensity with the transmitter beam aimed at a white wall. The two over-lapping red dots should be visible on the wall. Three plastic screws near the front end of the transmitter are used to adjust the beam position. Less than quarter turn adjustments are necessary. Two small screw drivers are used to adjust two of the screws at any one time. If one of the two pin-hole adjustment screws are loosened, the other one must be adjusted in the opposite sense to tighten with the aim being to maximise the beam intensity. Care is needed since loosening both screws may result in the beam becoming "lost". It is important that the one screw be tightened while the other is loosened. Once the beam intensity has been maximised by adjusting a pair of screws, the procedure needs to be repeated for each of the remaining two pairs of screws.

3.4.10 System inputs

Although five data inputs are required for the execution of the SLSRUN program, it is possible to perform a postdata recalculation with different values chosen for the five data inputs. Three of the inputs may in fact be measured using air temperature and atmospheric pressure sensors connected directly to the SPU. The system inputs include:

- atmospheric pressure (hPa);
- air temperature (°C);
- profile air temperature difference (°C);
- beam path length (m);
- beam height above the level at which wind speed is 0 m s^{-1}.

Routinely, for inputs, a fixed atmospheric pressure of 940 hPa and an air temperature of 25 °C between November 2003 to March 2004 and otherwise 15 °C was used. The sensors that can be connected to the SPU need to have a voltage output of 0 to 10 V. None of the sensors routinely used met this requirement so data loggers and other sensors were used to measure these inputs, apart from atmospheric pressure. Routinely, atmospheric pressure was not measured but estimated from latitude, longitude and altitude and measurements of air temperature and water vapour pressure (Eqs 3.2 to 3.5 of Savage et al. 1997). A sensitivity analysis, demonstrated later, showed that the SLS software outputs are not very sensitive to atmospheric pressure and air temperature changes. Note that in the calculation of the SLS outputs, air temperature is in K so that even a 10 °C change in air temperature is effectively only a 3 % change in K units.

The lack of an input for the profile air temperature difference is not crucial at the time of measurement since this input is only used to determine the direction of the sensible heat flux density - either towards or away from the surface - and not its magnitude. This direction was determined using measurements of air temperature at two heights using BR thermocouples (75 μm in diameter) and cross-checked against the sign of the EC sensible heat flux density measurements.

The most sensitive inputs affecting software outputs are beam path length and beam height inputs. Again however, incorrect inputs can be corrected post-data collection, by re-estimating the outputs using the correct data inputs. It is recommended that in spite of this, these two inputs be correct since then the screen-displayed outputs are as near as possible to being correct. This approach then allows decisions to be made in real-time. This may be particularly useful when performing real-time comparisons of SLS estimates of sensible heat flux density against EC estimates.

3.4.11 System outputs to the computer screen

The SLS is checked by examining the voltage signals shown by the various SLSRUN screens. The output screen displays the voltage signals for the two laser beams. In general, the voltages for the different channels should be between 700 and 1100. Voltage signals greater than 200 may still result in reliable measurements. Generally however, measurement accuracy decreases with decreasing voltage signals.

The SLS software shows three screens of information. The one screen display corresponds to stable conditions usually for the night, the second corresponds to unstable conditions mostly experienced during the day and the third displays the diagnostic data. For a 2-min averaging period, the first two displays are updated every two minutes but the diagnostic display is updated every 12 s. Routinely,

Table 3.4 Typical diagnostic data displayed for a 2-min period. The meaning of the headings of each column is presented in the text. Each data line represents a 12-s period

Sub no	n	<X>	<Y>	sigX	sigY	Cor	Xmin	Xmax	Ymin	Ymax	errX	errY	errW
0	11500	739.7	757.0	35.6	32.2	0.532	598	915	615	933	0	0	4
1	12000	737.5	757.9	34.1	30.5	0.514	598	880	606	901	0	0	4
2	11500	735.5	757.2	33.8	30.0	0.508	617	862	603	898	0	0	4
3	12000	734.5	761.0	31.5	27.8	0.512	613	878	642	893	0	0	4
4	11500	732.4	761.9	31.6	28.3	0.521	606	859	627	906	0	0	4
5	12000	728.7	760.1	32.9	29.8	0.531	586	861	616	890	0	0	4
6	12000	728.3	767.0	29.7	26.0	0.542	626	851	653	904	0	0	4
7	11500	727.4	771.1	28.1	24.2	0.569	623	856	660	943	0	0	4
8	12000	719.2	754.7	30.1	25.3	0.545	485	869	602	891	0	0	4
9	11500	724.5	763.4	31.6	27.8	0.538	604	860	642	978	0	0	4

during the day, it is only the diagnostic display and the display for unstable conditions that needs to be scrutinised to check for correct functioning of the SLS.

3.4.11.1 The diagnostic display

A typical diagnostic display of the SLS software is shown (Table 3.4).

The data line associated with the **sub number** column is generated every 12 s. For a 2-min data collection period, the run number is double the number of minutes since midnight. So for example a run number of 471, not shown, refers to $2 \times 471/60$ h = 15.7 h or the local time of 15h42. For a 2-min period, there are ten sub number lines: 10×12 s = 120 s, with each line associated with a 12-s period.

The second column, labelled **n**, refers to the number of data points evaluated within the diagnosis data period of two minutes, in this case. The maximum number of data points evaluated within a 12 s period is 12000. So the rate of data collection is 12000/12 s = 1000 Hz. This frequency is almost two orders of magnitude greater than that for EC measurements and three orders of magnitude greater than BR measurements. Notice that for some of the 12-s sub number lines, the number of data points used is 11500, which corresponds to 500 data points not used for the calculations. In these cases then $100 \times 11500/12000$ % = 95.83 % of the measurements are used. During conditions of poor visibility, excessive vibration or significant crosstalk, the number of data points used would decrease. Consistently low values of n may be an indication of beam misalignment, requiring operator intervention.

The third column with the heading **<X>** displays the average SLS voltage for channel 1. The display value is not raw data since three corrections have already been applied: a background correction, an analogue to digital range correction and a crosstalk correction. Ideally, the mean voltage should be between 700 and 1400. The voltages corresponding to <X> and <Y> need not be the same.

The fourth column with the heading **<Y>** displays the average SLS voltage for channel 2. As with the channel average, corrections for background, an analogue to digital range correction and a crosstalk correction have already been applied. As was the case for <X>, the mean voltage should be between 700 and 1400.

The fifth and sixth columns, with the heading **sigX** and **sigY**, refers to the standard deviation of the channel 1 and 2 signals during each 12-s period.

The seventh column, with the heading **Cor.** is the statistical correlation between the signals in channel 1 and channel 2 after the normal background correction, analogue to digital range correction and crosstalk correction.

The eighth to eleventh columns, **Xmin**, **Xmax**, **Ymin**, and **Ymax** refer to the minimum and maximum for channels 1 and 2 respectively. Ideally, these should be between 700 and 1100.

The twelveth column, **errX** refers to the error for channel 1 (0 for no error) for which there are numerous codes used to indicate the type of error. The numerous codes used are given as an appendix to the manual. The important codes for the operator to take note of are those larger than 4. Diagnostic data with such an error code that exceeds 4 are rejected and not used further for analysis. Values of 0 indicate that no data could be used in the calculations.

The thirteenth column, **errY** refers to the error for channel 2.

The final column, **errW** refers to the error associated with the wind option, not used in this case, for the SLS40-A.

At the bottom of the diagnostic data screen, there are other important data shown that are useful for error-checking the system. Three bits of information that need to be checked whenever there is a site visit are:

beam distance: The beam distance is the distance of the beam from the central position as a percentage of the possible scan range. So a value of 100 % means that the beam has reached the outer area of the scan cone and a value of 0 % means that the beam is in the centre. The manual of the SLS40-A recommends a manual re-alignment if the beam distance is greater than 80 %;

beam angle: The beam angle is the angle of the beam displacement from the centre in degrees (0 to 360°);

vibration index: The vibration index is defined as (cor1A1B + cor2A2B)/2, where cor1A1B is the correlation between main channel 1A and channel 1B and cor2A2B is the correlation between main channel 2A and channel 2B. If the vibration index is less than 0.5 the corrected data can usually be used. A vibration index greater than 0.5 usually occurs if C_n^2 is very small. Under these conditions, normally during the night, the signal fluctuations caused by vibration dominate over signal fluctuations caused by turbulence. There is therefore a high rate of data rejection.

3.4.11.2 Real-time display of turbulence data for unstable conditions

The real-time displays of the data are updated every 2 min. The display (Table 3.5) includes:

a run number corresponding to the number of 2-min intervals since midnight. In the example, 390 corresponds to 2 × 390 min = 780/[60 min h^{-1}] = 13 h or 13h00;

the Nok in column 2 is the percentage of error-free diagnosis data periods within the main data period. A data line is subsequently rejected if the Nok value is less than or equal to 25 %. During the day, this value is usually between 80 and 100 %. Consistently low Nok values requires the operator to realign the beam;

Table 3.5 Typical real-time data displayed every 2-min for unstable conditions from 13h00 to 13h18. The meaning of the headings of each column is presented in the text

Run	Nok	Time	C_n^2	l_o	C_T^2	ε Diss	Heat[1]	Mom	MO-L	Wind
390	100	13:00	0.912919	5.36	1.142808	0.01418	173.0	0.0526	-4.825	0
391	100	13:02	0.930667	4.91	1.165025	0.02009	182.1	0.0666	-6.527	0
392	90	13:04	0.761178	4.21	0.952856	0.03725	176.0	0.0980	-12.040	0
393	50	13:06	0.313806	2.74	0.392827	0.20746	166.1	0.2852	-63.370	0
394	90	13:08	0.284935	6.99	0.356687	0.00492	71.0	0.0257	-4.005	0
395	100	13:10	0.329552	6.97	0.412539	0.00496	78.5	0.0255	-3.594	0
396	100	13:12	0.401794	5.63	0.502973	0.01162	98.0	0.0462	-7.000	0
397	70	13:14	0.602809	3.37	0.754606	0.09131	187.3	0.1705	-25.000	0
398	100	13:16	0.782815	2.33	0.979942	0.39701	326.1	0.4399	-61.835	0
399	60	13:18	0.451371	3.67	0.565033	0.06463	145.9	0.1361	-23.771	0

[1]The SLS40-A system indicates normal daytime sensible heat flux density values as positive as shown here. The convention in the report however is that sensible heat flux density away from the surface corresponds to an energy loss to the surface and is therefore assigned a negative value

time (corresponding to the computer clock time);

C_n^2, the structure parameter for refractive index, with unit 10^{-12} $m^{-2/3}$;

l_o, the inner scale of refractive index fluctuations, with unit mm. A data line is subsequently rejected if l_o is less than or equal to 2 mm (for a 101 m beam path length). Note that l_o becomes smaller at larger wind speeds or closer to the ground. The height dependence of l_o may allow one to alter the height of the beam path for a defined beam path length so as to increase or decrease the voltages;

C_T^2, the structure parameter for air temperature fluctuations, with unit K^2 $m^{-2/3}$;

diss (ε), the rate of turbulent kinetic energy dissipation with unit m^2 s^{-3};

heat (F_s), the turbulent flux density of sensible heat, calculated using MOST, with unit W m^{-2} for which the sign is positive for unstable conditions and negative for stable conditions;

Mom ($-\tau$), the negative of turbulent flux density of momentum with unit N m^{-2} calculated using MOST for unstable conditions;

MO-L ($\mathscr{L}$), the Monin-Obukhov length with unit m calculated using MOST for unstable conditions;

Wind, in the last column, is not used since this requires a cross-wind optional extra.

3.4.11.3 Real-time display of turbulence data for stable conditions

The real-time display of the data for stable conditions is similar in format to that for unstable conditions except that MOST, for stable conditions, is applied (Eqs 2.43 and 2.44, for example).

3.4.12 Data files required or created during system operation

Various items of software are used with the SLS40-A. Most of the software requirements are bundled together in the SLSRUN.EXE program (MS-DOS based, version 2.24). However, the SLSFIL.EXE program, for example, needs to be executed first before data collection can be performed using the SLSRUN software.

For the SLS40-A scintillometer system, a number of data files are required or created. The file names are not case sensitive:

1. the SLSCAL.XXX files. The program SLSFIL software generates the path length calibration data files required by SLSRUN. The files generated by SLSFIL are named SLSCAL.XXX, where XXX represents the optical propagation path length specified during software execution. For each propagation path length used, a separate file is used. So for example, the file SLSCAL.101 needs to be created using SLSFIL for a path length of 101 m. These path length files need to be located in the same subdirectory in which SLSRUN is located and need to be created before execution of SLSRUN;

2. the slserr.dat file is an error file created whenever SLSRUN encounters a problem - for example, an incorrect specification of a data subdirectory;

3. the log file (SLSLOG.DAT). The file contains a single line of the date and time of when the beam was switched on. Each time the beam is switched on again, the content of the file is over-written;

4. the *.pos file (with pos as the file extension). This information file contains the record of the date and time when the position of the beam was automatically aligned. The "beam distance", "beam angle" and voltage signal values at the time of the alignment are also shown. A convenient file-naming extension that the SLSRUN software can use is the yymmdd format. For example the file name 040227.pos would correspond to a position realignment file created on 27 th February 2004;

5. the slsbck.grn file, the background and crosstalk file, is created by the Background Measurement procedure. The information from the background and crosstalk measurement procedure is stored in this file. Whenever a background and crosstalk procedure is followed, the contents of this file are overwritten;

6. the *.dgn diagnostic data file. If specified from within SLSRUN, the diagnostic data may be collected, usually one file per day (just less that 1 Mbyte for two-minute data). Each line of data in this file corresponds to a 12-s period. So, for example, the file 040227.dgn would be a diagnostic file created at midnight on the day before and closed at midnight on the 27 th February 2004;

7. the main output data file, the turbulence data file, is stored with a res extension, one file per day. So, for example, the file 040227.res would be created at midnight on the day before and closed at midnight on the 27 th February 2004. Usually, it is this file that is opened using a spreadsheet program such as Microsoft Excel. For a day of 2-min output data, this file has a size of 120 kbytes.

3.4.13 Sign convention for the energy balance terms and the profile air temperature difference

The energy balance equation used, $I_{net} + L_v F_w + F_h + F_s = 0$, implies that for the day when the net irradiance is usually positive, the remaining energy balance terms are generally negative. In the BR system, the profile air temperature difference, δT_{air} is defined as $\delta T_{air} = T_{lower} - T_{upper}$. This definition results in positive BR sensible heat flux density values during the day - in other words, the opposite sign convention. The on-screen SLS sensible heat values for unstable conditions occurring usually during the day are also positive, as are the values in the main output data files. The real-time EC sensible heat values are also positive for unstable conditions.

3.4.14 Rejection criteria for the exclusion of out-of-range and "bad" or doubtful SLS data

The SLSRUN software only uses error free diagnostic data to form the basis for the calculation of the main output data. SLSRUN detects errors due to one or more of the following:

- unrealistically low correlations. This can occur in the case of precipitation, or when the inner scale of refractive index fluctuations decreases below the measurement range (under strong wind conditions) or with transmitter vibration which usually occurs when C_n^2 is very low;

- unrealistically high correlations. This can occur if the beam is temporarily obscured or the transmitter position is unstable or when the laser beam has just been switched on;

- low signal-to-noise ratios. These low ratios can be avoided by increasing the beam path length if it is less than 100 m or by decreasing it if it is more than 200 m. In addition, reducing the beam height may increasing the signal-to-noise ratio. Extremely small thermal turbulence, which occurs when fluxes are small (sunset, sunrise, large and dense cloud cover) and in the case of laminar flow (calm nights) may also result in low signal-to-noise ratios. Note that reducing the measurement height reduces the influence of vibration due to wind;

- crossing of the beam by insects, rain, mist, or particles cause measurement errors.

The following are not errors directly detected by the system but may need attention:

- errors due to misalignment of the transmitter has only a minor effect on the accuracy of the measurements provided that the intensities are sufficiently high. Misalignment however does magnify the effects of vibration resulting in decreased signal-to-noise ratios;

- intensity differences between the mean intensities in the four channels of the SLS40-A scintillometer cause little error. However, large differences could be due to dirt or cobwebs on or near the window of the receiver.

In spite of SLSRUN rejection criteria, a number of conditions were imposed to reject data post-data collection. The rejection criterion were applied after the data was imported into Excel. When a main data file is opened in Excel (*.res file), Excel loads an import wizard. Specifying that the data file is delimited and then specifying that it is space delimited correctly imports the data into Excel into columns.

On occasion, when the collection of data is interrupted due to power failure or if manual alignment procedures are followed, there is missing data. The SLSRUN software always outputs data even rejected data. Naturally, for the collected data the percentage of error free data and the inner scale of turbulence less than defined critical values give clues as to the possible problems with the collected data. Due to the loss of data due to power problems or interruption of the beam, a time-stamp check for the 2-min data was performed within Excel, to ensure that there were no missing lines. This was necessary since for example, the air temperature profile differences and the EC sensible heat flux densities were copied from another spreadsheet and pasted into the SLS data spreadsheet. Time synchronization was therefore necessary between different spreadsheets containing different data sets. The day of year, decimalised, was calculated first as follows using the value function of Excel:

= value(date) - 37622 + value(time)

as an example where date refers to the cell containing the date in the mm/dd/yyyy format, -37622 corresponds to the number of days between 1 Jan 1900 and 1 Jan 2003, and time refers to the time of day cell in the hh:mm:ss format. Even though time is in the hh:mm:ss format, value(time) converts the time to fraction of a day. The expression therefore yields a number between 0 and 365, incrementing by 2 min (converted to a fraction of a day). A column for the "missing" tag was created. Each cell of this column contained the condition:

=IF(ABS(previousDOY+2/(60*24)-nextDOY)>0.002,"missing","")

where previousDOY and nextDOY refer to the cells containing the previously calculated DOY and the next DOY, respectively.

This test condition ensured that if there was more than a 2 min time difference between consecutive lines of data, the message "missing" would then be displayed in the tag column.

Procedures were used to determine the direction of the sensible heat flux density based on the sign of the measured profile air temperature differences from the BR thermocouples. In the absence of such data, the sign was determined using the EC sensible heat flux density values or based on time of day. When the rejection was based on time of day, it was assumed that unstable conditions occurred between 06h00 and 18h00.

Data rejection or filtering procedures were applied in Excel to the sensible heat flux density 2-min values. Sensible heat flux density values were rejected, blanks were created or data recalculated:

- if the percentage of error free data was less than or equal to 25 % (%EFD ≤ 25 %), data were rejected;
- if the inner scale of refractive index fluctuations was less than or equal to 2 mm (l_o ≤ 2 mm), data were rejected;
- for missing data, designated by zeros, a blank cell was used for sensible heat flux density;
- for positive $\delta T_{air} / \delta z - 0.01$ values, where δz is the vertical distance between the profile thermocouples, corresponding to unstable conditions, and %EFD > 25 % and l_o > 2 mm and non-blank sensible heat flux density values, -$F_{h,air}$ is displayed in the cell;
- for stable conditions, corresponding to $\delta T_{air} / \delta z - 0.01 < 0$ °C m^{-1}, and %EFD > 25 %, and l_o > 2 mm, -F_{single} is displayed in the cell.

Seven nested Excel if statements were used for these procedures (Table 3.6). In Excel, the single cell calculation, one such calculation for each 2-min period, explained in Table 3.6, is as follows:

= IF(OR(%EFD ≤ 25,l_o ≤ 2,AND($F_{h,air}$ = 0,F_{single}=0)),"",IF(AND(δT_{air} = "",DOY-INT(DOY)>0.25,DOY-INT(DOY)<0.75),-$F_{h,air}$,IF(AND(δT_{air}-0.01>0, %EFD>25, l_o>2),IF($F_{h,air}$ = 0,"",-$F_{h,air}$),IF(AND(δT_{air}-0.01<0, %EFD>25,l_o>2),IF(F_{single}=0,"",-F_{single}),IF(AND(δT_{air}="",OR(DOY-INT(DOY)<0.25,DOY-INT(DOY)>0.75)), IF(F_{single} = 0,"",IF(AND(%EFD > 25,l_o > 2),-F_{single},"")),IF(F_{single} = 0,"",IF(AND(%EFD > 25, l_o >2),-$F_{h,air}$, "")))))))

Table 3.6 A listing of the seven nested Excel If conditions (and three sub-conditions) used to reject bad or missing SLS sensible heat flux density data and to combine the stable and unstable measurements into one column, based on the sign of δT_{air}: if δT_{air}-0.01 > 0, unstable sensible heat flux densities are displayed, else the values for stable conditions are displayed

Excel code	Position of condition	Explanation
= IF(OR(%EFD ≤ 25,l_o ≤ 2,AND($F_{h\text{-}day}$ = 0,$F_{h\text{-}night}$ =0)), "";	1	1. If %EFD ≤ 25 % or $F_{h\text{-}day}$ = 0 W m^{-2} and $F_{h\text{-}night}$ = 0 W m^{-2} then display a blank
IF(AND(δT_{air} = "",DOY-INT(DOY)>0.25,DOY-INT(DOY)<0.75),	2	else 2. if δT_{air} is blank and time is between 6 am and 6 pm
-$F_{h\text{-}day}$,		then display -$F_{h\text{-}day}$
IF(AND(δT_{air} - 0.01 > 0, %EFD>25, l_o>2),	3	else 3. if δT_{air} - 0.01 > 0 °C, %EFD > 25 %, and l_o > 2 mm
IF($F_{h\text{-}day}$ = 0,	a	if $F_{h\text{-}day}$ = 0 W m^{-2}
"",	a	display a blank
-$F_{h\text{-}day}$),	a	else display -$F_{h\text{-}day}$
IF(AND(δT_{air} - 0.01 < 0, %EFD>25, l_o>2),	4, b	else 4. if δT_{air} - 0.01 < 0 °C, %EFD > 25 %, and l_o > 2 mm
IF($F_{h\text{-}night}$ = 0,"",-$F_{h\text{-}night}$),	b	then if $F_{h\text{-}night}$ = 0, display a blank else display -$F_{h\text{-}night}$
IF(AND(δT_{air} ="",OR(DOY-INT(DOY)<0.25, DOY-INT(DOY)>0.75))	5	else 5. if δT_{air} ="" and time is between 6 am and 6 pm
,IF($F_{h\text{-}night}$ = 0,		then display $F_{h\text{-}night}$ = 0 W m^{-2}
"",		else display a blank
IF(AND(%EFD > 25,l_o > 2),	c	if %EFD > 25 % and l_o > 2 mm
-$F_{h\text{-}night}$,""))	c	display -$F_{h\text{-}night}$ else display a blank
,IF($F_{h\text{-}night}$ = 0,	6	else 6. if $F_{h\text{-}night}$ = 0 W m^{-2}
"",		display a blank
IF(AND(%EFD > 25, l_o > 2),	7	else 7. if %EFD > 25 % and l_o > 2 mm
-$F_{h\text{-}day}$,		display -$F_{h\text{-}day}$
""))))))	1,2,3,4,5, 6,7	else display a blank

3.4.15 Estimation of latent energy flux density from net irradiance and SLS sensible and soil heat flux density measurements

3.4.15.1 Available energy flux density

The available energy flux density $A = I_{net} + F_{soil}$ (W m^{-2}) (Eq. 2.4) was calculated from measurements of net irradiance I_{net} (W m^{-2}) and soil heat flux density F_{soil} (W m^{-2}):

$$A = I_{net} + F_{soil}. \qquad 3.1$$

By definition, assuming that there are no other energy balance terms, such as advection energy flux density or canopy stored heat flux density, we may write:

$$A = I_{net} + F_{soil} = - L_v\ F_w - F_h. \qquad 3.2$$

If each of these four energy balance terms are measured independently, then the extent of closure may be tested; *viz*., using Eq. 2.5:

$$CR = (- L_v\ F_w - F_h) / (I_{net} + F_{soil}) \qquad 3.3$$

where $CR = 1$ would mean perfect closure (or balance), and $CR > 1$ would imply that one or more of latent energy and sensible heat heat flux density is an overestimate (or that net irradiance plus soil heat flux density is an underestimate).

Should the four terms not be measured independently, as is the case for BR, one-sensor EC (Table 3.1), and SLS methods, then closure is assumed to take place and the latent energy flux density is calculated using:

$$L_v\ F_w = - I_{net} - F_{soil} - F_h.$$

Clearly then, all three terms on the right hand side would be important in determining the latent energy flux density. Soil heat flux density, during the daytime, is often the smallest term in magnitude. However, for time scales of less than a day, its importance cannot be ignored especially when dealing with short vegetation such as grassland.

3.4.15.2 Net irradiance

Net irradiance was measured using two or three Q*7 net radiometers placed 2 m above the soil surface. During the early stages of the project only one net radiometer was used. The procedure for calibrating net radiometers was discussed in a previous report (Savage et al. 1997) and is not repeated here.

3.4.15.3 Soil heat flux density

Soil heat flux density was estimated every two minutes for the SLS measurements and every 20 min for the BR measurements from the sum of the average of measurements of soil heat flux density $\overline{F_{plate}}$ (W m^{-2}) at a depth of 80 mm (using four to five soil heat flux plates) and the average stored heat flux density $\overline{F_{stored}}$ (W m^{-2}) above the plates:

$$\overline{F_{soil}} = \overline{F_{plate}} + \overline{F_{stored}}.$$

The stored heat flux density $\overline{F_{stored}}$ was estimated from measurements of $\overline{\Delta T_{soil}}$ (°C), the average soil temperature difference (between 20 and 60 mm) from one 2-min time period for SLS measurements (or 20-min period for BR measurements) to another (Δt = 120 s for SLS energy balance calculations or 1200 s for BR calculations), the depth of soil Δz (m), and the volumetric soil water content θ ($m^3\ m^{-3}$):

$$\overline{F_{stored}} = \text{stored energy}/(\text{time difference} \times \text{area})$$

$$= M_{soil}\ \overline{\Delta T_{soil}}\ c_{soil}/(\text{time difference} \times \text{area}) = \rho_{soil}\ V_{soil}\ \overline{\Delta T_{soil}}\ c_{soil}/(\text{time difference} \times \text{area difference})$$

$$= \rho_{soil}\ \Delta z\ \overline{\Delta T_{soil}}\ c_{soil}\ /\ \Delta t$$

where ρ_{soil} is the bulk density of the soil (kg m^{-3}), the soil depth Δz = 0.08 m, c_{soil} is the specific heat capacity of the soil (J kg^{-1} °C^{-1}) and V_{soil} = area Δz. The specific heat capacity of the soil is calculated as the specific heat capacity of dry soil plus that of water using:

$$\rho_{soil}\ c_{soil} = \rho_{soil}\ c_{dsoil} + \rho_{soil}\ \theta_w\ c_w$$

where c_{dsoil} is the dry soil specific heat capacity, $\rho_{soil}\ \theta_w$ is the volumetric soil water content ($m^3\ m^{-3}$) and c_w = 4190 J kg^{-1} °C^{-1}, the specific heat capacity of water.

Five sets of type-E averaging thermocouples were used for the soil temperature measurements and five soil heat flux plates were used for calculating $\overline{F_{plate}}$. A CR7X data logger (Campbell Scientific, Logan, USA) was used for these measurements for much of 2003, including the volumetric soil water content in the first 50 mm of the surface which was measured using a frequency domain reflectometer (ThetaProbe, model ML2x, Delta-T Devices, Cambridge, UK). Most of these sensors were connected to the Campbell CR7X data logger and transferred to a 23X data logger after the 2003 fire.

3.4.16 Miscellaneous measurements and data logger programming

Other measurements included two-minute averages of solar irradiance, air temperature, water vapour pressure, and wind speed for the calculation of reference evaporation and wind direction and rainfall (at positions AWS and BR of Fig. 3.1). Two measurements of canopy temperature were made using infrared thermometers (model IRTS-P, Apogee Instruments Inc., USA) positioned at a height of 2 m above the soil surface (at position EB, Fig. 3.1) before the accidental fire and subsequently at a height of 1.5 m when they were attached to the lower BR arm. An ET-gage evaporimeter (model E, ETgage Company, Loveland, USA) was used to measure reference evaporation directly. This evaporimeter has a measurement depth resolution of 0.25 mm and was connected to the CR7X data logger. The evaporating surface was positioned at 1 m above the soil surface. A pair of CM3 pyranometers (Kipp and Zonen, Delft, Holland) were used to measure solar irradiance and reflected solar irradiance (at position EB, Fig. 3.1). Following the fire, the CR7X data logger sensors were connected to the BR CR23X data logger.

3.5 Results and discussion

3.5.1 Fraction of acceptable SLS data

The percentage of "acceptable" 2-min SLS sensible heat flux density measurements for the daytime hours (taken as 06h00 to 18h00) showed little seasonal variation and was consistently high - between 86.7 % and 94.8 % for the 18-month period (Fig. 3.10a). Acceptable values were defined according the criteria described in Table 3.6. The nighttime variation in the percentage had a more pronounced seasonal pattern with the lowest percentage acceptable measurements occurring between January and March of each year (Fig. 3.10b). The lower nighttime percentage values were due to the effects of dew and mist. Included in these percentages are the times for which the electrical power was interrupted.

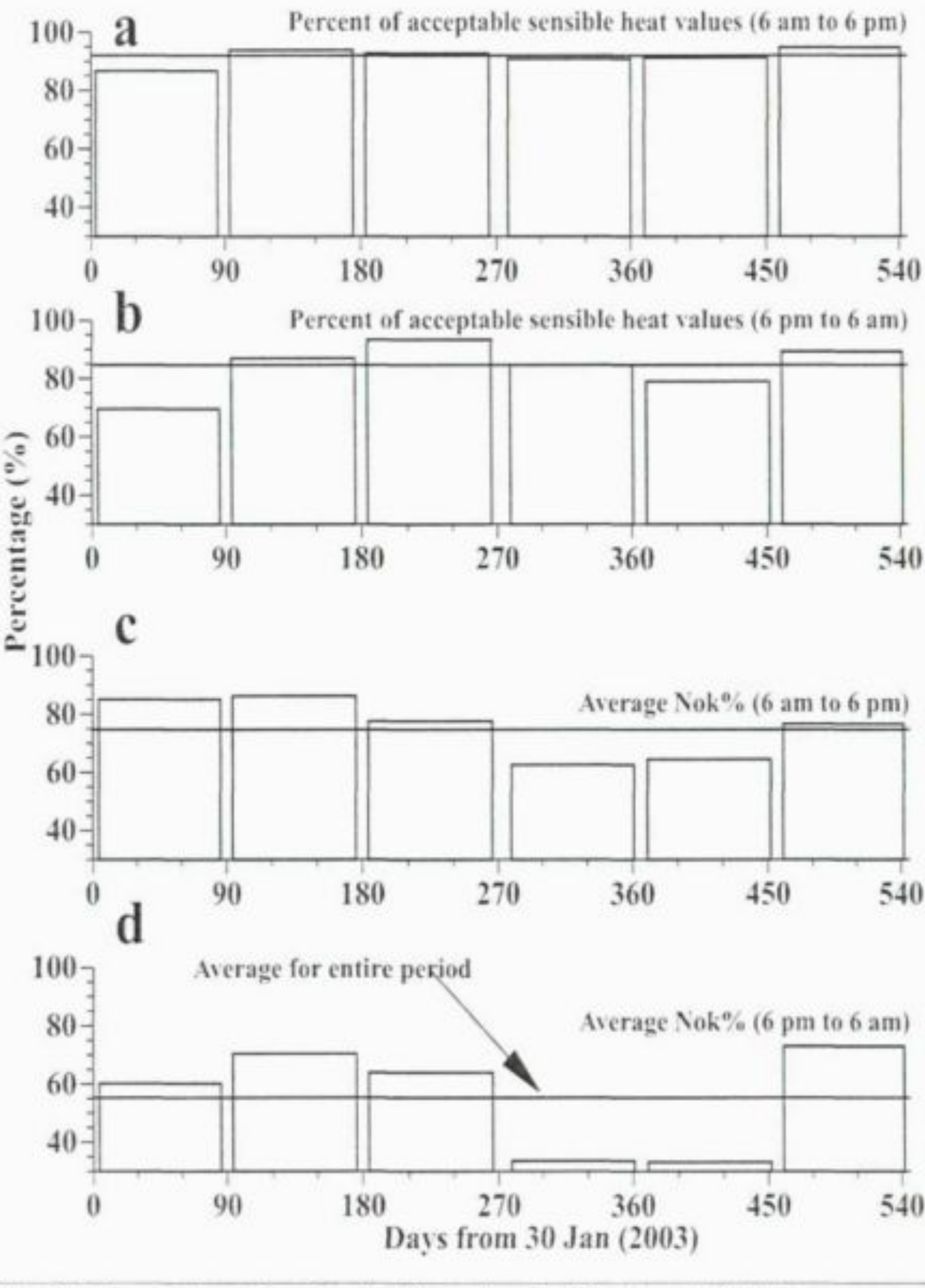

Fig. 3.10 Temporal variation, for the 18-month period, in: (a) and (b) bottom two graphs - percent of acceptable 2-min SLS sensible heat flux density measurements for the 06h00 to 18h00 period and for the 18h00 to 06h00 periods respectively; (c) and (d) top two graphs - the average 2-min SLS Nok% values for the 06h00 to 18h00 period and for the 18h00 to 06h00 periods respectively.
The horizontal line is the average for the entire 18-month period: 92 % for (a), 85 % for (b), 75 % for (c) and 55 % for (d)

At worst, this period was no longer than a day or so. Other minor interruptions, usually less than two-days in duration, were due to the accidental fire and accidental cutting of the cables.

The average Nok% varied between 62 and 85 % (Fig. 3.10c) for the 06h00 to 18h00 period and 33 to 73 % for the nighttime (Fig. 3.10d). The lowest Nok% values were during the summer rainfall period (September to March), due to the influence of rain events on beam transmission. The Nok% refers to the percentage of the 1000 measurements per second.

The seasonal variation in the inner scale of turbulence l_o (mm) for the daytime and nighttime periods are shown separately in Figs 3.11 and 3.12 respectively using histograms. Values of l_o less than 2 mm results in rejected sensible heat data. For most of the study, the most common (or at least 35 % of the time) l_o value is between 4 and 6 mm (Fig. 3.11). For the nighttime, the most common l_o value is less than 2 mm (Fig. 3.12). The second-most common nighttime value is that between 6 and 8 mm (Fig. 3.12) in contrast to the 4 to 6 mm value during the daytime hours (Fig. 3.11). The larger values of 6 to 8 mm at night are due to the more stable nighttime conditions compared to the more turbulent conditions during the day creating smaller and smaller eddies.

3.5.2 Sensitivity analysis to determine the relative importance of data inputs on evaporation estimates

A sensitivity analysis was conducted to determine the relative importance of the data inputs in determining the SLS sensible heat flux density. Errors in the input data affect the real-time measurements displayed and these inputs would also affect post-data recalculations. For the purposes of the sensitivity analysis calculations, data for 23 February 2003 (day of year 54) and 5 January 2004, relatively cloudless days, were used. The variation in the energy balance components for these days are shown (Fig. 3.13).

Each of the four data inputs were varied from below to above a "normal" value. The following were used for the normal values:

measured air temperature $T_{correct}$, for each 2-min period. The temperature $T_{correct}$ was calculated from the average of all available 2-min measurements of air temperature;

the estimated atmospheric pressure $P_{correct}$ based on the measured air temperature, altitude and the measured water vapour pressure;

the measured beam path length $L_{beam,correct}$ of 101 m;

the beam height above the level at which wind speed is 0 m s^{-1} ($h_{beam,correct}$) estimated, for example, at 1.04 m using:

$$h_{beam,correct} \approx z_{beam} - 0.77\ h$$

for a height of the beam above the soil surface z_{beam} of 1.68 m and for a canopy height of 0.83 m.

For each data input a fractional error was calculated:

$$\varepsilon_{T_{air}} = (T_{correct} - T) / T_{correct}$$

$$\varepsilon_{P} = (P_{correct} - P) / P_{correct}$$

$$\varepsilon_{L_{beam}} = (L_{beam,correct} - L_{beam}) / L_{beam,correct}$$

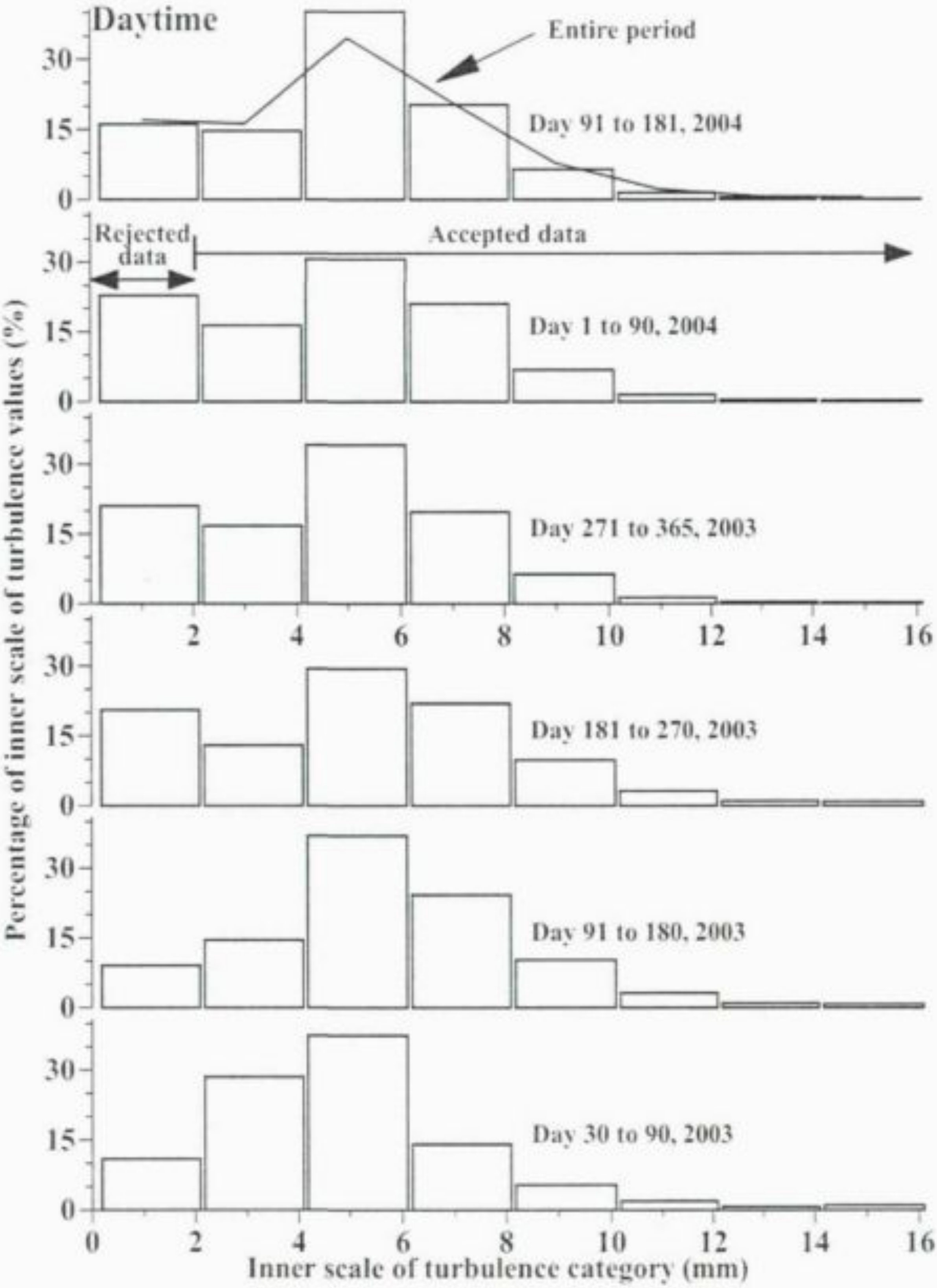

Fig. 3.11 Histogram plots, for the 18-month period, of the percentage of the inner scale of turbulence for the categories $l_o \leq 2$ mm, 2 to 4 mm, 4 to 6 mm to 12 to 14 mm and > 14 mm for the 06h00 to 18h00 period. Each plot is for roughly 90 days. The top histogram also includes a line plot for the entire period for average l_o values. The zones of l_o values for which data were accepted are shown by the horizontal arrows

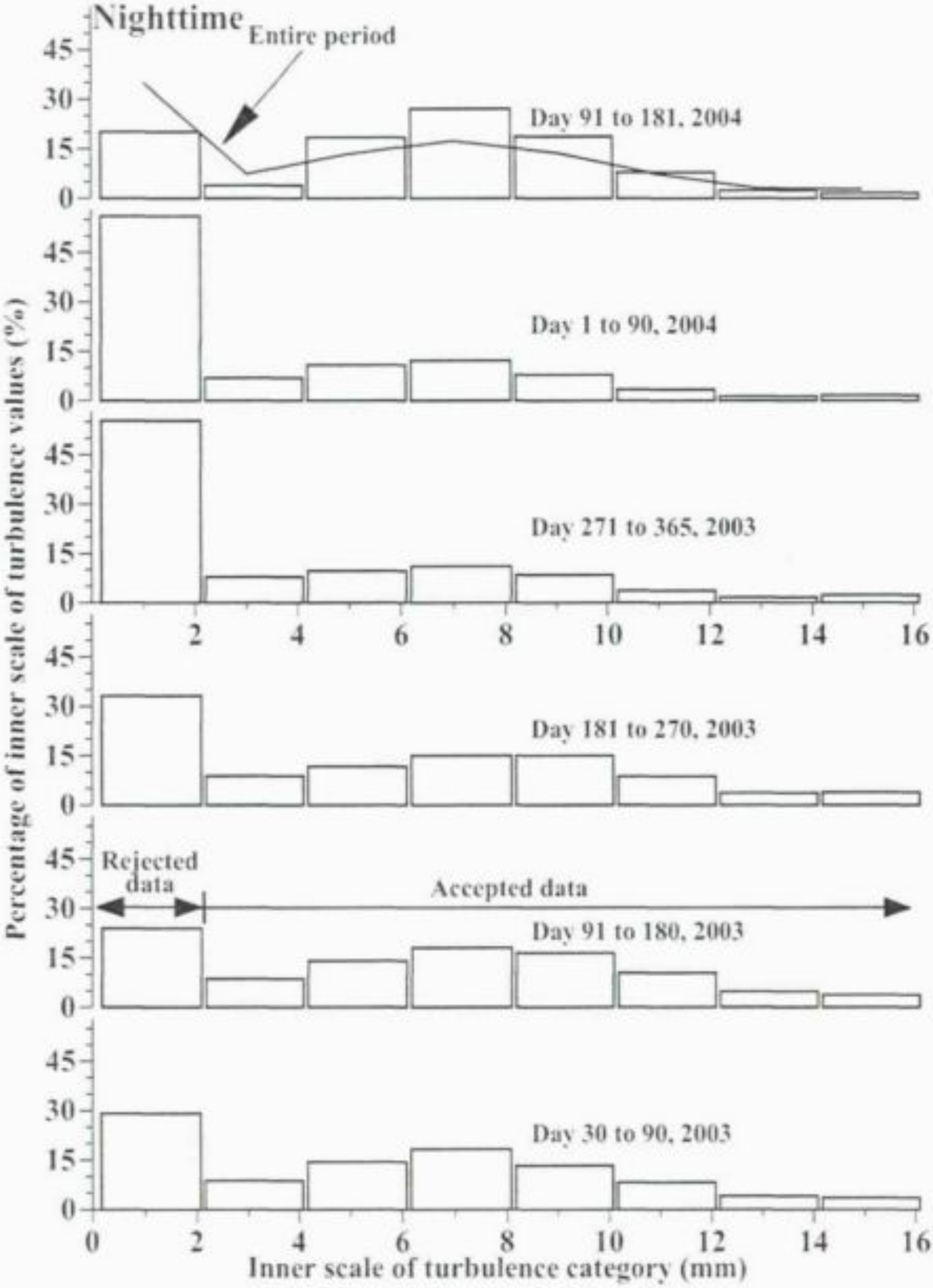

Fig. 3.12 Histogram plots, for the 18-month period, of the percentage of the inner scale of turbulence for the categories $l_o \leq 2$ mm, 2 to 4 mm, 4 to 6 mm to 12 to 14 mm and > 14 mm for the 18h00 to 06h00 period. Each plot is for roughly 90 days. The top histogram also includes a line plot for the entire period for average l_o values. The zones of l_o values for which data were accepted are shown by the horizontal arrows

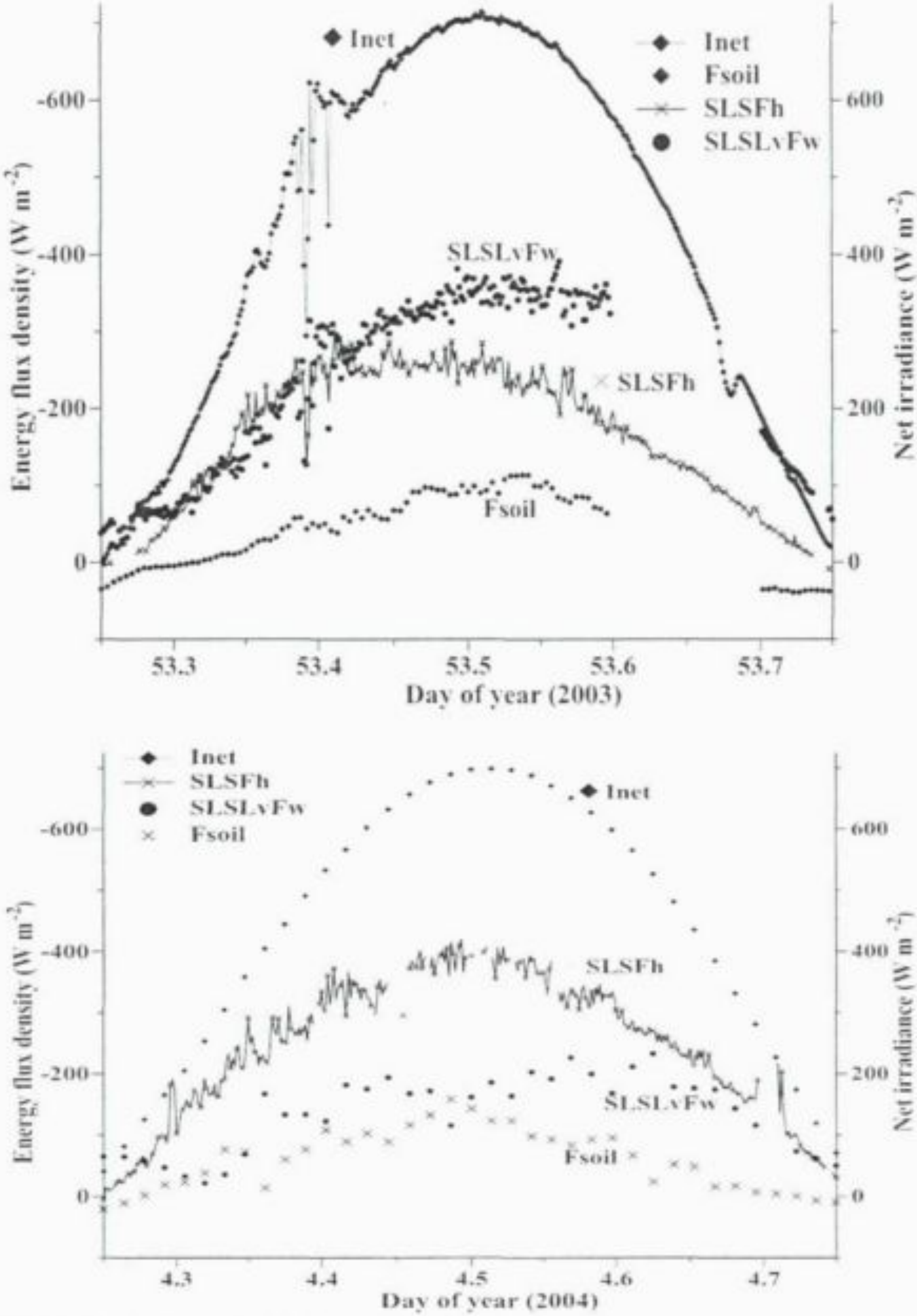

Fig. 3.13 The components of the energy balance for 23 Feb 2003 (day of year 54) [upper] and 5 Jan 2004 [lower]. Each point represents a 2-min period except on 5 Jan some of the data is 20-min data

and $$\varepsilon_{h_{beam}} = (h_{beam\,correct} - h_{beam}) / h_{beam\,correct}.$$

The effect of each fractional error, in turn, on the sensible heat flux density was calculated and converted into a fractional error, ε_{F_s}, based on the actual sensible heat flux density for each 2-min period:

$$\varepsilon_{F_s} = (F_{s\,correct} - F_s) / F_{s\,correct},$$

where $F_{s\,correct}$ is the sensible heat flux density estimated using the four correct data inputs.

For the measured air temperature $T_{correct}$, the fractional error was calculated by allowing T to vary from 50 % below to 50 % above $T_{correct}$. A wide range was used for T to calculate ε_T, since during routine measurements the data input for air temperature was altered very infrequently - sometimes every three or four months. What is the effect of not changing this data input on the real-time estimates of sensible heat flux density? The consequential change to atmospheric pressure, due to the change in air temperature, was accounted for in the sensitivity analysis.

Atmospheric pressure changes are typically very small in Pietermaritzburg. The atmospheric pressure was varied from 10 % below to 6 % above $P_{correct}$. The procedures used ensured that P did not exceed sea-level atmospheric pressure of 1013 hPa.

The fractional error in beam path length was varied from 10 % below to 10 % above $L_{beam\,correct}$.

The height of the beam above the height at which the wind speed is 0 m s^{-1}, $h_{beam\,correct}$, is based on the neutral wind profile relationship (Eq. 2.15). The fractional error in $h_{beam\,correct}$ was calculated by varying h_{beam} from 10.5 % below to 10.5 % above the $h_{beam\,correct}$ value of 1.04 m corresponding to z_{beam} = 1.68 m and a canopy height of 0.83 m.

3.5.2.1 Effect of errors in air temperature

The sensitivity of air temperature on sensible heat flux density is more complex since air temperature also affects atmospheric pressure. Clearly however, the overall effect is small (Fig. 3.14). An over-estimate in air temperature causes an under-estimate in sensible heat flux density. Assuming that measured air temperatures have a fractional error of 0.1, the fractional error in sensible heat flux density is $\mp$ 0.015. Even with a fractional error of 0.5 in the measured air temperature, the fractional error in sensible heat is only $\mp$ 0.07. The use of $\mp$ indicates that, for example, a fractional error in air temperature of 0.1 results in a fractional error in sensible heat flux density of -0.015 and an error in air temperature of -0.1 results in an error of 0.015.

3.5.2.2 Effect of error in atmospheric pressure

The effect of error in atmospheric pressure on sensible heat flux density estimates was more significant than that for air temperature (Fig. 3.15). Also, an over-estimated atmospheric pressure results in an over-estimated sensible heat flux density. The estimates for atmospheric pressure are to within 20 hPa, corresponding to a fractional error in sensible heat flux density of $\pm$ 0.013.

3.5.2.3 Effect of error in beam path length

For a fractional error in the beam path length of $\pm$ 0.02, corresponding to within about 2 m of the actual beam path length of 101 m, the fractional error in sensible heat flux density is $\mp$ 0.03 (Fig. 3.16). An over-estimate in beam path length resulted in an under-estimated sensible heat flux density.

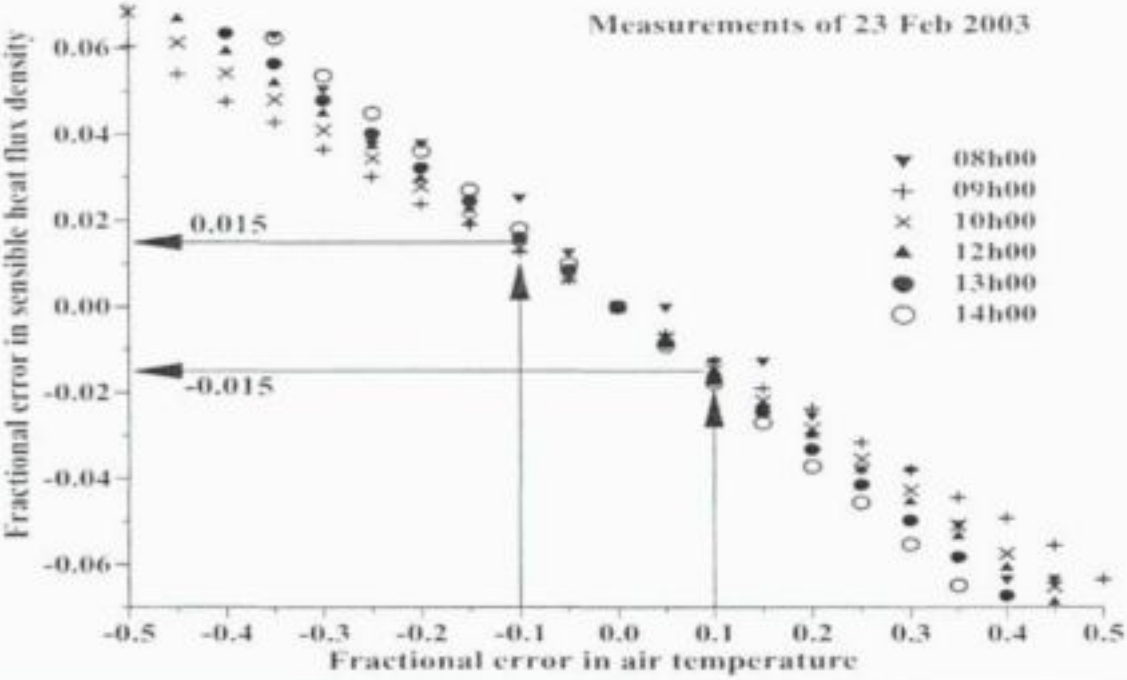

Fig. 3.14 The results of the sensitivity analysis for the effect of fractional error in air temperature (from 10 % below the measured value for the time indicated to 10 % above) on the fractional error in sensible heat flux density

3.5.2.4 Effect of error in beam height

The error in estimation of $h_{beam,correct}$ resulted in the largest error, compared to the errors for the other three data inputs (Fig. 3.17). For a fractional error in $h_{beam,correct}$ of $\pm$ 0.10, $\varepsilon_{H_s} = \pm$ 0.08. Typically, the estimate of $h_{beam,correct}$ is within 0.05 m, or a fractional error of within 0.05, corresponding to a fractional error ε_{H_s} of $\pm$ 0.04. An over-estimate in beam height results in an over-estimate in sensible heat flux density.

3.5.2.5 Overall error in SLS sensible heat due to errors in data input values

Attaching an equal weighting to each of the four errors, allows the overall fractional error to be calculated using:

$$\varepsilon_{H_s} = \sqrt{\varepsilon^2_{T_a} + \varepsilon^2_{P} + \varepsilon^2_{L_{beam}} + \varepsilon^2_{h_{beam}}} \qquad 3.4$$

with worst-case values as follows: $\mp$ 0.015 for ε_{T_a}, $\pm$0.013 for ε_P, and $\mp$ 0.03 for $\varepsilon_{L_{beam}}$. The fractional error for h_{beam} was typically $\pm$0.04. Overall, therefore, the worst-case total error $\varepsilon_{H_s} = \pm$ 0.054. Typical errors in air temperature are no worse that $\pm$ 0.05, $\pm$ 0.01 for atmospheric pressure, $\pm$ 0.015 for beam path length, and $\pm$ 0.025 for beam height. Overall, these typical fractional errors correspond to fractional errors in sensible heat flux density of $\mp$ 0.075, $\pm$ 0.065, $\mp$ 0.0225 and $\pm$ 0.02 for air temperature (Fig. 3.14), atmospheric pressure (Fig. 3.15), beam path length (Fig. 3.16) and beam height (Fig. 3.17), respectively. Overall, therefore, typical errors calculated using Eq. 3.4 amount to $\pm$0.032.

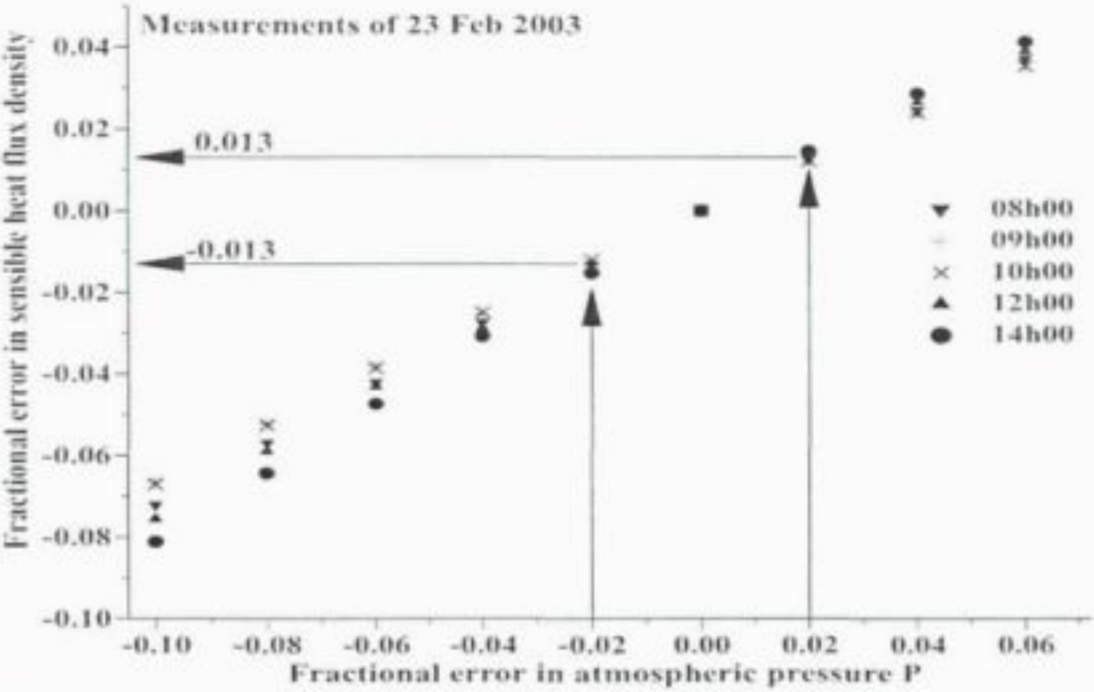

Fig. 3.15 The results of the sensitivity analysis for the effect of fractional error in atmospheric pressure (from 2 % below 941 hPa average for the day to 2 % above) on the fractional error sensible heat flux density. Atmospheric pressures greater than that at sea-level (1013 hPa) were excluded in the analysis

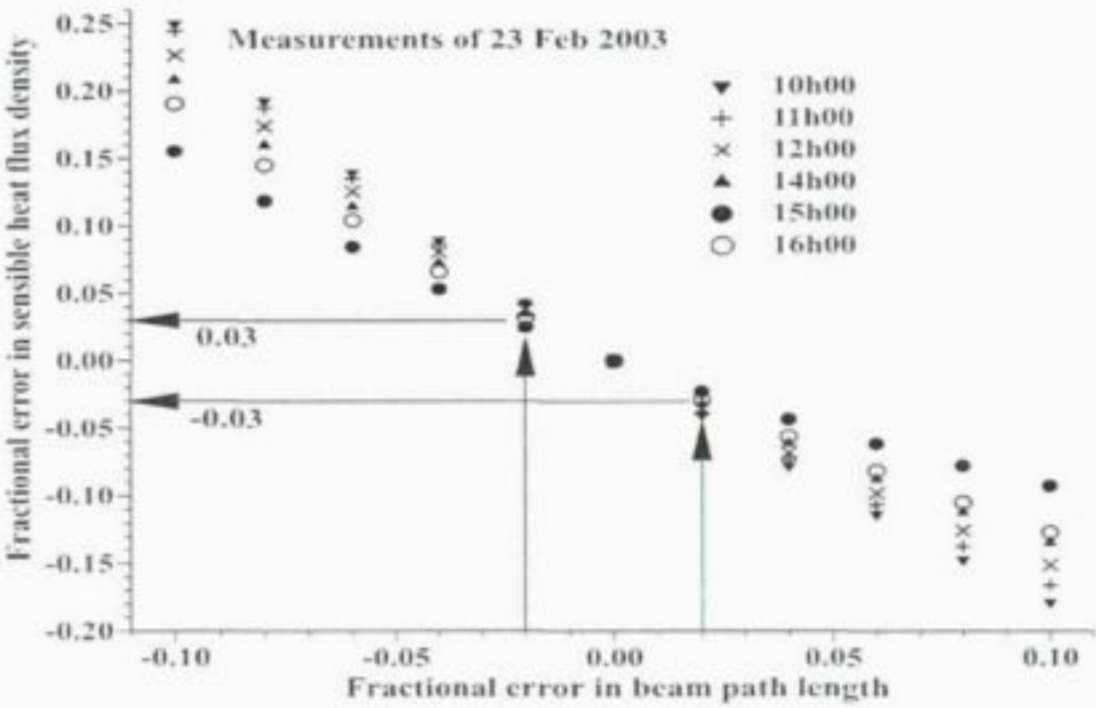

Fig. 3.16 The results of the sensitivity analysis for the effect of fractional error in beam path length (from 2 % below 101 m to 2 % above) on the fractional error in sensible heat flux density

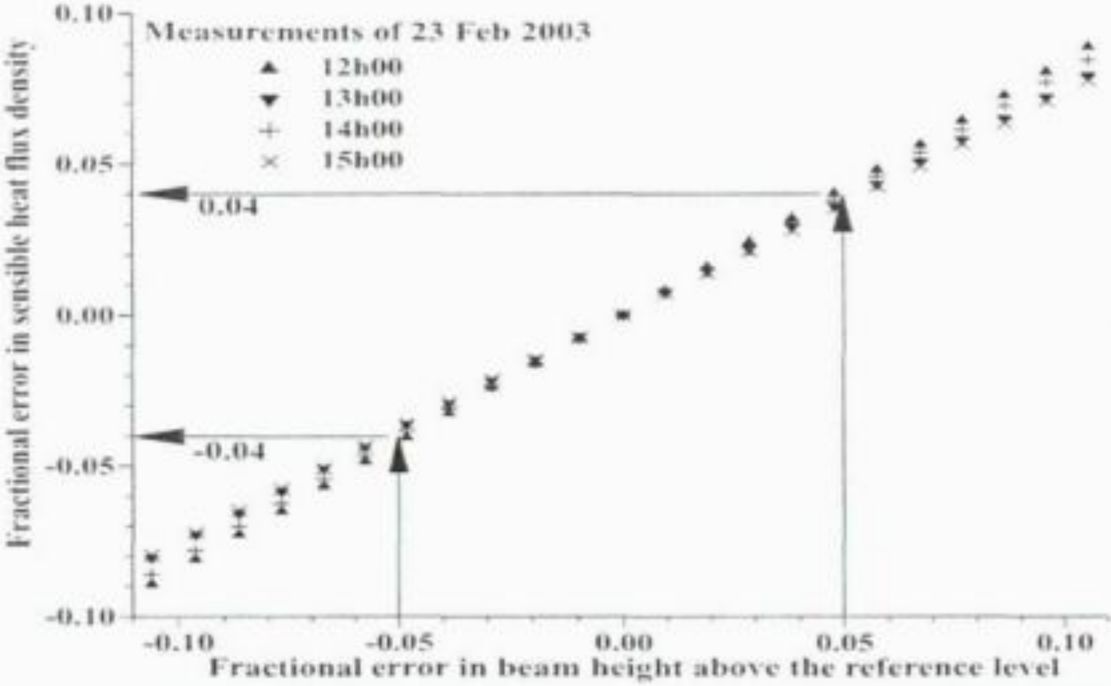

Fig. 3.17 The results of the sensitivity analysis for the effect of fractional error in beam height above the reference level at which the wind speed is 0 m s^{-1} (from 5 % below 1.04 m to 5 % above) on the fractional error in sensible heat flux density

3.5.2.6 Effect of beam height and beam angle on SLS sensible heat flux density estimates

Beam height, relative to the level at which the wind speed is 0 m s^{-1}, is affected by vegetation height. Defining effective beam height as the height of beam above the soil surface minus $d + z_o$ where the zero plane displacement height d is assumed to be two-thirds of the canopy height and the roughness length z_o is assumed to be one-tenth of the canopy height (Eq. 2.16). The variation in canopy height for the duration of the study is shown (Fig. 3.18). The canopy height was measured at various times during the study and on each occasion, canopy height was measured every 5 m of the direct line between transmitter and receiver. These heights were weighted according to a path-weighting function used for the log-amplitude variances (Thiermann 1992) which was then normalised so as to have an area under the curve of 1 (Fig. 3.19). Of note is that the weighting process favours effective beam heights midway between the transmitter and receiver units with vegetation height near the transmitter and receiver carrying little weight.

An alternative method for determining the zero plane displacement height, using the procedure proposed by de Bruin and Verhoef (1996) (Section 2.11.8), was investigated. For $|F_h| \geq 120$ W m^{-2} the estimated $z - d$ values were often greater than 3 m with the result that d was negative. Therefore, the normal method of estimating d was used (Eq. 2.16).

Theoretically, a non-horizontal beam relative to a horizontal surface, or *vice versa*, invalidates MOST. The influence of surface slope on sensible heat measurements was investigated by reducing the height of the receiver relative to the transmitter. A receiver to transmitter vertical height difference of 1.0 m for a horizontal distance of 101 m was used. For measurements performed over five days (Table 3.2), there was no significant consistent difference between 2-min SLS and EC sensible heat flux density measurements in spite of the fact that MOST is invalid for a non-horizontal beam (Fig. 3.20). Of note is the reduced variability of the SLS measurements since these represent

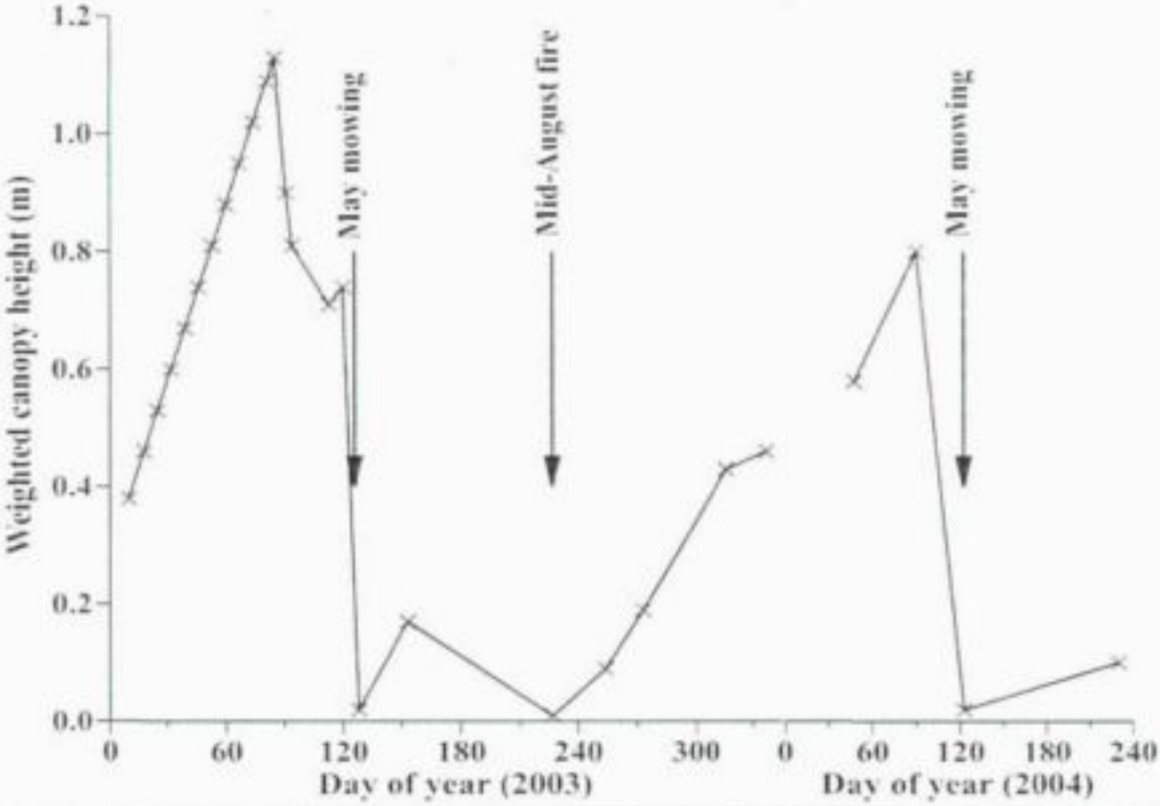

Fig. 3.18 The seasonal march of the path-weighted canopy height, for a path length of 100 m and an inner scale of turbulence l_o = 4 mm, for the duration of the study. Events such as the two mowings and the fire are indicated

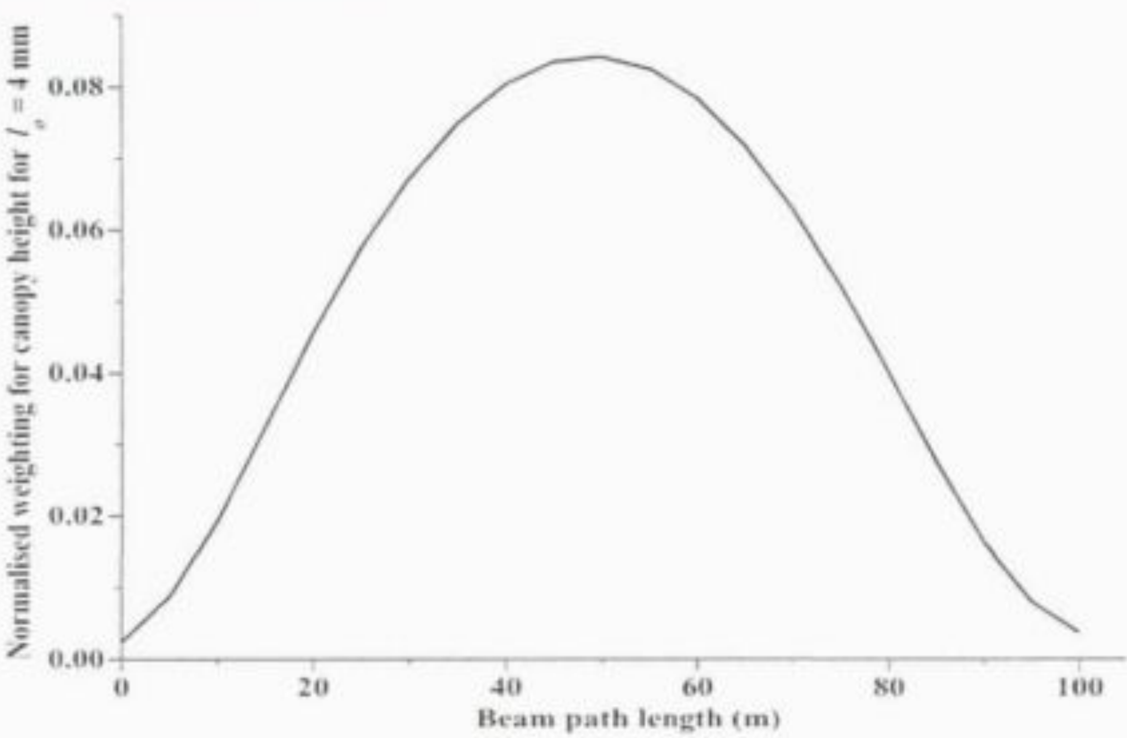

Fig. 3.19 The path-weighted function used for determining the path-weighted canopy height for a path length of 100 m and an inner scale of turbulence of 4 mm, based on the path-weighting function used by Thiermann (1992) for log-amplitude variances but normalised to an area of 1

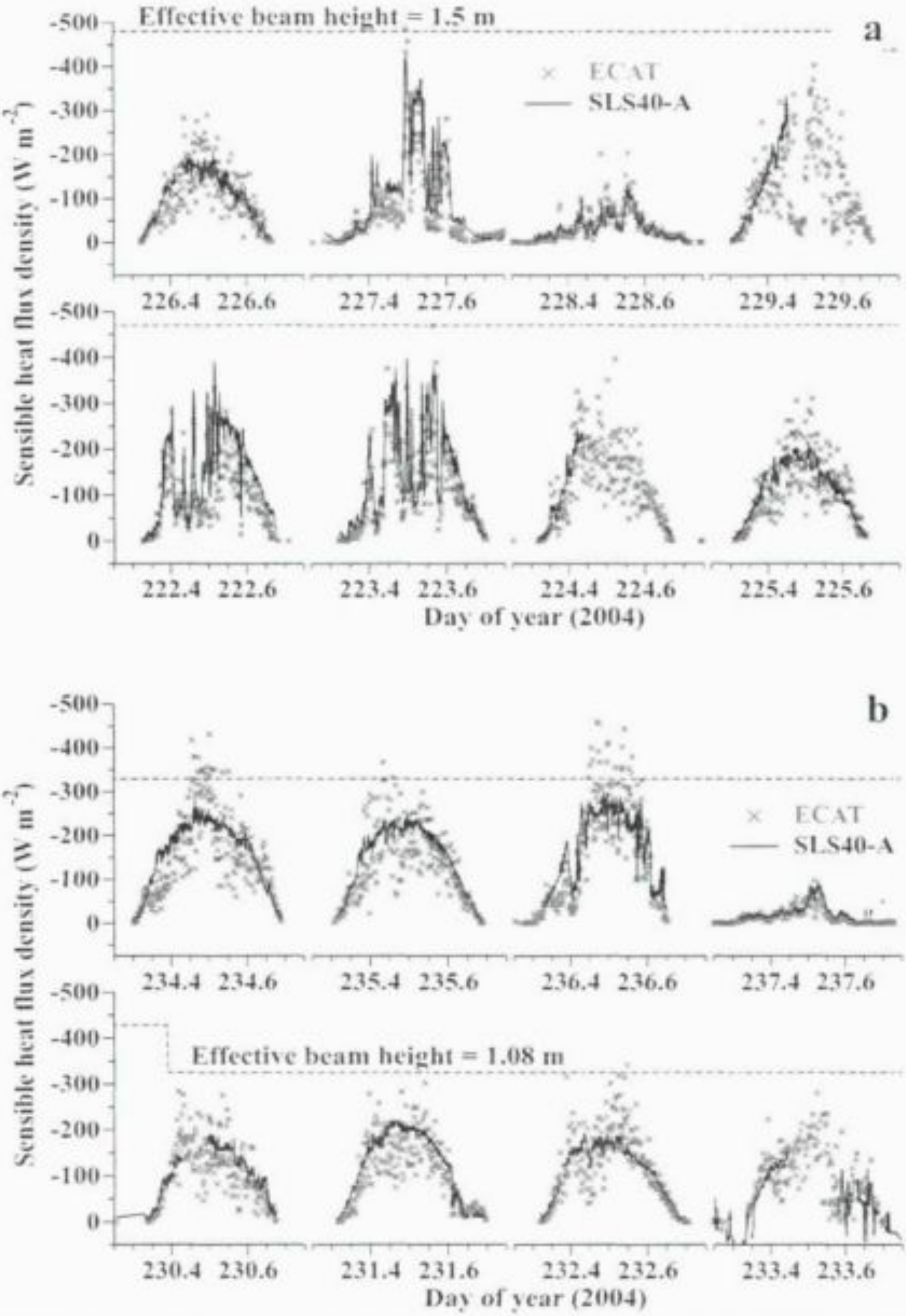

Fig. 3.20 Two-minute variation in SLS and ECAT sensible heat flux density for (a) above: a horizontal beam at an effective height of 1.5 m for day of year 223 to 230, 2004; (b) below: a non-horizontal beam angle. The change in angle was on day 231, indicated by the dotted line. The beam was distance was 101 m. The effective beam height was 1.08 m and the heights of the transmitter and receiver were 1.68 and 0.68 m respectively with the vegetation height about 0.1 m

measurements for the entire 101 m path length compared to the ECAT point measurements. For this same time period, differences in the inner scale of turbulence l_o as a result of the change in beam angle from the horizontal, were not noticeable (Fig. 3.21).

The influence of effective beam height on sensible heat flux density was investigated near the end of the study. For these measurements (Fig. 3.22, top), a very low effective beam height of 0.5 m was used. For all previous measurements, the beam was about 1.68 m above the soil surface with vegetation height varying between virtually 0.0 m and a maximum of 1.13 m. The effective beam height therefore varied between 0.82 m and 1.68 m except for the effective height of 0.5 m at the end of the study. The inner scale of turbulence (l_o) was noticeably more variable for this low height (Fig. 3.22, bottom). Also of note is that l_o was smaller than for the higher effective beam heights (Fig. 3.21), often as low as the cut-off value of 2 mm used for data rejection (Table 3.6). The smaller l_o value for lower effective beam heights is is to be expected since smaller eddies occur closer to the surface. Based on these measurements, higher placement heights are recommended but it would appear that the need for a non-horizontal beam does not invalidate MOST significantly for our site and the weather conditions experienced.

3.5.2.7 Errors in soil heat flux density and net irradiance measurement

Since latent energy flux density is estimated from the sensible heat flux density, soil heat flux density and net irradiance, the error in soil heat flux density and net irradiance measurements needs to be considered. The fractional error in soil heat flux density and that for net irradiance is due to calibration errors and errors associated with field measurements, including spatial variation differences. While the errors associated with calibration are known at the time when calibration is performed against an accurate and standard reference soil heat flux density or net irradiance reference, the error may change as a function of time after calibration in an unknown fashion. Furthermore, the errors associated with field measures of soil heat flux density are dependent on the measurement errors associated with change in soil temperature (for the 20 to 60 mm depth) from one measurement time period to another, the errors in measuring the placement depths, the error in measuring the soil heat flux density at the placement of 80-mm depth of the plate and the error in the measurement of the soil water content. Furthermore, spatial variability in soil heat flux density is affected by the soil and vegetation cover variability and vary with day of year as the canopy height changes. Most-often many measurements over a larger area, typically several tens of square metres, of soil heat flux density at plate depth and many measurements of soil temperature are performed to obtain reliable spatial averages.

The record of canopy height is important for two main reasons. Firstly, the vegetation height affects the soil heat flux density. Secondly, the SLS beam height is referenced to the height at which wind speed was estimated to be 0 m s^{-1}, namely to 0.77 *h* where *h* is the canopy height. Approximately therefore, the beam height input value was the height of the beam above the soil surface minus 0.77 *h*. The seasonal march of canopy height, weighted along the beam according to a path-weighted function given by Thiermann (1992) [also Fig. A.1 of Scintec (2000)] for a beam path length of 100 m, was determined by measuring canopy height every 5 m along the beam at different times during the study period, from transmitter to receiver. The path-weighted function of Thiermann (1992) was normalised so as to sum 1 along the full length of 100 m (Fig. 3.19). The function gives much greater weight to vegetation height near the mid-position of the beam and much less weighting to vegetation heights near either the transmitter or the receiver. The weighting function of Fig. 3.19 is then used to estimate the path-weighted canopy for a path length of 100 m (Fig. 3.18). The reductions in vegetation height due to the two mowings and the fire is shown by the arrows. The weighted canopy height varied

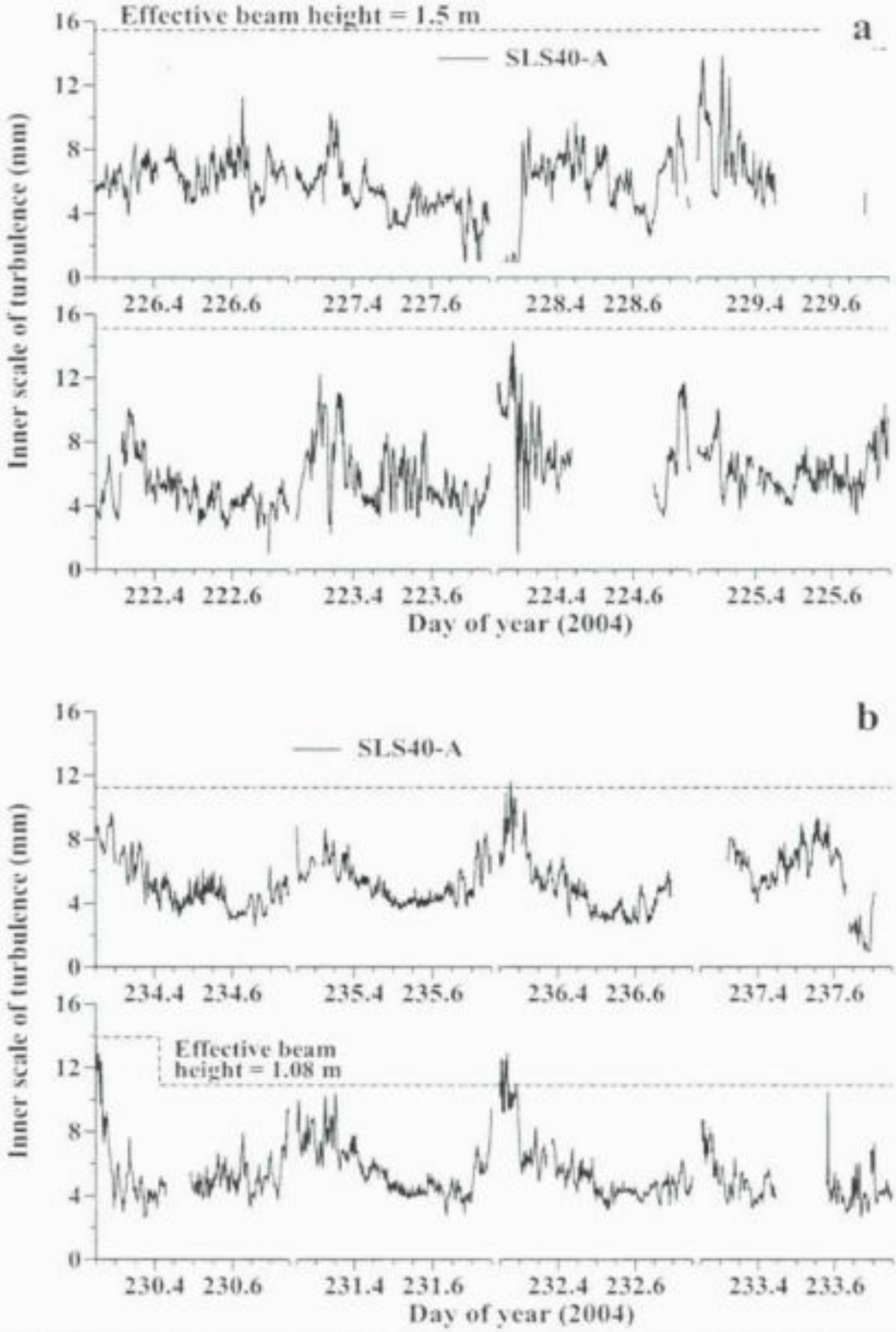

Fig. 3.21 Two-minute variation in inner scale of turbulence l_o (mm) (a) above: a horizontal beam at an effective height of 1.5 m for day of year 223 to 230, 2004; (b) below: a non-horizontal beam angle. The change in angle was on day 231, indicated by the dotted line. The beam distance was 101 m. The effective beam height was 1.08 m and the heights of the transmitter and receiver were 1.68 and 0.68 m respectively with the vegetation height about 0.1 m

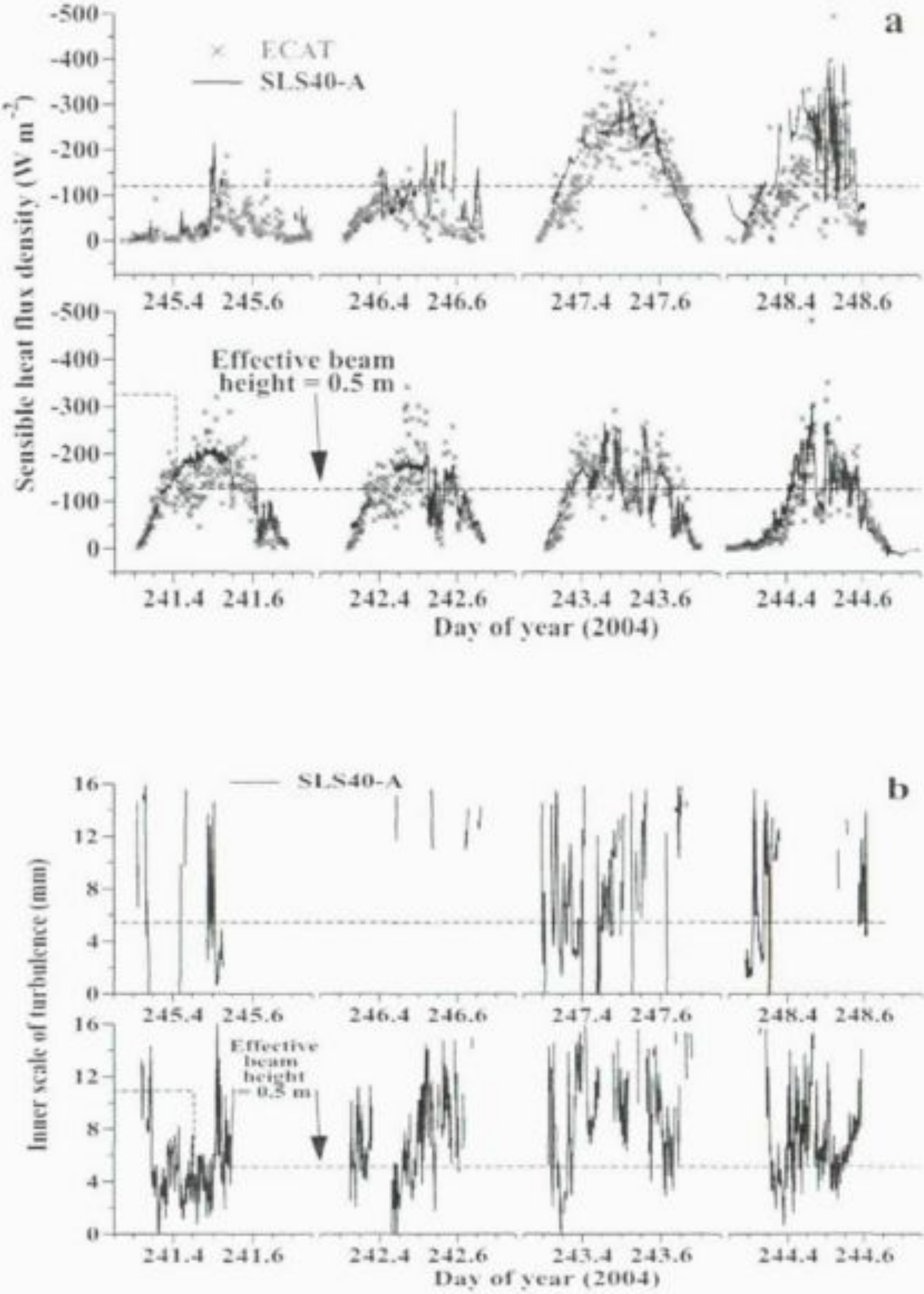

Fig. 3.22 Two-minute variation, for an effective beam height of 0.5 m for day of year 223 to 230, 2004 in (a) above: sensible heat flux density (W m^{-2}); (b) below: inner scale of turbulence l_o (mm).

The change in effective beam height was on day 242, indicated by the dotted line. The beam was in the horizontal position with the vegetation height about 0.1 m between practically 0 m after these events to a maximum of just over 1 m in March 2003 and 0.8 m in March 2004. Hence, during the periods January to March of each year, with canopy height increasing, the tendency is for soil heat flux density to decrease, all other factors equal.

In the case of net irradiance measurements, measurement errors are dependent on errors associated with calibration as well as errors associated with dome condition and errors associated with inadequate drying of the air inside the dome. The net irradiance measurements do however represent a large area, compared to soil heat flux density measurements and may therefore be less affected by soil and canopy spatial variability.

For the soil heat flux density, an overall error of 20 % of the F_{soil} value (Angus and Watts 1984) was used to take into account spatial variability and sampling problems inherent with these sensors, as well as errors in the determination of stored heat energy from the change in soil temperature, the soil bulk density and the specific heat capacities of soil and water.

3.5.2.8 Error in calculating latent energy flux density from SLS sensible heat flux density

In the case of the SLS method, the estimation of evaporation is based on the measurement of sensible heat flux density and the other energy balance components. Besides errors in the input data affecting the calculated sensible heat flux density, the calculation of latent energy flux density $L_v\ F_w$ using:

$$L_v\ F_w = -I_{net} - F_{soil} - F_{hSLS}$$

where F_{hSLS} is the SLS-estimated sensible heat flux density, results in additional errors. Hence, the standard deviation for a latent energy flux density measurement is given by:

$$\sigma_{L_v F_w} = \sqrt{(\partial L_v\ F_w / \partial I_{net})^2 \sigma^2_{I_{net}} + (\partial L_v\ F_w / \partial F_{soil})^2 \sigma^2_{F_{soil}} + (\partial L_v\ F_w / \partial F_{hSLS})^2 \sigma^2_{F_{hSLS}}}$$

or

$$\sigma_{L_v F_w} = \sqrt{\sigma^2_{I_{net}} + \sigma^2_{F_{soil}} + \sigma^2_{F_{hSLS}}}.$$

Angus and Watts (1984) used the following for error in net irradiance and soil heat flux density measurements:

$$\sigma_{I_{net}} = \pm 0.025\, I_{net} \qquad 3.5$$

and

$$\sigma_{F_{soil}} = \pm 0.2\, F_{soil}. \qquad 3.6$$

Approximately therefore, the final overall worst-case error in latent energy flux density is given by:

$$\sigma_{L_v F_w} = \sqrt{(0.025\, I_{net})^2 + (0.20\, F_{soil})^2 + (0.054\, F_{hSLS})^2} \qquad 3.7$$

and

$$\sigma_{L_v F_w} = \sqrt{(0.025\, I_{net})^2 + (0.20\, F_{soil})^2 + (0.032\, F_{hSLS})^2} \qquad 3.8$$

for typical errors.

Using five soil heat flux plates and averaging thermocouples, we investigated the actual spatial variation in soil heat flux density over an area of about a square metre. The variation in soil heat flux density, the standard deviation of the five measurements and 0.20 of the measured soil heat flux density (Eq. 3.6) is shown for cloudless summer and winter days (Fig. 3.23). From these data, typical of other cloudless days, the measured standard deviation is greater than the estimated amount for a summer day (Fig. 3.24, top) but smaller than that estimated for a winter day (Fig. 3.23, bottom).

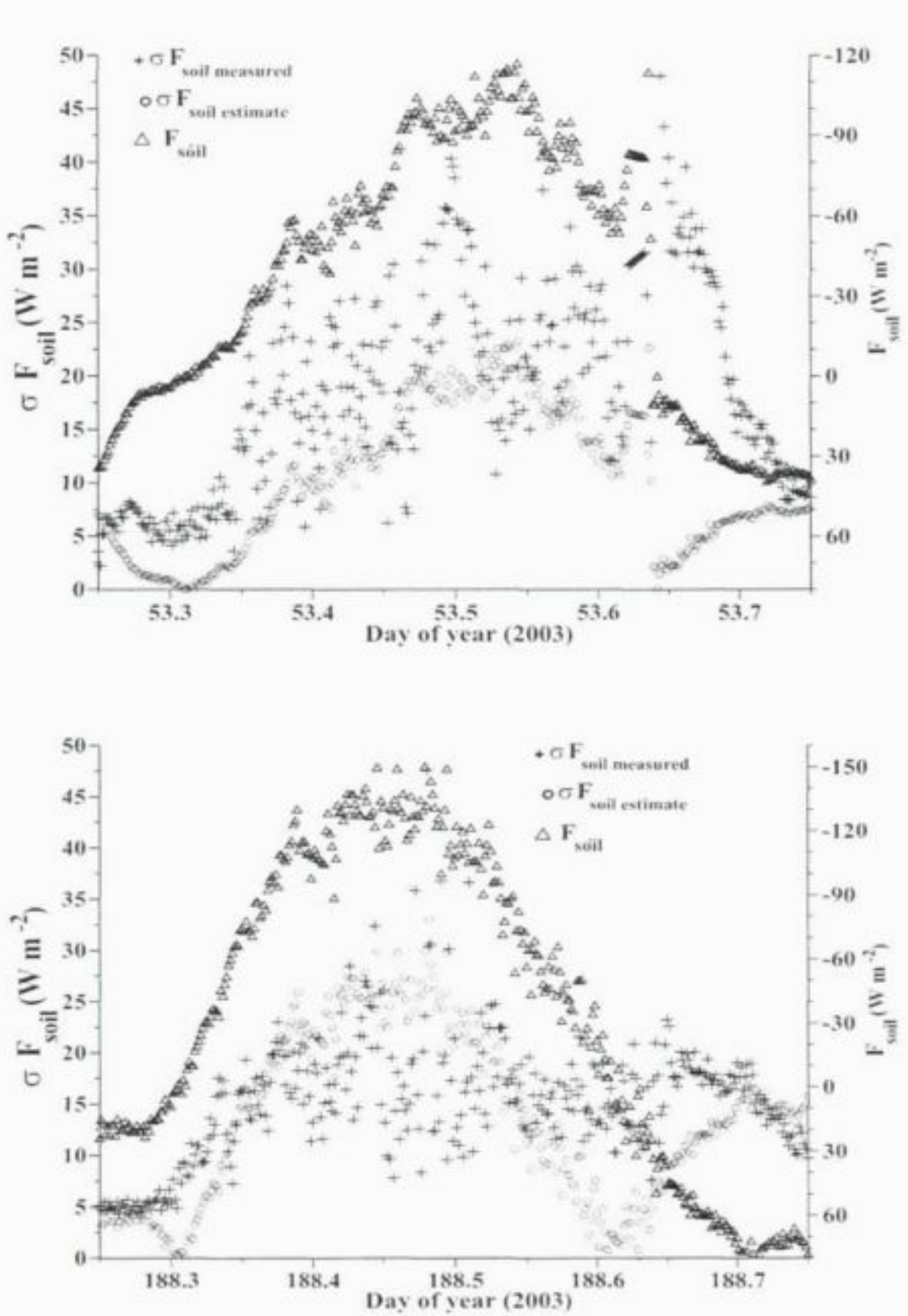

Fig. 3.23 Diurnal variation in 2-min soil heat flux density (right hand y-axis, and the standard deviation in soil heat flux density (measured and estimated) on the left hand y-axis for two almost cloudless days (day of year 54 (top) and 189 (bottom), 2003)

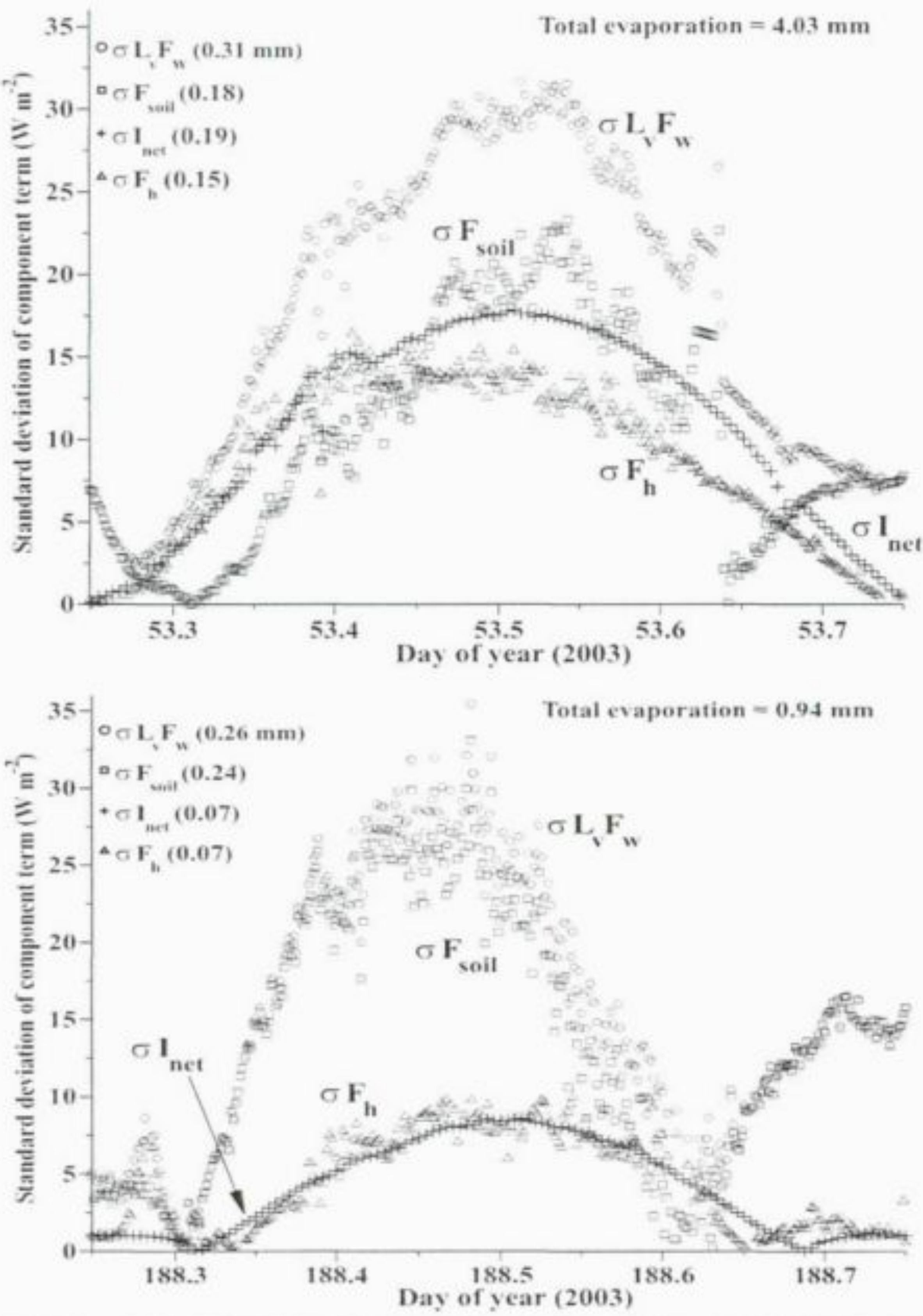

Fig. 3.24 The diurnal variation in the calculated component error terms (2-min data) of the energy balance for a summer (upper) and a winter day (lower). In brackets, upper left of both graphs, is the total error amount for the day for each component, converted into mm units. The worst-case error amount is used for sensible heat flux density

The component worst-case error terms of the energy balance are shown in Fig. 3.24 for two cloudless days, one in summer and one in winter. The variation in the error in net irradiance is estimated using Eq. 3.5. Of particular note is that while the overall error in latent energy flux density is similar for the two days, the component errors are different. The error in sensible heat flux density is greater in summer as is the error in net irradiance measurement. However, due to the greater amount of plant material covering the soil in summer, the error in soil heat flux density is smaller in summer than in winter. In brackets in the upper left legend of Fig. 3.24 is the evaporation equivalent of each component calculated by summing the 2-min error values for the 06h00 to 18h00 period and converting them to mm units.

The seasonal variation in $\sigma_{L_v F_w}$ in mm day^{-1}, shown in Fig. 3.25 for selected relatively cloudless days, is typically 0.2 mm day^{-1} (0.49 MJ m^{-2}) in winter when the daily evaporation rate was around 1 mm day^{-1} (2.45 MJ m^{-2}) and typically 0.4 mm day^{-1} (0.98 MJ m^{-2}) when the evaporation rate exceeded 4 mm day^{-1} (9.8 MJ m^{-2}) in summer. The evaporation totals shown in Fig. 3.25 (bottom) are calculated from 2-min totals between the times of 6 am and 6 pm. For these calculations, it is assumed that the error in soil heat flux density is 20 % of the measured soil heat flux density and the error in net irradiance 25 % of the measured value (Eqs 3.6 and 3.5 respectively).

Using typical fractional errors in sensible heat flux density measurement (within ± 0.032) instead of a worst-case fractional error (of ± 0.054) does not alter the overall error by much since both the net irradiance and soil heat flux density errors swamp that for sensible heat flux density: the net irradiance is generally the largest term of the energy balance and hence the contribution of $(0.025\, I_{net})^2$ in Eqs 3.7 and 3.8 is the largest. The contribution of error in soil heat flux density may also be significant because the fractional error is high (0.20 of the measurement) compared to 0.054 (for worst-case error) or 0.032 (for typical error) of the SLS-measured sensible heat flux density.

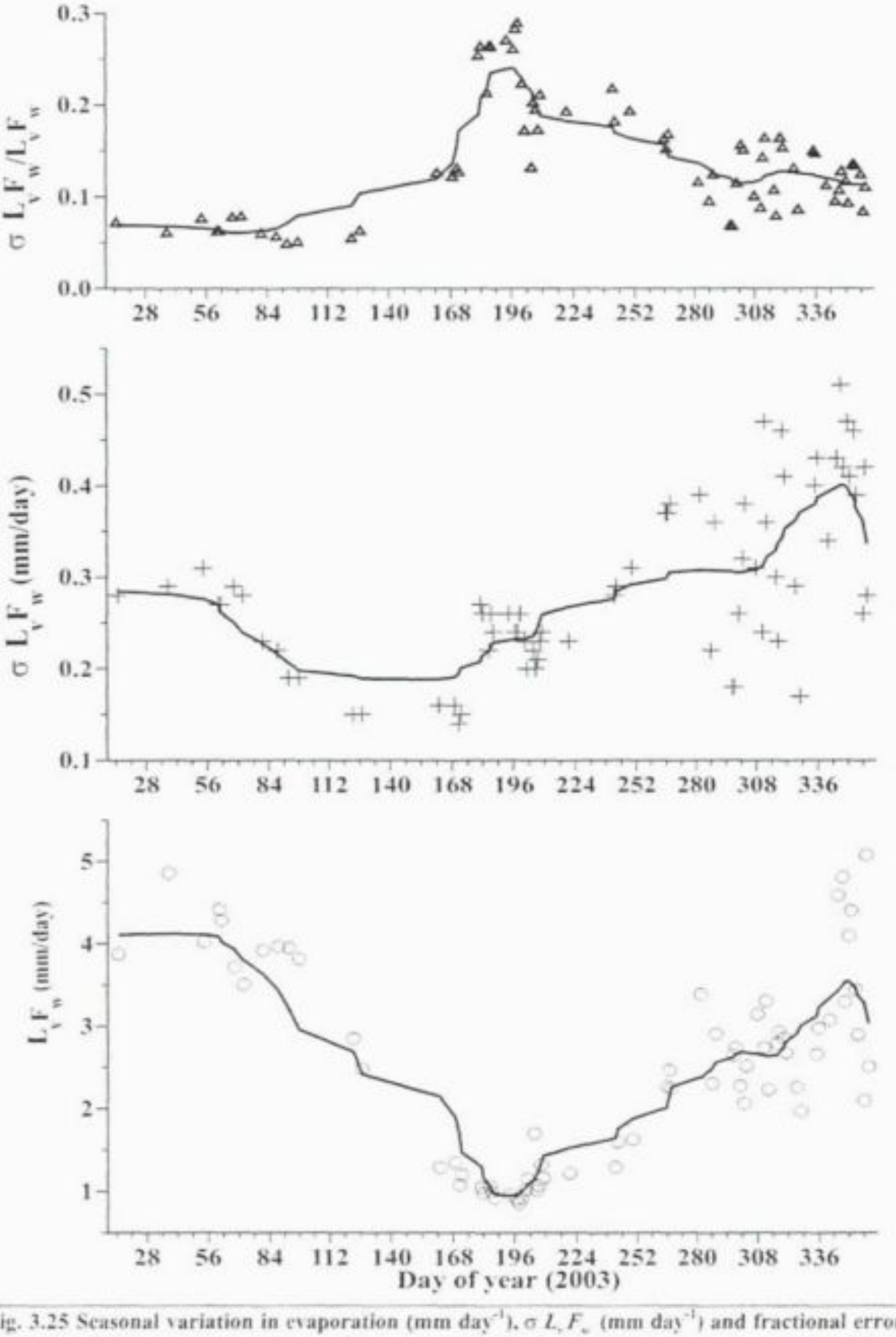

Fig. 3.25 Seasonal variation in evaporation (mm day^{-1}), $\sigma L_v F_w$ (mm day^{-1}) and fractional error in evaporation ($\sigma L_v F_w / L_v F_w$) for 2003. The smooth curves were created by smoothing the y values in x, y data using a smoothing factor of 0.4 (Scientific Programming Enterprises 1999). The worst-case error amount used for sensible heat flux density is used to determine $\sigma L_v F_w$

3.6 Conclusions

The methodology associated with the use of a dual-beam surface layer scintillometer is discussed in detail. The procedures associated with the crucial step of beam alignment are presented as are the procedures for the error-checking of the data post-data collection. While a horizontal beam and a horizontal surfaces is assumed by MOST, there was no consistent over- or under-estimate in SLS sensible heat flux density compared to ECAT measurements for a non-horizontal beam. A low effective beam height of 0.5 m resulted in more variable sensible heat flux density measurements, and variable inner scale of turbulence values that approached the defined lower value for acceptable data.

The percentage of error-free 2-min SLS sensible heat flux density measurements for the daytime hours showed little seasonal variation, varying between 86.7 % and 94.8 % for the 18-month period. The nighttime variation in the percentage had a more pronounced seasonal pattern with the lowest percentage acceptable measurements occurring between January and March of each year due to the effects of dew and mist.

Values of the inner scale of turbulence l_o less than 2 mm results in rejected sensible heat flux density data. For most of the study, the most common (or at least 35 % of the time) l_o value is between 4 and 6 mm. For the nighttime, the most common l_o value is less than 2 mm. The second-most common nighttime value is that between 6 and 8 mm in contrast to the 4 to 6 mm value during the daytime hours. The larger values of 6 to 8 mm at night is due to the more stable nighttime conditions compared to the more turbulent daytime conditions creating smaller and smaller eddies.

The procedures for the measurement of other energy balance components are reported. The theory associated with a sensitivity analysis of the estimated latent energy flux density was used to determine the relative importance of the SLS data inputs of air temperature, atmospheric pressure, beam path length and beam height on sensible heat flux density estimates. In addition, it was shown that errors in the measurement of soil heat flux density and net irradiance also affected the estimated latent energy flux density.

The worst-case errors in atmospheric pressure, air temperature, beam path length and beam height resulted in fractional errors in sensible heat flux density of ± 0.013, ∓ 0.015, ∓ 0.03 and ± 0.04 respectively. The beam height above $d + z_o$ needs to be known accurately as the error in beam height contributes the most to the overall error with errors in beam path length next most important. The worst-case total fractional error in sensible heat flux density was $\pm$ 0.054 and the typical fractional error amounted to $\pm$ 0.032.

The seasonal variation in the error in latent energy is generally less than 0.2 mm day^{-1} (equivalent to 0.49 MJ m^{-2}) in winter when the daily evaporation rate was around 1 mm day^{-1} (2.45 MJ m^{-2}) and typically less than 0.4 mm day^{-1} (0.98 MJ m^{-2}) when the evaporation rate generally exceeded 4 mm day^{-1} (9.8 MJ m^{-2}). Most-often, the measurement with the greatest contributing error is the soil heat flux density measurement which often expresses the spatial variability of canopy growth. Care therefore needs to be exercised to ensure that soil heat flux density measurement procedures do not compromise the calculated latent energy flux density when using SLS sensible heat flux density measurements, particularly for short vegetation where it is expected that the soil heat flux density term may not be small. This would also apply to BR estimates of latent energy flux density and the EC method when only sensible heat flux density is measured and latent energy flux density is estimated using the net irradiance and soil heat flux density energy balance components.

Chapter 4

Comparison of evaporation measurements using surface layer scintillometry, eddy covariance, Bowen ratio, and surface renewal methods

4.1 Abstract

The main aim of this research is to investigate dual-beam surface layer scintillometer (SLS) estimates of sensible heat flux density also obtained using the following methods: Bowen ratio (BR), eddy covariance (EC), reference evaporation, and surface renewal (SR). These measurements and measurements of net irradiance and soil heat flux density allowed evaporation to be be estimated as a residual using the energy balance. The influence of wind direction, in particular winds perpendicular and parallel to the SLS beam, on these measurement comparisons is examined. Since the measurement height of the various instrumentation was necessarily different, the relative contribution of upwind surface sources to the sensible heat flux density measured at a height above the canopy surface was investigated using a footprint analysis.

In order to obtain accurate comparisons using the BR method, we also investigated the possibility of replacing the often problematic Dew-10 cooled dew point mirror usually used with such systems with a thin film polymer capacitive sensor such as a Vaisala sensor. The main disadvantage of the use of a Vaisala sensor is that two measurements, relative humidity and temperature, from two different sensors was required for the estimation of the airstream water vapour pressure. A laboratory experiment showed that potentially, a Vaisala CS500 and the predecessor of the Vaisala HMP45C could replace the Dew-10 sensor. A four-month field-comparison between 20-min latent energy flux density obtained using the HMP45C and a Dew-10 sensor (6002 data points) yielded a slope of 0.9938 and y-intercept of -0.095 W m^{-2}. This excellent agreement shows that the HMP45C would be a cheaper and adequate replacement for the Dew-10 cooled mirror sensor. Furthermore, the HMP45C requires no servicing compared to the Dew-10 which requires a bias adjustment and mirror cleaning each week. The water vapour pressure measurement noise for the HMP45C sensor was greater than that for the Dew-10 but the average water vapour pressure profile difference for the two sensors was highly correlated (slope of 0.9334, r^2 = 0.9899, n = 12965). The HMP45C sensor used was not as accurate as the Dew-10 but the resolution of the HMP45C profile difference measurements was better than the minimum resolution of 0.01 kPa required for BR measurements when averaged over 20 min. The even cheaper Vaisala CS500 sensor was also used for field measurements. Comparison of the HMP45C with the CS500 yielded a slope of 1.0236 (r^2 = 0.9956, n = 213). The CS500 sensor exhibited greater variation in measured water vapour pressure mainly as a consequence of greater variation in temperature using the CS500 temperature sensor even when compared to the HMP45C temperature sensor. In spite of this, the resolution in the CS500 water vapour pressure was better than 0.01 kPa. The water vapour pressure variation could be reduced by replacing the temperature sensor with a thermocouple. These findings will make BR measurements of evaporation considerably cheaper, more reliable than in the past and easier to assemble.

Polar diagrams were used to show that during daytime hours, the wind vector wind direction is generally from the SE (180 to 270°) but sometimes from the NW (0 to 90°). The SLS beam was aligned from 20° east of S to 15° W of north - almost from S to N. The largest SLS and EC differences in the daily sensible heat density occurred for the 0 to 60° wind direction. These winds were from

residential areas and the fetch more limited than the other wind directions. However, there were many days when the wind direction was almost perpendicular to the beam and seldom parallel.

The footprint model of Hsieh et al. (2000) was corrected and extended to include a surface with a zero plane displacement height. The more unstable the atmospheric conditions, the closer was the peak location of the footprint to the measurement position. For convectively unstable conditions, the peak location was within metres of the measurement position. Generally, during the daytime hours, the 100:1 fetch to measurement height ratio is too stringent for the atmospheric conditions experienced. The general stability condition for the 9 am to noon hours is not the same as that for the noon to 3 pm period. Surprisingly, the morning hours are generally more unstable than are the afternoon hours. This asymmetry in stability often results in asymmetrical diurnal sensible heat flux density curves.

The general agreement between the 2-min SLS and EC measurements was very good. The EC measurements showed greater variability since they are point estimates. The SLS measurements represent a line-average and were much less variable. The correspondence between the two measurement techniques improved when there was reduced turbulence, particularly for uniformly cloudless days and before 10 am and after 2 pm. There did not appear to be a consistent bias between the two measurement methods. This implies that the correct value for the zero plane displacement height, based on two-thirds of the canopy height, was chosen. The 2-min SR sensible heat flux density was more variable than the other methods (error mean square of 2299.1 W m^{-2} when compared with SLS measurements). Averaging SR measurements over 20 min is recommended.

Latent energy flux density is estimated as a residual from the energy balance equation. Negative latent energy values correspond to normal evaporation but cases were found when the latent energy flux density was positive for brief periods. Positive latent energy flux density values correspond to the magnitude of the sensible heat flux density exceeding the available heat flux density. Counter-gradient fluxes of sensible heat were detected. Some of the selected data displayed show that counter-gradient fluxes may be associated with large reductions in solar irradiance but were short-lived.

The BR 20-min measurements of sensible heat and latent energy flux density were in good agreement with the corresponding SLS, EC and SR estimates. Examples of this correspondence were selected from the large data set collected. There was no consistent under- or overestimate in the SLS sensible heat flux density measurements compared to the sensible heat flux density measurements from the three other methods. The magnitude of the SR sensible heat flux density measurements, if anything, tended to be less than the sensible heat flux density measured using the other measurement methods and therefore tended to overestimate the latent energy flux density. The SR method is the least expensive in terms of instrumentation and datalogging requirements. The good agreement between the different measurements is remarkable considering the different underlying theory of each method, the different measurement heights, different footprints, differing spatial scales of measurement (i.e., point measurements *vs* path averaging) and differing measurement frequencies. Furthermore, it would appear that the EC sensible heat flux density measurements do not underestimate as stated in the literature.

Comparisons of the daily estimates of sensible heat density for EC and SLS techniques showed good agreement (error mean square of 0.188 MJ m^{-2} which is equivalent to 0.077 mm). These comparisons were separated out according to wind direction which showed that best comparisons between EC and SLS measurements were obtained for the 180 to 270° wind directions (error mean square of 0.171 MJ m^{-2} compared to 0.229 MJ m^{-2} for the 0 to 90° wind directions). The 0 to 90° wind directions corresponded to wind from residential areas and relatively limited fetch.

Measurement comparisons over a period in excess of 55 days showed that the ECopen system daily latent energy density measurements had a variable relationship with daily latent energy density estimated using SLS measurements, net irradiance and soil heat (error mean square of 0.632 MJ m^{-2}, r^2 = 0.239). Daily estimates of latent energy density for the SLS and EC techniques were compared for a period of about 250 days during 2003. The 95 % confidence bands for a single predicted value were within 0.5 mm of the regression line and the error mean square was 0.295 MJ m^{-2} or about 0.12 mm. There was no statistical difference between daily latent energy density estimates obtained using the EC method based on point measurements and the line-averaged estimates obtained using the SLS method.

4.2 Introduction

The accuracy of SLS measurements must be judged by comparison with sensible heat flux density measurements obtained using other methods (Table 3.1). Generally, the standard for sensible heat measurements is taken as the EC method.

The main objective of this chapter is to present the measurement comparisons of sensible heat flux density using a dual-beam SLS and the estimation of evaporation from sensible heat flux density, net irradiance and soil heat flux density. The various methods used in this study for estimating sensible heat flux density include: BR, EC and SLS methods, and to a limited extent the SR method. Microclimatic measurements allowed reference evaporation to be calculated. The averaging time period for the EC, SLS, SR and reference evaporation measurements was 2 min and 20 min whereas for the BR method, a period of 20 min was used as is often the case.

Agreement between BR and SLS measurements, for example, may be dependent on the footprint of the measurements, viz., the relative contribution of upwind surface sources to the sensible heat flux density measured at a height above the canopy surface. For this reason, a second objective was to perform a footprint analysis for the various measurement methods.

A third objective was to investigate the impact of wind perpendicular to the SLS beam on the SLS sensible heat flux density measurements compared to wind parallel to the beam.

Since the dew point hygrometer of the BR system was often unreliable in addition to other practical problems, a fourth objective included investigating the use of a BR system using a replacement for the dew point hygrometer with a Vaisala air temperature and relative humidity sensor. An error analysis was performed and the three types of Vaisala sensors were evaluated in the laboratory and in the field for their ability to measure water vapour pressure profile differences.

4.3 Theoretical considerations

Five measurement methods were used to estimate total evaporation (Table 4.1). In this section, the theory of each method is briefly discussed in relation to the measurement requirements. Other measurements methods are presented in Table 3.1 and some of these reviewed by Drexler et al. (2004).

4.3.1 Bowen ratio theory

For completeness, a brief description of the BR technique for measuring sensible and latent energy flux density is presented here.

Table 4.1 Brief details of the five total evaporation measurement methods used in this study. Symbols are defined in the text in each corresponding section

Method	Measurements	Position	Theory
Bowen ratio (BR)	$\overline{e_1}, \overline{e_2}, \overline{T_1}, \overline{T_2}, I_{net}, F_{soil}$	Point measurements of the 20-min average water vapour pressure and air temperature at two heights above the canopy	$L_v F_w = -(I_{net} + F_{soil})/(1+\beta)$ $F_h = -\beta(I_{net} + F_{soil})/(1+\beta)$ (Eqs 2.46, 4.5 and 4.6)
Eddy covariance (EC)	$w', U' = \sqrt{u'^2 + v'^2}, T_{sonic}'$, I_{net}, F_{soil}	Single-level measurement method (2-min and 20-min averages)	$F_h = -\rho_{air}\, c_p \cdot$ covariance $(w, T) =$ $-\rho_{air}\, c_p\, \overline{w'T'}$ (Eqs 2.45 and 4.18) $L_v F_w = -I_{net} - F_h - F_{soil}$
Reference evaporation	Solar irradiance, air temperature, water vapour pressure and horizontal wind speed	AWS measurements at a single level, typically 2 m (2-min and 20-min averages)	Penman-Monteith reference evaporation using $r_s = 70$ s m^{-1} and $r_a = 208/U$ (Eq. 4.37)
Surface layer scintillometer (SLS)	Covariance (B_{12}) and variances (B_1 and B_2) of the logarithm of the amplitude of the radiation together with inputs for air temperature, atmospheric pressure, beam height (above $d + z_o$) and beam path length	Dual beam measurements (2-min averages) at a single beam height across a path length of between 50 and 250 m	Measurements of B_{12} allow for the following calculations using MOST: C_n^2, F_h and friction velocity $L_v F_w = -I_{net} - F_h - F_{soil}$
Surface renewal (SR)	$\frac{\partial T}{\partial t} \approx [T(t+\delta t) - T(t)]/\delta t$ where δt is one or two lagging time steps; typically $\delta t = 0.125$ s	High frequency single point measurements (2- and 20-min averages) of air temperature above the canopy	$F_h = -\rho_{air}\, c_p\, z \frac{\partial T}{\partial t}$ (Eqs 2.48 and 4.10) $L_v F_w = -I_{net} - F_h - F_{soil}$

The BR method relies on the K-theory hypothesis for which the sensible heat flux density, for example, is proportional to an exchange coefficient for sensible heat flux density and the profile air temperature gradient.

Bowen (1926), building on previous work of Cummings (1925), John Dalton and others, attempted to obtain expressions for latent energy flux density in terms of water vapour pressure gradients above a surface. According to Fick's Law of Diffusion, the latent energy flux density $L_v F_w$ (W m^{-2}) is given in finite difference form by:

$$L_v F_w = (\rho_{air}\, c_p/\gamma) K_w\, \partial\overline{e}/\partial z \approx (\rho_{air}\, c_p/\gamma) K_w\, (\overline{e}_2 - \overline{e}_1)/(z_2 - z_1) \qquad 4.1$$

where ρ_{air} is the air density (kg m^{-3}), c_p the specific heat capacity of dry air at constant pressure (J kg^{-1} K^{-1}), γ the psychrometric constant (approximately 0.066 kPa K^{-1} at sea level), K_w the exchange coefficient (m^2 s^{-1}) for latent energy transfer, and $\overline{e}_2$ and $\overline{e}_1$ the time-averaged water vapour pressures (kPa) at heights z_2 and z_1 above the soil surface respectively. The averaging period is usually 20 min, 30 min or hourly.

Similarly, the sensible heat flux density F_h is related to, in finite difference form, by the change in heat energy content of air per unit time per unit area. Using Fick's Law for sensible heat flux density, we have:

$$F_h \approx (\rho_{air}\ c_p\ K_h)(\overline{T_2} - \overline{T_1})/(z_2 - z_1) \qquad 4.2$$

where K_h is the exchange coefficient for sensible heat transfer (m^2 s^{-1}), $\overline{T_2}$ and $\overline{T_1}$ are the time-averaged air temperatures (°C) at heights z_2 and z_1 above the soil surface respectively. In terms of the sign convention used in Chapter 2, $z_2 > z_1$, $\overline{T_2} > \overline{T_1}$ and $\overline{e_2} > \overline{e_1}$, as would be the normal case during daytime hours, would result in negative $L_v\ F_w$ and F_h values (Eqs 4.1 and 4.2) indicative of energy losses at the surface.

Following Bowen (1926), we consider the ratio β:

$$\beta = F_h / L_v\ F_w \qquad 4.3$$

where from Eqs 4.1 and 4.2, β can be written as:

$$\beta = (\gamma\ K_h / K_w)(\overline{T_2} - \overline{T_1})/(\bar{e}_2 - \bar{e}_1).$$

Hence β can be determined by measuring air temperature and water vapour pressure at two levels in the atmosphere. Ignoring photosynthesis and advection, the shortened surface energy balance (Eq. 2.3) is given by:

$$I_{net} = -L_v\ F_w - F_h - F_{soil} \qquad 4.4$$

where I_{net} is the net irradiance and F_{soil} is the soil heat flux density. Combining Eqs 4.3 and 4.4:

$$L_v\ F_w = -(I_{net} + F_{soil})/(1+\beta) \qquad 4.5$$

and

$$F_h = -\beta(I_{net} + F_{soil})/(1+\beta) \qquad 4.6$$

where

$$\beta = \gamma(\overline{T_2} - \overline{T_1})/(\overline{e_2} - \overline{e_1}) \qquad 4.7$$

if it is assumed that $K_h = K_w$ (Eq. 2.12). The equality of these two exchange coefficients, is referred to as the Similarity Principle (Section 2.6).

4.3.2 Surface renewal theory

The surface renewal (SR) method (for example, Paw U 1992, Paw U et al. 1992, Zhang et al. 1992, Paw U et al. 1995, Qiu et al. 1995, Snyder et al. 1996, Karipot 1999, Castellvi 2004) for estimating sensible heat flux density is relatively new. Sensible heat flux density F_h can be expressed as the change of heat energy content ($M_{air}\ dT\ c_p$) of air with time per unit area:

$$F_h = M_{air} \frac{dT}{dt} c_p / A$$

where M_{air} is the mass of air heated (or cooled) by the rate of change in the air temperature difference dT in time dt, c_p is the specific heat capacity of dry air at constant pressure (typically 1004 J kg^{-1} K^{-1}) and A is the horizontal area of the heated or cooled volume of air. Expressing the mass of air in terms of air density ρ_{air} and the volume of air V:

$$F_s = \rho_{air}\, c_p \frac{V}{A}\frac{dT}{dt}$$

where V / A is the volume of air heated per unit horizontal area of the heated volume of air. If the vertical distance of the heated air is the canopy height, then V / A is the canopy height h.

Assuming that the rate of change in air temperature can be written as a function of time t, and dimensions x, y, or z as follows:

$$\frac{dT}{dt} = \frac{\partial T}{\partial t} + \frac{\partial T}{\partial x}\frac{\partial x}{\partial t} + \frac{\partial T}{\partial y}\frac{\partial y}{\partial t} + \frac{\partial T}{\partial z}\frac{\partial z}{\partial t}$$

and then assuming that internal advection in the volume of air is negligible, the total rate of air temperature change is given by:

$$\frac{dT}{dt} = \frac{\partial T}{\partial t}, \qquad 4.8$$

This assumption may not be correct under all conditions or circumstances. For example, close to a canopy or a soil surface or when there is strong local advection, the partial change in temperature with x, y, or z may not be negligible. Making this assumption (Eq. 4.8),

$$F_s = \rho_{air}\, c_p \frac{V}{A}\frac{\partial T}{\partial t}$$

or

$$F_s = \rho_{air}\, c_p\, z \frac{\partial T}{\partial t}$$

where z is the measurement height for air temperature.

The SR analysis involves high frequency air temperature measurements and considering air temperature ramps (positive or negative) consisting of quiescent periods s (s) (for which there is no change in air temperature with time) and then ramping periods l (s) for which there is an air temperature ramp with an amplitude a (°C) and for which $a > 0$ °C for unstable conditions (that is, an air temperature increase) and $a < 0$ °C for stable (that is, an air temperature decrease) (Figs 4.1 and 4.2). Hence, SR analysis assumes that:

$$\frac{\partial T}{\partial t} = -\frac{a}{s + l}, \qquad 4.9$$

with unit °C m^{-1}, and

$$F_s = -\alpha\, \rho_{air}\, c_p\, z \frac{a}{s + l} \qquad 4.10$$

where α is a weighting factor. Generally, $\alpha = 0.5$ for coniferous forests, orchards and maize when the sensor is at canopy level. For short grass, $\alpha = 1$ for a sensor height of about 1 m (Paw U et al. 1995). The negative sign in Eqs 4.9 and 4.10 ensure that F_s is negative during daytime hours, indicative of energy loss at the surface.

The amplitude a of the air temperature ramp and the ramp period $s + l$ is estimated using the air temperature structure parameter approach based on measuring air temperature at a typical frequency of about 8 Hz or greater, using:

$$S^n(r) = \frac{1}{m - j}\sum_{i=1+j}^{m} (T_i - T_{i-j})^n \qquad 4.11$$

where n is the power of the air temperature structure parameter $S^n(r)$ (cf. Eq. 2.27 for a structure parameter operating over a distance) corresponding to a time lag r, m is the number of data points collected in the time interval measured at frequency f (Hz), and j is a sample lag between data points

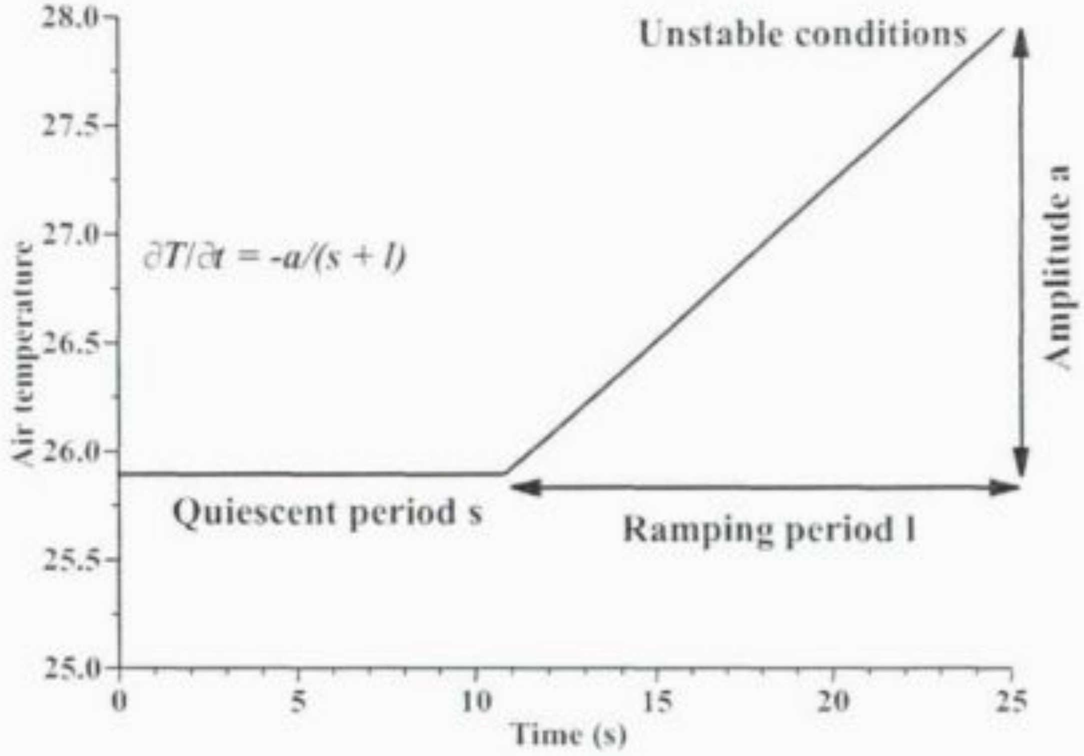

Fig. 4.1 An idealized air temperature ramp for unstable conditions, upon which the SR method depends, is visualised as consisting of a quiescent period (period *s* (s)) and a ramping period (period *l*) for which the amplitude is *a*

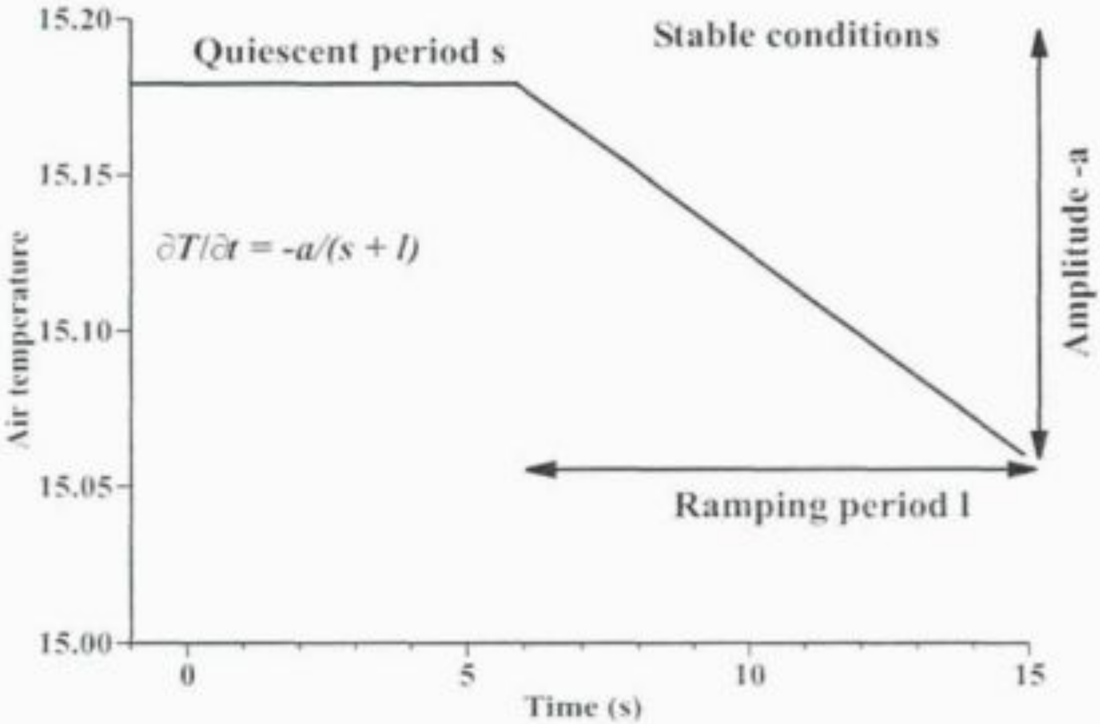

Fig. 4.2 An idealized air temperature ramp for stable conditions, upon which the SR method depends, is visualised as consisting of a quiescent period (period *s* (s)) and a ramping period (period *l*) for which the amplitude is *-a*

corresponding to a time lag $r = j / f$ and T_i is the ith air temperature sample. In this relation, the time lag r must be much less than $l+s$. The Van Atta (1977) approach involves estimating the air temperature amplitude a of Eq. 4.10 by solving for the real roots of the equation:

$$a^3 + p\,a + q = 0 \qquad 4.12$$

where

$$p = 10S^2(r) - \frac{S^5(r)}{S^3(r)} \qquad 4.13$$

and

$$q = 10S^3(r). \qquad 4.14$$

The ramp period $s+l$ (Figs 4.1 and 4.2) is then calculated from:

$$s + l = -\frac{a^3 r}{S^3(r)}. \qquad 4.15$$

Note then that the second, third and fifth order of the air temperature structure parameter are required for the SR method, viz., $S^2(r)$, $S^3(r)$ and $S^5(r)$.

The advantage of using Eqs 4.10 to 4.15 to obtain sensible heat flux density is that only high frequency measurements of air temperature at one atmospheric level (at at least 8 Hz) are required.

The main disadvantage of the method is that the changes in temperature following the ramp period, which can be quantified using additional theory and MOST, requires that the friction velocity be estimated (Chen et al. 1997a, b, Castellvi 2004).

4.3.3 Eddy covariance

For completeness, a brief description of the EC method for measuring sensible heat flux density is presented here. From the continuity equation for a compressible and homogenous medium, $\partial(\overline{w\rho_{air}})/\partial z = 0$ where w is the vertical wind speed (m s^{-1}) and ρ_{air} is the density of air (kg m^{-3}) and where $\partial(\overline{w\rho_{air}})/\partial z$ represents the change in the mass flux density of air (kg s^{-1} m^{-2}) in the vertical direction. Integrating between the surface $z = 0$ and the measurement height z, we get

$$(\overline{w\rho_{air}})_z - (\overline{w\rho_{air}})_o = 0 \qquad 4.16$$

where the subscripts z and o refer to measurement height and canopy surface respectively. Since $\overline{w} = 0$ at the surface, the time-averaged vertical flux density of dry air (kg s^{-1} m^{-2}) at the measurement height (-the first term of Eq. 4.16) is zero. Removing reference to the measurement height:

$$\overline{w\rho_{air}} = 0 \qquad 4.17$$

where the bar indicates the time average (over 20 min, say). The instantaneous vertical wind speed can be written as a mean value $\overline{w}$ and a fluctuation w':

$$w = \overline{w} + w'.$$

Similarly, the instantaneous air density may be expressed as a mean value $\overline{\rho_{air}}$ and a fluctuation ρ_{air}':

$$\rho_{air} = \overline{\rho_{air}} + \rho_{air}'.$$

Hence $\overline{w\rho_{air}} = 0$ (Eq. 4.17) may be written as:

$$\overline{(\overline{w} + w')(\overline{\rho_{air}} + \rho_{air}')} = 0.$$

Expanding, and noting that, by definition the mean of a fluctuation is zero:

$$\overline{w'} = \overline{\rho_{air}'} = 0,$$

and hence

$$\overline{w'\rho_{air}'} = -\overline{\rho_{air}}\,\overline{w}.$$

Hence $\overline{w} = 0$ only if $\overline{w'\rho_{air}'} = 0$.

The flux density F_E of an entity E, over a specified time period, is given by:

$$F_E = \overline{w\rho_{air}E}.$$

By expansion and since $\overline{w'\rho_{air}'} = -\overline{\rho_{air}}\,\overline{w}$:

$$F_E = \overline{\rho_{air}}\,\overline{w'E'} = \text{covariance}\,(w, E).$$

The only assumptions in this derivation are that

$$\overline{w\rho_{air}} = 0,$$

from the continuity equation, and that

$$\overline{w}\,\overline{\rho_{air}'E'} << \overline{\rho_{air}}\,\overline{w'E'}.$$

Note that it has not been necessary to assume that $\overline{w} = 0$.

For sensible heat flux density F_s (W m^{-2})

$$F_s = -\rho_{air}\,c_p\cdot\text{covariance}\,(w, T) = -\rho_{air}\,c_p\,\overline{w'T'}, \qquad 4.18$$

where c_p and T are, respectively, the specific heat capacity of dry air at constant pressure (J kg^{-1} °C^{-1}) and air temperature (°C) and where the fluctuations in vertical wind speed and air temperature are represented by w' and T' respectively. The negative sign ensures that the flux density is negative during normal daytime unstable conditions, corresponding to a loss of energy at the surface. For momentum flux density τ (Pa),

$$\tau = \rho_{air}\ \text{covariance}\,(\overline{w'U'}) = \rho_{air}\,\overline{w'U'} \qquad 4.19$$

where $U' = \sqrt{u'^2 + v'^2}$ is the fluctuation in the horizontal wind speed (m s^{-1}) where u' and v' are the fluctuations of the resolved components of the horizontal wind speed in the x and y directions respectively. Friction velocity u_* may be calculated using:

$$\tau = \rho_{air}\,u_*^2 = \rho_{air}\,\overline{w'U'}$$

from which

$$u_* = \sqrt{\overline{w'U'}}. \qquad 4.20$$

4.3.4 Scintillometer theory

Turbulent motions require a supply of energy for their maintenance on the one hand and are dissipative on the other hand. They involve a spectrum of space and time scales and are inherently unsteady or even random, and occur in three dimensions. Pertinent to any discussion of scintillometer theory is the Kolmogorov (1941a, b) cascade theory of turbulence. This cascade theory, based on dimensional analysis, deals with the scale of turbulence. The so-called outer scale of turbulence is denoted L_o and l_o is the inner scale of turbulence. Large eddies have a typical size of 100 m (outer scale) and small eddies have a typical size of the order of 10 mm (inner scale of turbulence). Near the surface of the earth, the inner scale l_o is of the order of a few millimetres. Eddies between these sizes are from the so-called inertial subrange, where no energy enters or leaves the system of turbulent motion. As the turbulent eddy size becomes smaller and approaches the inner scale of turbulence l_o, the relative amount of energy dissipates by viscous forces in the form of heat.

The energy spectrum of turbulence shows that for the high frequency range, increasing frequencies result in reduced energy (Fig. 2.2). Kolmogorov (1941b) showed that the structure parameter in the inertial subrange is a measure of the energy amount.

The SLS40-A dual-beam SLS system consists of two parallel beams of radiation of wavelength (670 ± 10) nm emitted from two laser diode radiation sources separated by a distance that results in a beam separation of 2.7 mm (Scintec 2000). The receiver detects the transmitted radiation using two 2.5 mm detectors separated by 2.7 mm. The covariance of the logarithm of the amplitude of the radiation transmitted to the receiver position is measured and denoted B_{12} where the correlation coefficient r relates the single detector variances B_1 and B_2 to the covariance B_{12}:

$$r = B_{12} / (B_1 \, B_2)^{1/2} \qquad 4.21$$

(cf $r = \Sigma \, x \, y / [\Sigma x \, \Sigma y]$). Thiermann (1992) stated that the correlation coefficient r is a known function of the inner scale of turbulence l_o, and the detector diameter D and detector separation distance d. For known and fixed D and d values, the relationship between r and l_o is given by Thiermann (1992) and is shown in Fig. 4.3 for a 100-m path length. For this relationship, if r is known from measurements, then the inner scale of turbulence l_o can be calculated for a known path length. These relationships assume that d and D are fixed.

The term B_1 refers to the variance of the logarithm if the amplitude of the beam signal. However, since the system measures the variances of the intensity σ_1^2, the following equation is applied for a log-normally distributed amplitude:

$$B_1 = \frac{1}{4} \cdot \log\left(\frac{\sigma_1^2}{\bar{I}_1^2} + 1\right)$$

where $\bar{I}_1$ is the mean intensity for beam 1 (Scintec 2000). A similar equation is used for beam 2 of the dual-beam SLS40-A system.

The measured covariance B_{12}, and the variances B_1 and B_2 are key in the algorithm used to estimate sensible heat flux density, as shown by the shaded elements of Fig. 4.4. The covariance B_{12} is a function of the following:

- beam wavelength which is fixed at between 660 and 680 nm for the SLS40-A SLS system;
- beam path length L_{beam} which is usually a reasonably accurate measurement;
- detector diameter D;
- detector separation d;
- Φ_n, the 3-dimensional spectrum of refractive index inhomogeneities, dependent on wave number (defined as $2\pi / \lambda$) where $\Phi_n = \Phi_n \, (2\pi / \lambda)$;

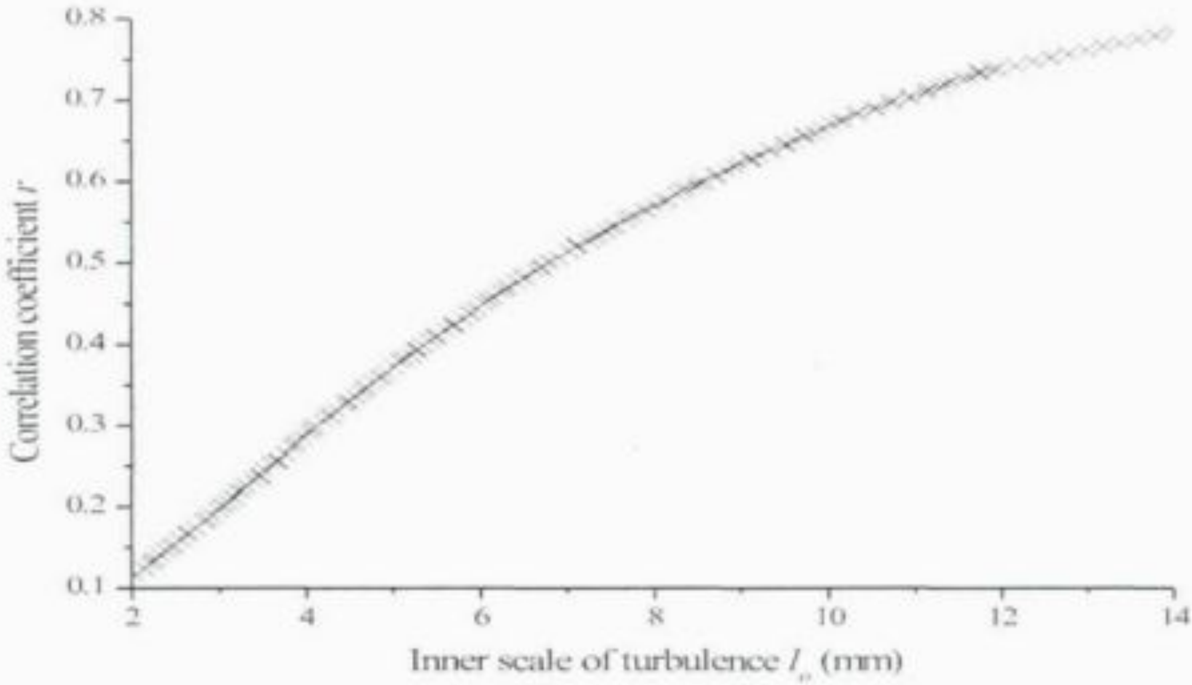

Fig. 4.3 The relationship between the inner scale of turbulence l_o and the correlation coefficient r where $r = B_{12} / (B_1 B_2)^{1/2}$ for a 100-m path length where B_{12} is the covariance of the logarithm of the amplitude of the radiation received and B_1 and B_2 are the single detector variances for the SLS method

- and two Bessel functions of the first kind with arguments of $2\pi d / \lambda$ and $\frac{(2\pi/\lambda) D x}{2 L_{beam}}$ where x is the horizontal distance measured from the receiver.

In the inertial and dissipation ranges of turbulence, Φ_n depends on wave number $k = 2\pi / \lambda$ for beam wavelength λ, where in the notation used by Thiermann (1992),

$$\Phi_n(2\pi/\lambda) = 0.033\, C_n^2 \cdot (2\pi/\lambda)^{-11/3} \cdot f_\phi(l_o, 2\pi/\lambda) \qquad 4.22$$

where C_n^2 is the structure parameter that describes the spectral amplitude of refractive index fluctuations in the inertial range of turbulence, and $f_\phi(l_o, 2\pi/\lambda)$ describes the decay of refractive index fluctuations in the dissipation range of turbulence. An expression for f_ϕ has been given by Hill (1978a) assuming pure temperature fluctuations.

Combining the mathematical expression for B_{12} (not shown) and the expression for wave number $\Phi_n(2\pi/\lambda)$ (Eq. 4.22), Thiermann (1992) used the following expression to estimate C_n^2:

$$B_{12} = 0.124\, C_n^2\, (2\pi/\lambda)^{7/6} L_{beam}^{11/6} f_B\left(\frac{l_o}{\sqrt{\lambda L_{beam}}}, \frac{d}{\sqrt{\lambda L_{beam}}}, \frac{D}{\sqrt{\lambda L_{beam}}}\right) \qquad 4.23$$

where f_B describes the decrease of B_{12} with increasing l_o, d and D.

Finally then, if r is known from measurements (Eq. 4.21), and l_o determined using Fig. 4.3 for example, then C_n^2 can be determined if B_1 or B_2 are known for which it is assumed that $d = 0$.

So the covariances between the transmitted radiation intensity for the two beams are used to calculate C_n^2 and the correlation of the transmitted radiation intensity for the two beams is used to calculate l_o (Fig. 4.4).

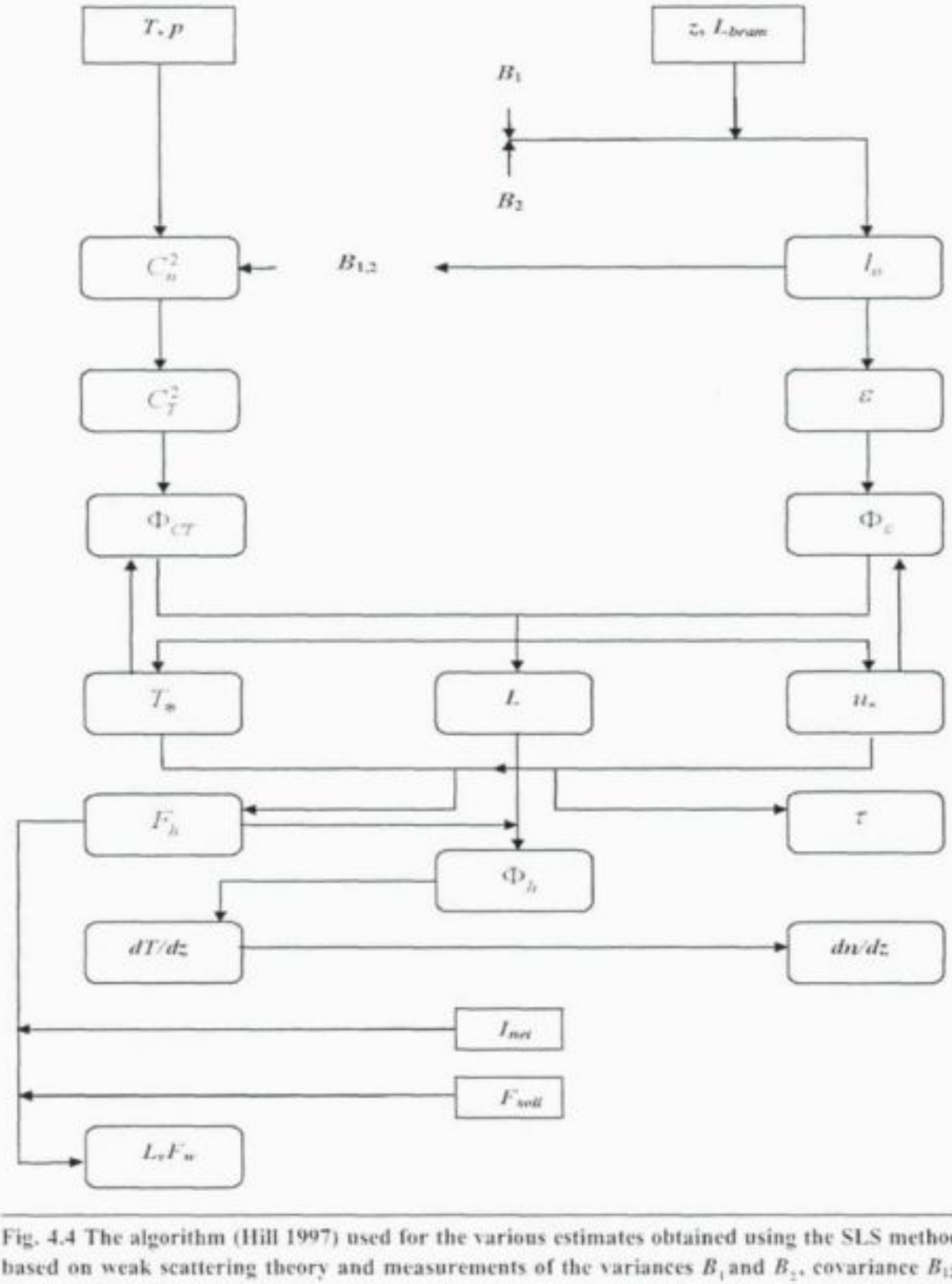

Fig. 4.4 The algorithm (Hill 1997) used for the various estimates obtained using the SLS method based on weak scattering theory and measurements of the variances B_1 and B_2, covariance B_{12}, inputs of beam height z above the zero plane displacement height, beam distance L_{beam}, air temperature T, atmospheric pressure and measurements of net irradiance I_{net} and soil heat flux density F_{soil} (based on Weiss (2002) but modified to reflect the role of single detector variances B_1 and B_2, that T_* and u_* are required to calculate Φ_{CT} and Φ_ε and to reflect the estimation of $L_v F_w$). The square boxes indicate data inputs and the shaded boxes are statistical calculations (variances and covariances) based on measurement of the logarithm of the amplitude of the radiation transmitted to the receiver detectors

Monin-Obukhov similarity theory (MOST) is used to relate the structure parameter for the refractive index fluctuations, C_n^2 to the structure parameter for temperature, C_T^2:

$$C_T^2 = \frac{1}{a_1^2}\frac{T^4}{p^2}C_n^2$$

(Wesely 1976) and $$l_o = 7.4\,\upsilon^{3/4}\,\varepsilon^{-1/4} \qquad 4.23$$

where a_1 is a proportionality constant where

$$a_1 = a_2\,[1 + (\frac{\lambda_o^2}{\lambda^2})]$$

and $a_2 = 77.6 \times 10^{-6}$ K hPa^{-1}, p is the atmospheric pressure (hPa), T is the air temperature (K) and υ = 14.6×10^{-6} m^2 s^{-1} is the kinematic viscosity of air. Rearranging Eq. 4.23, the dissipation rate of the turbulent kinetic energy (referred to as TKE in the literature) is estimated using the Hill and Clifford (1998) relationship for the dissipation range (range B, Fig. 2.2):

$$\varepsilon = \upsilon^3\,(\frac{7.4}{l_o})^4. \qquad 4.24$$

The contribution of humidity to C_T^2, typically one order of magnitude smaller than the contribution due to temperature, is neglected (Fig. 2.5).

The stability parameter for the structure parameter for temperature (C_T^2), and a normalized dissipation rate of turbulent kinetic energy, used for MOST, are defined as follows:

$$\Phi_{CT} = \frac{C_T^2\,(k\,z)^{2/3}}{T_*^2} \qquad 4.25$$

and $$\Phi_\varepsilon = \frac{\varepsilon\,k\,z}{u_*^3} \qquad 4.26$$

where T_* is the temperature scale for turbulence, u_* is the friction velocity (m s^{-1}), k is von Karman's constant ($\approx$ 0.41) and z is the height above the level at which the wind speed is 0 m s^{-1}. These relationships alone do not allow T_* and u_* to be determined. Semi-empirical relationships are used to determine Φ_{CT} and Φ_ε (Thiermann and Grassl 1992) where:

for $(z-d)/L < 0$, $$\Phi_{CT} = 4\beta_1\,(1 - 7\zeta + 75\zeta^2)^{-1/3} \qquad 4.27$$

for $(z-d)/L > 0$, $$\Phi_{CT} = 4\beta_1\,(1 + 7\zeta + 20\zeta^2)^{1/3} \qquad 4.28$$

for $(z-d)/L < 0$, $$\Phi_\varepsilon = (1 - 3\zeta)^{-1} - \zeta \qquad 4.29$$

and for $(z-d)/L > 0$, $$\Phi_\varepsilon = (1 + 4\zeta + 16\zeta^2)^{1/2} \qquad 4.30$$

where $$\zeta = (z-d)/L \qquad 4.31$$

is the stability parameter and

$$L = \frac{T \rho_{air} c_p u_*^2}{k g F_h} \qquad 2.40$$

is the Monin-Obukhov length (m), T is the air temperature (K), g is the acceleration of gravity (m s^{-2}) and β_1 is referred to as the Obukhov-Corrsin constant. A value of 0.86 for β_1 was used by Hill (1978). Sensible heat and momentum flux densities, where

$$F_h = -\rho_{air} c_p u_* T_* \qquad 4.32$$

and

$$\tau = \rho_a u_*^2 \qquad 2.34$$

(Eqs 2.34 and 2.26 respectively), are determined from u_* and T_* by combining Eqs 4.24 to 4.26 where:

$$u_*^2 = \upsilon^2 \cdot (\frac{7.4}{l_o})^{4/3} (k\,z)^{2/3} \Phi_\varepsilon^{2/3} \qquad 4.33$$

and

$$T_*^2 = C_T^2 \cdot (k\,z)^{2/3} \Phi_{CT}^{-1}. \qquad 4.34$$

Combining expressions for ζ, L, u_*^2 and T_*^2 (Eqs 4.31, 2.40, 4.33 and 4.34 respectively):

$$\zeta^2 \Phi_{CT} \Phi_\varepsilon^{-4/3} = C_T^2 \frac{z^2}{T^2} \cdot \frac{k^2 g^2 \rho_{air}^2 c_p^2}{\upsilon^4 (k\,z)^{4/3}} \cdot (\frac{l_o}{7.4})^{16/3}. \qquad 4.35$$

The right hand side of Eq. 4.35 is a function of beam height z, air temperature T (K), the inner scale of turbulence l_o and the structure parameter for temperature C_T^2. Other terms include the density of air ρ_{air}, the specific heat capacity of dry air c_p, von Karman constant (≈0.41), acceleration of gravity g and the viscosity of air υ.

Using the semi-empirical expressions for Φ_{CT} and Φ_ε (Eqs 4.27 to 4.30), and Eq. 4.35, it is possible to solve for L, u_*, and T_* using iteration. Hence, sensible heat flux density F_h may be calculated using Eq. 4.32 and momentum flux density calculated using Eq. 2.34. The iterative procedure is not entirely reflected in Fig. 4.4.

Finally, invoking the shortened energy balance, latent energy flux density may be calculated as a residual amount given measurements of net irradiance I_{net} and soil heat flux density F_{soil} (bottom part of Fig. 4.4) using:

$$L_v F_w = -I_{net} - F_h - F_{soil}. \qquad 4.36$$

4.3.5 Reference evaporation

Grass reference evaporation was calculated every two minutes using the Penman-Monteith method. The method used followed that of FAO 56 (Allen et al. 1998) for daily reference evaporation estimation. In spite of net irradiance and soil heat flux density measurements being available (Eq. 4.36), the FAO 56 method of estimating these was used for estimating reference evaporation:

$$L_v F_{w\,reference} = -\frac{\Delta \cdot r_a (I_{net} + F_{soil}) + \rho_{air} c_p\, vpd}{\gamma \cdot (r_a + r_c) + \Delta\, r_a} \qquad 4.37$$

where Δ (kPa °C^{-1}) is the slope of the saturation water vapour pressure *vs* temperature relationship, r_a (s m^{-1}) is the aerodynamic resistance (= 208 / (U + 0.01) where U is the horizontal wind speed in m s^{-1} and the offset of 0.01 m s^{-1} ensures a non-zero denominator), the soil heat flux density F_{soil} < 0 W m^{-2}

during daytime hours is taken as 0.1 of the estimated net irradiance I_{net}, ρ_{air} is the density of air (kg m^{-3}), c_p is the specific heat capacity of dry air at constant pressure (J kg^{-1} K^{-1}), *vpd* is the water vapour pressure deficit (kPa), γ (kPa °C^{-1}) is the psychrometric constant and r_c is the canopy resistance set to 70 s m^{-1} for grass reference evaporation (Allen et al. 1998).

4.3.6 Footprint estimation

A footprint describes the relative contribution of upwind surface sources to the measured flux density. The sources of the flux are at the surface - a combination of soil and vegetation surfaces usually - whereas for most measurement techniques, apart from the weighing lysimetric technique (Table 3.1), the flux density is measured at a height above the soil surface. Using notation similar to that used by Calder (1949) and Gash (1986), the relationship between flux density $F(x, z_m - d)$, sensible heat flux density for example, at distance x from the source and at measurement height z_m, for a surface with a zero plane displacement height d, and the footprint $f(x, z_m - d)$ is given by:

$$F(x, z_m - d) = \int_{-\infty}^{x} S(x) f(x, z_m - d)\, dx \qquad 4.38$$

where $S(x)$ is the source strength (W m^{-1} for sensible heat flux density footprints) at distance x. Most often, distance x is taken as the downwind fetch distance. The basis of the K-theory hypothesis upon which Eqs 4.1 and 4.2 and the BR method is based, is that the vertical eddy flux density can be represented as a gradient diffusion process. Using K-theory, the vertical diffusion of a passive scalar quantity of concentration C (usually in kg m^{-3}) with the eddy diffusivity K_z (also referred to as the exchange coefficient) in the vertical direction (m^2 s^{-1}) can be written as the so-called advection-diffusion equation where $\bar{u}(z)$ is the mean wind speed at height z:

$$\frac{\partial C}{\partial t} = \frac{\partial x}{\partial t} \cdot \frac{\partial C}{\partial x} = \bar{u}(z) \cdot \frac{\partial C}{\partial x} = \partial (K_z \cdot \frac{\partial C}{\partial z}) / \partial z. \qquad 4.39$$

For homogeneous terrain, and if there are no other sources or sinks, the horizontal concentration gradient of the scalar vanishes ($\partial C / \partial x = 0$) with the result that the vertical divergence of the flux of the scalar vanishes ($K_z \cdot \partial C / \partial z$ is constant with height).

An approximate solution to the advection-diffusion equation (Eq. 4.39) is given by Calder (1949) for an infinite crosswind line source of passive scalars using power expressions of height for wind speed and eddy diffusivity. Calder indicated that the solution was actually provided by Roberts (unpublished) [see Sutton (1953)]. Calder's work was the first description for the vertical diffusion of material released at ground level. Early work by Monin (1959) using a similarity approach to the diffusion of particles and research for neutral flow by Batchelor (1964) and Gifford (1961) for stratified flow was followed by Pasquill (1972) who introduced the concept of upwind "source area". Pasquill (1972) pointed out that: "measurements made at an elevated point may be accepted as representative of underlying patchy terrain only if the patchiness is predominantly small compared to the effective source area". Using a Gaussian (Fickian or normal) plume dispersion model, he quantified the dimensions of the source area and its influence on concentration for smooth and rough surfaces and for three stability classes. Pasquill and Smith (1983) noted that observations of passive plumes have confirmed that the Gaussian form is a satisfactory description for the crosswind distribution, in an ensemble sense. For the vertical distribution, the shape is not generally Gaussian but somewhere between Gaussian and exponential. Gash (1986) extended the approach of Pasquill (1972) by estimating the effect of a limited fetch on micrometeorological evaporation measurements assuming a uniform wind field. He favourably compared the 90 % fetch and consequent fetch to measurement height ratios using his assumption of constant wind field (between surface and measurement height) and the treatment by Dyer (1963) using empirical power functions of the vertical variation of wind speed and eddy diffusivity. Gryning et al. (1983) investigated dispersion from a continuous ground level source using a K-theory model and Gryning et al. (1987) used meteorological scaling parameters to develop a probability density function plume model to evaluate the source area. Applying the work of Pasquill (1972) and Gryning et al. (1987), Schmid and Oke (1990) developed a source area model to estimate the source area contributing to turbulent exchange in the surface layer above patchy terrain.

The estimation of the footprint of sensible heat and latent energy, and other fluxes, is an important application of micrometeorology to the fields of hydrology and boundary layer meteorology. Two basic types of models, Eulerian analytical (Horst and Weil (1992, 1994), for example) and Lagrangian stochastic dispersion models (Leclerc and Thurtell (1990), for example), have been used to calculate the footprint $f(x, z_m - d)$ and the flux density $F(x, z_m - d)$ at a height above the surface and a defined distance away from the source (Eq. 4.38). The Eulerian approach considers changes as they occur at a fixed point in the fluid whereas the Lagrangian approach considers changes which occur as a fluid particle is followed along its trajectory. The Eulerian analytic models are relatively simple with the Lagrangian models somewhat more complex. Hsieh et al. (2000) used a model based on similarity theory, dimensional analysis and Lagrangian stochastic dispersion model simulation output. Their model framework was based on relationships among parameters such as flux, fetch, atmospheric stability, surface roughness and measurement height. They developed an approximate analytic expression, analogous to that of Gash (1986). Gash (1986) used the solution to the advection-diffusion equation, in a neutral atmosphere, provided by Calder (1952). For a given surface flux density S_o, Gash (1986) showed that the flux density $F(x, z_m)$ at a distance x (m) [where x is the down-wind fetch requirement to achieve the desired normalised flux density], and at measurement height z_m from the surface flux, decreases exponentially with increasing distance x. Intuitively, an exponential decrease in the flux density with increasing downwind fetch distance is not unexpected. Gash (1986) showed:

$$F(x, z_m) = S_o \exp\left(-\frac{U_a z_m}{k\, u_*\, x}\right),$$

where U_a is the average wind speed between the height $z_o + d$ and the measurement height z_m:

$$U_a = \frac{\int_{z_o+d}^{z_m} u\, dz}{\int_{z_o+d}^{z_m} dz} \qquad 4.40$$

where

$$u = \frac{u_*}{k} \ln \frac{z - d}{z_o} \qquad 2.15$$

is the log-wind profile equation for neutral stability as a function of vertical height z above the soil surface. Note that at height $z = z_o + d$, the wind speed is 0 m s^{-1} according to the neutral wind profile equation and hence the requirement that $z \geq d + z_o$. Combining Eqs 4.40 and 2.15 and assuming that the friction velocity u_* is constant with height z:

$$U_* = \frac{(\frac{u_*}{k}) \int_{z_o+d}^{z_m} \ln \frac{z-d}{z_o} dz}{z_m - (z_o + d)}.$$

Making the two substitutions $z' = \frac{z-d}{z_o}$ and $y = \ln z'$:

$$dz' = dz / z_o$$

and therefore

$$\ln \frac{z-d}{z_o} dz = z_o \ln z' dz'$$

where

$$dz' = z' dy.$$

Hence:

$$\ln \frac{z-d}{z_o} dz = y\, z_o\, dz' = y\, z_o\, z'\, dy = y\, z_o\, e^y\, dy$$

so that

$$U_* = \frac{(\frac{u_*}{k}) \int_{z_o+d}^{z_m} \ln \frac{z-d}{z_o} dz}{z_m - (z_o + d)} = \frac{(\frac{z_o u_*}{k}) \int_{y=0}^{y_{z_m}} y\, e^y\, dy}{z_m - (z_o + d)}$$

assuming that z_o is constant with height.

Integrating by parts:

$$U_* = \frac{(\frac{z_o u_*}{k}) \, [y \frac{d}{dy} e^y - e^y \frac{d}{dy} y] \,\Big|_{y=0}^{y=y_m}}{z_m - (z_o + d)}$$

or

$$U_* = \frac{(\frac{z_o u_*}{k}) \, e^y \, [y - 1] \,\Big|_{y=0}^{y=y_m}}{z_m - (z_o + d)} = \frac{(\frac{z_o u_*}{k}) \, z' [\ln z' - 1] \,\Big|_{z'=1}^{z'=(z_m - d)/z_o}}{z_m - (z_o + d)}.$$

Hence

$$U_* = \frac{(\frac{z_o u_*}{k}) [\frac{(z_m - d)}{z_o} (\ln \frac{z_m - d}{z_o} - 1) - (-1)]}{z_m - (z_o + d)} = \frac{(\frac{z_o u_*}{k}) (\frac{z_m - d}{z_o}) (\ln \frac{z_m - d}{z_o} - 1 + \frac{z_o}{z_m - d})}{z_m - (z_o + d)}.$$

or

$$U_* = (\frac{u_*}{k}) (\frac{z_m - d}{z_m - (z_o + d)}) (\ln \frac{z_m - d}{z_o} - 1 + \frac{z_o}{z_m - d}). \qquad 4.41$$

Hsieh et al. (2000) used an equation similar in form but assumed that $d << z_m$ and $z_o + d << z_m$ and defined:

$$U_* = (\frac{u_*}{k}) \, (\ln \frac{z_m}{z_o} - 1 + \frac{z_o}{z_m}). \qquad 4.42$$

If d and $z_o + d$ is not ignored relative to z_m, then

$$U_* = (\frac{u_*}{k}) (\frac{z_m}{z_m - z_o}) (\ln \frac{z_m}{z_o} - 1 + \frac{z_o}{z_m}).$$

For their work using potatoes, a relatively short crop, ignoring d and z_o relative to z_m may result in negligible error for measurement heights about 2 m or more. However, for taller vegetation, d and z_o cannot be ignored.

Their model involved redefining a length scale, z_u (m), for which:

$$z_u = z_m \cdot [\ln(\frac{z_m}{z_o}) - 1 + \frac{z_o}{z_m}]$$

Extending this to a surface with a zero displacement d and surface roughness z_o, and incorporating the term $z_m / (z_m - z_o)$ which Hsieh et al. (2000) assumed sufficiently close to 1, the following more exact equation defines a new length scale z_u:

$$z_u = (z_m - d) \cdot \frac{z_m - d}{z_m - (z_o + d)} \cdot [\ln \frac{(z_m - d)}{z_o} - 1 + \frac{z_o}{z_m - d}] \qquad 4.43$$

Using the outputs from the Lagrangian model of Thomson (1987) for a range of stability conditions, Hsieh et al. (2000) expressed $x/|L|$, the horizontal distance to the MO length, as a function of their similarity parameters D and P, the ratio of the length scale z_u to L and the ratio F/S_o:

$$x/|L| = \frac{-1}{k^2 \ln(F / S_o)} \cdot D \cdot (z_u / |L|)^P \qquad 4.44$$

where $D = 0.28$ and $P = 0.59$ for unstable conditions,

$D = 0.97$ and $P = 1$ for near neutral and neutral conditions, 4.45

and $D = 2.44$ and $P = 1.33$ for stable conditions.

Hence, to estimate the horizontal distance x for which the flux density F at measurement height to surface flux density S_o ratio is 0.9, or setting $F / S_o = 0.9$, rearranging and dividing Eq. 4.44 by z_m, the 90 % fetch to measurement height ratio is given by:

$$x / z_m = \frac{9.491}{k^2 z_m} \cdot D z_u^P |L|^{1-P}. \qquad 4.46$$

Hsieh et al. (2000) used a restricted condition for near neutral conditions, viz., $|z_u / L| < 0.04$ ($\approx |z / L| < 0.02$).

Following Hsieh et al. (2000), the cumulative fraction of the flux density F to surface source flux density S_o ratio, at distance x from the source and at an effective height of $z_m - d$ from the soil surface, can be estimated using:

$$\frac{F(x, z_m - d)}{S_o} = \exp(\frac{-1}{k^2 x} \cdot D z_u^P |L|^{1-P}) \qquad 4.47$$

and the footprint of the surface flux density using

$$f(x, z_m - d) = \frac{1}{k^2\, x^2} \cdot D\, z_u^P\, |L|^{1-P} \exp\left(\frac{-1}{k^2\, x} \cdot D\, z_u^P\, |L|^{1-P}\right). \qquad 4.48$$

Using an approach similar to Calder (1952) and Gash (1986), they also showed that the peak location of the footprint, x_{peak} (m), can be calculated using:

$$x_{peak} = \frac{D\, z_u^P\, |L|^{1-P}}{2\, k^2}. \qquad 4.49$$

The Hsieh et al. (2000) model is analytically based, combines the results from a Lagrangian stochastic model and uses dimensional analysis. Their model results were in good agreement with those calculated by detailed Eulerian and Lagrangian models. They used EC latent energy flux density measurements collected along a transect as confirmation of the model estimates.

For convenience, Eqs 4.47 and 4.49, for calculation the ratio of the flux density $F(x, z_m - d)$ to surface source flux density S_o, can be written as:

$$\frac{F(x, z_m - d)}{S_o} = \exp\left(\frac{-2}{x} \cdot x_{peak}\right). \qquad 4.50$$

Combining Eqs 4.48 and 4.49, the footprint may be determined using

$$f(x, z_m - d) = \frac{2}{x^2} \cdot x_{peak} \exp\left(\frac{-2}{x} \cdot x_{peak}\right) \qquad 4.51$$

and combining Eqs 4.46 and 4.49, the 90 % fetch to measurement height ratio determined using:

$$x / z_m = \frac{2 \times 9.491}{z_m} \cdot x_{peak}. \qquad 4.52$$

4.4 Material and methods

4.4.1 Bowen ratio laboratory measurements

The BR system is used for measurement of sensible heat and latent energy flux density. It would be appropriate to compare BR-measured sensible heat flux density against that measured using the SLS system. Bowen ratio systems are critically dependent on the profile water vapour pressure and air temperature profile difference measurements. The most-commonly used BR system uses a cooled dew point mirror for water vapour pressure measurements. However the limitations of this sensor include the cost of the Dew-10 sensor (General Eastern Instruments, Wilmington, Massachusetts, USA) commonly used and the requirement that the electronic bias of the sensor needs to be adjusted frequently - usually weekly. The first BR system used in this study did not function well. The cooled mirror consistently measured negative dew point temperatures. The system was removed from the field and tested in the laboratory.

In the laboratory, a reference dew point generator (LI610, Li-Cor Inc., Lincoln, Nebraska, USA), controlled by a Campbell 21X datalogger, was used to obtain simultaneous measurements of water vapour pressure from both sensors. The datalogger controlled the dew point generator to increment the dew point temperature generated in an airstream. Dew points ranged between 0 °C and a few degrees below room temperature after which the datalogger reset the dew point to 0 °C. In this way, unattended measurements were performed. The Vaisala (Helsinki, Finland) HMP35C sensor was replaced by a Vaisala CS500 air temperature and relative humidity sensor and the methodology repeated. The procedure was repeated by replacing the Vaisala CS500 with a new Dew-10 dew point sensor.

4.4.2 Bowen ratio field measurements

Three BR systems, modified after the 023A system of Campbell Scientific Inc. and connected to a Campbell 21X datalogger (Fig. 3.1), were used to measure air temperature and water vapour pressure profile differences between heights of 1.55 and 2.96 m above the soil surface. The first system used a HMP45C Vaisala air temperature and relative humidity sensor, the second a cooled mirror Dew-10 hygrometer and the third system used a CS500 Vaisala air temperature and relative humidity sensor.

Each Vaisala sensor was sealed in a chamber. Unlike the Dew-10 chambers, the chambers were heavily insulated using layers of mirror tape to dampen sudden changes in temperature. Tubing in the vicinity of the chamber was covered with adhesive aluminium tape in an attempt to further reduce temperature differences between the sensor chip and the airstream. Measurements were performed every 1 s and averages calculated every 20 min. Differential voltages corresponding to the HMP35C or HMP45C air temperature and relative humidity were performed. The CS500 voltages were single-ended, as recommended by the manufacturers. Every 1 s, the airstream atmospheric water vapour pressure was calculated using the CS500 temperature and relative humidity measurements. The Bev-a-line (Cole-Parmer, Vernon Hills, Illinois, USA) tubing used for the water vapour pressure measurements was as short as possible to minimise the transport time of the air to the sensor. Furthermore, the filter cover of the Vaisala sensors was removed. The inlet filter at each of the two intake positions was however retained for both of the BR Vaisala systems.

Air temperature was measured at two levels using 75-µm type-E thermocouples. At each level, a parallel combination of 75-µm thermocouples was used. Extra insulation was used to cover the thermocouple connectors at the thermocouple join. Extra precautions were taken to cover and thermally insulate the point at which the thermocouple wires were connected to the datalogger. The thermocouples were regularly inspected for damage, cleanliness, insects and cobwebs.

For measuring the remaining components of the energy balance, three Q*7 (REBS, Seattle, Washington, USA) net radiometers placed at 2 m above the soil surface were used to measure net irradiance. Seven soil heat flux plates (model HFT-3, REBS) were used to measure soil heat flux density at a depth of 80 mm and a system of parallel thermocouples at depths of 20 and 60 mm used to calculate the soil heat flux density stored above the plates (Tanner 1960). Volumetric soil water content in the first 60 mm of the surface was measured using a frequency domain reflectometer (ThetaProbe, model ML2x, Delta-T Devices, Cambridge, UK) and a 615 soil reflectometer (Campbell Scientific). Most of these sensors were connected to a Campbell CR7X datalogger and transferred to a CR23X datalogger after the 2003 accidental fire. Measurements were every 1 s and averages obtained every 2 min which were in turn used to calculate 20-min averages for the BR calculations. The net radiometers, soil heat flux plates, infrared thermometers for canopy temperature (model IRTS-P, Apogee Instrument Inc., Logan, USA), and other EC sensors were positioned approximately midway between the transmitter and receiver units of the SLS40-A scintillometer (Fig. 3.1).

4.4.3 Surface renewal measurements

For the SR method, we used several unshielded type-E thermocouples (75-μm diameter) to measure air temperature, placed at heights of 0.5, 0.8, 1.0 and 1.5 m above the canopy surface. Each sensor consisted of a pair of thermocouples in parallel. Some of the thermocouples were connected to a Campbell CR10X datalogger that also had a reference thermistor for thermocouple measurements. The remaining thermocouples were connected to a CR23X datalogger. The thermocouples were pointed into the predominant wind direction which occurred during daylight hours. Measurements were made every 0.125 s (equivalent to a frequency of 8 Hz) and then lagged by 0.125 s and 0.25 s before forming the second, third and fifth order temperature moments required by the Van Atta (1977) approach for SR analysis (Eqs 4.12 to 4.15) and then these were averaged every two minutes. Since measurements from a number of thermocouples were stored in one datalogger, it was necessary to split the data so that each data file corresponded to data from just one thermocouple. For this purpose, the Split program, part of PC208 (version 3.08) or LoggerNet 2.1, both from Campbell Scientific, was used.

Software calculations, post-data collection, were used to calculate two-minute SR sensible heat flux densities using the Van Atta (1977) approach. For this purpose, QuickBASIC 4.0, under MS-DOS, was used to modify and compile a program used to solve for the real roots of a cubic equation (Eq. 4.12). Following the data split, the data file, for the 0.8 m height say, surfren.exe QuickBASIC program was executed. The information file surfren.fac contains information required when executing the surfren.exe program (Table 4.2). The required parameters are self-explanatory. The program requires two versions of the data file. For example if surfre08.dat is the data file for the 0.8 m height, the comma separated value (csv) file surfre08.csv must also exist in the subdirectory c:\surfren. Following successful execution of the program, the file, in this example, surfre08.out is created (or overwritten if it already exists).

Table 4.2 The parameters required for the execution of the SR surfren.exe program together with some example specifications

Parameter	Specification	Explanation
path	c:\surfren\	Subdirectory for files
file	surfree08	Data file names
alpha	1	Set to 1 for grassland canopies
rr	.5	Not used
z	0.8	Height of measurements
DRn	9.17	An energy balance parameter (not used)
NRn	11.25	An energy balance parameter (not used)
G	36.7	An energy balance parameter (not used)
Z_G	.05	An energy balance parameter (not used)
Cv	2.0	Not used

This file may be opened in Excel, specifying that it is comma delineated. The file contains the values for a, $s + l$ and the sensible heat flux density (Eq. 4.10) for each 2-min time period. The 2-min SR sensible heat flux density measurements were then averaged to 20 min, 30 min or daily.

4.4.4 Eddy covariance measurements

Adjacent to the automatic weather station, a three-dimensional sonic anemometer (SWS-211/3V, Applied Technologies, Boulder, USA), referred to as the ECAT system (Fig. 3.1), was used as an EC system to measure the sensible heat flux density at a height of 1.45 m above the soil surface. Late in the study, the measurement height was increased to a height above soil surface of 2.12 m (Table 3.2). This anemometer, with a 100-mm sonic path length, was connected to a digital to analogue converter that then connected to a 21X datalogger (Campbell Scientific, Logan, USA). Measurements of the three components of wind velocity, u, v, w in the x, y and z directions respectively and sonic temperatures T were performed every 0.1 s (frequency of 10 Hz). Following the accidental fire (day of year 227, 2003), the 21X data logger was replaced by a Campbell CR23X datalogger and a replacement three-D sonic anemometer was used (same model). The sonic anemometer measurements were processed on-line and the two-min covariance between the w and T (for determining sensible heat flux density F_h) and the covariance between w and the horizontal wind speed $U = \sqrt{u^2 + v^2}$ (for determining momentum flux density τ) were calculated (Eqs 4.18 and 4.19 using $\rho_{air}\ c_p = 1136.3$ J m^{-3} K^{-1} and $\rho_{air} = 1.12$ kg m^{-3}). The two-minute averages of u, v, w and sonic temperature T and wind direction θ (= arctan v / u) were also stored. For a limited time, net irradiance (model Q*7 net radiometer), vertical wind speed and air temperature were sampled every 0.2 s using a Campbell CA27 one-dimensional sonic anemometer and fine wire thermocouple, respectively, and data processed using a Campbell 21X datalogger and two-minute averages, standard deviations and covariances stored for further data analysis. Data rejection rules were fairly simple: sometimes, usually whenever there was condensation, covariances of -99999 were excluded. Missing values and also periods when incorrect sonic temperatures approaching 50 °C were also used to exclude sensible heat data. These incorrect values were caused by dirt on the sonic transducers or faulty transducers. nighttime EC measurements were often unreliable due to condensation or mist affecting the acoustic signal.

Calibration of the ECAT system and its replacement was performed by placing the 3D system in a box for which each component of the wind speed was 0 m s^{-1}. The air temperature and relative humidity, required for accurate speed of sound estimation (from which the sonic temperature is calculated), was independently measured using averaging thermocouples and a Vaisala CS500 air temperature and relative humidity sensor placed inside the box.

A fast responding water vapour pressure and carbon dioxide concentration sensor (LI-7500, LI-COR Inc., Lincoln, USA) and a second Applied Technologies 3-D sonic anemometer (model SATI/3V) with a sonic path length of 150 mm were used to calculate the following flux densities using the EC technique: sensible heat, latent energy, momentum, and carbon dioxide. This system is referred to as ECopen (Fig. 3.1).

4.4.5 Scintillometer measurements

The procedures used for two-minute SLS sensible heat flux density measurements are described in Chapter 3. The beam path length was kept at 101 m and the beam height varied between 1.5 and 1.65 m except near the end of the study. For a limited time, the influence of beam height and beam angle on the sensible heat flux density was investigated. A beam angle of 22° for the non-horizontal beam measurements was used. For the variable beam height measurements, effective beam heights of between 0.5 m and about 1.5 m were used (Table 3.2). The canopy height was measured regularly and this height was used to calculate $d + z_o$ where it was assumed that the zero plane displacement height $d \approx 0.67\ h$ and the roughness length $z_o \approx 0.1\ h$. The effective beam height input, which is required for SLS measurements, was set at beam height above the soil surface minus $d + z_o$.

For some of the time, the voltage range was altered (Fig. 3.9) due to low voltage signals. The transmitter and receiver units required little attention apart from inspecting for dirt and cobwebs obscuring the beam and occasional realignment following storms. The cables had to be replaced twice - once due to the accidental fire and a second time accidentally when the grass was cut (Table 3.2).

4.4.6 Reference evaporation estimation

The procedures for the estimation of grass reference evaporation are described by Allen et al. (1998). The calculations (Eq. 4.37) were performed in Excel and cross-checked against those used with real-time estimates of reference evaporation (Campbell Scientific Application note, undated). Grass reference evaporation was estimated every two minutes using these procedures. While the AWS system was available, all reference evaporation estimates were based on the AWS data. After the system was removed, data from the same model sensors were used except that for solar irradiance, a Kipp and Zonen CM3 thermopile sensor was used. For some of the time, horizontal wind speed from the 3-D sonic anemometer was used. Water vapour pressure was measured using a Vaisala CS500 air temperature and relative humidity sensor from the AWS system, or by one of the following humidity sensors: another CS500, a Vaisala HMP35C or HMP45C air temperature and relative humidity sensor or a Dew-10 cooled dew point hygrometer.

4.4.7 Footprint analyses

The model of Hsieh et al. (2000) relies on the definition of a length scale z_u for determining the footprints. Their definition was adapted to include a surface with a zero plane displacement height d and a surface roughness z_o and also included the factor:

$$\frac{z_m - d}{z_m - (z_o + d)}$$

which they assumed sufficiently close to 1 (- see Eq. 4.43). The peak location of the footprint x_{peak} was calculated using Eq. 4.49, the ratio of the flux density $F(x, z_m - d) / S_o$ ratio calculated using Eq. 4.50, the footprint calculated using Eq. 4.51, and the 90 % height to fetch ratio calculated using Eq. 4.52. In the case of the BR system, the measurement height for footprint calculations was taken to be the geometric mean of the upper and lower measurement heights for unstable conditions, as recommended by Horst (1999). Effectively then, as far as footprints are concerned, the Bowen ratio system was at a height of $\sqrt{1.55 \times 2.96}\ \mathrm{m} = 2.14\ \mathrm{m}$ which is almost the same height as the ECAT system after day of year 362, 2003 (Table 3.2).

4.5 Results and discussion

Before the results of the measurements for the various methods could be compared, a study was undertaken to investigate the replacement of the cooled dew point mirror with a Vaisala sensor. Furthermore, the results of the wind direction and footprint analyses needs to be known before conclusions can be made about the various measurement techniques.

4.5.1 Bowen ratio measurements

The BR method requires a humidity sensor that has a resolution of ± 0.01 kPa or better. The stability of the Dew-10 dew point measurements is about 0.05 °C, resulting in a water vapour pressure resolution within 0.01 kPa for chamber temperatures less than 26 °C. Between 26 °C and 40 °C, dew point measurements within 0.05 °C results in a water vapour pressure resolution within 0.02 kPa. The limitation in the measurement of the profile difference in air temperature is the datalogger temperature resolution of ± 0.006 °C. This is normally achievable using unshielded 75-µm type-E thermocouples.

4.5.1.1 Error analysis of Vaisala HMP45C and CS500 water vapour pressure measurements

The error in water vapour pressure for a dew point sensor is only dependent on the random error and bias due to the measured dew point. The one disadvantage of using a relative humidity sensor, such as a Vaisala air temperature and relative humidity sensor, compared to a dew point sensor, is that the calculated water vapour pressure depends on the measurement of temperature and relative humidity from two different spatially-separated sensors both of which have their own random error and bias; the relative humidity and air temperature sensors cannot make their measurements at exactly the same position of the airstream. Ideally, when calculating the water vapour pressure from relative humidity measured using a Vaisala chip, the temperature of the chip needs to be known and not the temperature of the airstream. Usually however, the two sensors are located in very close proximity - millimetres apart. Also, the humidity chamber could be insulated but this alone may not eliminate all differences in temperature between the chip and the airstream. The airstream-chip temperature difference should decrease with increased flow rate.

The manufacturers state that the accuracy of the temperature sensor of the HMP35C or HMP45C sensor varies with temperature and is ± 0.2 °C at 20 °C and the humidity sensor error is ± 2 % RH where the % unit is in relative humidity units and not a percentage of the measured relative humidity (for RH between 0 and 90 %). For the CS500, the error in humidity measurements is ± 3 % RH and the error for the temperature sensor also varies with temperature and is ± 0.46 °C at 20 °C. Vaisala do not however give any indication of the resolution limits for their sensors. The datalogger resolution for the water vapour pressure measurements is 0.0001 kPa. The limitation of water vapour pressure measurements is the stability of the measurements. The manufacturers present a graph showing the error in the temperature sensor as a function of temperature. Based on this information, the error in temperature, δT (°C) for a Vaisala HMP45C is given by:

for $T \geq 20$ °C $\qquad\qquad$ $\delta T = 0.2 + 0.1\,(T - 20)/20$

and for $T \leq 20$ °C $\qquad\qquad$ $\delta T = 0.2 + 0.1\,(20 - T)/20$

and that for a CS500 for $T \geq 0$ °C is given by:

$$\delta T = 0.3 + 0.008\,T.$$

These relationships are depicted in Fig. 4.5. So between 0 and 40 °C, the error in temperature for the CS500 varies linearly between ±0.3 to ±0.62 °C respectively compared to between ±0.2 and ±0.3 °C for the HMP45C for the same temperature range but with the minimum error being ±0.2 at 20 °C. Clearly then, the HMP45C temperature has a more accurate temperature sensor than that used in the CS500.

Since the water vapour pressure is calculated using:

$$e = RH \times e_s\,/100,$$

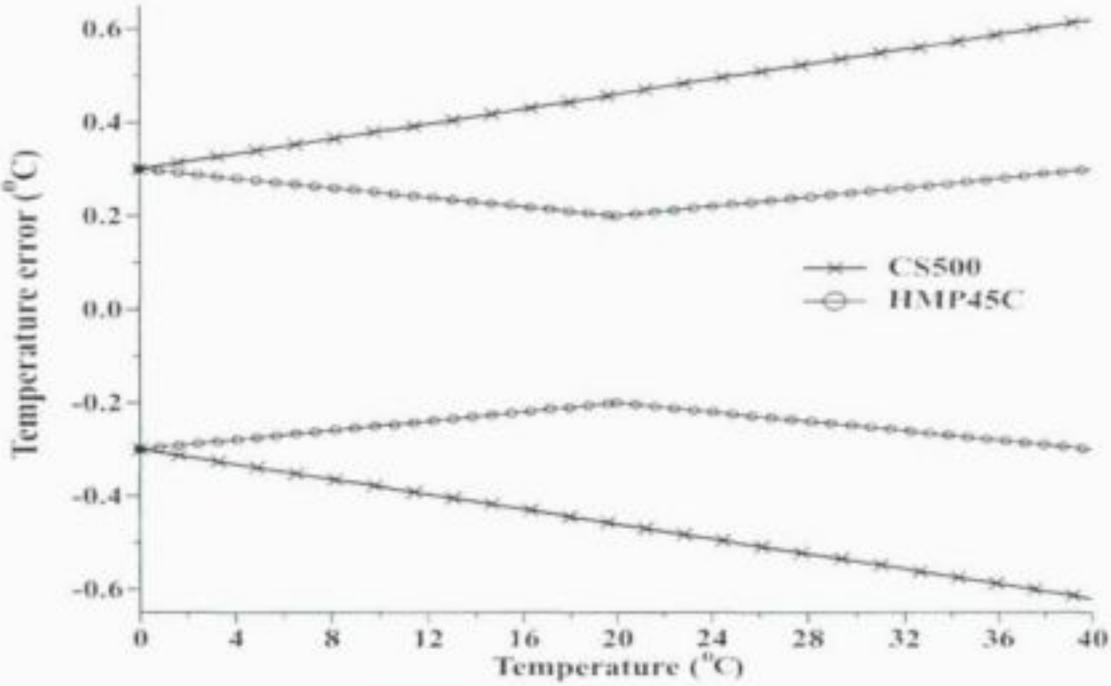

Fig. 4.5 The error in temperature (°C) for the two Vaisala relative humidity and temperature sensors. The error for any given temperature is between the upper and lower corresponding set of sensor curves. So for example, at 20 °C, the error for the CS500 is ± 0.46 °C and ± 0.2 °C for the HMP45C

the error in water vapour pressure, δe, may be estimated using:

$$\delta e = \sqrt{(\partial e / \partial RH)^2 \cdot \delta RH^2 + (\partial e / \partial e_s)^2 \cdot \delta e_s^2}$$

where using rules of calculus, $\partial e / \partial RH = e_s / 100$ and $\partial e / \partial e_s = RH / 100$ and where $\delta e_s = (\partial e_s / \partial T) \cdot \delta T = \Delta \cdot \delta T$ (kPa) where Δ (kPa °C^{-1}) is the slope of the saturation water vapour pressure *vs* temperature relationship:

$$\Delta = 409802862 \cdot e_s / (2373 + T)^2$$

where T (°C) is the air temperature and

$$e_s = 06108 \cdot \exp[172694\, T / (2373 + T)].$$

Finally, then,

$$\delta e = \sqrt{(e_s / 100)^2 \cdot \delta RH^2 + (RH / 100)^2 \cdot \Delta^2 \cdot \delta T^2}.$$

Clearly then, the error in water vapour pressure is temperature dependent since both e_s and Δ are temperature dependent and the information provided by the manufacturer shows that δT is also temperature dependent.

Also, the relative humidity and the error in relative humidity determine the error in water vapour pressure. For the HMP45C sensor:

$$\delta e_{HMP45C} = \sqrt{(e_s / 100)^2 \cdot \delta RH^2 + (RH / 100)^2 \cdot \Delta^2 \cdot (0.2 + 0.1 \cdot (T - 20) / 20)^2}$$

for $T \geq 20\,^{\circ}C$ or for $T < 20\,^{\circ}C$

$$\delta e_{HMP45C} = \sqrt{(e_s / 100)^2 \cdot \delta RH^2 + (RH / 100)^2 \cdot \Delta^2 \cdot (0.2 + 0.1 \cdot (20 - T) / 20)^2}$$

and for the CS500 sensor:

$$\delta e_{CS500} = \sqrt{(e_s / 100)^2 \cdot \delta RH^2 + (RH / 100)^2 \cdot \Delta^2 \cdot (0.3 + 0.008 \cdot T)^2}$$

for $T \geq 0\,^{\circ}C$.

Using the manufacturer's recommendation of $\delta RH = \pm 2$ % for the HMP45C and $\delta RH = \pm 3$ % for the CS500, δe was determined as a function of temperature between 5 and 50 °C and relative humidity between 10 and 90 %. The calculations show (Fig. 4.6) that the error in absolute water vapour pressure exceeds the limits required by the BR technique. However, these errors should be regarded as the maximum error in water vapour pressure. Typically in summer, air temperature on hot days may vary from 15 to 40 °C and this temperature variation may be typical of that experienced by the air in the hygrometer block. If this is the case, then error for the HMP45C water vapour pressure measurements may range from ± 0.03 kPa in the early morning to ± 0.15 kPa (for a relative humidity of 50 %) at 14h00 (Fig 4.6b). These errors exceed the ± 0.01 kPa resolution value of the Dew-10 dew point hygrometer. The errors for the CS500 are larger, particularly for high relative humidities and temperatures exceeding 30 °C (Fig. 4.6b bottom).

One option to reduce the error shown in Fig 4.6 is to reduce temperature to below 30 °C. While it may be possible to reduce enclosure temperature, which contributes to the hygrometer block temperature, it is not possible to reduce the temperature of the air flowing through the block.

If the same Vaisala sensor is used for water vapour pressure measurements at both heights, and if it can be assumed that the errors shown in Fig. 4.6 are systematic, then the errors existing for measurements at both heights would tend to cancel. However, laboratory proof of this would be required before the sensor can be used in the field for BR measurements. Furthermore, if the temperature of the airstream for the two levels is different, as might be expected for sensible heat flux density directed away from the surface, the errors may not cancel due to the non-linear nature of the error as a function of temperature.

4.5.1.2 Use of Vaisala sensors for water vapour pressure profile difference measurements in the laboratory

In the laboratory, profile differences in water vapour pressure were created using a LI610 dew point generator. The differences were measured in three separate experiments using a Dew-10 cooled mirror hygrometer, a Vaisala HMP35C and a Vaisala CS500 humitter. The Vaisala CS500 sensor, much cheaper than the Dew-10 dew point sensor and the HMP35C, had the greatest variability in water vapour pressure difference measurements (Fig. 4.7a). The Dew-10 dew point mirror had the smallest error mean square (Fig. 4.7c) but is more expensive and suffers from the problems of maintenance of a stable bias as mentioned previously. The 2003 field measurements of water vapour pressure using the Dew-10 could not be relied upon.

The Vaisala HMP35C sensor (now replaced by the HMP45C) seemed the most promising in terms of an alternative to the Dew-10 cooled dew point mirror. The ability of the HMP35C to measure very

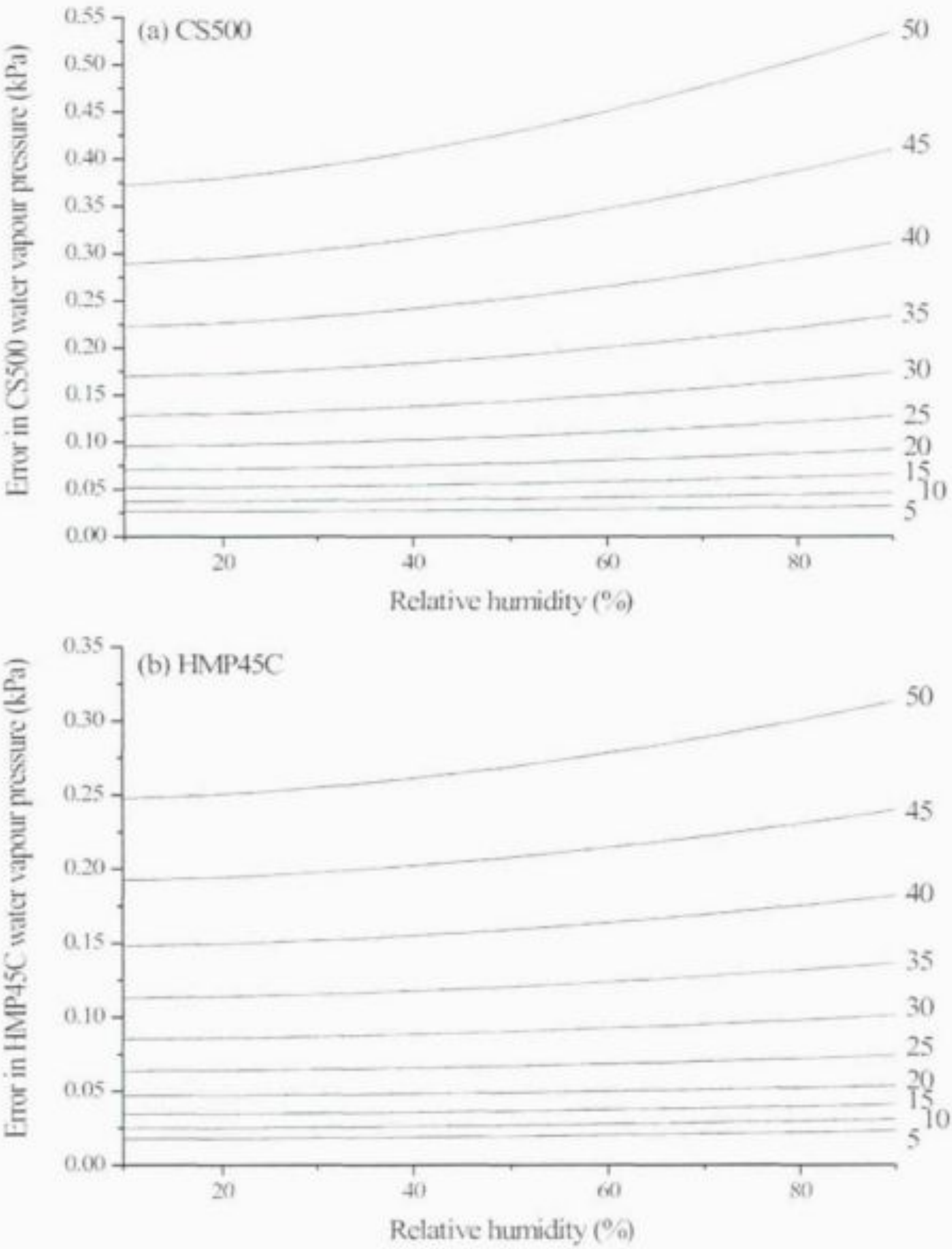

Fig. 4.6 (a) Top: the error in the water vapour pressure for a Vaisala CS500 sensor as a function of relative humidity and air temperature based on the manufacturers specification of an error of ± 3 % RH for RH between 10 and 90 % and a temperature error that varies with temperature and is a minimum of ± 0.3 °C at 0 °C and a maximum of ± 0.62 °C at 40 °;
(b) bottom: the error in the water vapour pressure for a Vaisala HMP45C sensor as a function of relative humidity and air temperature based on the manufacturers specification of an error of ± 2 % RH for RH between 10 and 90 % and a temperature error that varies with temperature and is a minimum ± 0.2 °C at 20 °C and a maximum of ± 0.3 °C at 0 and 40 °C

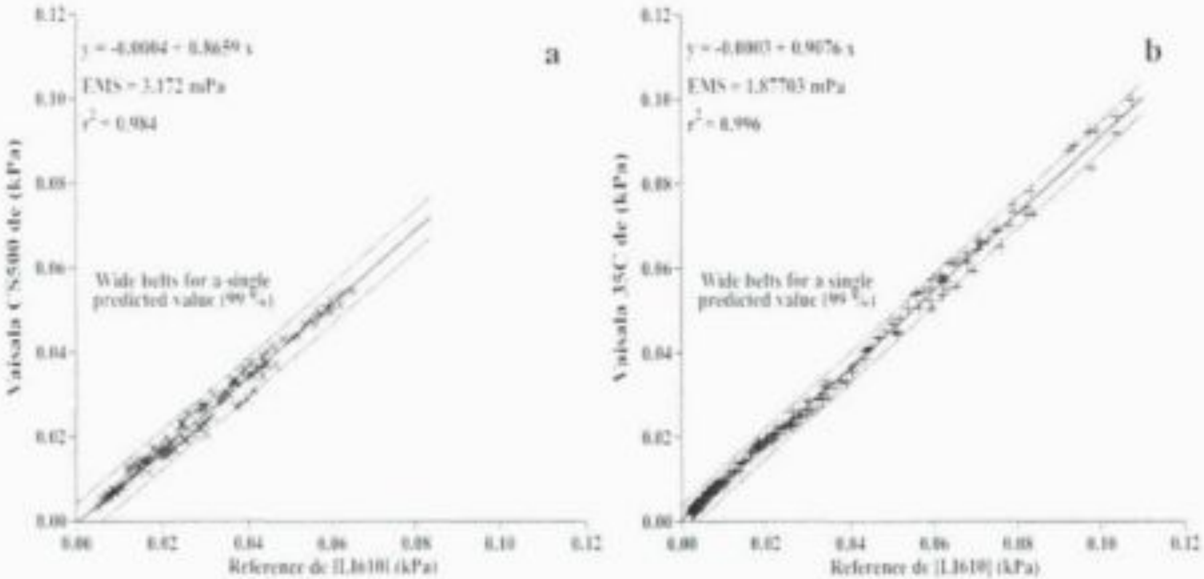

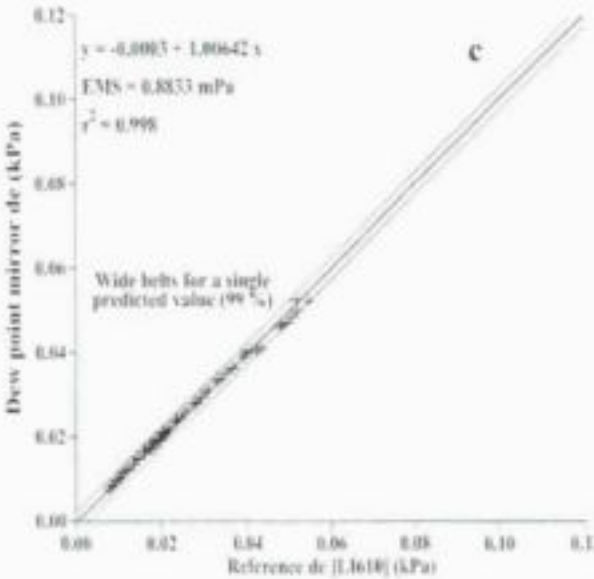

Fig. 4.7 Reference water vapour pressure differences in kPa (*de*) measured using the LI610 Dewpoint Generator compared with the measured water vapour differences (*de*) using:
(a) Vaisala CS500 sensor air temperature and relative humidity sensor;
(b) Vaisala HMP35C air temperature and relative humidity sensor;
(c) Dew-10 cooled dew point mirror

small water vapour pressure differences appears good in this laboratory experiment in which the air temperature had a much reduced diurnal range compared to that that may be experienced in the field. The slope (Fig. 4.7b) is close to 1 but somewhat lower than that for the Dew-10 dew point mirror (Fig. 4.7c). Flow rates using the laboratory calibration procedure were limited by the dew point generator and this may explain the slope values of less than 1.

Of particular note is that in spite of the error in water vapour pressure shown in Fig. 4.5, the Vaisala sensors are capable of resolving the water vapour pressure differences to within 0.005 kPa or better, when compared to the dew point generator, under fairly temperature-controlled conditions.

4.5.1.3 Field use of a Vaisala sensor for water vapour pressure profile difference measurements

Water vapour pressure profile difference comparisons were made in the field. In this section, we report on comparisons between profile water vapour pressure differences measured using a conventional cooled mirror hygrometer (the Dew-10 hygrometer) and HMP45C and CS500 Vaisala sensors. The cooled mirror sensor is more expensive and requires a bias adjustment for the sensor to converge on the correct dew point. The Vaisala sensors require no attention. The calculated BR sensible heat and latent energy flux density comparisons with EC and SLS estimates of sensible heat and latent energy are reported on in Section 4.5.4.6.

In the first field experiment, two Vaisala sensors (HMP45C and CS500) were each placed in individual humidity chambers. The outlet of the one chamber was connected to the inlet of the other. The inlet of the first chamber was connected to the inlet air stream from the mixing bottles and the outlet of the second bottle was connected to the inlet to the pump. In this fashion, the two sensors measured the water vapour pressure and air temperature of the same air stream. Water vapour pressure and Vaisala temperature were measured every 1 s. At the end of each 20-min period, the mean and standard deviation of all water vapour pressures and temperatures were stored.

Measurements were obtained over a period of about a week (Fig. 4.8). There was very good agreement between the water vapour pressure profile differences *de* (Fig. 4.8 bottom) during the daytime and during the nighttime. Negative *de* measurements corresponded to latent energy directed toward the surface. Dew occurred during the measurement period, corresponding to the negative *de* measurements shown. The experiment was repeated (data not shown) for a period of a month with similar results.

The standard deviation in the water vapour pressure difference is calculated as the square root of the sum of squares of the standard deviation of the upper level and lower level water vapour pressures and is shown in Fig. 4.8 middle for both the CS500 and HMP45C sensors for all or part of the period day of year 9 to 14, 2004. There is good agreement between the standard deviations for the two Vaisala sensors with the standard deviations for both sensors swamping the mean determined for each 20-min interval (compare Figs 4.8 bottom and middle). The standard deviations agreed with each other (Fig. 4.8 middle) showing greatest standard deviations during the daytime hours (Fig. 4.8 top). The spikes usually correspond to sunset. So in spite of the greater absolute error in water vapour pressure measurements for the CS500, according to the manufacturer, there appears to be little apparent measurement advantage in the use of the more expensive HMP45C sensor for the purpose of determining water vapour pressure profile differences. The one advantage of the HMP45C however is that it does have a switch control option to turn the sensor on using datalogger control just before measurements and then immediately off. This disadvantage is obviated when using a CR10X and CR23X that can provide for switch control of the CS500. The CS500 does not have a built-in switch control option and this results in an increased current drain if the sensor is continuously powered. However, in terms of price, the CS500 is significantly cheaper ($335 *vs* $545 for the HMP45C, Jan 2004 prices) and compared to $730 for the Dew-10 sensor).

In a second experiment, measurements were made using two chambers connected *in*-line with the one chamber containing an HMP45C Vaisala sensor and the second chamber containing a Dew-10 cooled mirror. Most of the measurements were done with the inlet air passing through the Vaisala chamber first and then entering the Dew-10 chamber and then out to the pump. This arrangement would reduce the influence of the Dew-10 cooled mirror measurement method affecting the Vaisala measurements. Measurements were conducted for more than four months (Fig. 4.9). As was the case for the first experiment, the standard deviation in the water vapour pressure profile differences increased during the daytime hours (Fig. 4.9 top). From the temporal plot (Fig. 4.9 top), the standard deviation for the HMP45C measurements were similar to that of the cooled mirror measurements except for when the water vapour pressure differences were small. This is confirmed by Fig. 4.9 middle. Statistically, there is very little difference between the cooled mirror Dew-10 and HMP45C water vapour pressure profile difference measurements (Fig. 4.9 bottom). All three sensors (CS500,

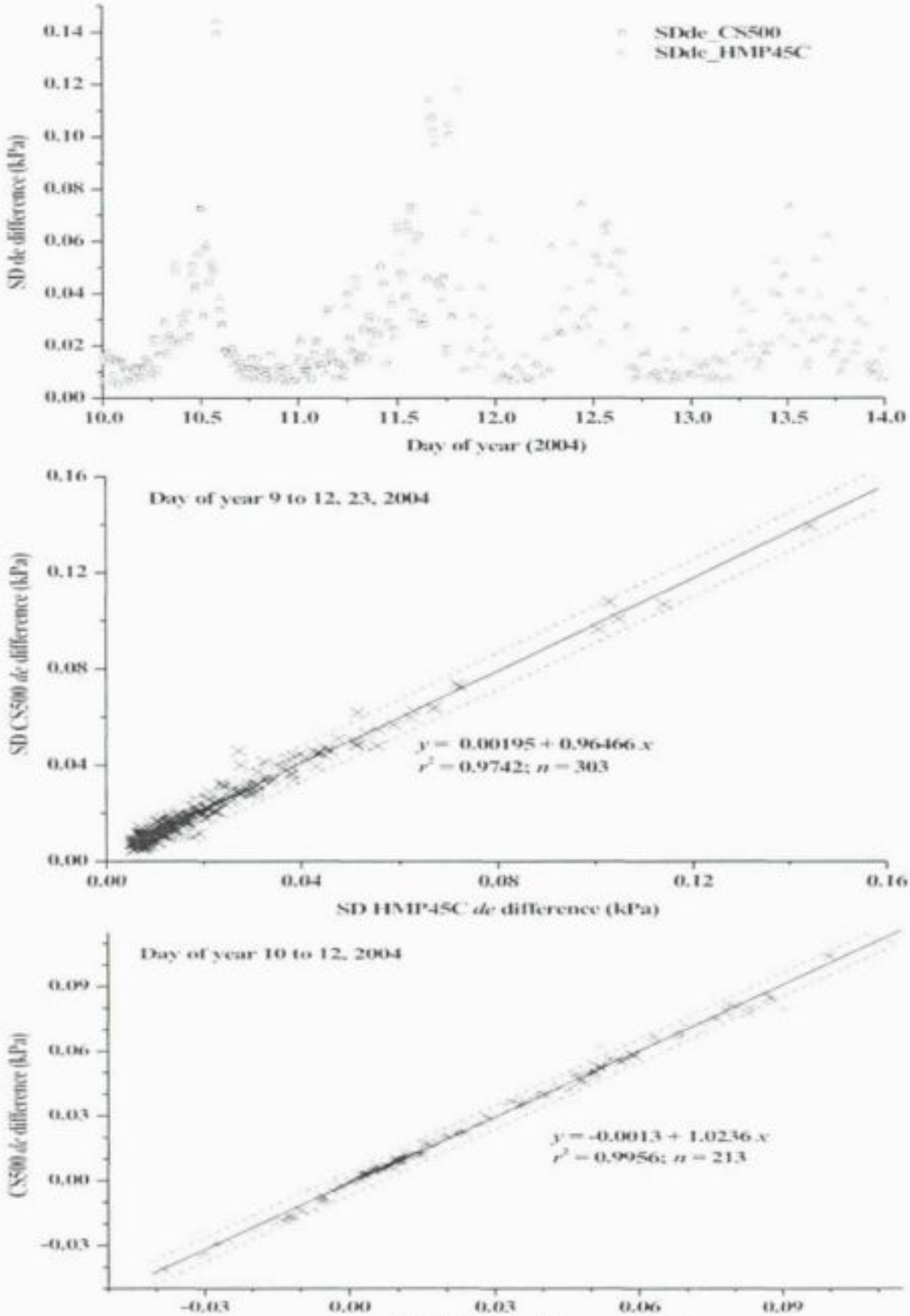

Fig. 4.8 Comparison of the mean of the standard deviation of the water vapour pressure profile differences (*de*) measured in the field using Vaisala HMP45C and the CS500 sensors for the periods indicated

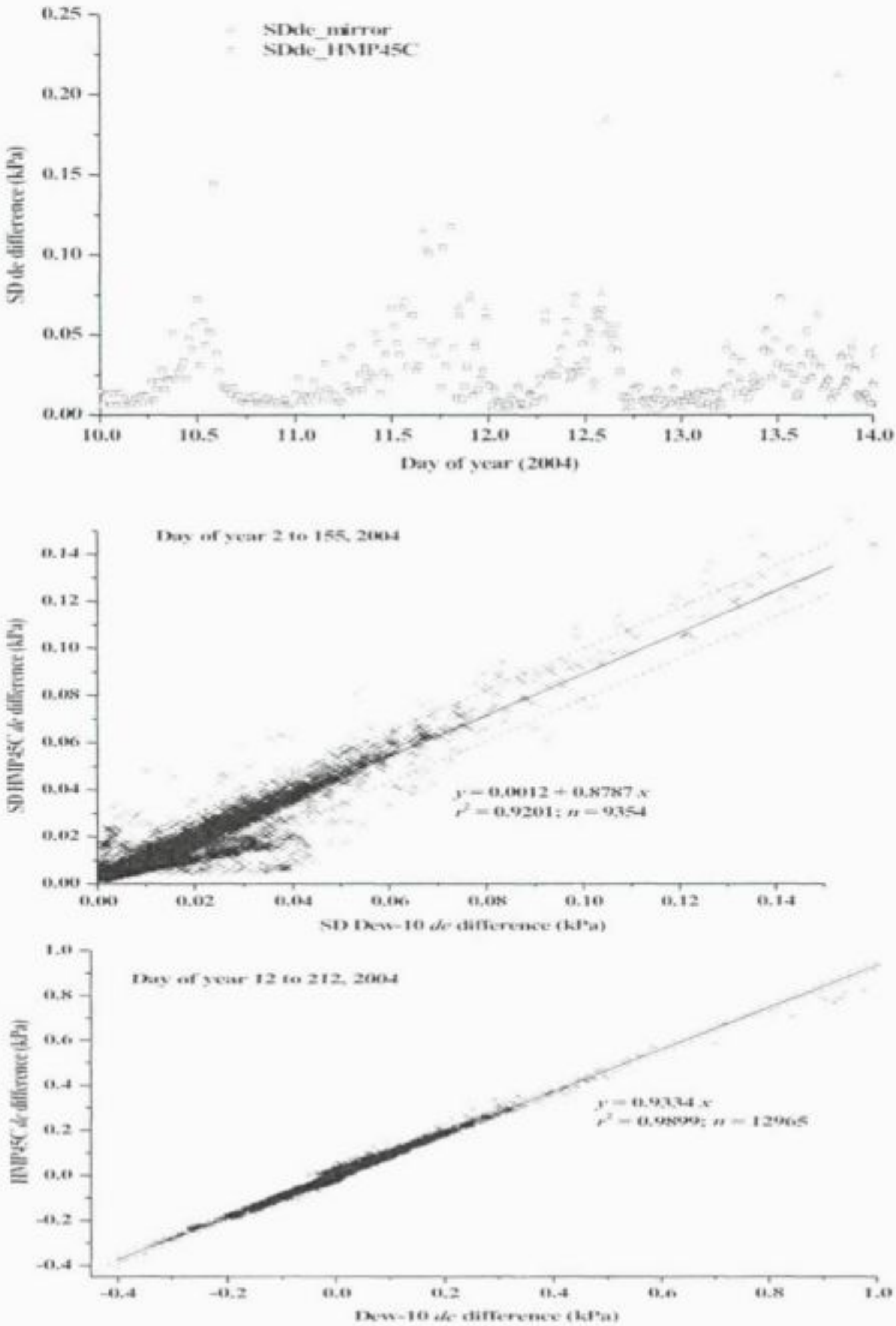

Fig. 4.9 Comparison of the mean of the standard deviation of the water vapour pressure profile differences (*de*) measured in the field using Dew-10 and Vaisala HMP45C sensors for the periods indicated

HMP45C and Dew-10) detected negative water vapour pressure profile differences, corresponding to dew deposition, equally well (Figs 4.8 bottom, 4.9 bottom).

Typically, the 20-min standard deviation of the profile differences in water vapour pressure is nearly 50 % greater for the HMP45C than for the Dew-10 (0.0233 kPa *vs* 0.0161 kPa) for the higher evaporative demand conditions (Fig. 4.10 bottom) and more than five times greater (0.0009 kPa *vs* 0.0050 kPa) for the low evaporative demand conditions (Fig. 4.10 top). Both sensors respond within 10 s to an abrupt change in the BR system water vapour pressure (Fig. 4.11 top). The Dew-10 sensor responds slightly more quickly (within 5 s) than the Vaisala HMP45C sensor that responds within 10 s (Fig. 4.11 middle and top). However this advantage and the advantage of decreased variability of the Dew-10 measurements do not disqualify the use of the Vaisala sensor for this application since measurements are averaged over the last 80 s of a two-minute period following which the difference in water vapour pressure between the two levels is calculated. Generally, the greatest change in water vapour pressure is at the beginning of the 2-min period and not during the 80-s averaging period. In some case, in particular for low evaporative demand conditions, the HMP45C showed large variations in water vapour pressure profile differences during the 40-s equilibration period (Fig. 4.11, bottom).

A report by the World Meteorological Organisation (2004) gives the time response of Vaisala Humicap sensors such as that used in the HMP45C sensor as 0.5 s at 25 °C (and 10 s at -40 °C) for a ventilation speed of 5 m s^{-1}. The report did not state if this response time was with the filter removed. Presumably it was.

In the case of BR measurements, since the water vapour pressure is calculated from the relative humidity and the adjacent chip temperature, it is not only the time response of the humidity sensor that is of concern. The time response of the temperature sensor was only considered as a possible limitation after the completion of these measurements and not addressed. The influence of this time response could be reduced by using a high flow rate, thereby ensuring that the sensor is exposed to a rapidly moving airstream. Alternatively, the sensor could be replaced by a fine wire thermocouple with a faster time response. However, whatever sensor is used, no adjacent sensor apart from an infrared thermometer could measure the temperature of the humidity chip. It is the temperature of the humidity chip that is required together with the measured relative humidity to calculate the water vapour pressure. The possible impact of any time response problem due to the temperature or relative humidity sensor could be reduced by increasing the 40-s stabilization period before measurements are made. Measurements are made every 1 s for the last 80 s of each 2-min period. Increasing the stabilization time from 40 s to 60 s should not materially affect measurement accuracy. The disadvantage of this is that evaporation measurements are only collected 50 % of the time.

The variation in block temperature (Fig. 4.11 middle) is shown for a two-minute period. The block was insulated, and the hose entering the chamber covered with adhesive aluminium. The variation in the block temperature measurements is within 0.05 °C (Fig. 4.11 middle) for this time period and, for the measured relative humidity of 46.7 %, this variation would result in a variation of 0.005 kPa in water vapour pressure even if there was no variation in measured relative humidity. A variation of 0.005 kPa in water vapour pressure is reasonably consistent with the variation in the water vapour pressure measurements shown in Fig. 4.10 bottom. The variation in air temperature and water vapour pressure are in-phase (Fig. 4.11 middle), largely through the influence that air temperature has on the calculated water vapour pressure. This in-phase nature is indicated by the vertical arrow, for example. The in-phase nature is due to the fact that the water vapour pressure of the airstream, $e_{air\ stream}$, is estimated using:

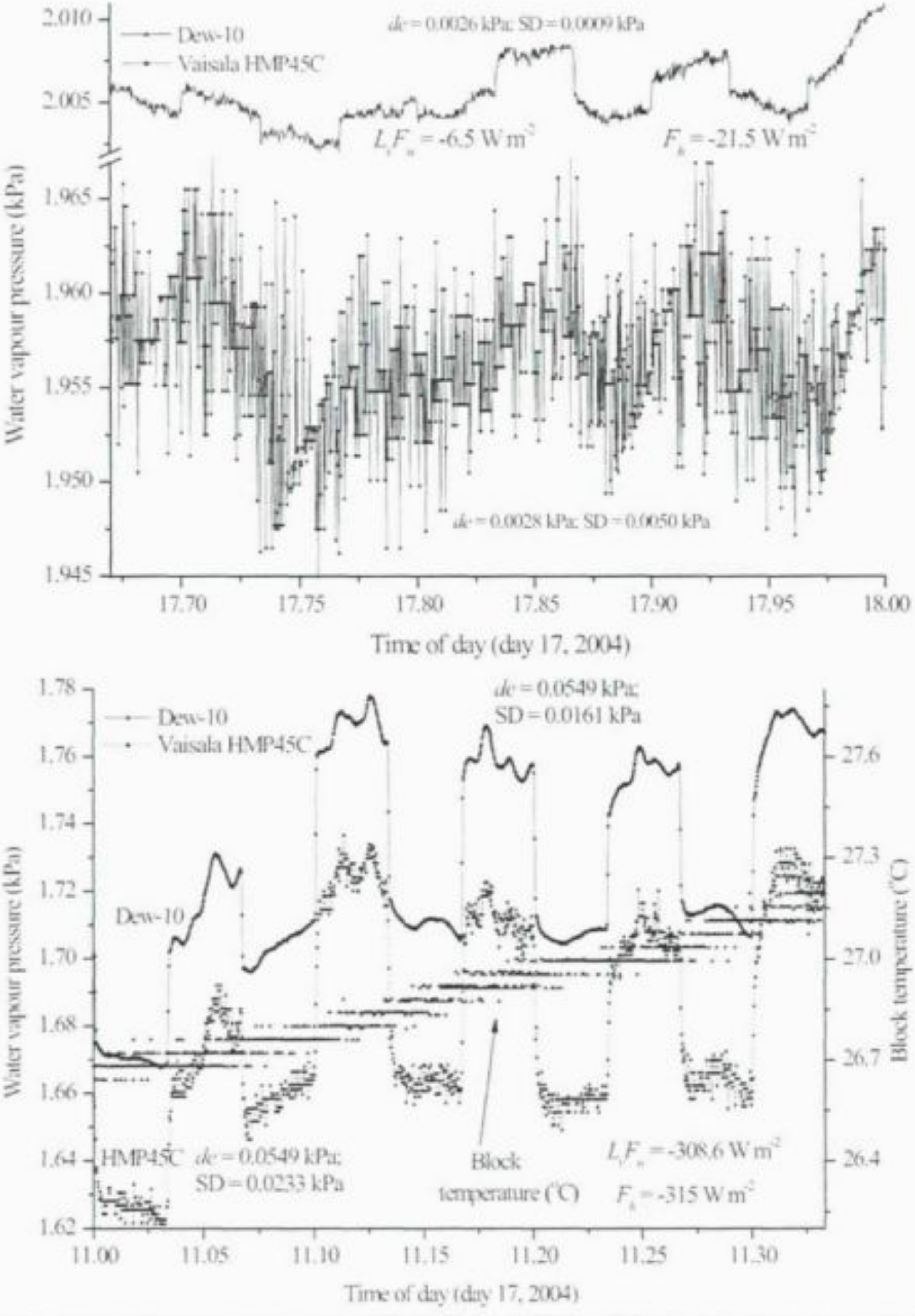

Fig. 4.10 One second measurements of water vapour pressure for a 20-min period for Dew-10 and HMP45C sensors during conditions of: top (a) low evaporative demand; bottom (b) high evaporative demand. Also shown in the bottom graph on the right-hand y-axis is the block temperature, which illustrates the resolution problem

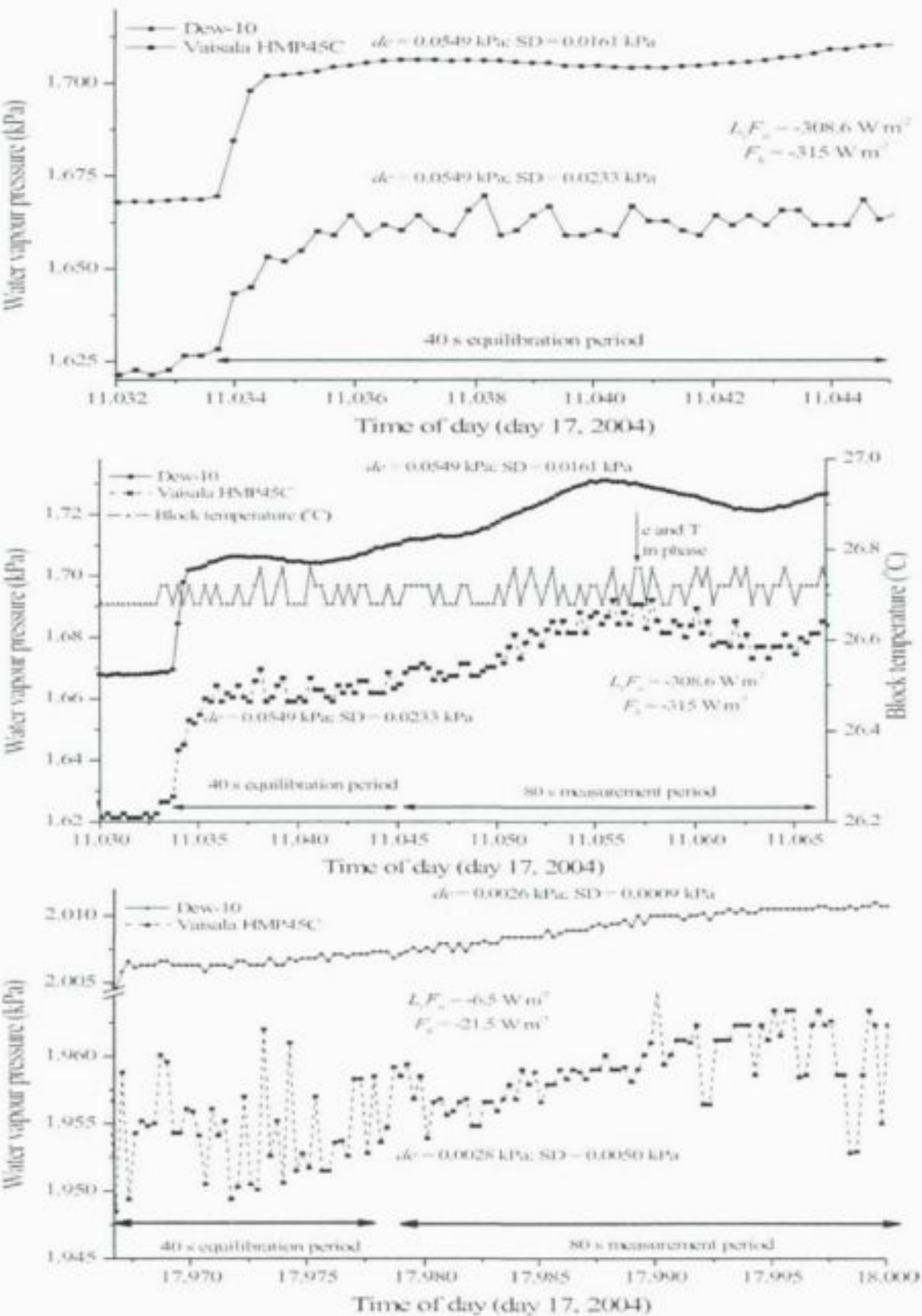

Fig. 4.11 One-s variation in water vapour pressure for Dew-10 and Vaisala HMP45C sensors top (a) for a 40-s equilibration period; middle (b) for a 40-s equilibration period followed by an 80-s averaging period for high evaporative demand conditions. The variation in block temperature is also shown; bottom c) for a 40-s equilibration period followed by an 80-s averaging period for low evaporative demand conditions

$$e_{air\ stream} = RH_{Vaisala} \times e_s(T_{Vaisala})/100$$

where $RH_{Vaisala}$ is the measured relative humidity and $e_s(T_{Vaisala})$ is the saturated water vapour corresponding to the Vaisala temperature $T_{Vaisala}$. Clearly therefore, assuming that $RH_{Vaisala}$ is unchanged, an increase in $T_{Vaisala}$ results in an increase in $e_s(T_{Vaisala})$ causing an increase in $e_{air\ stream}$. Similarly, a decrease in $T_{Vaisala}$ results in a decrease in $e_s(T_{Vaisala})$ causing a decrease in $e_{air\ stream}$. The question however that deserves attention is: what causes the step-like variation in temperature shown in Fig. 4.11 middle?

The step-like variation in air temperature (Fig. 4.11 middle) is due to the 21X datalogger voltage resolution limitation for the 0 to 5 V voltage range. The resolution on the 5 V range for the 21X datalogger is 0.33 mV and this translates to a temperature resolution limit of 0.033 °C for the Vaisala temperature sensor. The limitation of the voltage resolution on the temperature measurements affecting the water vapour pressure estimates could be avoided by using an alternative temperature sensor that does not suffer from the same problem. The replacement sensor should also be small since it would need to be mounted very close to the relative humidity chip. A fine wire thermocouple satisfies all of these requirements but this suggested replacement was only pursued at the very end of the study. The datalogger resolution for thermocouple measurements are 0.006 °C compared to 0.033 °C for the Vaisala temperature sensor. Some preliminary tests showed that a fine-wire thermocouple showed a greater variation in temperature than the Vaisala temperature sensor, mainly due to the small size of the thermocouple. This greater temperature variation caused a greater variation in the estimated water vapour pressure than if the Vaisala temperature sensor was used.

Some of the data collected (not shown) indicate that the water vapour pressure measurements of the CS500 are more variable than those obtained using a Dew-10 or a Vaisala HMP45C sensor. The reason for this could be that the CS500 temperature sensor is less accurate than that used by the HMP45C (Fig. 4.5). For example, at 20 °C, the CS500 temperature sensor has more than double the error of the HMP45C temperature sensor. The increased error in temperature measurement impacts directly on the error in water vapour pressure measurement.

A relatively long-term measurement comparison between latent energy flux density $L_v F_w$ (W m^{-2}) obtained using the Vaisala HMP45C and Dew-10 sensors is shown (Fig. 4.12). The comparison is good with little statistical difference between the estimates for the two different sensor types. The Vaisala HMP45C sensor is cheaper, more reliable and requires much less attention than the Dew-10 sensor.

From the data collected, it would appear that either the Vaisala CS500 or the Vaisala HMP45C may be used as a replacement sensor for the Dew-10. To reduce the noise in the temperature measurements and the temperature difference between the humidity chip and the airstream temperature, the chamber used for water vapour pressure measurements should be insulated and the hose immediately adjacent the chamber covered with adhesive aluminium tape. Measurements of water vapour pressure profile differences with a resolution of at least 0.01 kPa were possible using the Vaisala sensors (Figs 4.8 bottom, 4.9 bottom, 4.11 middle). Furthermore, there was no statistical difference in latent energy flux density obtained using the Vaisala HMP45C and the Dew-10 sensors (Fig. 4.12).

4.5.1.4 Practical issues related to BR measurements

A number of practical difficulties may arise with the use of the BR system. These are listed below.

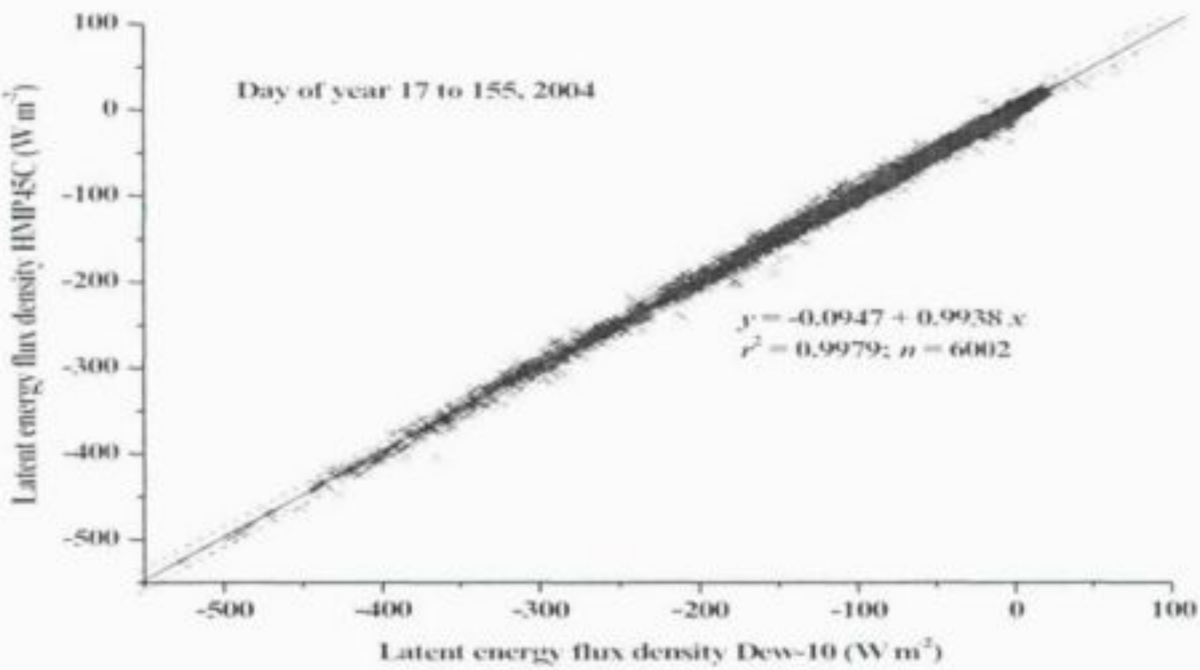

Fig. 4.12 Regression of 20-min field-measured BR latent energy flux density obtained using a Dew-10 and Vaisala HMP45C sensors for the period 17 January to 3 June 2004

1. Incorrect dew point measurement. Some of the Dew-10 mirror sensors often cannot hold the correct dew point for extended periods of time. This is often made worse in condensing conditions. This may be due to the electronics but it could be dirt or due to other things. Resetting the bias and cleaning the mirror may correct the problem but sometimes only for a limited period, typically no more than a week;

2. Leaky bottles. The mixing bottles weaken in their corners with time. They become brittle and crack. The cracks are not easily visible in the field with the bottles in their enclosure. If both bottles have cracks, leaks may occur and then smaller than actual profile water vapour pressure difference (de) values are measured. A crack in one bottle but not the other would probably also reduce measured de values. Bottles should be routinely replaced after a year and then tested in the laboratory for leaks due to cracks;

3. Poor hose connections. We found that the nylon Swagelok connectors (NY-600-61) work best. Hoses should not be joined from one size to another but rather connected directly to the bottle connector with no joins. However with time, any of the various connector types shrink the end of the hose causing a looser fit and hence may leak. Even over a period of a couple of weeks the end of the tube can shrink and result in leaks. The NY-600-61 connectors allow a reasonably long length of hose to be sealed, reducing the chance of leaks. It is a good idea to check all hose connections at each site visit. The fit can be tested by pulling to see if the hose is loose. If it is loose, cut off 20 mm of tubing and reinsert and seal;

4. Dirty hoses. In polluted environments, the inside of hoses gets covered with dirt. This was the case for the first BR system used at the site. Eventually the hoses become almost grey in colour. This dirt can contaminate the solenoid and also the humidity sensor. An annual replacement of the hoses for dirty environments is advisable;

5. Faulty solenoids. Solenoids can stick in which case they do not alternate air from one level to another. This was the case for the first BR system used at the site. This results in smaller *de* values. Also, solenoids can leak in which case air is taken from one level and partly from another at the same time. This will also cause smaller *de* values. If a solenoid does not sound a loud click when it switches, it is best to have it checked in the laboratory. It could be that high humidity causes problems with these solenoids. Solenoids should also be tested in the laboratory for leaks using two air streams of known but different dew points. Under high evaporative demand conditions, one can observe the water vapour pressure change at the end of a two-minute period. Under high radiative conditions during summer after 11h00, the change in water vapour pressure should exceed 0.04 kPa;

6. Long hoses. Long hoses that are wrapped up behind the enclosure cause nothing but trouble. Usually these dangle quite close to ground and experience low temperatures at night (compared to if kept at higher elevations). At night, the air flowing in the hose may therefore condense. Once there is condensation in these hoses and in the mixing bottles, it may take days of warm weather for the water to completely evaporate. Applying tape to the hoses to reduce UV degradation in the hose does not help since then one cannot see the condensation. One way to prevent condensation inside the hoses is to insert a constantan wire that is heated to maintain the air temperature just above the dew point. The heating could be controlled by the datalogger based on the measured relative humidity. Condensation inside a hose may mean that there is liquid water in the mixing bottle as well. If condensation inside the hose is noticed, one would have to disconnect the bottle and remove the liquid from the bottle and the inside dried with a paper towel. The bottle should then be resealed and connected to the hoses. Hose condensation can be removed by first removing the inlet filter and then connecting the bottle end of the hose to the outlet end of the pump. If one has to have long hoses, it is a good idea to ensure that the hose is as high above ground as possible and wrapped around the enclosure. Alternatively, most of the excess length could be pushed to the inside of the enclosure (where the temperatures are greater due to the electronics). Better still, the length of hose needed should be as short as possible. It is always advisable to inspect the hoses very carefully at each visit to see if there is condensation. Site visits in the early morning should show the condensation either at the bottom of the dangling hose or inside the enclosure just as the hose attaches to the bottle. The change in water vapour pressure for two or three two-minute periods should be viewed to see if the *de* values are as expected. Water vapour pressures close to saturation for either level may indicate condensation. In addition, it is advisable to store the standard deviation of water vapour pressure for both profile levels. Experience has shown that during the night, the standard deviation should be low and approximately the same for both levels. Large standard deviations for the one height but not the other is an indication of possible condensation or leaks. Similarly, the daytime standard deviations of the water vapour pressure for both levels should be fairly similar in the absence of condensation or leaks;

7. Dirty filters or incorrect filter orientation. Dirty filters obstruct the flow of air causing longer times for air to get to the bottles. The filters need to be oriented so that the smooth side is exposed to the sensor and the coarse side to the incoming air;

8. Thermocouples. At every thermocouple connection point, errors can result. Unlike the water vapour pressure measurements, these errors are "invisible" in the sense that the measurements themselves give no clue that something is amiss. There are two connecting points for the fine wire thermocouples. Insulation can be used to cover these connecting points and then aluminium used to cover the insulation. This method often reduces temperature measurement errors if there are sudden changes in temperature. At the datalogger end, the panel for covering the connecting channels should be used.

Both the 21X and the CR23X have connecting strips (insulation covered by metal). These should be used whenever BR temperature measurements are made. As a last resort, a large piece of Prestik could be used to cover the area where the thermocouples are connected to the datalogger and the Prestik covered with aluminium foil;

9. Cobwebs on thermocouples. These are a problem since they affect the measured profile air temperature differences. Also, care is needed when removing cobwebs since the thermocouple is easily broken. The Bowen ratio manual recommends the use of dilute hydrochloric acid washing followed by distilled water washing to remove the cobwebs;

10. Viewing the temperature measurements at the datalogger display is advisable. There have been cases where the thermocouple looks intact but does not make electrical contact with the thicker metal post. Very carefully pushing on the thermocouple with a small tooth pick will show if it is joined there or not. Care is needed to avoid damaging the thermocouple with this procedure;

11. Broken/dirty net radiometer domes. The top domes need to be inspected using a ladder to view the sensor from above for close-checking for small cracks in the dome or removing excessive dirt. Cracks in the dome let water on to the sensor which can discolour it and change the calibration factor irreversibly. Distilled water and a camel hair brush should be used to clean the dome;

12. With some 21X dataloggers, the program causes the pump to switch off at some time after sunset. This can be prevented by removing the call to subroutine (at the end of datalogger Table 2). The consequence of this is that the system does not suspend when battery voltage goes low.

It should be possible to use a CR10X datalogger as part of a Bowen ratio system. Care however is needed with regard to ensuring that the reference thermistor used is very well insulated so as to not compromise the reliability of the air temperature profile measurements;

13. The soil heat flux measurements are crucial, particularly for short vegetation, since they define the calculated sensible heat and latent energy. Stannard et al. (1994) recommended that at least three soil heat flux plates were required for their heterogeneous terrain measurements. Care is needed to ensure that the correct depth placement is used.

4.5.1.5 Conclusions

From the available data, either the Vaisala HMP45C or the CS500 can be used to replace the Dew-10 cooled mirror hygrometer sensor of a BR system. This replacement makes the BR system much cheaper with little attention required by the humidity sensor compared to the Dew-10 sensor. The issue is the Vaisala air temperature and water vapour pressure variability during the last 80 s of each 2-min period. The Vaisala sensors show more noise that the Dew-10 water vapour pressure but the 20-min averages of the profile water vapour pressure difference compare well with the corresponding Dew-10 measurements. Further modifications could include increasing the equilibration time from 40 s to 60 s and using a fine-wire thermocouple to measure the temperature of the airstream.

4.5.2 Analysis of wind direction

Besides the investigation on a replacement for the Dew-10 sensor of the BR system, an analysis of wind direction impacts is needed before comparisons between sensible heat flux density for the different measurement methods can be made.

When viewed from the transmitter, the receiver position was 20° W of compass N (Fig. 3.1), almost from S to N. For this location, the magnetic declination for compass N is 22°. In other words, compass N is 22° W of true N. All directions were referenced in degrees from compass N in an anticlockwise direction. Winds exactly perpendicular to the beam correspond to a wind direction of 110 or 290° from compass N. Wind directions between 90 and 180° and between 270 and 360° were rare. Winds parallel to the beam correspond to a wind direction of 20 or 200° from compass N. Wind directions corresponding to the 0 to 90° sector sometimes were the result of Berg winds and also correspond to wind for the residential area including trees. For the 0 to 90° sector, the main wind direction is about 50° and 215° for the 180 to 270° sector.

Since wind direction for this site is highly variable, the following conditions were used to define wind perpendicular and parallel to the beam:

parallel to beam: wind directions between 350 and 50 degrees or between 170 and 230 degrees;

perpendicular to beam: wind directions between 80 and 140 degrees or between 260 and 320 degrees.

In other words, wind directions within 30 degrees of the directions corresponding to exactly parallel (20 or 200°) and perpendicular to the beam (110 or 290°).

4.5.2.1 Daily wind vector analysis

Sub-hourly wind speed and wind direction from measurements from the ECAT 3D sonic anemometer system (Fig. 3.1), for every two minutes, can only be presented for window periods. A wind direction perpendicular to the SLS beam results in SLS measurements representing a much larger footprint area than if the direction is parallel to the beam. Initial impressions were that the main winds during the day were from the SE.

The daily (06h00 to 18h00 only) wind speed and wind direction values were calculated from the two-minute values, of the horizontal wind speed U and wind direction θ, referenced to N and anticlockwise from N, using vector algebra:

$$\overline{u_x} = u = (\Sigma U \cos\theta) / n$$

$$\overline{u_y} = v = (\Sigma U \sin\theta) / n$$

$$U = \sqrt{(\overline{u_x})^2 + (\overline{u_y})^2}$$

$$\theta = \arctan(\overline{u_y} / \overline{u_x})$$

where n is the number of acceptable two-minute measurements between 06h00 and 18h00. The polar diagrams, for day of year 28 to 276 (2003), together with the resultant wind vector for the 0 to 90° and 180 to 270° sectors, are shown (Fig. 4.13). Clearly, during the daytime hours, the wind vector wind direction, referenced to compass north, is generally SE (180 to 270°) (Fig. 4.13a) but sometimes from the NW (0 to 90°). The strongest winds were from the 20 to 50° directions. The magnitude of the largest daily SLS sensible heat densities occurred when the wind direction was between 240 and 270° (Fig. 4.13b) corresponding to an upslope flow of air (anabatic flow). The difference between SLS and ECAT sensible heat densities as a function of wind vector wind direction is larger for the 0 to 60° wind directions (Fig. 4.13c) indicating that the EC and SLS systems may be responding to different footprints for these wind directions. Generally however, for most wind directions, it would appear that

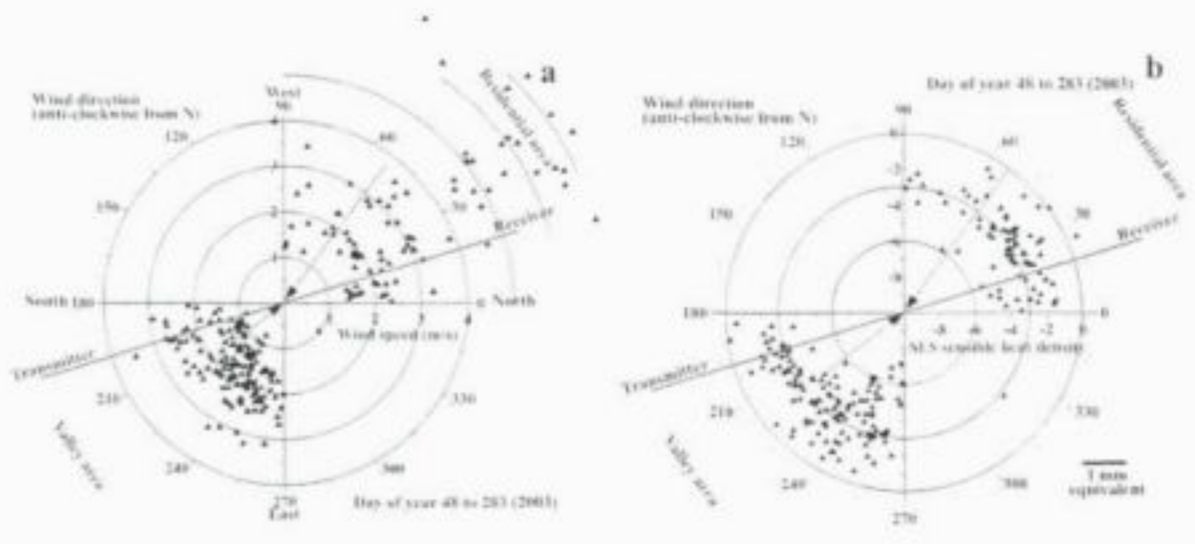

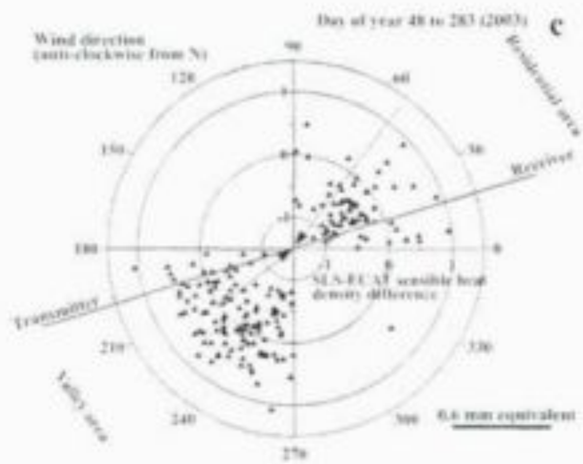

Fig. 4.13 Polar diagrams for daytime (06h00 to 18h00) measurements of:
(a) wind speed (m s^{-1}) and wind direction (for the period day of year 48 to 283, 2003);
(b) SLS sensible heat density (MJ m^{-2}) and wind direction;
(c) for SLS and ECAT sensible heat density difference (MJ m^{-2}) and wind direction.
The two arrows in each of a, b and c show the resultant wind vector for the 0 to 90° and 180 to 270° sectors for the entire measurement period for day of year 48 to 283 (2003)

both the ECAT and SLS systems were similarly affected by the various wind directions experienced during the measurement period.

4.5.2.2 Two-minute wind vector analysis

Wind direction details for selected days are presented in Table 4.3. The two-minute wind direction measurements, referenced to compass north, were investigated in more detail for these days to isolate periods for which the wind direction was perpendicular to the beam and days for which the wind direction was parallel to the beam. The display of wind speed and wind direction for these days are shown for the selected days (Fig. 4.14, a to e). The x-axis shows the time in minutes for a particular hour shown on the y-axis. So, for example, a point with $x = 30$ and $y = 13$ would correspond to 13h30. The wind speed is indicated by the length of each arrow. An arrow from right to left corresponds to S to N and an upward pointing vertical arrow corresponds to W to E.

On some of the days chosen, the wind direction appeared to be random (day of year 127, 2003 for example). On other days, the wind direction was regarded as being perpendicular to the beam (day of year 187, 2003 and day of year 5, 2004 for example). On day of year 186 (2003) the wind direction

Table 4.3 Wind direction details for selected days. When viewed from the transmitter position, the SLS beam pointed approximately 20 degrees W of compass N (Fig. 3.1)

Year	Day of year	Wind direction	Comment
2003	127	Variable	Maximum air temperature = 26.0 °C
	186	NW (10h00 to 10h20); mostly SW (11h00 to 15h00); mostly S (15h00 to 16h20); N (16h20 to 16h50)	Not perpendicular to the beam Maximum air temperature = 17.7 °C
	187	Mostly E (13h00 to 16h00)	Mostly perpendicular to the beam Maximum air temperature = 17.7 °C
	278	Mostly NW; W between 14h50 and 15h50; SE between 15h50 and 16h40 and S or SE after that	Not perpendicular to the beam; Berg wind conditions Maximum air temperature = 35.8 °C
2004	5	E	Day with the most consistent wind direction: always perpendicular to beam Maximum air temperature = 31.3 °C

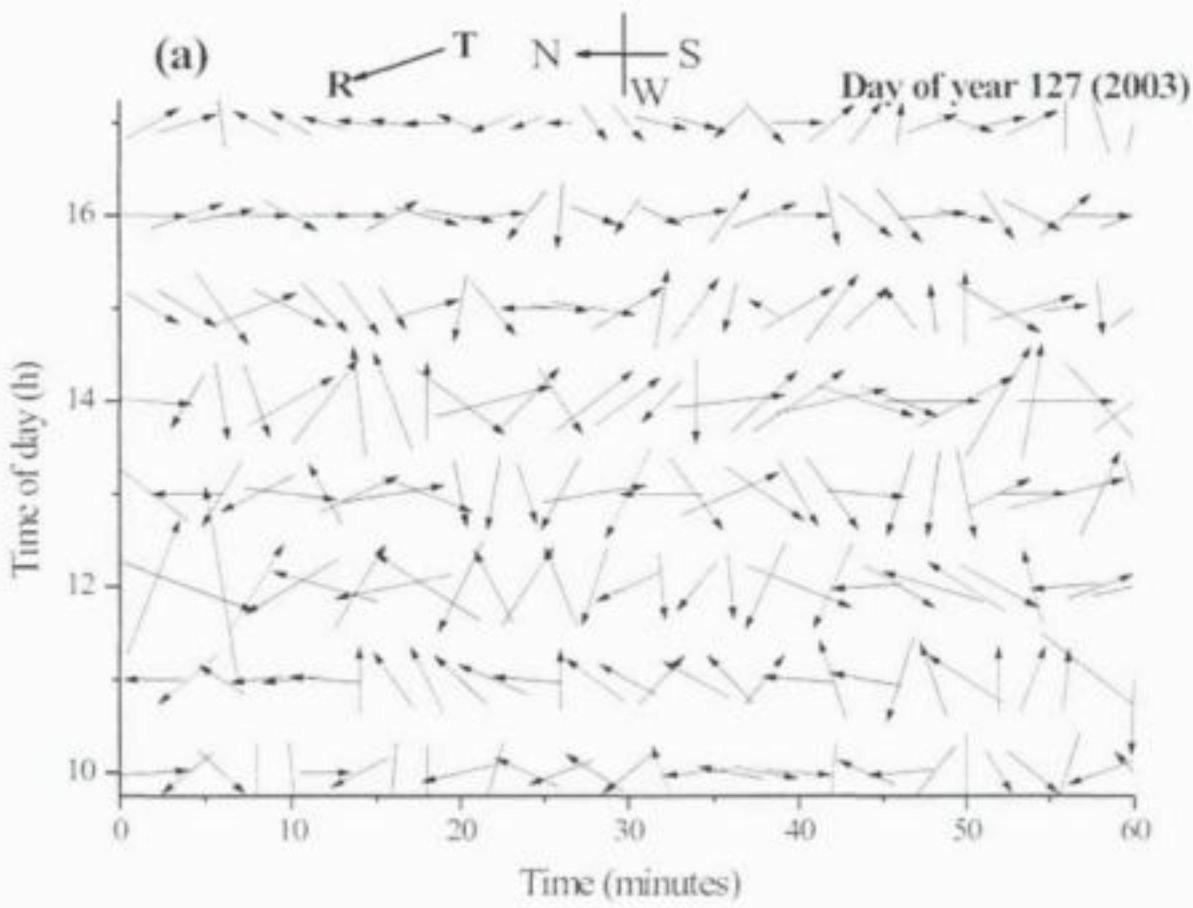

Fig. 4.14 a to e Wind direction for selected days. A horizontal arrow from right to left is S-N. The orientation of the beam is shown by an arrow from the transmitter (T) to the receiver (R)

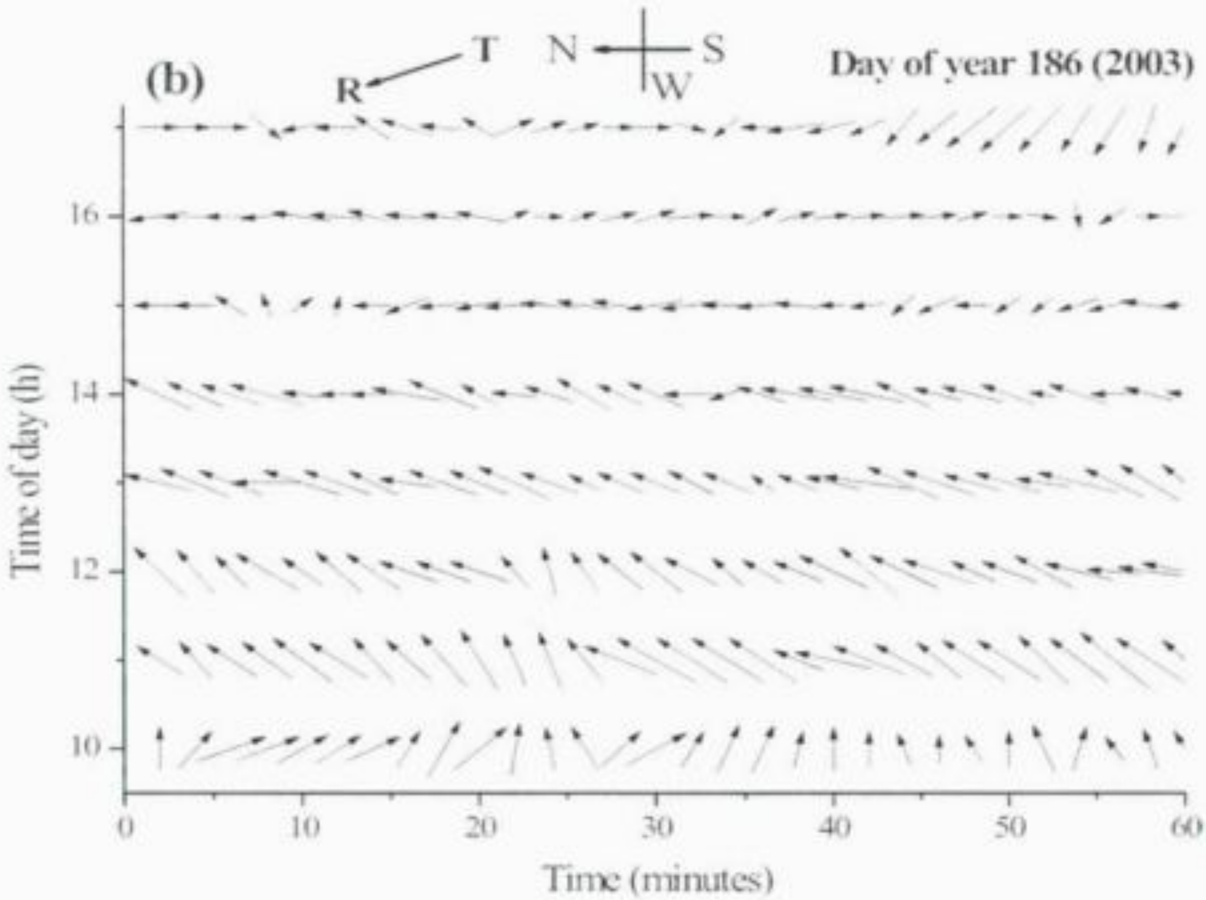
(b)
R
T
N
S
W
Day of year 186 (2003)
Time of day (h)
10
12
14
16
0
10
20
30
40
50
60
Time (minutes)

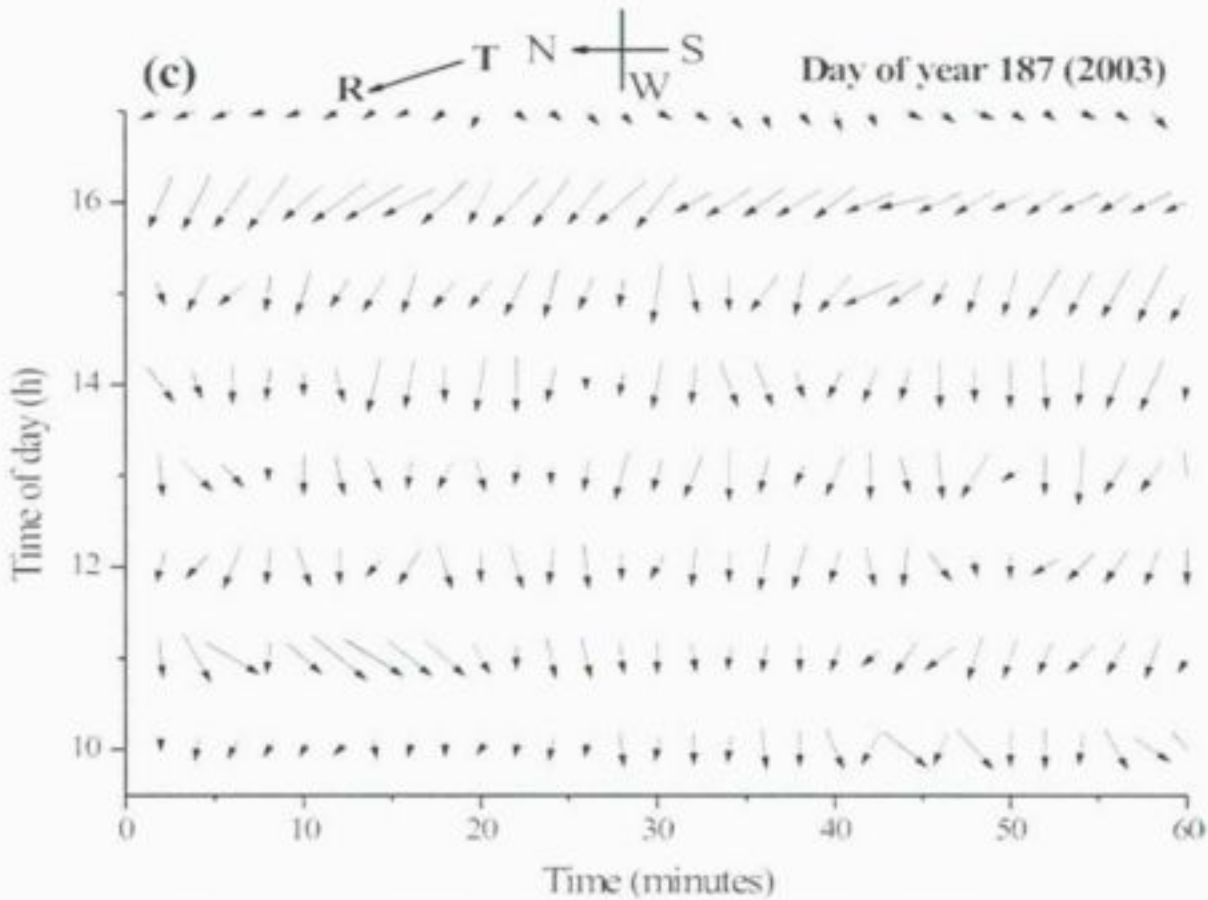
(c)
R
T
N
S
W
Day of year 187 (2003)
Time of day (h)
10
12
14
16
0
10
20
30
40
50
60
Time (minutes)

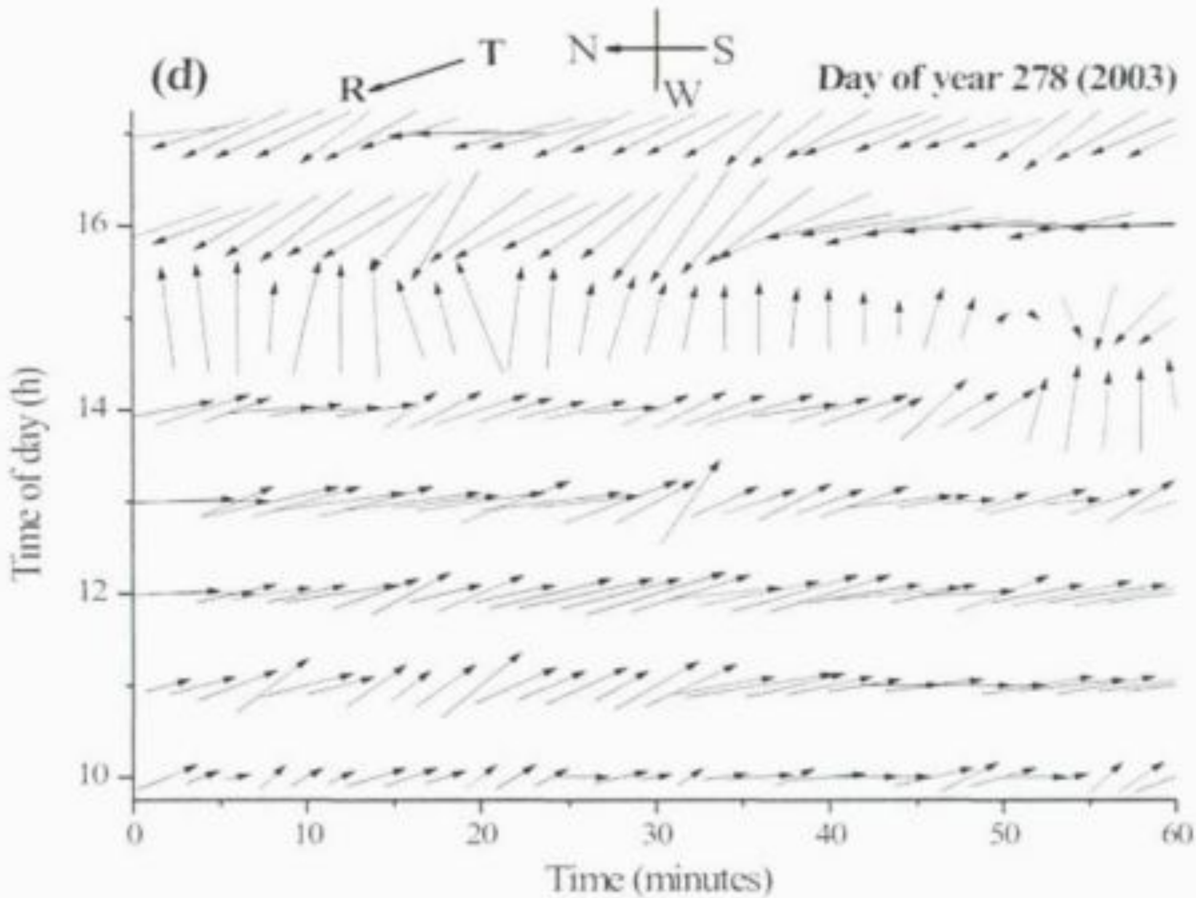
(d)
R
T
N
S
W
Day of year 278 (2003)
Time of day (h)
10
12
14
16
0
10
20
30
40
50
60
Time (minutes)

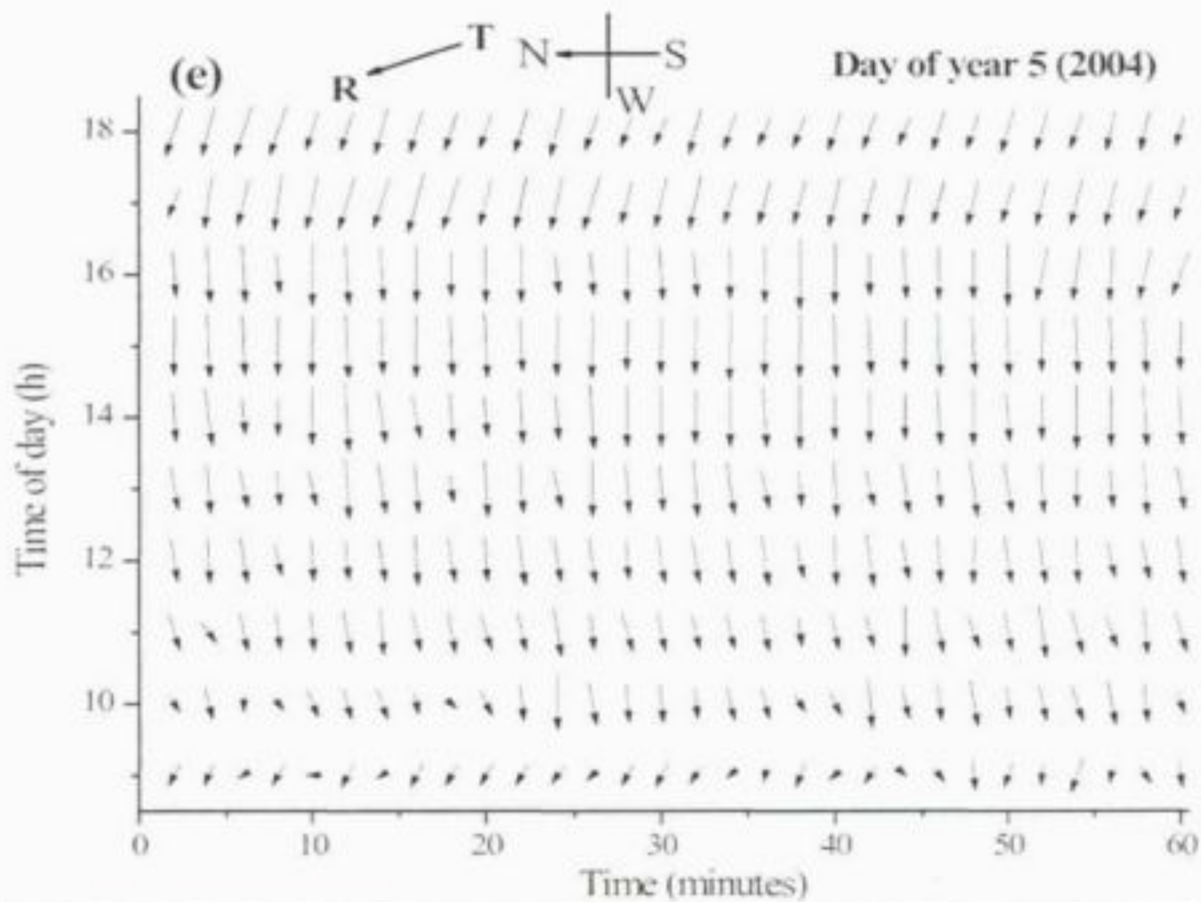
(e)
R
T
N
S
W
Day of year 5 (2004)
Time of day (h)
10
12
14
16
18
0
10
20
30
40
50
60
Time (minutes)

was parallel to the beam for some of the time and perpendicular later. These graphs, for the different days, demonstrate the variability in wind direction from one day to the next and indeed in some cases from one 2-min time period to the next.

In retrospect, the original beam position chosen was a good one with many days with the wind direction perpendicular to the beam and seldom parallel to the beam.

For day of year 5 (2004), the wind direction was consistently from the west, corresponding to perpendicular to the beam. Fortunately, for this day, measurements from all four measurement methods were made (BR, EC, SLS, and SR). These are reported on later.

When winds are near-parallel to the SLS beam, the SLS method no longer has the advantage over the BR and EC methods than would be the case if the winds were perpendicular to the beam. When perpendicular to the beam, the main advantage of the SLS method is the line-averaging capability of the point measurements. An hypothesis (Green et al. 1997) therefore is that for winds parallel to the beam, that is roughly from the N or from the S, there should be greater correspondence between SLS and EC sensible heat measurements.

Correspondence between 2-min sensible heat flux density for the SLS and EC methods for the five days selected is shown (Fig. 4.15). The upper horizontal trace for each day indicates periods when the wind was regarded as being perpendicular to the beam and the lower when the wind is parallel to the beam. If anything, there appears to be poorer correspondence between the SLS and EC sets of measurements when the wind is parallel to the beam (day of year 127 (2003) and 278 (2003) in Fig. 4.15, for example). On day of year 5 (2004), when the winds were almost always perpendicular to the beam, there is good correspondence between SLS, EC and (20-min) BR estimates of sensible heat flux density.

Between January and the end of March 2004, 35 % of the daytime hours (06h00 to 18h00) had winds perpendicular to the SLS beam compared to less than 5 % of the time for winds parallel to the beam. This situation is however seasonal - with almost 9 % of the daytime hours consisting of winds parallel or perpendicular to the beam for the period April to end August 2004.

4.5.3 Footprint analyses

The footprint of the sensible heat flux density measurements would affect the measurement comparison between the different methods. The footprint calculations included the peak location of the footprint x_{peak} (Eq. 4.49), the ratio of the flux density $F(x, z_m - d)$ to surface source flux density S_u (Eq. 4.50), the footprint calculations (Eq. 4.51) and the 90 % fetch to measurement height ratio (Eq. 4.52). These calculations are stability dependent *via* the Monin-Obukhov length L (m) (in turn dependent on SLS-measured friction velocity and sensible heat flux density, Eq. 2.40) and the similarity parameters D and P of Eq. 4.45 from the model of Hsieh et al. (2000). Similarity parameters D and P are determined by the atmospheric stability condition and for this determination, as mentioned in Section 2.11.6, we used the Deardorff (1978) set of definitions of atmospheric boundary layer stability, repeated here for convenience and extended to a surface with a zero plane displacement height d:

$$\text{unstable, convective } (z-d)/L < -0.5;$$

$$\text{unstable } -0.5 \le (z-d)/L < -0.02;$$

$$\text{neutral } -0.02 \le (z-d)/L < 0.02;$$

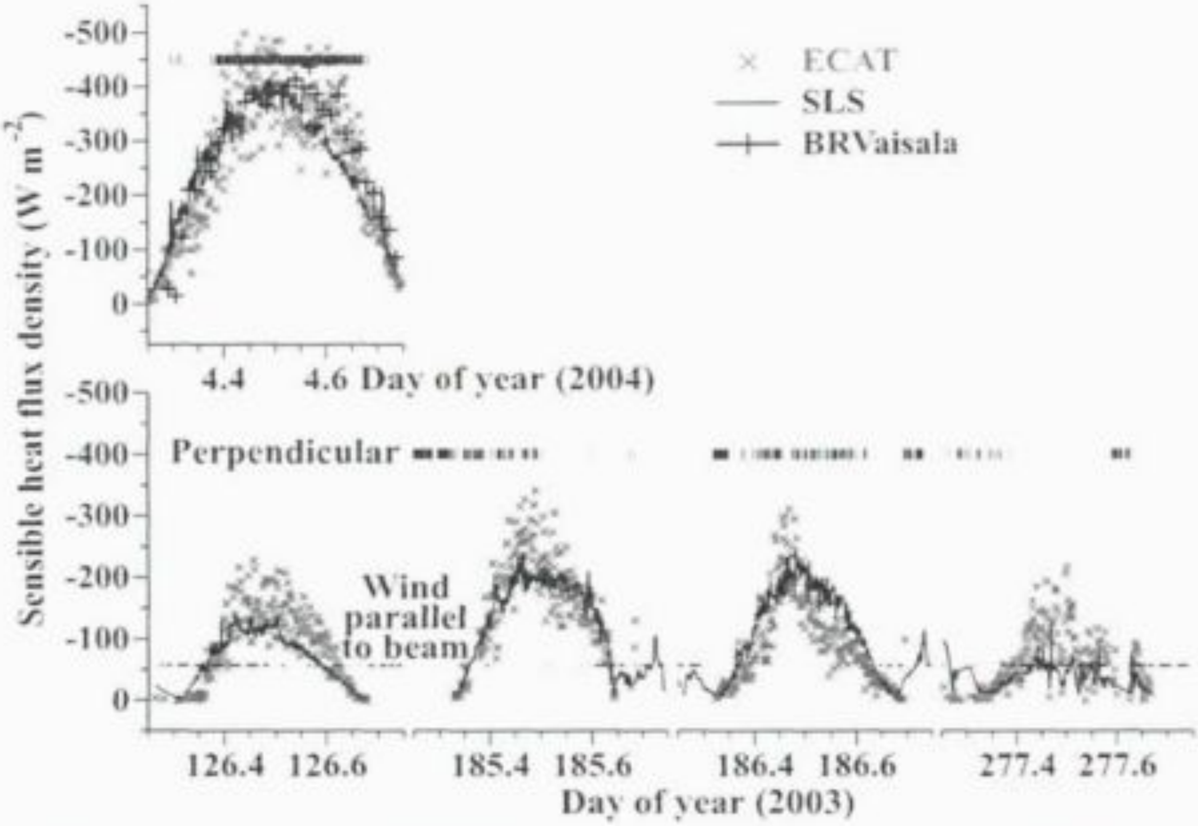

Fig. 4.15 Two-minute variation in SLS and ECAT sensible heat flux density for selected periods for which the wind direction is predominantly perpendicular (indicated by the upper trace labelled "Perpendicular") or predominantly parallel to the beam (indicated by the lower trace labelled "Wind parallel to beam"). For day of year 5 (2004), the 20-min BR measurements obtained using a Vaisala HMP45C sensor are also shown.
The effective beam height was approximately 1 m and the beam path length is 101 m. Winds perpendicular or parallel to the beam are defined as winds within 30 degrees of perpendicular or parallel to the beam position

$$\text{stable, continuous } 0.02 < (z-d)/L < 0.2;$$

and

$$\text{stable, sporadic } (z-d)/L > 0.2.$$

All calculations were performed every two minutes. An important reminder here about the definition of the MO length L: it is the height above d at which free convection dominates.

Data for days that were relatively cloudless apart from those in September 2003 were chosen for graphical display. The days chosen covered a range of atmospheric stability conditions. The wind direction data for three of the days selected are shown in Fig. 4.14. Of particular note is that as x_{peak} increased (Fig. 4.16), the atmospheric condition changed from convectively unstable to stable. Furthermore, the more unstable the conditions, the closer was the peak location of the footprint to the measurement position. For convectively unstable conditions, the x_{peak} values were within metres of the measurement position of the SLS beam. The measurements of sensible heat flux density were therefore fairly localised compared to measurements for which x_{peak} values were greater for these convectively unstable conditions.

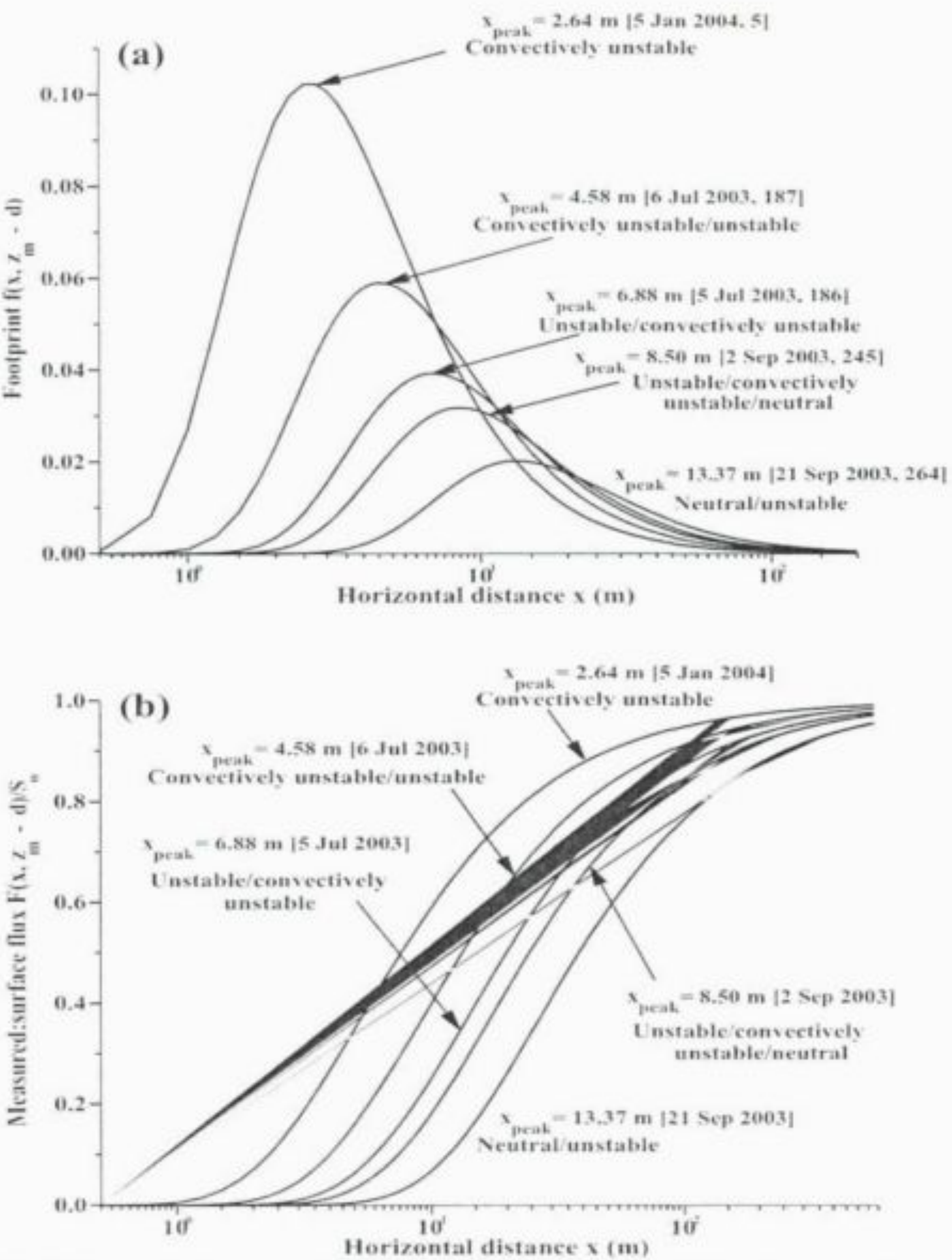

Fig. 4.16 (a) Top: Comparison between the estimated footprint (Eq. 4.51) for selected days based on 2-min SLS measurements of the Monin-Obukhov stability length L, horizontal distance x (m) from the measurement positions, beam height relative to the zero plane displacement height d, and the stability-dependent similarity constants D and P of Hsieh et al. (2000). The peak location of the footprint x_{peak} (m) is shown for each date as is the stability condition. The x_{peak} value used was the average of the 2-min x_{peak} values between 09h00 and 15h00

(b) Bottom: Comparison between the ratio of the flux density $F(x, z_m - d)$ to surface source flux density S_u (Eq. 4.50) for selected days based on 2-min SLS measurements of L

The final footprint calculation is the 90 % fetch to measurement height ratio, estimated using Eq. 4.52, and shown for four days (Fig. 4.17). The dynamic nature of stability is evident on these days and in fact on most days. These are many cases where atmospheric stability changes from convectively unstable to stable from one 2-min period to the next. The data shows that it is more often than not that the 100:1 fetch to measurement height ratio is too stringent.

Based on the x_{peak} estimation, one trend that has emerged is that the general stability condition for the 9 am to noon hours is not the same as that for the noon to 3 pm period. For much of the time, or at least for 75 % of the 9 am to 3 pm periods, the x_{peak} values in the morning are less than that for the afternoon (Fig. 4.18). Referring to Eq. 4.49 for the estimation of the location of the peak footprint, shows that for unstable conditions for which $P = 0.59$, larger x_{peak} values correspond to greater L values which in turn corresponds to greater $(z - d)/L$ values when L is negative or corresponds to increased level of stability. Greater instability in the period 09h00 to noon than between noon and 15h00 is a significant finding since the x_{peak} estimate affects the footprint, F/S_c and the 90 % fetch to measurement height ratio. The 90 % fetch to measurement height ratio difference between morning and afternoon hours may impact on measurement comparisons between the different techniques particularly when comparing a line-averaged measurement of sensible heat flux density with a point measurement. Furthermore, the diurnal shape of the sensible heat flux density curve may be asymmetrical given that morning hours are generally more unstable than are afternoon hours. By comparison, the asymmetrical nature of the diurnal sensible heat flux density curve is shown in Figs 4.19 and 4.20. The asymmetrical shape of the diurnal sensible heat flux density curve for EC measurements, shown by the open circles in the bottom right of Fig. 4.20, is not as noticeable due to the variability of the point measurements.

4.5.4 Flux comparisons

4.5.4.1 Averaging periods

The averaging periods for the various measurement systems are two minutes for EC, energy balance, reference evaporation, SLS and SR systems, 20 min for the BR system and 30 min for the open path EC system (ECopen). The 2-min averages are easily scaled to 20 min, 30 min and daily time intervals but the reverse is not possible.

4.5.4.2 EC (2-min) vs EC (20-min) sensible heat flux density comparisons

The EC technique is often regarded as the standard for flux measurements against which all comparisons of sensible heat flux density are usually made. Initially, EC measurements were made at intervals of 20 min using the CA27 EC system consisting of a 1-D sonic anemometer and a fine-wire thermocouple. A field experiment using two EC systems was conducted with one system performing the covariance every 20 min and the other every 2 min. The 2-min sensible heat flux densities were averaged over 20 min and compared with the flux densities determined for the 20-min time period (Fig. 4.21). The correspondence is good and this partly justifies using the 2-min time period for the EC method.

4.5.4.3 EC and SLS 2-min sensible heat flux density comparisons

Generally, the agreement between 2-min SLS and ECAT sensible heat flux density values, as depicted by diurnal variations, was very good (Figs 4.22 and 4.23). This is in spite of the SLS yielding path-averaged measurements and the ECAT value essentially yielding point measurements, different footprints for the SLS and ECAT measurement techniques, and the different measurement heights

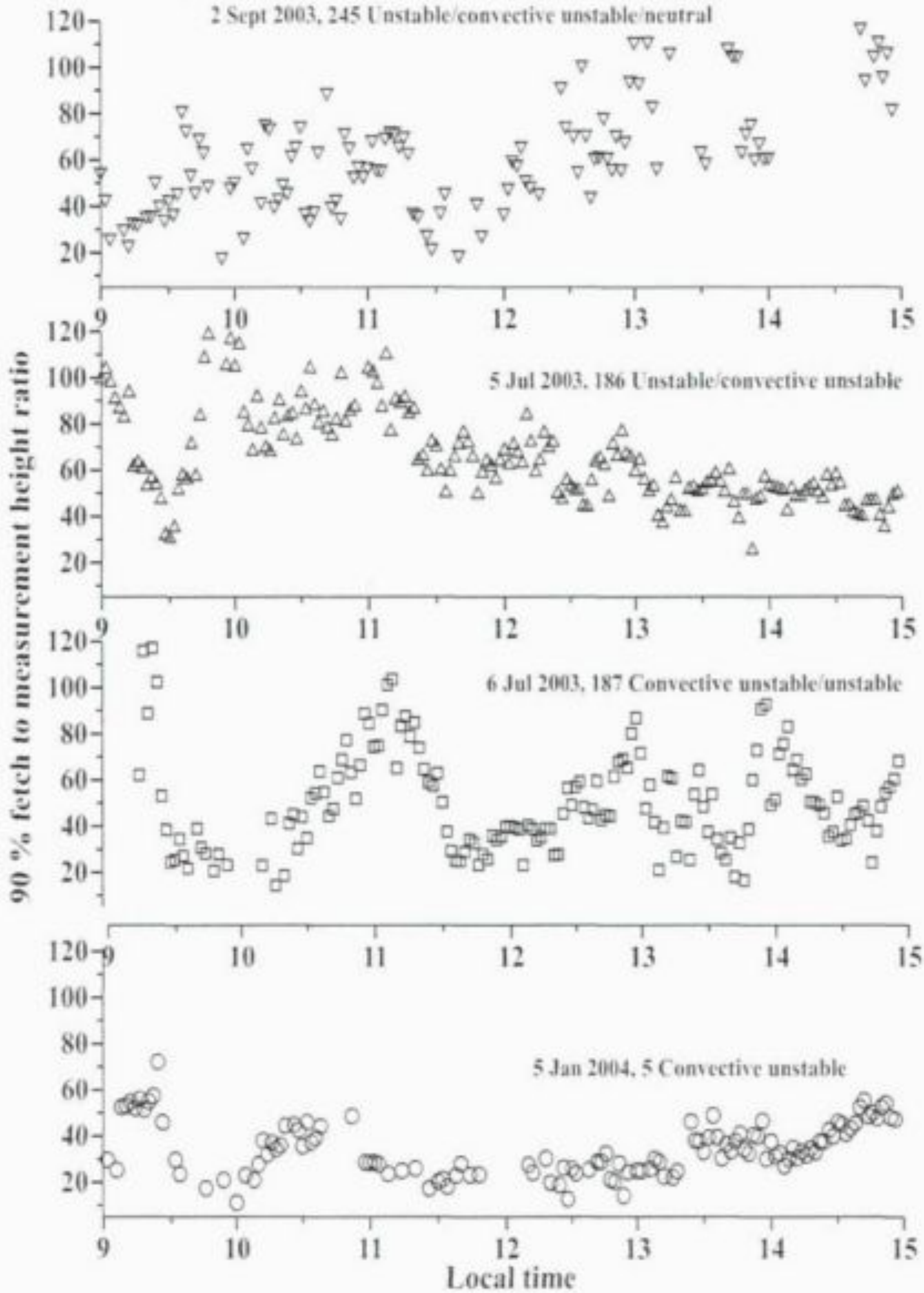

Fig. 4.17 Diurnal variation in the 2-min values of the 90 % fetch to measurement height ratio (Eq. 4.52) for three relatively cloudless days (5 Jan 2004, and 6 and 5 July 2003) and one partly cloudy day (2 Sept 2003). Days with the lowest ratios have the greatest instability, 5 Jan 2004 for example, and days with the highest ratio, 2 Sept 2003 for example, have the greatest stability. The points are the 2-min values based on SLS estimates of L and the consequential stability state

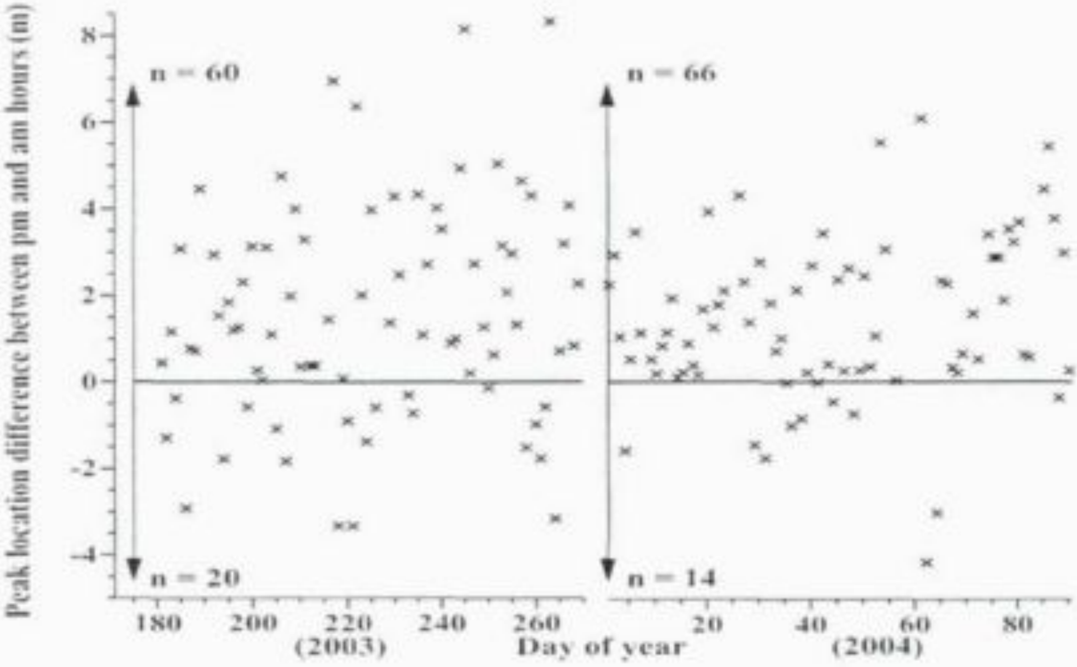

Fig. 4.18 The difference in the average x_{peak} values between 9 am to noon and noon to 3 pm for two 90-day periods where n is the number of points for which there is a positive or negative peak location difference. The x_{peak} values were estimated using Eq. 4.49 and are based on estimations of L from SLS measurements and the stability-dependent similarity constants D and P (Eq. 4.45)

(Table 3.2). The ECAT point measurements show a marked variation from one 2-min measurement to the next whereas there is a much reduced variation in the corresponding line-averaged SLS measurements. The correspondence between the two measurement methods is improved on most days under conditions when there is reduced turbulence, particularly on uniformly cloudy days and times before 10 am and after 2 pm (Figs 4.22 and 4.23). On some days, the SLS measurements were about midway between the ECAT highs and lows (for example, day of year 61 and 62 of Fig. 4.22 and 86 of Fig. 4.23) but for other days, the ECAT measurements were sometimes greater in magnitude than the SLS measurements (for example, day of year 72 to 74, 2003 of Fig. 4.23) and yet smaller in magnitude for other days (for example day of year 47, 54 and 70 of Fig. 4.22). There no evidence for a consistent underestimation in sensible heat measurements by the EC method compared to the SLS measurements over and extended period of time. Furthermore, there is no evidence to indicate that the incorrect effective beam height input was incorrect (Cain et al. 2001). An incorrect input would have caused a consistent overestimation or underestimation in the SLS sensible heat measurements compared to EC measurements: the results of the error analysis (Section 3.5.2.4) showed that a fractional error in the beam height of 5 % would result in a sensible heat flux density fractional error of 4 %.

4.5.4.4 Two-minute latent energy flux density estimates using EC and SLS methods and the saga of positive latent energy

Latent energy flux density $L_v F_w$ (W m^{-2}) is estimated using the shortened energy balance as a residual term:

$$L_v F_w = -I_{net} - F_h - F_{soil} \qquad 4.36$$

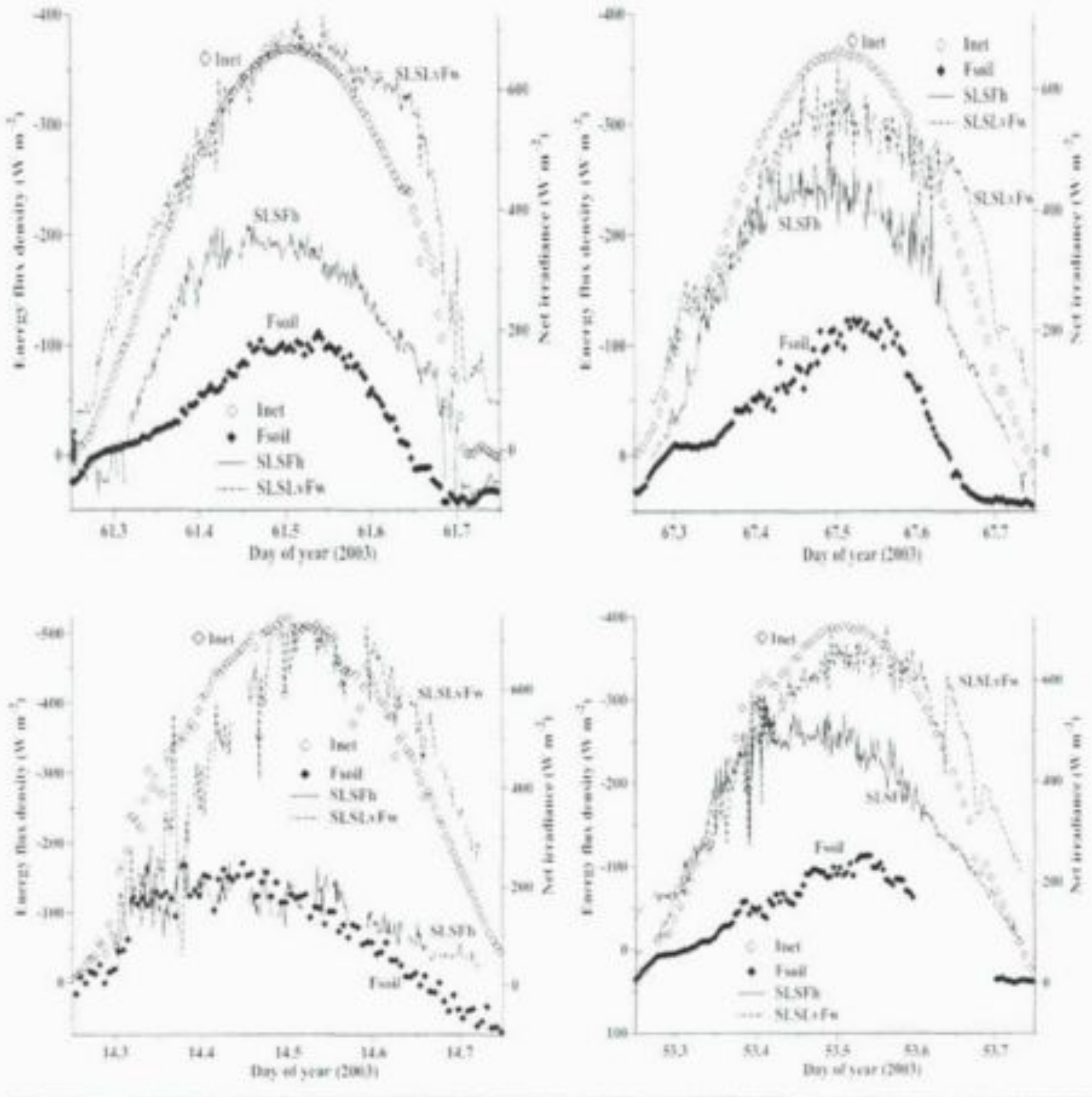

Fig. 4.19 Diurnal variation in 2-min values of SLS-measured sensible heat flux density F_h for four near-cloudless days: day of year 15, 54, 62 and 68, 2003. The asymmetrical shape of the F_h curves are evident on most cloudless days. The other components of the energy balance, I_{net}, L_vF_w and F_{soil} are shown

Generally, $L_v F_w < 0$ W m^{-2} during daytime hours, and this corresponds to evaporation, except for when dew, mist or rain occurs. However, positive $L_v F_w$ values, as estimated from BR, ECAT and SLS measurements of sensible heat flux density, have been noted during daytime hours and this deserves a closer examination. These positive $L_v F_w$ values would correspond to a downward flux of latent energy flux density which in turn implies condensation. This would seem to be impossible given that all other environmental conditions such as high solar irradiance, moderate wind speed, moderate relative humidity, implies that evaporation should be occurring. The 2-min estimates of reference evaporation for these environmental conditions result in evaporation and not condensation. However, overriding larger turbulent flows may be the cause of this downward direction.

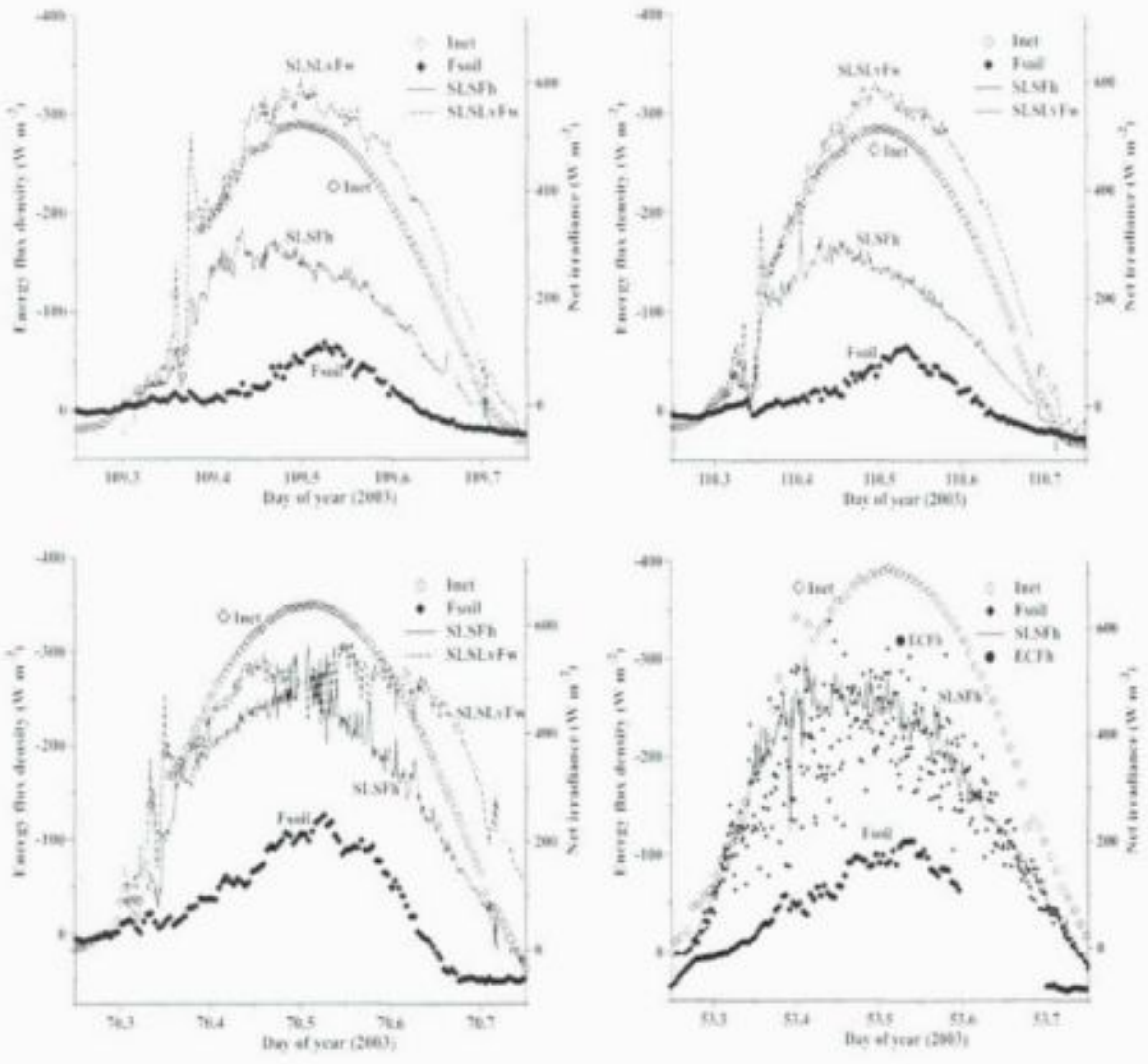

Fig. 4.20 Diurnal variation in 2-min values of SLS-measured sensible heat flux density F_h for four near-cloudless days: day of year 71, 110 and 111, 2003. The asymmetrical shape of the F_h curves is evident on most cloudless days. The other components of the energy balance, I_{net}, L_vF_w and F_{soil} are shown. The bottom-right graph, a repeat for day of year 54 (2003) also shows the 2-min ECAT sensible heat flux density measurements

From Eq. 4.36, it is noted that for positive $L_v F_w$ values, implying condensation or an energy gain at the surface

$$-F_h > I_{net} + F_{soil}. \qquad 4.53$$

In other words, the magnitude of the sensible heat flux density exceeds the available energy flux density $I_{net} + F_{soil}$. This situation could arise if there really is a downward flux density corresponding to condensation or if there is an unaccounted for term such as advection contributing to the energy balance, or if one or more of the energy balance components are in error, or if there are counter-gradient fluxes. Counter-gradient fluxes (Deardorff 1966) appear to contradict Fick's Law (Eq. 2.6, for example) since under counter-gradient fluxes, negative $\partial \overline{T} / \partial z$ (air temperature gradient)

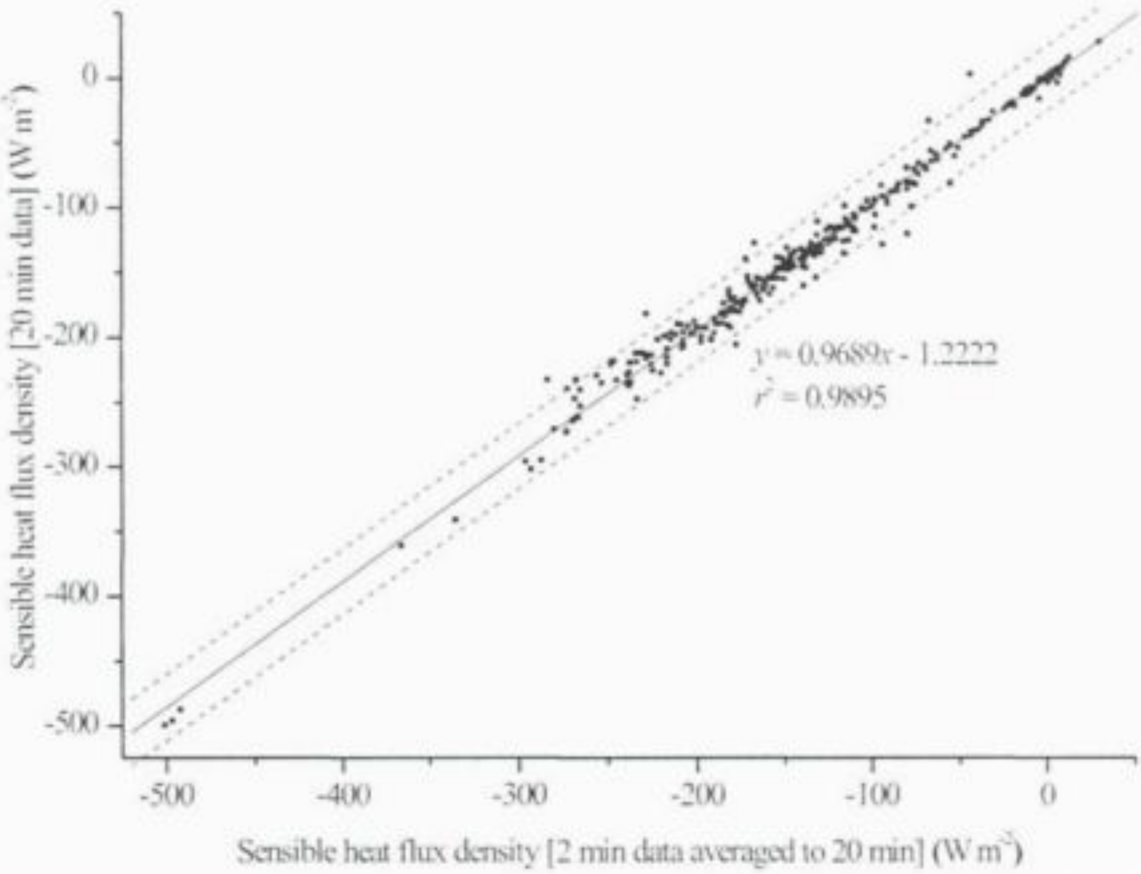

Fig. 4.21 A comparison between EC sensible heat flux density (CA27 system) measured using a 20-min average and two-minute averages then averaged to 20 min

values result in positive F_s values. This implies a flux from cold to hot instead of the expected hot to cold. As the American Meteorological Society Glossary (2000) explains, while this appears to violate a law of thermodynamics that states heat flows from hot to cold, those laws are found not to be violated when non-local motions (air parcels moving across finite distances) are considered. Flux is not caused by, nor related to, the local gradient when coherent structures are present. The Glossary defined coherent structures as: "Three-dimensional regions in a turbulent flow with characteristic structures and lifetimes in terms of velocity, temperature, etc., that are significantly larger or longer-lived than the smallest local scales."

An examination of the 2-min data collected during 2003 show that there are occurrences for which:

$$-(F_s)_{EC} > I_{net} + F_{soil} \text{ [equivalent to } (L_v F_w)_{EC} > 0 \text{ W m}^{-2}\text{]},$$

and/or

$$-(F_s)_{SLS} > I_{net} + F_{soil} \text{ [equivalent to } (L_v F_w)_{SLS} > 0 \text{ W m}^{-2}\text{]}$$

(Eq. 4.53). the result of this examination is shown in Fig. 4.24: about 40 % of the positive values are less than 15 W m^{-2} for both ECAT and SLS 2-min measurements, while the SLS method has about 20 % more occurrences. the ECAT measurements only commenced on day of year 46, 2003 and the EC measurements were suspended between day of year 227 and 243 (Table 4.2). The data set used also included the daytime dew/mist/rain events.

An examination of the 2-min air temperature gradients, collected since day of year 229 (2003), showed that positive air temperature gradients were rare - usually only occurring in the presence of

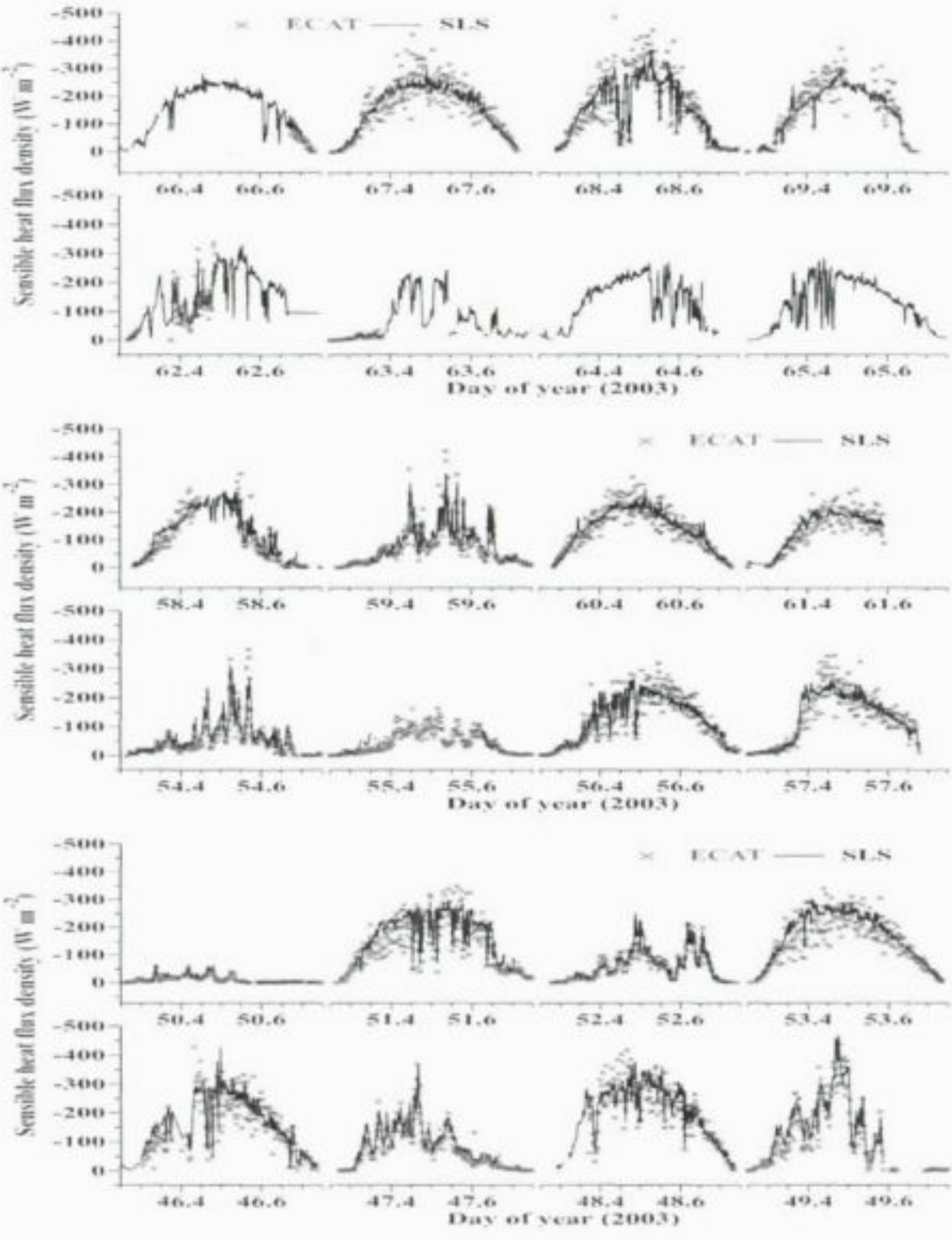

Fig. 4.22 Diurnal variation in 2-min sensible heat flux density as measured by SLS and ECAT systems for a period of 24 consecutive days (day of year 47 to 70 or 16 February to 11 March, 2003). On some of the days, ECAT measurements were not performed. Also, occasional power disruptions prevented ECAT or SLS measurements

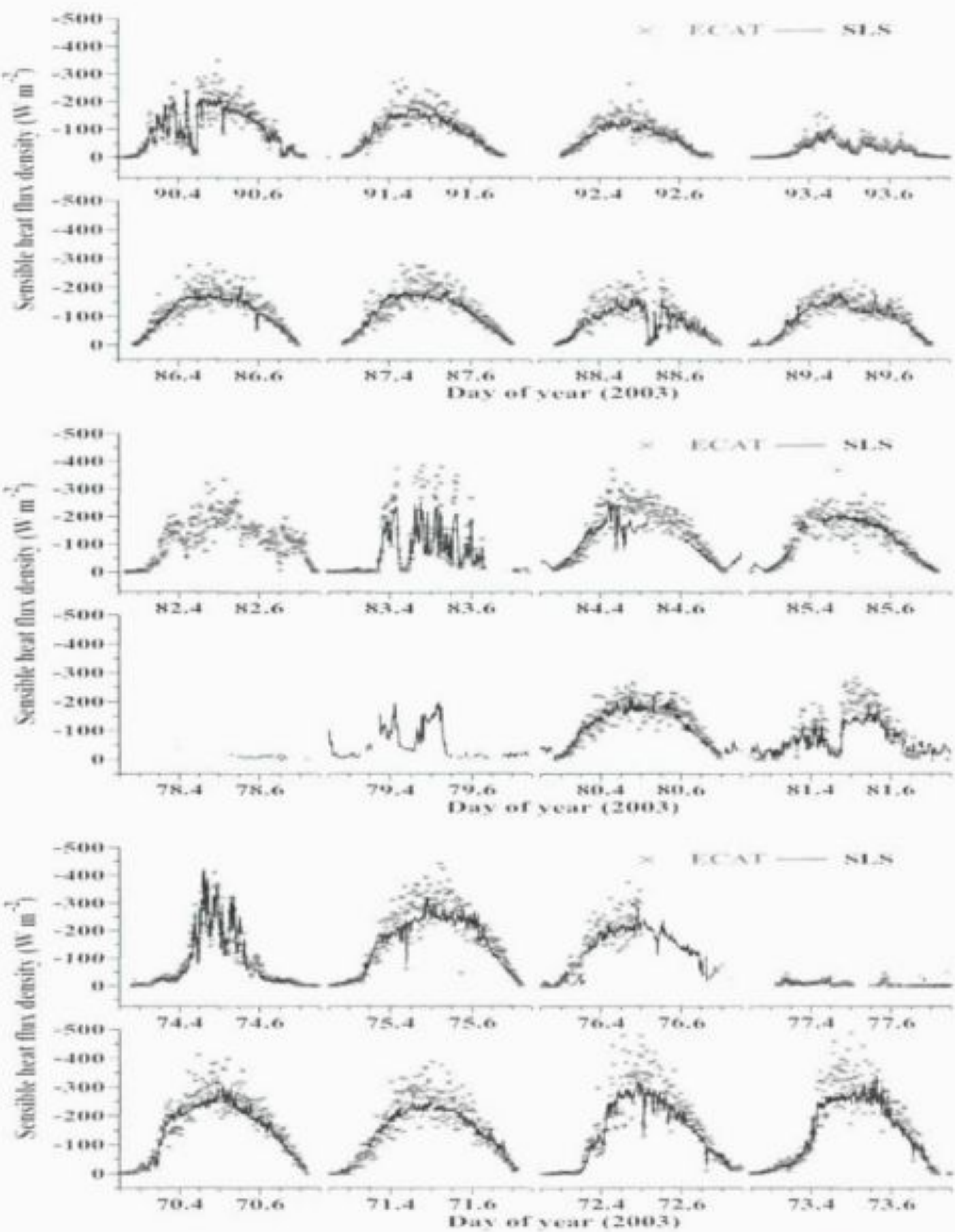

Fig. 4.23 Diurnal variation in 2-min sensible heat flux density as measured by SLS and ECAT systems for a period of 24 days (day of year 71 to 94 or 12 March to 4 April, 2003)

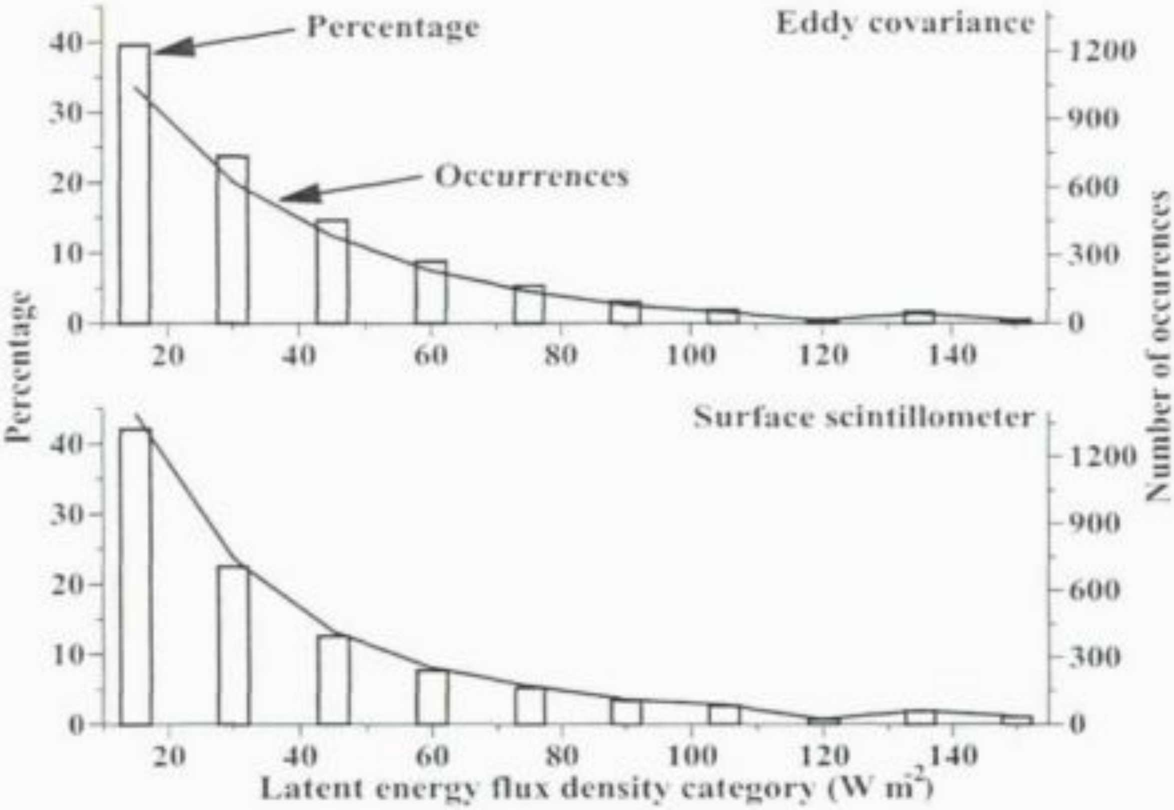

Fig. 4.24 Histogram plots of the percentage frequency (left-hand y-axis) and number of occurrences (right-hand y-axis) of positive 2-min latent energy flux densities for the 2003 data set for ECAT and SLS measurements. The histogram limits used were < 15 W m^{-2}, between 15 and 30 W m^{-2}, between 30 and 45 W m^{-2}, etc. up to 135 to 150 W m^{-2}. The total number of occurrences was 3318 for SLS measurements and 2638 for ECAT measurements

low net irradiance and/or dew/mist/rain. Days for which there were large changes in net irradiance, day 320 (2003) for example, show large changes in air temperature gradient and air to measured infrared temperature (IRT) differentials but these differentials seldom change sign (Fig. 4.25, top two curves). This however does not mean that counter-gradient fluxes do not occur since the measured fluxes could indeed be opposite to that expected by Fick's Law. Counter-gradient fluxes occurred on day of year 274 (2003), Fig. 4.26, again associated with a reduction in solar irradiance.[1] Interestingly, the air to canopy temperature differentials did not illustrate the counter-gradient flux but the profile air temperature measurements using the 75-µm diameter thermocouples did. Of particular note in

1 The role that clouds play in modifying the surface solar irradiance has been investigated by Gu et al. (2001). They used a spectral analysis. Two temporal regimes were shown to modulate the surface irradiance by clouds. They reported on a convective/mesoscale of tens of minutes to hours and a turbulent scale of several minutes. Paw U et al. (1992) reported on organised temperature ramp patterns for flow above and within agricultural plant canopies. They noted that such patterns have been seen for all stabilities in traces of air temperature, water vapour and carbon dioxide. They postulated that ramp-like patterns are associated with the presence of turbulent coherent structures that occur much of the time in the lower boundary layer. They did not discuss the possible role that solar irradiance may play in creating turbulent coherent structures - the data of Figs 4.25 and 4.26 seems to show this

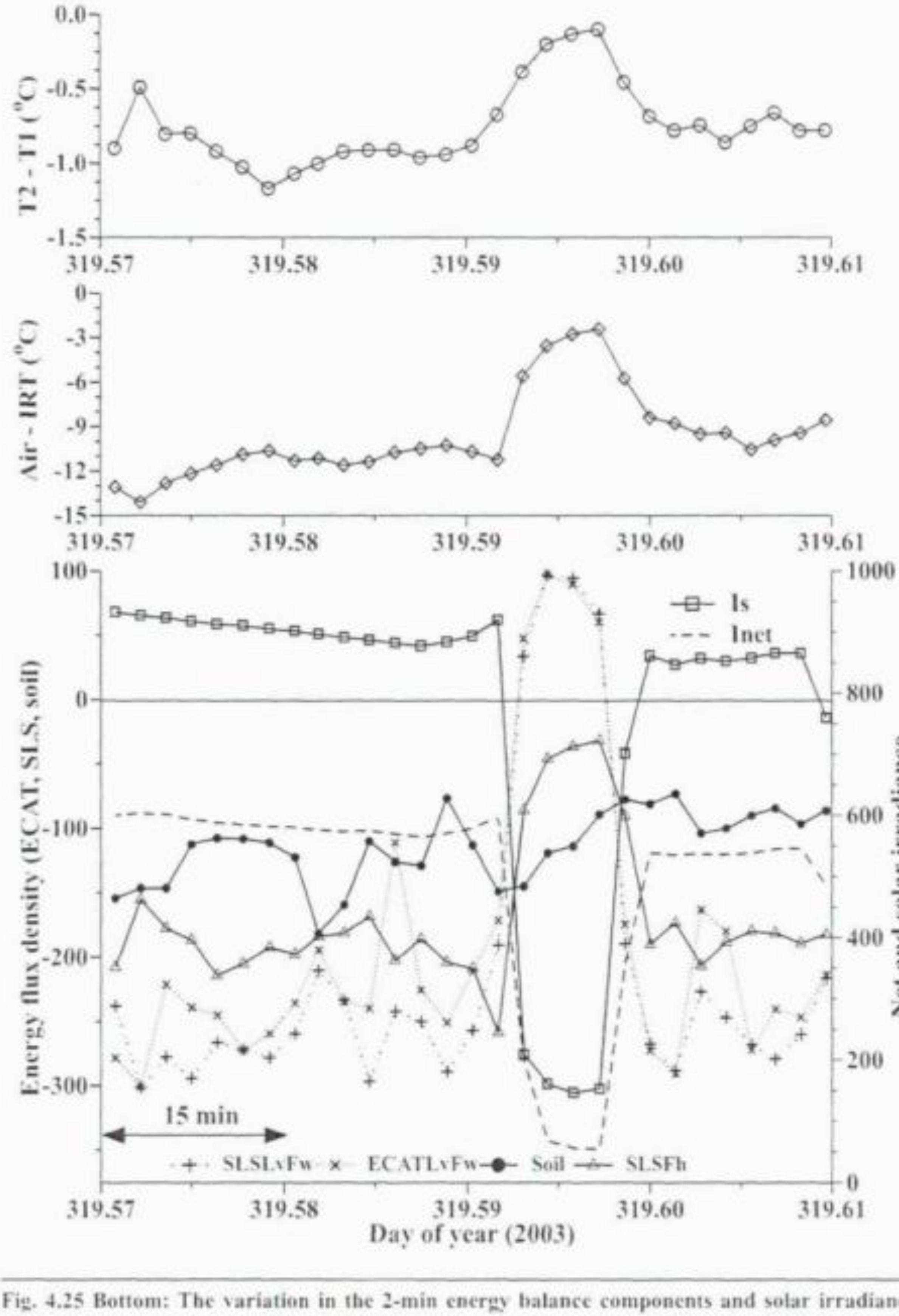

Fig. 4.25 Bottom: The variation in the 2-min energy balance components and solar irradiance for day of year 320 (2003) before, during and after a large reduction in solar irradiance. Of note is the positive latent energy flux densities after the reduction;
Top two graphs: The variation in the air and IRT and the air profile temperature differences showing that a change in sign due to the reduced solar irradiance did not occur

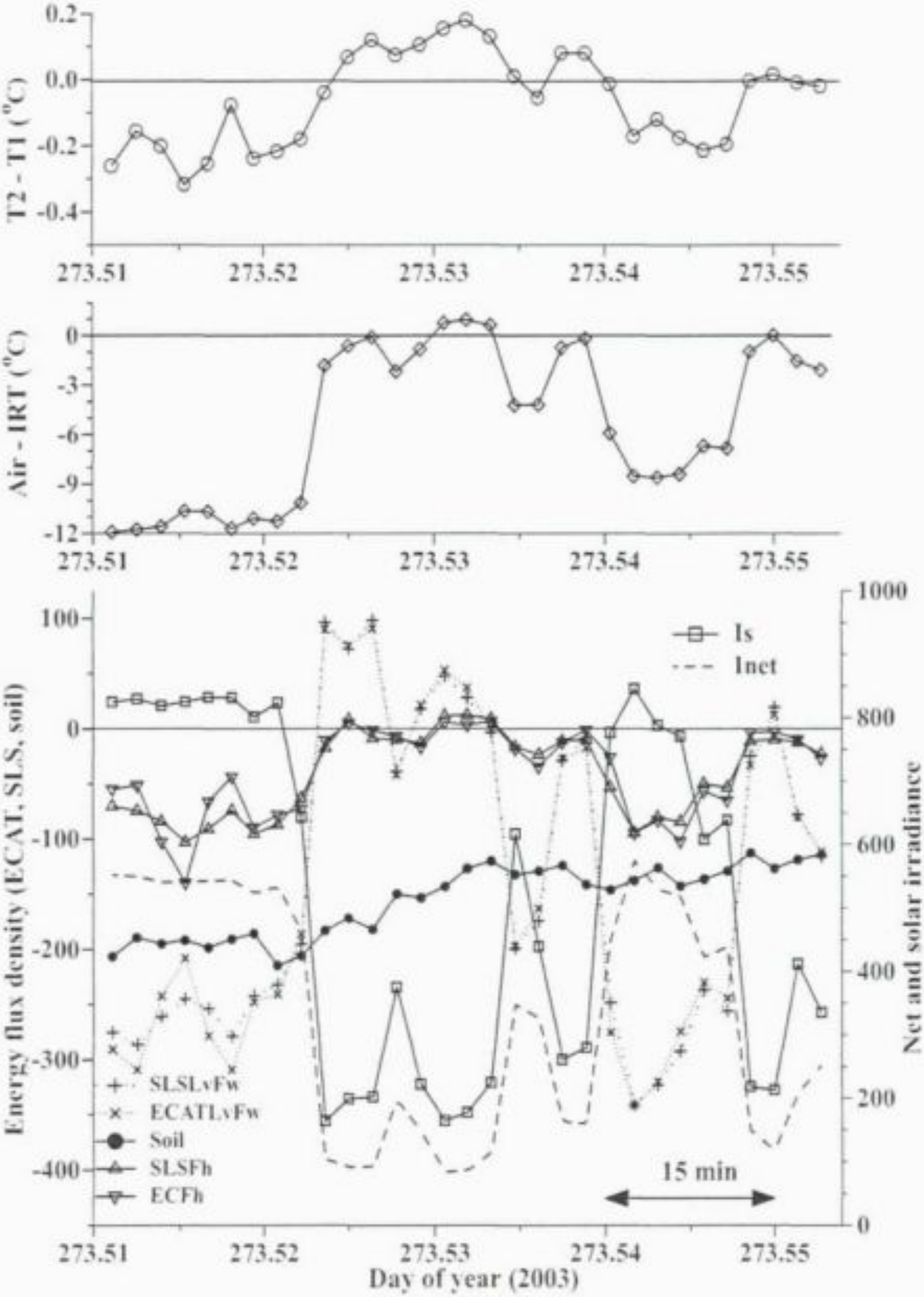

Fig. 4.26 Bottom: The variation in the 2-min energy balance components and solar irradiance for day of year 274 (2003) before, during and after a large reduction in solar irradiance. Of note is the positive latent energy flux densities after the reduction;
Top two graphs: The variation in the air and IRT and the air profile temperature differences showing a change in sign due to the reduced solar irradiance

Fig. 4.26 is the excellent correspondence between sensible heat flux density measured using ECAT and SLS methods. Both methods were able to detect the positive sensible heat values.

The data shows that of the total set of positive latent heat values, they most often occur following a transition from a high net irradiance condition to a lower value due to cloud (Figs 4.25 and 4.26). For example for day of year 320, 2003 (Fig. 4.24), there was a rapid reduction in solar irradiance over 10 min following a return to almost the same irradiance. Both EC and SLS measurements were in phase with the net irradiance changes but the soil heat measurements showed a slower response. One would expect that the soil temperature and soil heat measurements, at a depth, would be lagged. Hence, if the magnitude of F_{soil} does not change much, the available energy flux density would decrease by much more than that expected with the possibility therefore that $-F_h > I_{net} + F_{soil}$. However, given the magnitude of the soil heat flux density, rarely greater than 200 W m^{-2}, the positive latent energy amounts associated with sudden and rapid reductions in net irradiance cannot be attributed only to a lag of the soil measurements. The net irradiance measurements are also lagged but only slightly since the time constant, which refers to the time taken for the net radiometer to respond to 63.2 % of a change in the actual net irradiance, is given by the manufacturers as approximately 30 s.

As expected, whenever there is a decrease in net irradiance I_{net}, the estimated latent energy flux density $L_v F_w$ increases since $L_v F_w$ is estimated using: $L_v F_w = -I_{net} - F_h - F_{soil}$ (Figs 4.25 and 4.26).

Counter-gradient fluxes are probably not easily noticed in practise if averaging periods of the order of 30 min or longer are used. The longer the averaging period, the greater the chance that the high and low magnitudes of the sensible heat flux density, for example, are averaged. Even with the 2-min data collected here, the counter-gradient events were not immediately obvious.

To summarize: given the good agreement between the 2-min EC and SLS sensible heat flux density, the estimates of latent energy are also in good agreement as a result of invoking the energy balance. Positive latent energy fluxes were detected and it is unlikely that these are due to measurement method error. Unfortunately, we did not perform 2-min profile measurements of water vapour pressure to confirm that these latent energy fluxes were not counter to the profile gradients.

4.5.4.5 SLS and SR 2-min sensible heat flux density comparisons

The SR measurements, which rely on an unshielded 75-µm fine-wire type-E thermocouple and high frequency measurements of air temperature (10 Hz when using a Campbell CR23X, 21X or CR5000 datalogger) and 8 Hz when using a CR10X logger, tend to follow the SLS 2-min measurements of sensible heat flux density (Fig. 4.27). Almost a month of data showed fair correspondence with some scatter but a slope close to unity (Fig. 4.28). Due to the variation exhibited, SR measurements should be restricted to 20- or 30-min averages for this size thermocouple. Very few of the nighttime SR measurements could be used.

For the future, the influence of the following needs to be tested: measurements above different surfaces; 25-µm *vs* 75-µm diameter thermocouples; measurement frequency on estimated sensible heat flux density; optimum height above soil surface.

The SR technique appears to have considerable promise for the measurement of hourly sensible heat flux density. The main advantage of the technique is that it is extremely cheap and set-up time is less than an hour. A two-channel datalogger (one channel for reference temperature and one for the

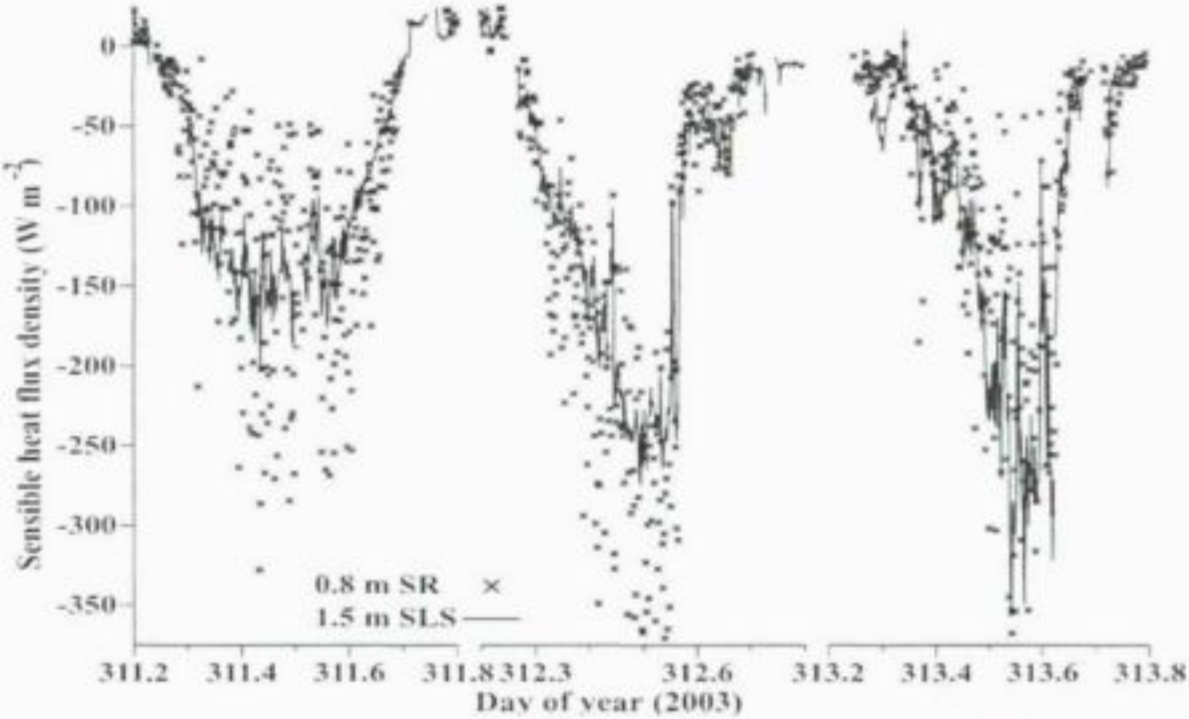

Fig. 4.27 Diurnal variation in 2-min SR and SLS sensible heat flux density for three consecutive days. For the SR measurements, a frequency of 10 Hz and a 75-μm type-E fine-wire thermocouple was used

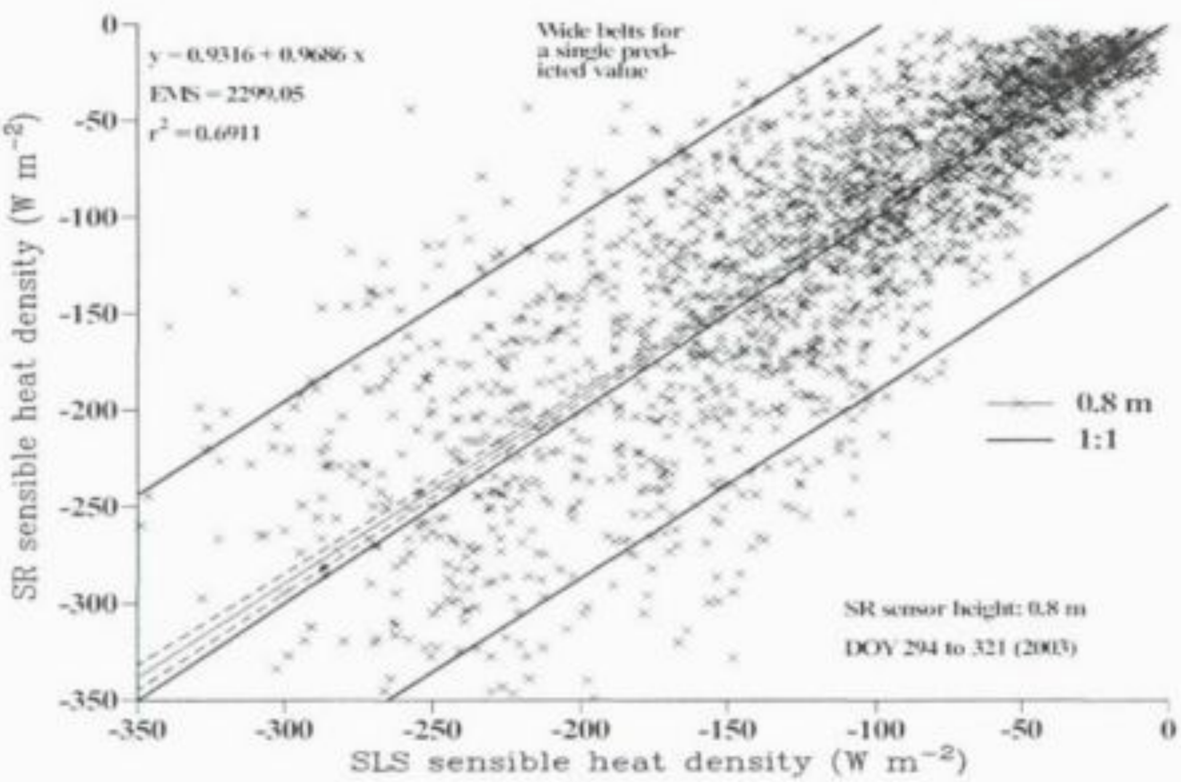

Fig. 4.28 Comparison of 2-min SLS and SR sensible heat flux density for the period 21 st Oct to 17 th Nov 2003. The SLS beam was at 1.5 m above the soil surface and the SR thermocouple was at a height of 0.8 m

thermocouple), an enclosure, the thermocouple and a support arm and stand are all that is required for the technique. The capability of performing the on-line calculations is required (Eqs 4.11 for $n = 2, 3$ and 5).

The main disadvantage of the SR technique is that the fine-wire thermocouple can easily be damaged and collect dirt, particularly cobwebs. Dew, mist or rain on the thermocouple invalidates measurements. Dew, mist or rain events may also affect BR, ECAT and SLS measurements. Another disadvantage is that at present real-time SR sensible heat measurements are not possible but with improvements in datalogger capabilities, that may change.

4.5.4.6 BR, EC, SR and SLS 20-min sensible heat and latent energy flux density comparisons

Reliable BR measurements were only collected in the second half of the project, commencing in January 2004. Previously, in Section 4.5.1, we reported on the suitability of the Vaisala HMP45C and CS500 air temperature and relative humidity sensors as an alternative to the Dew-10 cooled dew point mirror hygrometer. The BR measurements reported on here are from mid-Jan to late June 2004. Routinely, we used a 20-min averaging period although there have been reports on using a time interval shorter than this. The 2-min EC and SLS measurements were scaled to a 20-min time interval.

The aim of this section is to establish the credibility of the SLS sensible heat measurements against the BR measurements although comparisons of BR *vs* EC and BR *vs* SR measurements would be more appropriate since then point-measurements would be compared.

For easy comparison of the data, temporal plots are used to allow for visual comparisons for a range of weather conditions. For convenience, net irradiance and soil heat flux density as well as the BR, EC, SLS and SR flux densities are displayed. So as to separate out the curves for a particular graph, different y-axis and second y-axis scales had to be used. Since the data set is large, only four contrasting days were used for displaying the data (Fig. 4.29 for sensible heat flux density comparisons and Fig. 4.30 for latent energy flux density comparisons). Two of the days were near cloudless (lower two graphs of Figs 4.29 and 4.30) and two of the days had widely varying net irradiance conditions (upper two graphs of Figs 4.29 and 4.30).

On day of year 5 (2004), the wind direction was almost perpendicular to the SLS beam for the entire day (Fig. 4.14). There was remarkable agreement among all measures of the 20-min sensible heat flux density measurements for this day (Fig. 4.29, bottom left). The two BR measurement methods (using the Vaisala HMP45C and Dew-10 sensors) agreed with each other and the SR method, based on measurements at a height of 0.8 m also showed good agreement. If anything, the BR method appeared to underestimate the sensible heat in the early morning and overestimate just after 12 noon. The agreement for day of year 78 (2004), also almost cloudless (bottom right, Fig. 4.29) does not appear as good but notice the expanded scale for the left-hand y-axis. Again, the two BR methods track each other very well indeed. The SLS measurements lie between the lowest (EC in the morning and SR in the afternoon) with the BR measurements being the greatest for most of the day.

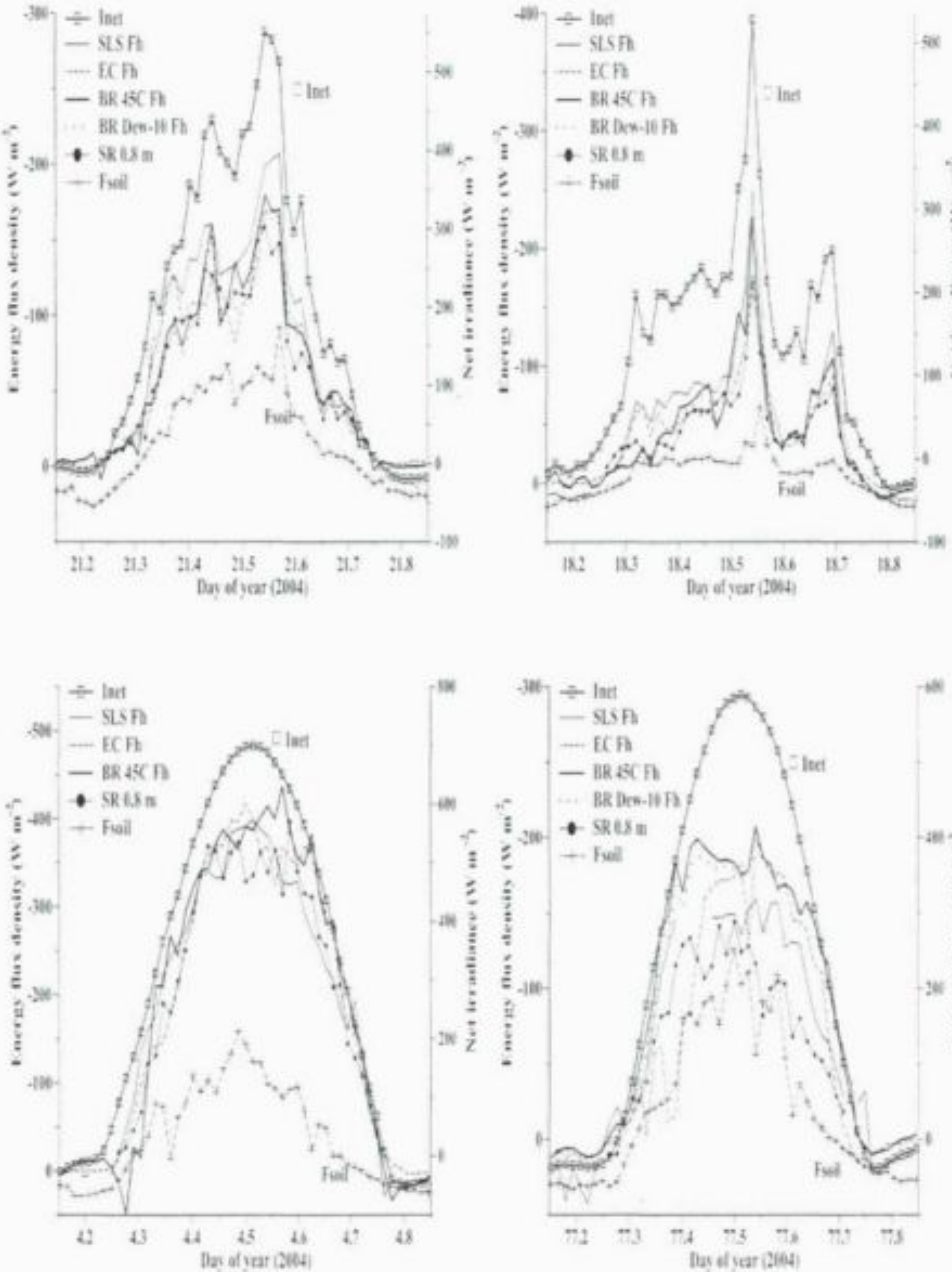

Fig. 4.29 Diurnal variation in 20-min sensible heat flux density for two cloudless days (lower set of graphs for day of year 5 and 78, 2004) and for two days with variable cloud (upper graphs for days 19 and 22, 2004). The variation in sensible heat flux density for all techniques used are shown, including the net irradiance (right-hand y-axis) and the soil heat flux density (left-hand y-axis). The height of the SLS beam was about 1.5 m above the soil surface and the SR measurement was at 0.8 m. The BR arm heights were at 1.55 m and 2.96 m above the soil surface

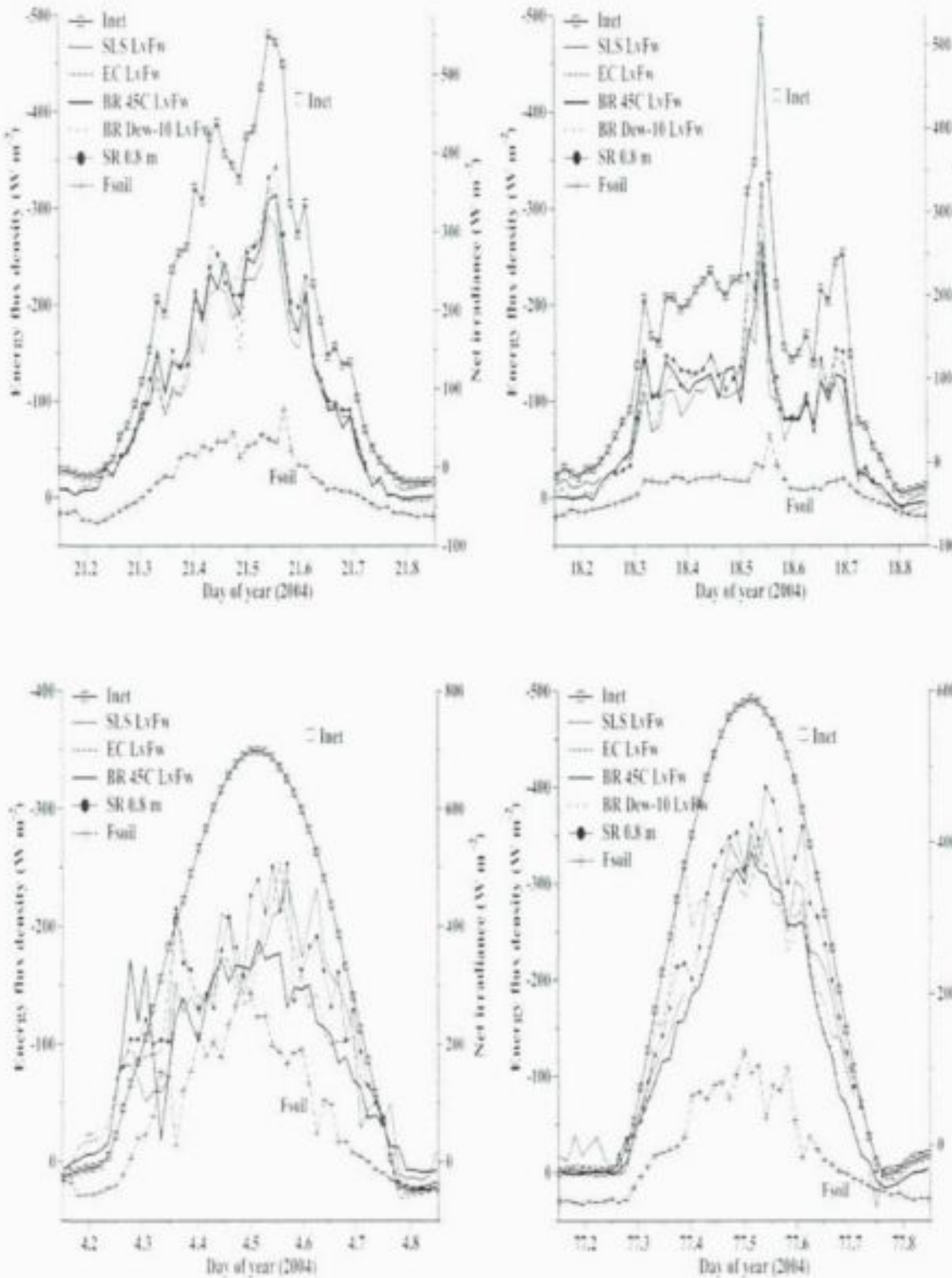

Fig. 4.30 Diurnal variation in 20-min latent energy flux density values for two cloudless days (lower set of graphs for day of year 5 and 78, 2004) and for two days with variable cloud (upper graphs for days 19 and 22, 2004). The latent energy flux density was estimated as a residual from the energy balance. Also shown is the net irradiance (right-hand y-axis) and the soil heat flux density (left-hand y-axis). The height of the SLS beam was about 1.5 m above the soil surface and the SR measurement was at 0.8 m. The BR arm heights were at 1.55 m and 2.96 m above the soil surface

4.5.4.7 EC and SLS 30-min sensible heat flux density comparisons

A comparison of SLS and EC (two EC systems, one of them part of an open path EC system) estimates of sensible heat flux density are shown for day of year 54 to 60, 2003 (Fig. 4.31). Some of the data shown includes test periods of the open EC system. There is reasonable agreement between the two EC systems. Sensible heat flux density comparisons between measurements from a second independent 3-D sonic system and the SLS system are good (Fig. 4.31). The variation that the 2-min EC measurements exhibited (Figs 4.22 and 4.23), has now been removed by the 30-min averaging.

4.5.4.8 SLS and EC sensible heat density comparisons (daily values)

The 2-min sensible heat measurements were scaled to daily totals. In this section, the emphasis is on the daily energy density (MJ m^{-2}) values (06h00 to 18h00) for the period day of year 28 to 283 (2003) corresponding to 28 January to 10 October. We report on the sensible heat densities, the net radiant densities, the soil heat densities, the available energy densities (sum of sensible and latent energy values) as well as the latent energy densities calculated from the net radiant and available energy densities.

The comparison between daily EC measurements using the EC system that was part of the open path system (ECopen system, 150 mm sonic path, half-hourly measurements summed for each 06h00 to 18h00 measurement period) and an adjacent EC measurement system (ECAT, 100 mm sonic path, two-minute measurements summed for each 06h00 to 18h00 measurement period) are shown (Fig. 4.32a). The two independent EC systems show reasonable agreement (slope = 0.931, r^2 = 0.853). Also shown is the comparison between the SLS and ECAT measurements (Fig. 4.32b). The agreement is reasonable, considering that the SLS measurement system is a path-averaging system whereas the ECAT system is a point measurement system, with the regression line accounting for 87.8 % of the variation in the measured y-values (slope = 0.896, r^2 = 0.878). The energy equivalent needed to evaporate 1 mm of water is shown in Figs 4.32a to e as 2.43 MJ m^{-2}. The error mean square of 0.204 MJ m^{-2} (Fig. 4.32b) is equivalent to 0.084 mm. Of particular note is the positive SLS sensible heat density value shown (top right of Fig. 4.32b) for a cloudy and cold day (maximum air temperature of 16.8 °C). Also of note is the lower estimate of SLS sensible heat for large magnitude values (bottom

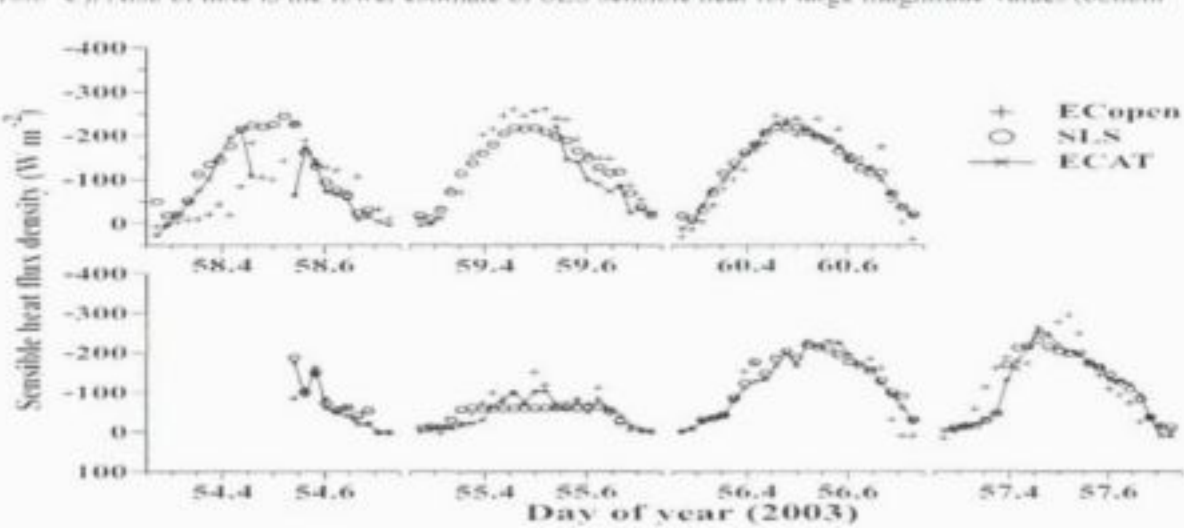

Fig. 4.31 Half-hourly sensible heat flux density measurements for the two EC systems and the SLS system for one week. All points represent 30-minute averages between 6 am to 6 pm of the specified day

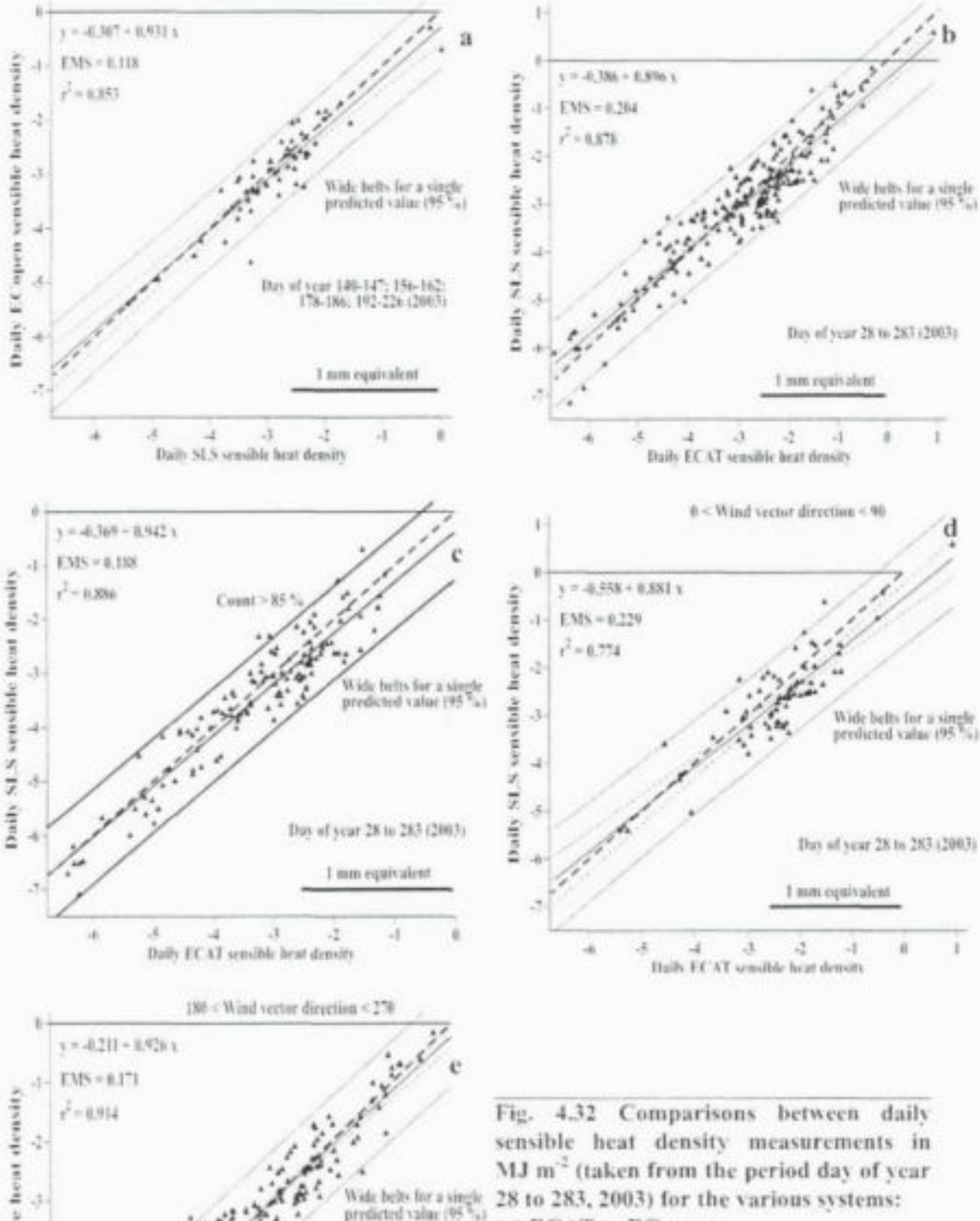

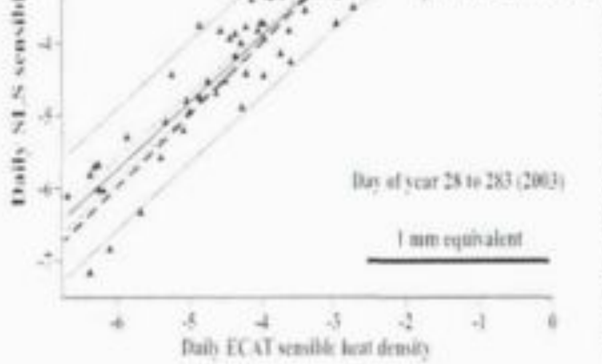

Fig. 4.32 Comparisons between daily sensible heat density measurements in MJ m^{-2} (taken from the period day of year 28 to 283, 2003) for the various systems:
(a) ECAT *vs* ECopen;
(b) ECAT *vs* SLS;
c) ECAT *vs* SLS for daily percentage count of good data exceeding 85 %;
(d) ECAT *vs* SLS for wind directions between 0 and 90° mainly from residential areas;
(e) ECAT *vs* SLS for wind directions between 180 and 270° (largely perpendicular to beam)
The dotted line in each case is the 1:1 line

left of Fig. 4.32b). These measurements correspond to largely cloudless days. If the measurements are restricted to days for which the percentage count of good two-minute data exceeds 85 % (Fig. 4.33c), the comparisons are improved (slope = 0.942, r^2 = 0.886). Missing two-minute data results in an incomplete record and larger (- closer to zero) sensible heat densities. In many cases, the count of missing two-minute data was not the same for the SLS and ECAT systems and were associated with rain or dew events or misalignment of the SLS. The error mean square is 0.188 MJ m^{-2} (Fig. 4.32c), equivalent to 0.077 mm.

Separating the SLS sensible heat measurements according to the 0 to 90° and 180 to 270° wind directions (Fig. 4.32d, e) indicate reasonable agreement with ECAT sensible heat densities (slope of 0.881 and 0.926 respectively; r^2 = 0.774 and r^2 = 0.914 respectively) with the 180 to 270° comparisons marginally better. The sensible heat density comparisons for the SLS and ECAT methods were more variable for the 0 to 90° wind directions (error mean square is 0.229 compared to 0.171 MJ m^{-2} for the 180 to 270° directions). This is expected since the 0 to 90° wind directions correspond to wind from residential areas including trees and also have the shortest fetch distance.

4.5.5 Latent energy density comparisons

Latent energy flux density was indirectly calculated, using two-minute data, as a residual from net irradiance, soil heat and SLS or ECAT sensible heat flux density except for the case of the open path eddy covariance system ECopen for which it was measured directly from the covariance between the fluctuations in water vapour density and vertical wind speed. The two-minute data were then integrated for the 06h00 to 18h00 periods. Data, not shown, indicate that the sum of the sensible heat and latent energy fluxes measured using the open path eddy covariance system ECopen was significantly less in magnitude than the available energy flux density. Twine et al. (2000) reported an underestimation for both sensible heat and latent energy fluxes using the EC method. They recommended a procedure to correct the EC measurements. The EC sensible heat measurements compare favourably with BR, SLS and SR measurements and therefore do not need correction. Of note is that Savage et al. (2000) found no evidence for the under-estimation in sensible heat using the EC methods for a whole range of surfaces: grassland, vineyard, bare soil, forest (pine).

For the ECopen system, the closure ratio was significantly different from 1 due to the poor comparison between the SLS-estimated latent heat and the open path eddy covariance latent heat density (Fig. 4.33a) with a slope of 1.094 but with an error mean square of 0.632 MJ m^{-2}, and r^2 = 0.239. Some of this poor agreement may be due to a reported manufacturer error and some of it due to the spatial separation between the sensors causing an underestimate in the covariance. This underestimation of latent energy density has been reported in the literature (Twine et al. 2000, for example) but the exact cause not clearly identified.

Clearly though, the EC latent energy flux measurements do require correction (Mauder et al. 2004). However, these authors warn that in spite of all the corrections applied, "further investigations are necessary because the energy balance still cannot be closed by measurements during the daytime."

The comparison between the ECAT-estimated and SLS-estimated latent heat density, both using net irradiance and soil heat flux density in calculating two-minute latent heat flux density summed to a day, is reasonable (Fig. 4.32b) with a slope of 1.059, r^2 = 0.962 with an error mean square of 0.295 MJ m^{-2}, equivalent to 0.121 mm.

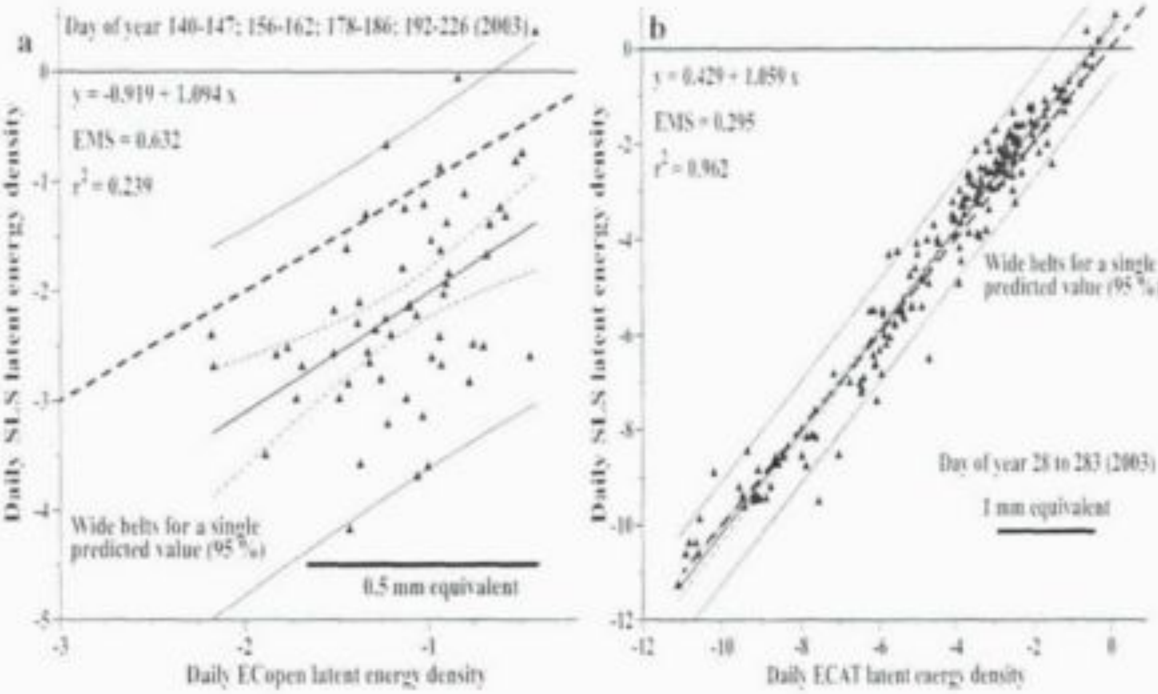

Fig. 4.33 Comparisons between latent energy density in MJ m^{-2} (taken from the period day of year 28 to 283, 2003):
(a) measured using the open path EC system ECopen and that estimated from SLS sensible heat density, net radiant and soil heat densities;
(b) estimated from SLS sensible heat density, net radiant and soil heat densities and estimated from ECAT sensible heat density, net radiant and soil heat densities
All measurements were 2-minute measurements summed over 06h00 to 18h00 apart for the ECopen system which involved 30-min measurements summed over 06h00 to 18h00

4.6 Conclusions

1. Laboratory and field measurements showed that for BR measurements, either the Vaisala CS500 or the HMP45C capacitive sensor may be used as a replacement for the Dew-10 cooled dew point mirror sensor. Water vapour pressure profile differences of at least 0.01 kPa, as is required for BR measurements, were possible with these thin film polymer capacitive sensors.

2. An examination of wind direction demonstrated that the largest differences between SLS and EC sensible heat densities occurred for wind directions between 0 and 60° corresponding to winds from residential areas with a limited fetch. Comparisons between SLS- and EC-measured sensible heat flux density, for selected days, did not appear to be affected by differences between wind perpendicular to the beam and winds parallel to the beam. For the period January to end March 2004, the wind was perpendicular to the beam 35 % of the daytime hours compared to less than 5 % for wind parallel to the beam.

3. A footprint analysis, for a short grass surface, allowed three key parameters to be calculated: the peak location of the footprint, the footprint fraction itself and the 90 % fetch to measurement height ratio. For daytime hours, conditions were most often convectively unstable which resulted in fetch to height ratios less than the commonly accepted 100:1 ratio and also resulted in peak footprint locations very close, between 2 and 10 m, to the point/line of measurement. The SLS-measured sensible heat

flux density curves tended to be asymmetrical. This asymmetry is likely due to the greater instability before noon that in the afternoon.

4. Two-minute measurements of EC, SLS and SR sensible heat flux density were in good agreement much of the time, particularly for cloudless conditions. There were however periods for which the magnitude of the SLS-measured sensible heat flux density exceeded the measured available heat flux density. The result was that the calculated latent energy flux density was positive, apparently corresponding to condensation. Further examination showed that some of these events corresponded to counter-gradient events dominated by overriding coherent structures of undetermined origin.

5. Twenty-minute measurements of BR, EC, SLS and SR sensible heat flux density were also in good agreement much of the time, particularly for cloudless conditions. No measurement method resulted in measurements that were consistently greater or larger than the other measurement techniques apart from the SR method which generally resulted in lower sensible heat magnitudes. The ECopen system underestimated latent heat magnitude compared to the residual SLS amount estimated from SLS sensible heat, net irradiance and soil heat.

6. Daily estimates of latent energy density for the SLS and EC methods were compared for a period of about 250 days during 2003. The 95 % confidence bands for a single predicted value were within 0.5 mm of the regression line and the error mean square was 0.295 MJ m^{-2} or about 0.12 mm. Statistically, there was no significant difference between the point measurements using the EC residual method and the line-averaged estimate obtained using the SLS method.

Chapter 5

Estimation of seasonal evaporation using surface layer scintillometer and eddy covariance measurements

5.1 Abstract

The main aim of this research is to investigate the application of the dual-beam surface layer scintillometer (SLS) and eddy covariance (EC) methods for estimating evaporation in an open and mixed grassland community in a summer rainfall area. Evaporative water loss is often the largest component of the hydrological cycle and is usually calculated as the remainder term of the soil water mass balance. Quantifying the total evaporative loss is difficult but necessary for an informed, objective long-term management plan of catchment areas. Determination of total evaporation from a grassland site in the midlands of KwaZulu-Natal, South Africa (-29.6348° S, 30.4329° E) with an altitude of 671.32 m with a very slight slope) was carried out over eighteen months (mid January 2003 to June 2004). The measured sensible heat flux density, net irradiance and soil heat flux density were used to estimate latent energy flux density every two minutes. The 2-min estimates were then totalled for each day for the 6 am to 6 pm period. The estimates from the SLS and EC methods were averaged for each day. The daily values were totalled to form a monthly total. The seasonal trend in latent energy density (evaporation) and the impact of the mowing and fire treatments over the 18-month period is discussed. After the 2004 mowing, the Bowen ratio increased significantly. Following the removal of vegetation, the sensible heat daily total increased and the latent energy daily total decreased. The levels were maintained for nearly two months, except for rain days.

Priestley-Taylor evaporation was a poor estimate of evaporation amounts during this period with below-average expected rainfall, overestimating the measured evaporation. The evaporation total of 673 mm for 2003 and 306 mm for the first six months of 2004 exceeded the rainfall totals of 532 and 248 mm respectively. The magnitude of the daily total latent energy density typically varied from a summer maximum of about 12 MJ m^{-2} (4 mm) to a winter season minimum of 2 MJ m^{-2} (less than 1 mm). The SLS and EC methods were shown to be suitable for long-term monitoring of daily total evaporation and capable of detecting the effects of management fires and mowing.

5.2 Introduction

One of the most important factors affecting water supply from any catchment is the evaporative loss from the vegetative community and soil surface. Evaporation is an important part of the hydrological cycle. This component also appears as a term in the energy balance in the form of latent energy. Various techniques are used to measure evaporation and these are discussed in Chapters 3 and 4. The available energy flux density defines the sum of sensible heat and latent energy flux density. The seasonal variation in available energy therefore plays a crucial role and in part contributes to the seasonal variation in sensible heat and latent energy. However, other factors define the partitioning of the available energy.

The main aim of this chapter is to present the results of the seasonal measurements of the evaporation measurements, a period spanning almost eighteen months. Two treatments imposed by the farmer included fire and mowing. The grass is used as winter feed for animals. One fire treatment and two mowings were imposed during the eighteen-month period.

5.3 Material and methods

Evaporation measurement techniques included a surface layer scintillometer (SLS) method and the eddy covariance (EC) technique. The SLS beam path-length was 101 m and the beam height above the soil surface was between 1.5 and 1.65 m. The 3-D sonic placement height was 1.45 m until the end of December 2003 and thereafter 2.12 m. The details of these measurements are discussed in Chapters 4 and 5. Details of operations are listed in Table 4.2. For both SLS and EC methods, the measured sensible heat together with the measured surface net irradiance and the soil heat flux density were used to estimate the latent energy flux density. Initially only two net radiometers were used. During 2004, three net radiometers were used. Between two and five soil heat flux plates were used. The 2-min measurements between 6 am and 6 pm were then totalled for each day. The SLS and EC measurements were at various times cross-checked against Bowen ratio and other EC measurements of sensible heat. Since the SLS and EC estimates of sensible heat from the two methods are highly correlated (Chapter 5), the two estimates were averaged. The daily latent energy density was then converted into mm units by dividing by the specific latent heat of vapourisation. Other measurements included volumetric soil water content at a depth of 50 mm and the surface reflection coefficient. Measurements from an automatic weather station were also available.

Field measurements were conducted from 14 January 2003 to August 2004 above an open and mixed grassland community in the Hay Paddock area neighbouring Ashburton and close to Pietermaritzburg, South Africa (-29.617° S, 30.417° E) with an altitude of 706 m. The average slope of the study site (Fig. 4.1) is 1° 15' to the SE. To the south of the instrumentation, the site is exposed and the slope increases significantly. To the north of the study area, there is a residential area and tall trees (Fig. 4.1).

The long-term annual rainfall for Pietermaritzburg (South African Weather Bureau data) is 928 mm (58 years of data) and the mean maximum and minimum air temperatures are 24.8 and 12.3 °C respectively. During winter, there is frequent dewfall but frost hardly ever occurs. Management practices included mowing (normally in April each year) and burning (in August when firebreaks are established and in October).

5.4 Results and discussion

The energy balance components for the entire 18-month period, for weekly totals, are shown in Fig. 6.1. The conversion from the left-hand y-axis units of MJ m^{-2} to mm of evaporated water is shown in the top left of Fig. 6.1. The right-hand y-axis shows the cumulative evaporation at seven-day intervals and the daily rainfall totals. The three management events (two mowing and one fire) are indicated by arrows. Fig. 6.1 serves as a useful reference and also removes some of the large variations in latent energy and sensible heat when a daily time-step is used. The 18-month period is divided into three six-month periods with a daily time-step (Figs 6.2 to 6.4). The x- and y-axes scales for each graph are almost the same which enables comparisons to be made across the eighteen-month period. In each graph, the right-hand y-axis represents the scale for rainfall and the same scale is used for the cumulative evaporation for the month depicted. The total rainfall for each month is indicated at the bottom right of each graph. The total recorded rainfall for the period 1 Jan to 31 Dec 2003 was 532 mm, well below the long-term annual rainfall for Pietermaritzburg of 928 mm. The total

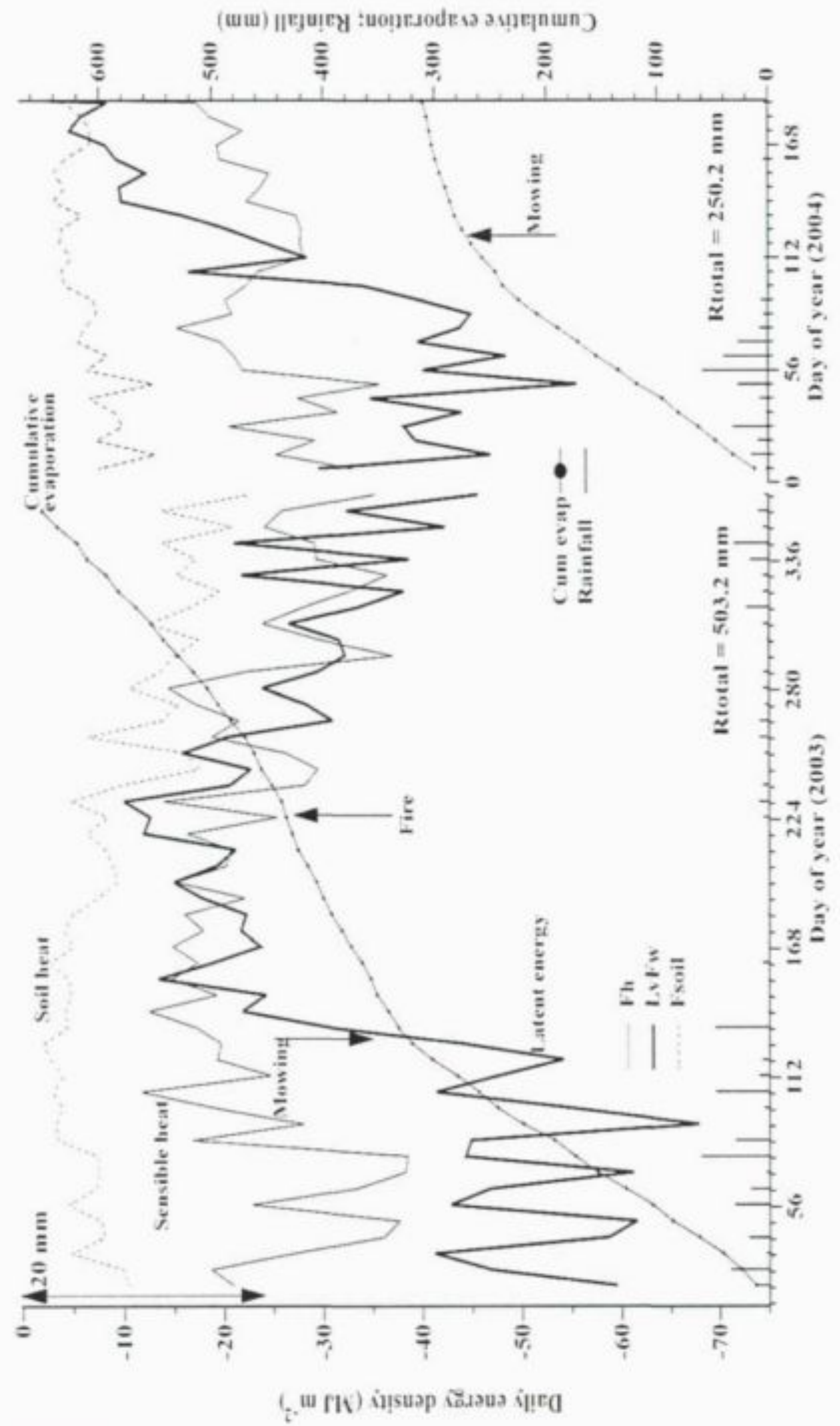

Fig. 6.1 Seasonal variation in weekly sensible heat, latent energy and soil heat density (left-hand y-axis, MJ m^{-2}), cumulative evaporation and daily rainfall (mm) for the period 14 Jan 2003 and 30 June 2004. The total rainfall to date is shown, bottom right of each graph

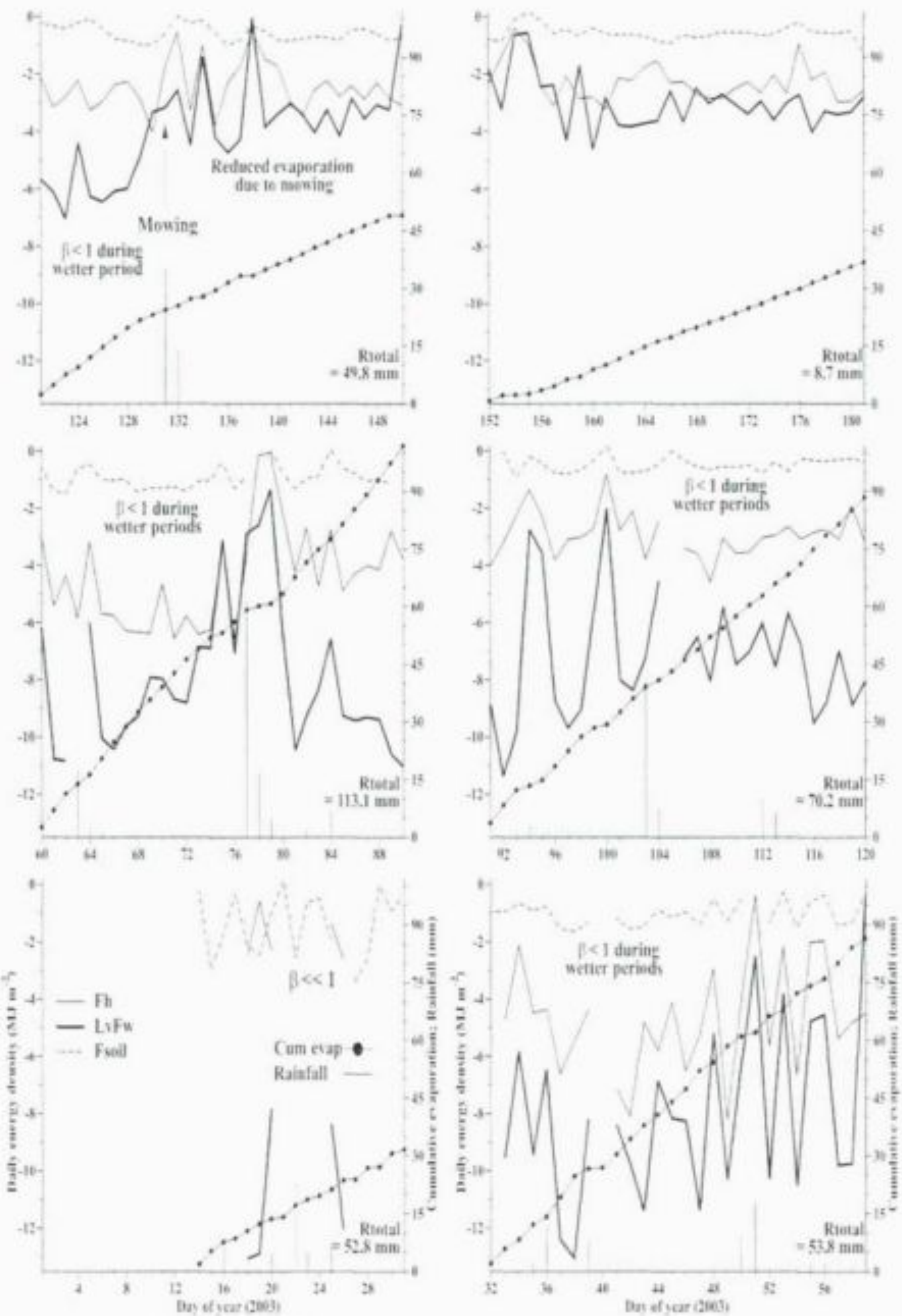

Fig. 6.2 Seasonal variation in daily sensible heat, latent energy and soil heat density (left-hand y-axis, MJ m^{-2}), cumulative evaporation and daily rainfall (mm) for the period 14 Jan and 30 June 2003. The total monthly rainfall is shown, bottom right of each graph

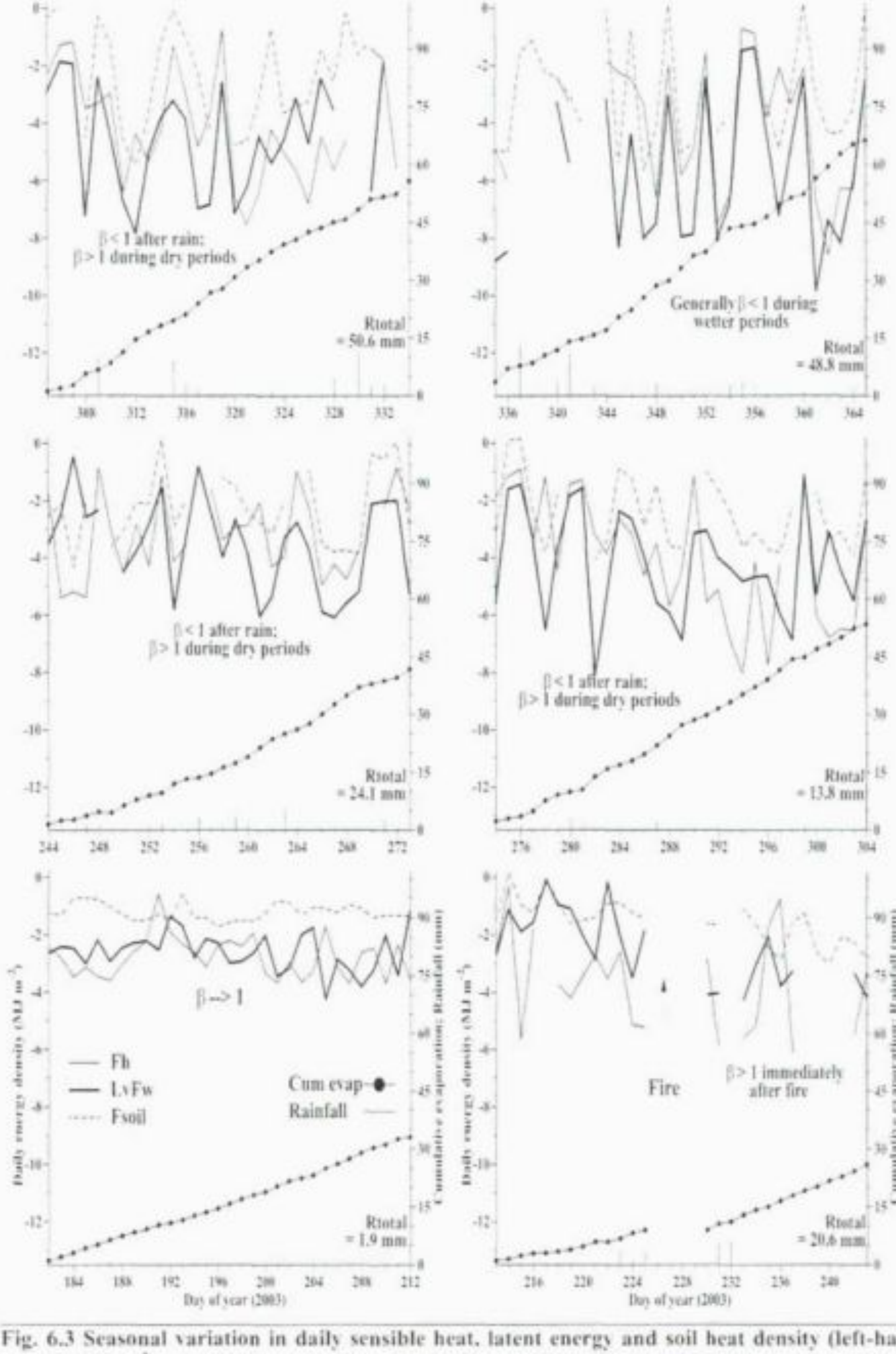

Fig. 6.3 Seasonal variation in daily sensible heat, latent energy and soil heat density (left-hand y-axis, MJ m^{-2}), cumulative evaporation and daily rainfall (mm) (right-hand y-axis) for the period 1 Jul and 31 Dec 2003. The total monthly rainfall is shown, bottom right of each graph

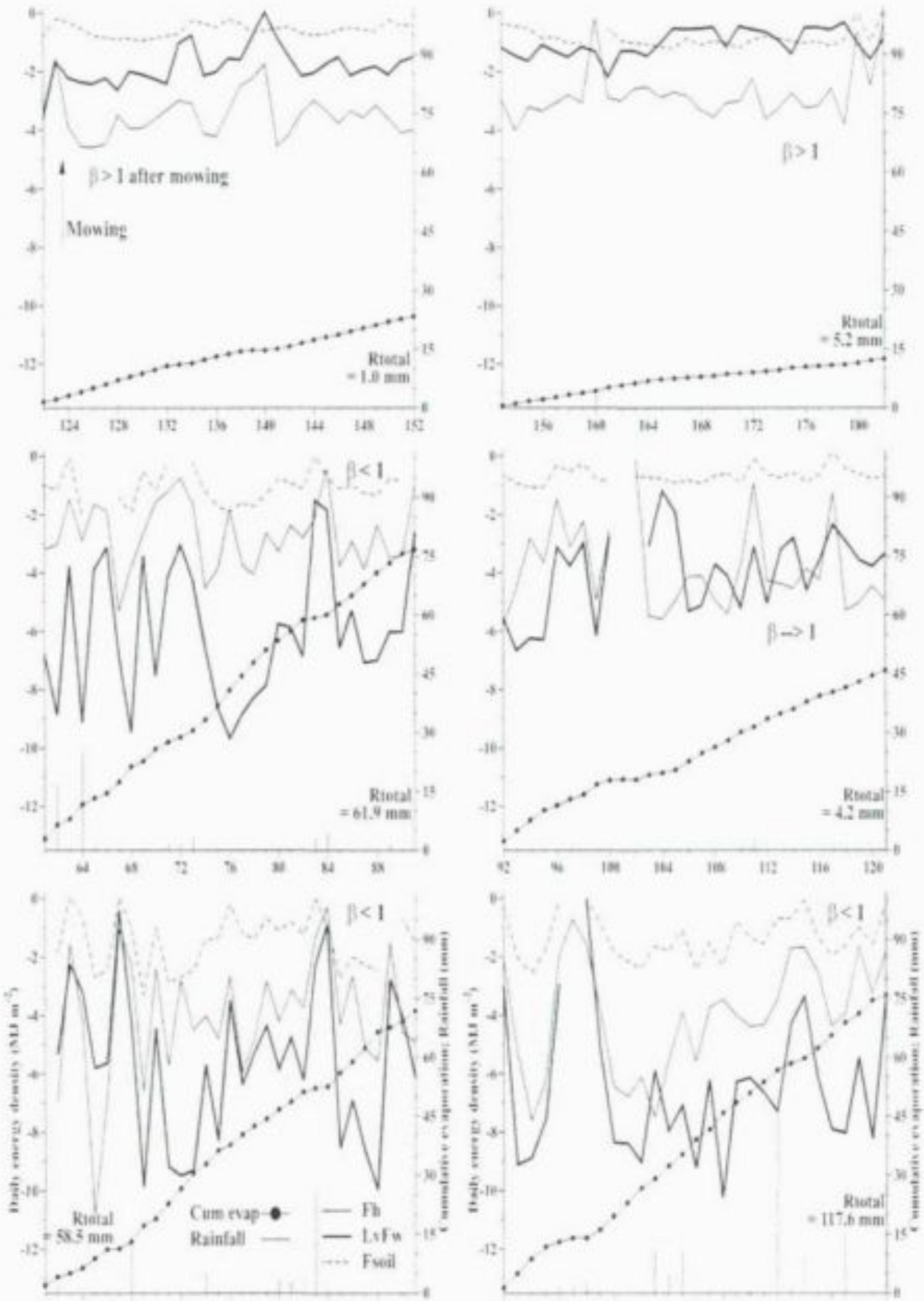

Fig. 6.4 Seasonal variation in daily sensible heat, latent energy and soil heat density (left-hand y-axis, MJ m^{-2}), cumulative evaporation and daily rainfall (mm) (right-hand y-axis) for the period 1 Jan and 30 June 2004. The total monthly rainfall is shown, bottom right of each graph

evaporation for 2003 exceeded 673 mm. This total is for the period 14 Jan to the end of Dec 2003. There were also periods for which no evaporation measurements were made due to power problems or equipment damage due to the fire. Conditions during 2004 were even drier with a total rainfall for the first six months of 248 mm and a total evaporation of 306 mm.

The maximum daily evaporation amount seldom exceeded 5 mm (equivalent to a latent energy density magnitude of less than 12.2 MJ m^{-2}). In the summer rainfall months, the cumulative monthly evaporation amount seldom exceeded 90 mm, corresponding to an average daily evaporation amount of about 3 mm. In winter, the evaporation amounts were extremely low, particularly for the May and June 2004 months. During this period, monthly evaporation totals seldom exceeded 50 mm and daily evaporation rates were seldom greater than 1 mm (Fig. 6.4).

The increases and decreases in sensible heat, latent energy and soil heat magnitudes shown (Figs 6.2 to 6.4) are mainly due to the increases and decreases in net irradiance due to clouds affecting the solar irradiance and the consequential impact on the available energy density. During drier periods, these increases and decreases are less pronounced but still occur. While the net irradiance is important in defining the available energy, the partition of this into sensible heat and latent energy is dependent on a range of factors including soil water availability, dew deposition, atmospheric humidity, air temperature, wind speed and surface cover. During the wetter periods, the daily Bowen ratio is usually much less than 1 (Fig. 6.2, Jan to Apr 2003; Fig. 6.3, Dec 2003; Fig. 6.4, Jan to Mar 2004). Generally, during dry periods, the Bowen ratio approaches 1 (e.g., day of year 140 to 212, 2003 of Figs 6.2 and 6.3) and then exceeds 1 during even drier periods (e.g., day of year 291 to 304 and 321 to 329, 2003 of Fig. 6.3). Since 2004 was generally much drier than 2003, periods for which the Bowen ratio exceeded 1 were more evident (e.g., day of year 124 to 179, 2004, Fig. 6.4).

The soil heat density magnitudes increased after the fire (day of year 227, 2003, Figs 6.1 and 6.3), reaching their greatest magnitudes during the summer rain season (exceeding 5 MJ m^{-2} during Nov and Dec 2003). Generally, while the soil heat term has the smallest magnitude of all the energy balance components, it is significant in late-spring and summer (Fig. 6.4, Oct to Dec 2003). During very dry periods, the soil heat magnitude exceeded the evaporation amount (Fig. 6.4, May and Jun 2004). The results for this grassland system demonstrate that significant errors to the estimate of evaporation would result if the soil heat measurement were excluded.

The Priestley and Taylor (1972) evaporation prediction for humid climates is approximately $1.26 \times [\Delta/(\Delta+\gamma)]\cdot A$ where Δ is the slope of the saturation water vapour pressure *vs* temperature relationship (kPa °C^{-1}), γ the psychrometric constant (kPa °C^{-1}) and A (expressed in MJ m^{-2}) the available energy density. Hence, the Priestley and Taylor (1972) evaporation estimate for the Bowen ratio is given by:

$$\beta = [1 - 1.26 \cdot \Delta/(\Delta+\gamma)] / [1.26 \cdot \Delta/(\Delta+\gamma)].$$

Since Δ/γ = 1, 2 and 3 at 6, 18 and 26 °C respectively, the Bowen ratio for Priestley-Taylor evaporation would typically be 0.59, 0.19 and 0.058 respectively. During the dry periods in the winter of 2004, clearly, Bowen ratios exceed 1 and hence Priestley-Taylor evaporation cannot apply (Figs 6.4, May and June 2004). During the wetter periods of summer, the Bowen ratios fluctuate between 0.33 and 1 (Fig. 6.2, Jan and Feb 2003; Fig. 6.3, Nov and Dec 2003). Certainly then, for the duration of this work, the Priestley-Taylor formulation for estimating evaporation cannot be relied upon.

The impact of fire and mowing on the energy balance components was investigated. The two events are shown and indicated by arrows: mowing (Figs 6.1 and 6.2) on day of year 131, 2003 and on day of year 124, 2004 (Figs 6.1 and 6.3) and burning due to an accidental fire (Figs 6.1 and 6.3) on day of year 227, 2003.

Figs 6.5 to 6.8 show the soil and latent energy density, and the volumetric soil water content and reflection coefficient. The fire resulted in a large reduction in the surface reflection coefficient (from about 22 % to 6 %, Figs 6.5 and 6.6, Aug 2003). Not shown is the consequent increase in net radiant density following the fire. The magnitude of the soil heat density also increased after the fire - before the fire, this was less than 1.75 MJ m^{-2} in magnitude but exceeded 3 MJ m^{-2} after the fire. The limited evaporation data after the fire seemed to indicate increases in the magnitude of the latent energy density. These comparisons are however difficult to make since rainfall events mask general trends. There were, for example, rainfall events before and after the fire. Because of the masking of management (or similar) practices during dry periods by rainfall events, management practices do not appear to result in large changes in sensible heat and/or latent energy density. However, another reason is that the increase in net radiant density is offset by the magnitude increases in soil heat density following burning or mowing. In other words, while the net radiant density may increase after the fire, the available energy density is less affected. If the available energy density is less affected, the sum of latent energy and sensible heat densities would also be less affected by the management practice.

The two mowing events resulted in slight increases in the surface reflection coefficient (Figs 6.5 and 6.6, May 2003; Figs 6.5 and 6.8, May 2004). The 2003 mowing also coincided with two rain events making it difficult to directly assess its impact in isolation. However, the mowing event in May 2004 was not accompanied by rainfall events and did show a large divergence between sensible heat and latent energy immediately after the mowing compared to the trends in late April (Figs 6.1 and 6.4). The Bowen ratio increased from around 1 before mowing to in excess of 4 some three weeks after mowing. This high value was increased even further to until day of year 160 when a rain event occurred (Figs 6.1 and 6.4, June 2004). After this, the very high Bowen ratio values were maintained until the next rain event on day of year 180. Clearly, removal of vegetation, in the absence of rain results in higher Bowen ratio values due to relatively higher sensible heat values and relatively lower latent energy values.

The volumetric soil water content, measured at a depth of 50 mm, varied between 0.119 m^3 m^{-3} (Figs 6.5 and 6.7, July 2003) and 0.504 m^3 m^{-3} (Figs 6.5 and 6.8, Mar 2004). The very low water contents experienced in winter prevented installation of a different type of sensor horizontally at 50 mm. The measurements were however confirmed using a probe inserted from the surface.

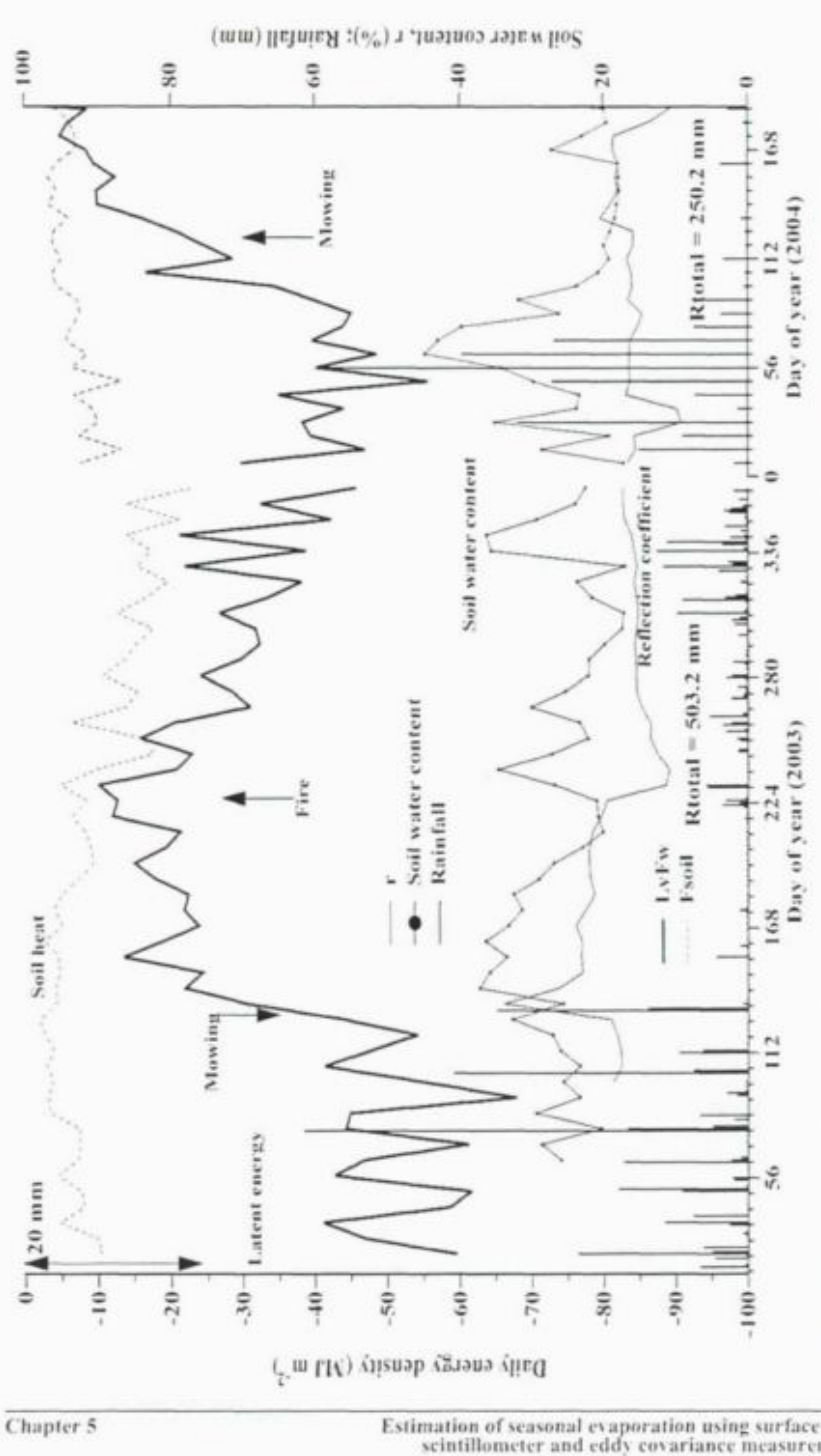

Fig. 6.5 Seasonal variation in weekly latent energy and soil heat density (left-hand y-axis, MJ m^{-2}), volumetric soil water content and surface reflection coefficient r (right-hand y-axis, %) for the period 14 Jan 2003 and 30 June 2004

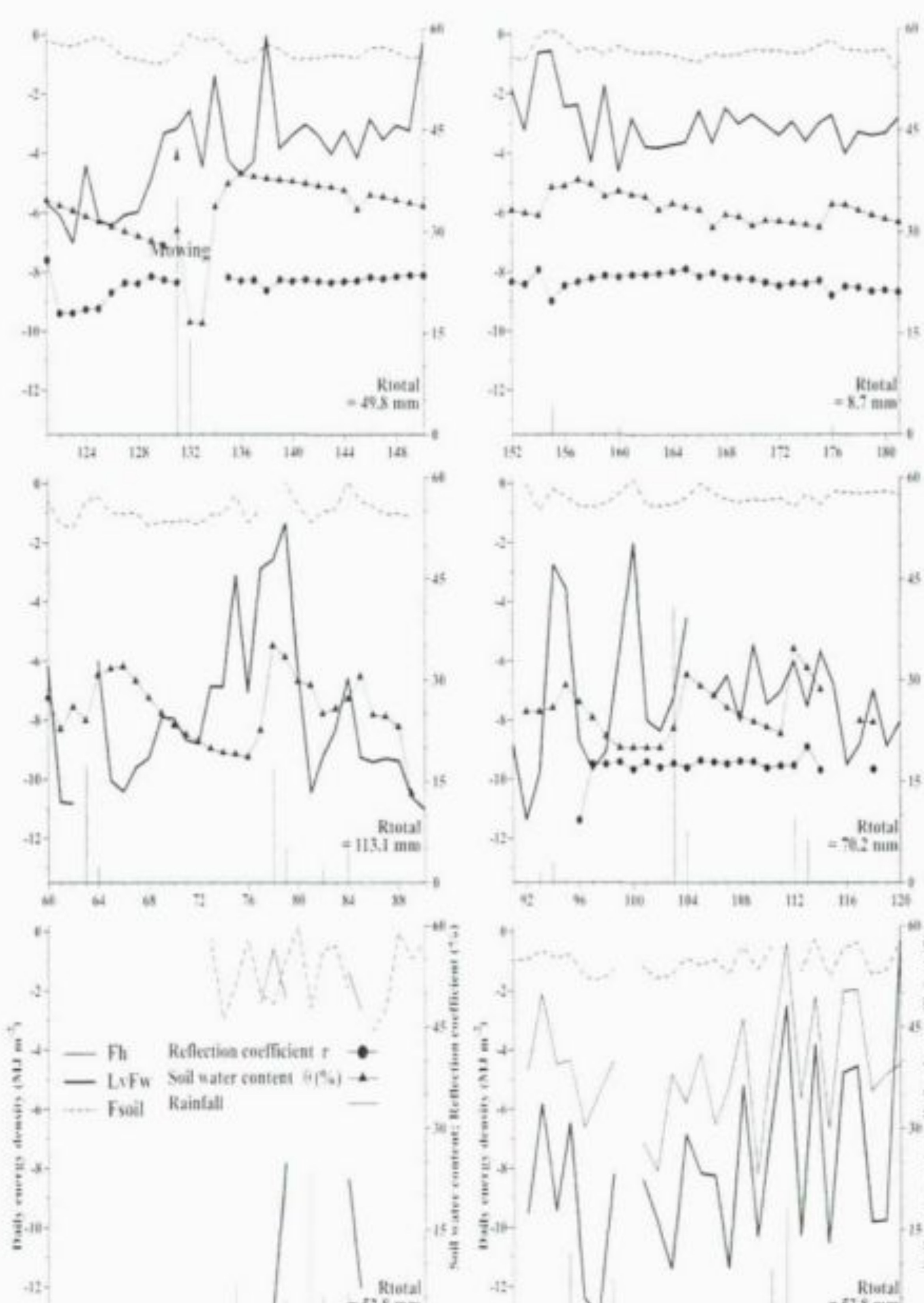

Fig. 6.6 Seasonal variation in daily latent energy and soil heat density (left-hand y-axis, MJ m^{-2}), volumetric soil water content and surface reflection coefficient (%) and daily rainfall (mm) (right-hand y-axis) for the period 14 Jan and 30 June 2003

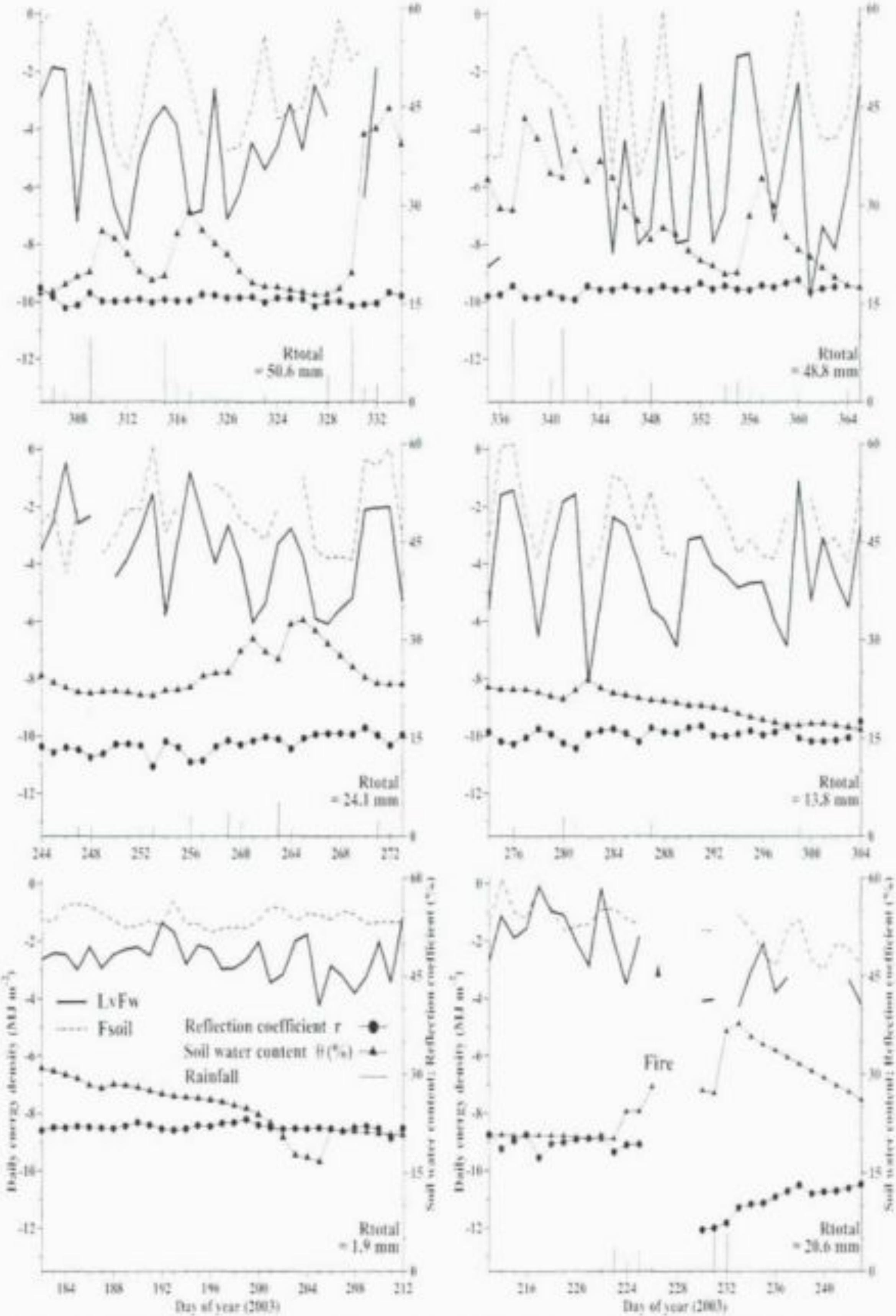

Fig. 6.7 Seasonal variation in daily latent energy and soil heat density (left-hand y-axis, MJ m^{-2}), volumetric soil water content and surface reflection coefficient (%) and daily rainfall (mm) for the period 1 Jul and 31 Dec 2003

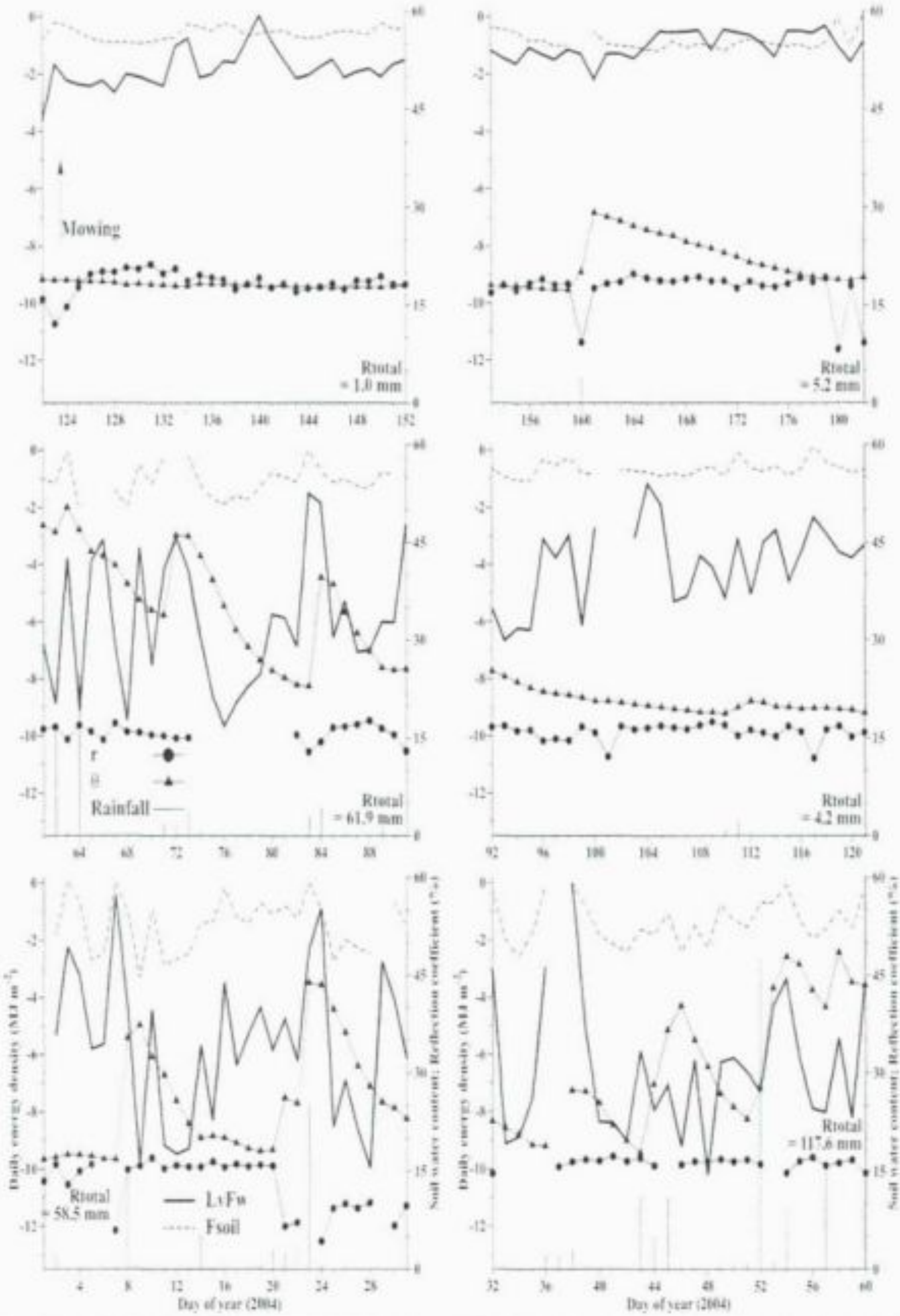

Fig. 6.8 Seasonal variation in daily latent energy and soil heat density (left-hand y-axis, MJ m^{-2}), volumetric soil water content and surface reflection coefficient (%) and daily rainfall (mm) for the period 1 Jun and 30 June 2004

5.5 Conclusions

The data demonstrates that it is possible to estimate evaporation continuously using the SLS and EC measurement methods. Priestley-Taylor evaporation, dependent on the net irradiance, soil heat flux density and air temperature, is not a good indicator of the measured evaporation.

Peak summer evaporation rates were dictated primarily by the available energy flux density, often varying wildly from one day to the next due to the influence of clouds.

The total net radiant density for the 18-month period was 3197.85 MJ m^{-2}. The soil heat density total was -463.79 MJ m^{-2}, the sensible heat total -1101.64 MJ m^{-2} and latent energy total -1588.85 MJ m^{-2}. Evaporation (latent energy) is therefore a significant fraction of both the energy and water balances. It represented just less than 50 % of the net radiant density during 2003 and exceeded the measured rainfall during 2003 and during the first six months of 2004: the total evaporation was 979 mm and the rainfall was 780 mm. It appears that the removal of vegetation by mowing during periods of low and sustained low rainfall results in very high sensible heat magnitudes and low latent heat magnitudes that may have further negative influences on the surface cover. The influence of burning was masked by rainfall events that occurs at the same time. Following a fire, the decreases in the surface reflection coefficient resulted in increases in the net irradiance. These increases in net irradiance on the available energy were however somewhat offset by the increases in the magnitude of the soil heat that occurred at the same time.

Chapter 6

Conclusions and recommendations for future research

6.1 Conclusions

The specific objective of this research is the use of the surface layer scintillometer (SLS) method to estimate areally averaged sensible heat flux over a mixed-community grassland canopy and comparison with measurements obtained using an eddy covariance (EC) method. Since the SLS method measures sensible heat, the methodology relies on the energy balance and in particular the measurement of the net irradiance and the soil heat flux density to estimate latent heat. The SLS method also depends on the Monin-Obukhov similarity theory (MOST). Other methods used for comparison purposes are the traditional Bowen ratio (BR) and eddy covariance (EC) methods. In addition the surface renewal (SR) method, also previously untested in South Africa, was used.

The eddy covariance (EC) method is the only method that allows for independent estimation of sensible heat and latent energy flux densities provided sonic temperature, vertical wind speed and concentrations of water vapour and carbon dioxide are measured using fast-responding sensors. Alternatively, the EC method may be used to measure the sensible heat flux density and the latent energy flux density estimated as a residual term from the energy balance. The Bowen ratio (BR) and surface layer scintillometer (SLS) measurements allow sensible heat flux density to be estimated from which latent energy may be estimated as a residual component of the energy balance.

The methodology associated with the use of a dual-beam SLS is discussed in detail. The procedures associated with the crucial step of beam alignment are not complicated. These procedures are presented as are the procedures for the error-checking of the data post-data collection. Once the receiver is correctly aligned with the transmitter beam, the system runs virtually unattended. The automatic alignment system could be programmed to perform an automatic alignment between daily and hourly time intervals. This allowed the system to run unattended for weeks on end. If the automatic alignment option was disabled, the system could run unattended for up to a week or so. There would be a cost savings if the auto-alignment feature were not required but this feature would be necessary if the system were mounted on a tower above tall trees. While a horizontal beam and a horizontal surfaces is assumed by MOST, there was no consistent over- or under-estimate in SLS sensible heat flux density compared to ECAT measurements for a non-horizontal beam angle. A low effective beam height of 0.5 m resulted in more variable sensible heat flux density measurements, and variable inner scale of turbulence values that approached the defined lower value for acceptable data.

Routine site visits usually required that the beam position be set using a computer and computer software and an alignment procedure performed. These procedures usually take less than 10 min to perform. If the beam was no longer aligned, alignment at the receiver would normally be required. This procedure usually took no longer than half an hour. If alignment from the position of the transmitter was also required, the procedure could take an hour or more.

The rate of data accumulation using the SLS method is not excessive. In one month, about 35 Mbytes of data, including both the 2-min and 12-s data, are accumulated. When compressed, this amounted to about 16 Mbyte. Copying the collected data from the PC does not take long and can be done without switching the beam off. If only the 2-min data are required, which was often the case, only 3.5 Mbytes of data were accumulated each month.

One of the main problems was that the clock of the computer would drift off by up to 30 s per week. A computer with a more accurate clock should be used if measurement comparisons with other measurement systems are undertaken. It is possible to dispense with the use of a computer on-site if the PC card option is used for data storage. This option requires the use of a PC or laptop to launch the system but then the data is stored on a PC card without the necessity of a computer. The second main problem with the system was the power requirement. Relying on electrical power supplied to a residence resulted in gaps in the data record. This problem could be avoided by having a bank of batteries as a power supply for the SLS system and a DC to AC convertor for powering the computer if the PC card option is not used. The third main problem is that the beam alignment would drift off during conditions of high wind and/or rainfall. Rainfall would soften the ground around the stands used for the transmitter and receiver units and create the misalignment. For a more permanent installation, a concrete base for each unit would solve this problem. Extensive use of cords to reduce wind vibration worked well but the cords required monthly checking and possible replacement. The fourth main problem was the possibility of accumulated dirt and cobwebs on the transmitter and/or receiver windows interfering with the transmitted beam. The check for dirt on the windows should be routinely done at each visit. The fifth main problem with the use of SLS and LAS measurement systems is that theoretically, the methods do not predict the direction of the sensible heat flux. The direction was routinely estimated from the direction of the sensible heat flux measured using the EC system and confirmed by the fine-wire profile air temperature differences. These measurements were however obtained using additional data logging systems. In the absence of such measurements, it may be possible to estimate when the sensible heat changes sign from noting how its trace with time approaches 0 W m^{-2} around sunset for example and then increases with conditions becoming darker.

The procedures for the onscreen and real-time checking of the SLS data and system are fairly simple. Early identification of errors or potential errors can avoid significant data loss. Vegetation height for every 10 m of the SLS beam path length needs to be measured every ten to fourteen days or so during the growing season and probably monthly in the off-season. The frequency of height measurement would depend on the growth rate of the vegetation. This height can then be used to input the height of beam above the level corresponding to a wind speed of 0 m s^{-1}. This procedure would avoid a recalculation of the data following data collection.

Error-checking of the data post-data collection is also not very complicated. In summary: the system allowed for the real-time estimation of sensible heat flux density every two minutes.

The percentage of error-free 2-min SLS sensible heat flux density measurements for the daytime hours showed little seasonal variation, varying between 86.7 % and 94.8 % for the 18-month period. The nighttime variation in the percentage had a more pronounced seasonal pattern with the lowest percentage acceptable measurements occurring between January and March of each year due to the effects of dew and mist.

Values of the inner scale of turbulence l_o less than 2 mm results in rejected sensible heat flux density data. For most of the study, the most common (or at least 35 % of the time) l_o value is between 4 and 6 mm. For the nighttime, the most common l_o value is less than 2 mm. The second-most common nighttime value is that between 6 and 8 mm in contrast to the 4 to 6 mm value during the daytime hours. The larger values of 6 to 8 mm at night is due to the more stable nighttime conditions compared to the more turbulent daytime conditions creating smaller and smaller eddies.

The data inputs for the SLS method include atmospheric pressure, air temperature, beam path length and the beam height relative to the level at which wind speed is 0 m s^{-1}. Cain et al. (2001) used a different basis level from the level at which wind speed is 0 m s^{-1}. The collected data did not support this.

The influence of surface slope on sensible heat flux density measurements was investigated by altering the height of the receiver relative to the transmitter. Theoretically, a non-horizontal beam relative to a horizontal surface, or *vice versa*, invalidates MOST. The receiver to transmitter vertical height difference used was 1.0 m. For measurements performed over five days, there was no significant consistent difference between 2-min SLS and EC sensible heat flux density measurements in spite of the fact that MOST is invalid for a non-horizontal beam.

The influence of beam height was investigated by also altering the height of the transmitter and receiver units. For most of the study, the beam was about 1.68 m above the soil surface with vegetation height varying between virtually 0.0 m and a maximum of 1.13 m. The effective beam height therefore varied between 0.82 m and 1.68 m. The lowest beam height used was a height of 0.5 m. The comparison between sensible heat flux density measured using the EC and SLS methods showed that the SLS measurements were not significantly influenced by even this low beam height.

The worst-case errors in the SLS data inputs of atmospheric pressure, air temperature, beam path length and beam height resulted in fractional errors in sensible heat flux density of ± 0.013, ∓ 0.015, ∓ 0.03 and ± 0.04 respectively. The beam height above $d + z_o$ needs to be known accurately as the error in beam height contributes the most to the overall error with errors in beam path length next most important. The worst-case total fractional error in sensible heat flux density was ± 0.054 and the typical fractional error amounted to ± 0.032. Furthermore, the sensible heat can in any case be recalculated post-data calculation using the correct values for the data inputs. This procedure is however time-consuming since the input for atmospheric pressure and air temperature would have to be input for each 2-min period. This is easily done by importing the data into a spreadsheet, combining and then exporting the data for recalculation purposes. This procedure would however reduce the error in SLS sensible heat from the worst-case total fractional error of ± 0.054.

The procedures for the measurement of other energy balance components, the net irradiance and soil heat flux density, are reported. The theory associated with a sensitivity analysis of the estimated latent energy flux density was used to determine the relative importance of the SLS data inputs of air temperature, atmospheric pressure, beam path length and beam height on sensible heat flux estimates. In addition, it was shown that errors in the measurement of soil heat flux density and net irradiance also affected the estimated latent energy.

The seasonal variation in the error in the evaporation rate is generally less than 0.2 mm day^{-1} (equivalent to a latent energy density of 0.49 MJ m^{-2}) in winter when the daily evaporation rate was around 1 mm day^{-1} (2.45 MJ m^{-2}) and typically less than 0.4 mm day^{-1} (0.98 MJ m^{-2}) when the evaporation rate generally exceeded 4 mm day^{-1} (9.8 MJ m^{-2}). Most-often, the measurement with the greatest contributing error is the soil heat flux measurement which often expresses the spatial variability of canopy growth. Care therefore needs to be exercised to ensure that soil heat flux measurement procedures do not compromise the calculated latent energy fluxes when using SLS sensible heat measurements, particularly for short vegetation where it is expected that the magnitude of the soil heat term may not be small. This would also apply to BR estimates of latent energy and the EC method when only sensible heat is measured and latent energy is estimated using the net irradiance and soil heat energy balance components. While the term "error" implies that the soil heat and net irradiance measurements are sensor errors, they also reflect the nature of spatial variability in the site landscape. It is simply not possible to have an infinite number of soil heat flux plates and net radiometers for sites typical of that used here. However, the use of a line-averaging SLS system goes part of the way compared to other point measuring devices.

Laboratory and field BR data collected showed that the Vaisala CS500 or the HMP45C capacitive sensor may be used as a replacement for the Dew-10 cooled dew point mirror sensor of the BR systems used. Water vapour pressure profile differences of at least 0.01 kPa, as is required for BR measurements, were possible with these Vaisala CS500 and HMP45C thin film polymer capacitive. The CS500 or HMP45C sensors required no servicing compared to the Dew-10 which required a bias adjustment and mirror cleaning each week. The water vapour pressure measurement noise for the HMP45C sensor was greater than that for the Dew-10 but the average water vapour pressure profile difference for the two sensors was highly correlated. The CS500 exhibited greater variation in measured water vapour pressure but its resolution was better than the required 0.01 kPa. These findings will make BR estimates of evaporation considerably cheaper and more reliable than when using just the Dew-10.

An examination of wind direction demonstrated that the largest differences between SLS and EC sensible heat densities occurred for wind directions between 0 and 60° corresponding to winds from residential areas with limited fetch. Comparisons between SLS- and EC-measured sensible heat flux density, for selected days, did not appear to be affected by differences between wind perpendicular to the beam and winds parallel to the beam. For the period January to end March 2004, the wind was perpendicular to the beam 35 % of the daytime hours compared to less than 5 % for wind parallel to the beam.

A footprint analysis allowed three key parameters to be calculated: the peak location of the footprint (x_{peak}), the footprint fraction itself and the 90 % fetch to measurement height ratio. For daytime hours, conditions were most often convectively unstable which resulted in fetch to height ratios less than the commonly accepted 100:1 and also resulted in peak footprint locations very close to the point/line of measurement. Based on the x_{peak} estimation, one trend was that the general stability condition for the 9 am to noon hours was not the same as that for the noon to 3 pm period. For much of the time, or at least for 75 % of the 9 am to 3 pm periods, the x_{peak} values in the morning were less than that for the afternoon. The 90 % fetch to measurement height ratio difference between morning and afternoon hours may impact on measurement comparisons between the different techniques particularly when comparing a line-averaged SLS measurement of sensible heat flux density with a point EC measurement. Also, the diurnal shape of the sensible heat flux density curve may be asymmetrical given that morning hours are generally more unstable than are afternoon hours. The asymmetrical shape of the diurnal sensible heat flux density curve for EC measurements, was not as noticeable due to the temporal variability of the point EC measurements.

Two-minute measurements of EC, SLS and SR sensible heat flux density were in good agreement much of the time, particularly for cloudless conditions. There were however periods for which the magnitude of the SLS-measured sensible heat flux density exceeded the measured available heat flux density. The result was that the calculated latent heat was positive, apparently corresponding to condensation. Further examination showed that some of these events corresponded to counter-gradient events dominated by overriding coherent structures apparently of undetermined origin. Indications were that the counter-gradient events occurred whenever high solar irradiance events were followed by large reduction due to clouds.

There was no evidence for a consistent underestimation in sensible heat measurements by the EC method compared to the SLS measurements. Furthermore, there was no evidence to indicate that the effective SLS beam height input was incorrect as suggested by Cain et al. (2001). An incorrect beam height input would have caused a consistent overestimation or underestimation in the SLS sensible heat measurements compared to EC measurements.

Twenty-minute measurements of BR (using polymer and Dew-10 cooled mirror sensors), EC, SLS and SR sensible heat flux density were also in good agreement much of the time, particularly for cloudless conditions. No measurement technique resulted in measurements that were consistently greater or larger than the other measurement techniques apart from the SR method which generally resulted in slightly lower sensible heat magnitudes. The ECopen system, which measures the latent energy flux density directly without resorting to use of the energy balance, consistently underestimated the latent heat magnitude compared to the residual SLS amount estimated from SLS sensible heat, net irradiance and soil heat.

Daily estimates of latent energy density for the SLS and EC methods were compared for a period of about 250 days during 2003. The 95 % confidence bands for a single predicted value were within 0.5 mm of the regression line and the error mean square was 0.295 MJ m^{-2} or about 0.12 mm. The 95 % population confidence bands were easily within 0.1 mm .Statistically, there was no significant difference between the point measurements using the EC residual method and the line-averaged estimate obtained using the SLS method.

The seasonal data collected demonstrates that it is possible to estimate evaporation continuously using the SLS and EC measurement methods. Priestley-Taylor evaporation, dependent on the net irradiance, soil heat flux density and air temperature, is not a good indicator of the measured evaporation.

Peak summer evaporation rates were dictated primarily by the available energy flux density, often varying wildly from one day to the next due to the influence of clouds.

The total net radiant density for the 18-month period was 3197.85 MJ m^{-2}. The soil heat density total was -463.79 MJ m^{-2}, the sensible heat total -1101.64 MJ m^{-2} and latent energy total -1588.85 MJ m^{-2}. The sum of all of these values is not exactly zero since occasionally, there was no evaporation data but there was net irradiance data. Evaporation (latent energy) is therefore a significant fraction of both the energy and water balances. It represented just less than 50 % of the net radiant density during 2003 and exceeded the measured rainfall during 2003 and during the first six months of 2004: the total evaporation for the 18-month period was 979 mm and the rainfall was 780 mm. It appears that the removal of vegetation by mowing during periods of low and sustained low rainfall results in very high sensible heat magnitudes and low latent heat magnitudes that may have further negative influences on the surface cover. The influence of burning was masked by rainfall events that occurred at the same time. Following a fire, the decrease in the surface reflection coefficient resulted in an increase in the net irradiance. The increase in net irradiance on the available energy was however somewhat offset by the increase in the magnitude of the soil heat that occurred at the same time.

6.2 Recommendations for future research

6.2.1 General comments

One of the major limitations to real economic growth of South Africa is the limitation imposed by inadequate water resources to support the given human population and their activities. Evaporation is a process whereby water is used consumptively. The measurement and/or the estimation of evaporation is key to quantifying this consumption in relation to the productive or beneficial use of water. Also, the quantification of water use can assist management in shifting from less to more productive consumptive water use and therefore research into evaporation measurement or its estimation is crucial to South Africa.

6.2.2 Large aperture scintillometer and surface layer scintillometer comparisons

Our research has concentrated on use of the SLS method for which the measurement range is typically 50 m to 250 m. There was insufficient time to extend the focus to comparisons with a LAS system. Such a comparison would prove useful and allow evaporation measurements to be scaled to pixel size with confidence.

6.2.3 Bowen ratio methodology

Our research has concentrated on energy and water movement exclusively and therefore has ignored the important aspect of plant productivity in terms of the amount of water used. We believe that the BR research needs to be extended to research on a BR carbon dioxide and water vapour system. This research would allow such a BR CO_2 system to determine water use efficiency in real-time. Open path EC systems can also be used for determining water use efficiency is real-time, but there are reports in the literature indicating that the EC method underestimates latent energy (also demonstrated in Chapter 5 for the ECopen system measurements) and carbon dioxide fluxes.

6.2.4 Surface renewal methodology

Preliminary work on this method is reported on in this report (Chapter 5). Given the simplicity of the technique theoretically and practically, the results found and that it is inexpensive, the technique certainly deserves further attention.

6.2.5 Soil heat flux and net irradiance influences

This report has shown the importance of the soil heat and net irradiance measurements. Since these measurements are required for both SLS and LAS estimations of latent energy, future research would need to consider these two energy balance measurements in more detail. In particular, for short vegetation, the measurement of soil heat flux closer to the surface requires attention and even more so for more heterogeneous vegetation consisting of grass and shrubs or trees.

6.2.6 Collected data not used in the report

Theoretically, it is possible to use the canopy temperature data (not reported on) collected as part of this work and remote sensing techniques for the determination of sensible heat if measures of aerodynamic resistance are also possible either from measurements of wind speed or from using the

SLS or LAS methods. In view of the possibility of "areal" measures of sensible heat, it may then be possible to also calculate surface evaporation from estimates of net irradiance and soil heat flux.

6.2.7 Technology transfer

In a sense, this project has already resulted in technology transfer. The results produced early on were valuable and resulted in much greater confidence in the use of the EC method for the measurement of sensible heat. Prior to these results, the correctness of previous BR and EC evaporation measurements or estimates could not be gauged. Furthermore, the results of 2004 have confirmed the suspicion that BR measurements would be more reliable by the use of a sensor replacement for the cooled dew point mirror sensor. Also, preliminary investigations involving the use of the SR method, indicated that this technique can be implemented at comparatively low cost.

It is proposed that a variety of methods be used to transfer some of the technology of the research investigated here: small workshops, conference workshops and e-mail interest groups. A cooperative effort is needed. The WRC has been proactive in this regard through a call for solicited research proposals on evaporation estimation. Technology transfer forums should encourage young scientists as much as possible. These processes would quickly permit the transfer of the technology described in this report.

Much of the research described here has already benefited students, researchers and technical staff at the University of KwaZulu-Natal and the CSIR.

References

Albertson, J.D., Parlange, M.B., 1999. Natural integration of scalar fluxes from complex terrain. Adv. Water Resour. 23, 239-252.

Allen, R.G, Pereira, L.S., Raes, D., Smith, M., 1998. Crop evapotranspiration - Guidelines for computing crop water requirements - FAO Irrigation and drainage paper 56 FAO - Food and Agriculture Organization of the United Nations Rome., Italy. 315 pp.

Anandakumar, K., 1999. Sensible heat flux over a wheat canopy: optical scintillometer measurements and surface renewal analysis estimates. Agric. For. Meteorol. 96, 145-156.

Andreas, E. L. (ed.), 1990. Selected Papers on Turbulence in a Refractive Medium. SPIE Milestones Series, 25. Society of Photo-Optical Instrumentation Engineers, Bellingham WA, USA. 693 pp.

Andreas, E.L., 2000. obtaining surface momentum and sensible heat fluxes from crosswind scintillometers. J. Atmos. Oceanic Technol. 17, 3-16.

Andreas, E.L., Fairall, C.W., Persson, P.O.G., Guest, P.S., 2003. Probability distributions for the inner scale and the refractive index structure parameter and their implications for flux averaging. J. App. Meteorol. 42, 1316-1329.

Angus, D.E., Watts, P.J., 1984. Evapotranspiration: how good is the Bowen ratio method? Agric. Water Mgt. 8, 133-150.

Arya, S.P., 1988. Introduction to Micrometeorology. Academic Press, London, UK.

Bange, I., Beyrich, F., Engelbart, D.A.M., 2002. Airborne measurements of turbulent fluxes during LITFASS-98: Comparison with ground measurements and remote sensing in a case study. Theoretical App. Climatology 73, 35-51.

Batchelor, G.K., 1964. Diffusion from sources in a turbulent boundary layer. Archiv. Mechaniki Stoswanej. 3, 661 pp.

Beyrich, F., de Bruin, H.A.R., Meijninger, W.M.L., Schipper, J.W., Lohse, H., 2002a. Results from one-year continuous operation of a large aperture scintillometer over a heterogeneous land surface. Boundary-Layer Meteorol. 105, 85-97.

Beyrich, F., Richter, S.H., Weisensee, U., Kohsiek, W., Lohse, H., de Bruin, H.A.R., Foken, T., Gockede, M., Berger, F., Vogt, R., Batchvarova, E., 2002b. Experimental determination of turbulent fluxes over the heterogeneous LITFASS area: Selected results from the LITFASS-98 experiment. Theoretical App. Clim. 73, 19-34.

Bowen, I.S., 1926. The ratio of heat losses by conduction and by evaporation from any water surface. Phys. Rev. 27, 779-787.

Brutsaert, W.H., 1982. Evaporation into the atmosphere. Reidel, Dordrecht, Holland. 299 pp.

Byers, H.R., 1974. General Meteorology, 4 th ed. McGraw-Hill, New York, USA.

Cain, J.D., Rosier, P.T.W., Meijninger, W., de Bruin, H.A.R., 2001. Spatially averaged sensible heat fluxes measured over barley. Agric. For. Meteorol. 107, 307-322.

Calder, K.L., 1949. Eddy diffusion and evaporation in flow over aerodynamically smooth and rough surfaces: a treatment based on laboratory laws of turbulent flow with special reference to conditions in the lower atmosphere. Q. J. Mech. App. Math. 2, 153-176.

Calder, K.L., 1952. Some recent British work on the problem of diffusion in the lower atmosphere. In: Proceedings of the US Tech. Conf. on Air Poll. McGraw-Hill, New York, USA. Pp 787-792.

Castellvi, F., 2004. Combining surface renewal analysis and similarity theory: a new approach for estimating sensible heat flux. Water Resour. Res. 40, 1-20.

Chandrapala, L., Wimalasuriya, M., 2003. Satellite measurements supplemented with meteorological data to operationally estimate evaporation in Sri Lanka. Agric. Water Mgt. 58, 89-107.

Chehbouni, A., Seen, Lo., Njoku, E.G., Monteny, B.A., 1996. Examination of the differences between radiative and aerodynamic surface temperatures over sparsely vegetated surfaces. Remote Sensing Environ. 58, 177-186.

Chehbouni, A., Seen, Lo., Njoku, E.G., Lhomme, J-P., Monteny, B.A., Kerr, Y.H., 1997. Estimating of sensible heat flux using radiative surface temperatures. J. Hydrol. 188, 855-868.

Chehbouni, A., Kerr, Y.H., Watts, C., Hartogensis, O., Goodrich, D., Scott, R., Schieldge, J. Lee, K. Shuttleworth, W.J, Dedieu, G., de Bruin, H.A.R., 1999. Estimation of area and average sensible heat flux using a large aperture scintillometer. Water Resource Res. 35, 2505-2511.

Chehbouni, A., Watts, C., Kerr, Y.H., Dedieu, G., Rodriguez, J-C., Santiago, F., Cayrol, P., Boulet, Goodrich, D.C., 2000a. Methods to aggregate turbulent fluxes over heterogeneous surfaces: application to SALSA data set in Mexico. Agric. For. Meteorol. 105, 133-144.

Chehbouni, A., Watts, C., Lagouarde, J.-P., Kerr, Y.H., Rodriguez, J.-C., Bonnefond, J.-M., Santiago, F., Dedieu, G., Goodrich, D.C., Unkrich, C., 2000b. Estimation of heat and momentum fluxes over complex terrain using a large aperture scintillometer. Agric. For. Meteorol. 105, 215-226.

Chen, Wenjun, Novak, M.D., Black, T.A., 1997a. Coherent eddies and temperature structure functions for three contrasting surfaces. Part 1: Rump model with finite microfront time. Boundary-Layer Meteorol. 84, 99-123.

Chen, Wenjun, Novak, M.D., Black, T.A., 1997b. Coherent eddies and temperature structure functions for three contrasting surfaces. Part II: Renewal model for sensible heat flux. Boundary-Layer Meteorol. 84, 125-147.

Choudhury, B.J., Reginato, R.J., Idso, S.B., 1986. An analysis of infrared temperature observations over wheat and calculation of latent heat flux. Agric. For. Meteorol. 37, 75-88.

Corsin, S., 1974. Limitations of gradient models in random walks in turbulence. Adv. Geophys., 18A: 25-60.

Cummings, 1925. Phys. Rev., 25, 721..and J. Elect. 46, 491. (Cited by I.S. Bowen).

Daoo, V.J., Panchal, N.S., Sunny, F., Raj, V.V., 2004. Scintillometric measurements of daytime atmospheric turbulent heat and momentum fluxes and their application to atmospheric stability evaluation. Exp. Thermal Fluid Sci. 28, 337-345.

Deardorff, J.W., 1966. The countergradient heat flux in the lower atmosphere and in the laboratory. J. Atmos. Sci. 23, 503-506.

Deardorf, J.W., 1978. Observed characteristics of the outer layer. AMS course on the planetary boundary layer. Boulder, Colo. (unpublished manuscript).

de Bruin, H.A.R., 2002. Renaissance of scintillometry. Boundary-Layer Meteorol. 105, 1-4.

de Bruin, H.A.R., Meijninger, W.M.L., 2002. Displaced-beam small aperture scintillometer test. Part I: the WINTEX data-set. Boundary-Layer Meteorol. 105, 129-148.

de Bruin, H.A.R., van den Hurk, B.J.J.M., Kohsiek, W., 1995. The scintillation method tested over a dry vineyard area. Boundary-Layer Meteorol. 76, 25-40.

de Bruin, H.A.R., Verhoef, A., 1997. A new method to determine the zero-plane displacement. Boundary-Layer Meteorol. 82, 159-164.

Drexler, J.Z., Snyder, R.L., Spano, D., Paw U, K.T., 2004. A review of models and micrometeorological methods used to estimate wetland evapotranspiration. Hydrological Processes 18, 2071-2101.

Dye, P.J., Olbricht, B.W., 1993. Estimating transpiration from six year old Eucalyptus grandis trees: development of a canopy conductance model and comparison with independent sap flux measurements. Plant, Cell Environ. 16, 45-53.

Dye, P.J., Olbrich, B.W., Poulter, A.G., 1992. The influence of growth rings in Pinus patula on heat pulse velocity measurement. J. Exp. Bot. 42, 867 -870.

Dyer, A.J., 1963. The adjustment of profiles and eddy fluxes. Q. J. R. Meteorol. Soc. 98, 276-280.

Dyer, A.J., 1974. A review of flux-profile relationships. Boundary-Layer Meteorol. 7, 363-372.

Elliot, W.P., 1958. The growth of the atmospheric internal boundary layer. Trans. Amer. Geophys. Un. 39, 1048-1054.

Furger, M., Drobinski, P., Prévôt, A.S.H., Webber, R.O., Werner, K.G., Neininger, B., 2001. Comparison of horizontal and vertical scinitillometer crosswinds during strong Foehn with lidar and aircraft measurement. J. Atmos. Oceanic Technol. 18, 1975-1988.

Garrat, J.R., 1978. Flux profile relations above tall vegetation. Q. J. R. Meteorol. Soc. 104, 199-211.

Gash, J.H., 1986. A note on estimating the effect of a limited fetch on micrometeorological evaporation measurements. Boundary-Layer Meteorol. 35, 409-413.

Gifford, F.A., 1961. Use of routine meteorological observations for estimating atmospheric dispersion. Nucl. Safety 2, 47-51.

Gimmestad, G.G., Roberts, D.W., 2003. Laser remote sensing of atmospheric turbulence. Proceedings of the Society of Photo-Optical Instrumentation Engineers, edited by Thompson, W.E., Merritt, P.H. Conference on Laser Systems Technology, April 21-23, 2003, Orlando, Florida, USA. (Abstract).

Glossary of Meteorology (2 nd ed). 2000. American Meteorological Society, Boston, USA.

Gracheva, M.E., Gurvich, A.S., Lomadze, S.O., Pokasov, V.I., Khrupin, A.S., 1974. Probability distribution of strong fluctuations of light intensity in the atmosphere. Radiophysics Quantum Electronics 17, 83-87.

Green A.E., 2001. The practical application of scintillometers in determining the surface fluxes of heat, moisture and momentum. Doctoral Thesis, Wageningen University, Holland. ISBN 90 5808 336 5. Pp 177.

Green, A.E., McAneney, K.J., Lagouarde, J.-P., 1997. Sensible heat and momentum flux measurements with an optical inner scale meter. Agric. For. Meteorol. 85, 259-267.

Green, A.E., Astill, M.S., McAneney, K.J., Nieveen, J.P., 2001. Path-averaged surface fluxes determined from infrared and microwave scintillometers. Agric. For. Meteorol. 109, 233-247.

Gryning, S.E., Holtslag, A.A.M., Irvin, J.S., Sivertsen, D., 1987. Applied dispersion modelling based on meteorological scaling parameters. Atmos. Environ. 21, 79-89.

Gryning, S.E., van Ulden, P., Larsen, S.E., 1983. Dispersion from a continuous ground-level source investigated by a K-model. Q. J. R. Meteorol. Soc. 109, 355-364.

Gu, L., Fuentes, J.D., Garstang, M., Tota da Silva, J., Heitz, R., Sigler, J., Shugart, H.H., 2001. Cloud modulation of surface solar irradiance at a pasture site in southern Brazil. Agric. For. Meteorol. 106, 117-129.

Ham, J.M., Heilman, J.L., 2003. Experimental test of density and energy-balance corrections on carbon dioxide flux as measured using open-path eddy covariance. Agron. J. 95, 1393-1403.

Han, L.J., Liu, S.M., Wang, J.M., Wang, J.D., 2003. Study on energy balance over different surfaces. IEEE International Geoscience and Remote Sensing Symposium, Vols I to VII, Proceedings - Learning From Earth's Shapes and Sizes, Jul 21-25, 2003, Toulouse, France. (Abstract).

Hanson, P.J., Amthor, J.S., Wullschleger, S.D., Wilson, K.B., Grant, R.E., Hartley, A., Hui, D., Hunt, E.R., Johnson, D.W., Kimball, J.S., King, A.W., Luo, Y., McNulty, S.G., Sun, G., Thornton, P.E., Wang, S., Williams, M., Baldocchi, D.D., Cushman, R.M., 2004. Oak forest carbon and water simulations: Model intercomparisons and evaluations against independent data. Ecol. Monographs 74, 443-489.

Hartogensis, O.K., de Bruin, H.A.R., van de Wiel, B.J.H., 2002. Displaced-beam small aperture scintillometer test. Part II: CASES-99 stable boundary layer experiment. Boundary-Layer Meteorol. 105, 149-176.

Hartogensis, O.K., Watts, C.J., Rodriguez, J.C., de Bruin, H.A.R., 2003. Derivation of an effective height for scintillometers: La Poza experiment in Northwest Mexico. J. Hydrometeorol. 4, 915-928.

Heilman, J.L., Brittin, C.L., Neale, C.M.U., 1989. Fetch requirements for Bowen ratio measurements of latent heat and sensible heat fluxes. Agric. For. Meteorol. 44, 261-273.

Heilman, J.L., McInnes, K.J., Gesch, R.W., Lascano, R.J., Savage, M.J., 1996. Effects of trellising on the energy balance of a vineyard. Agric. For. Meteorol. 81, 79-93.

Heilman, J.L., McInnes, K.L., Savage, M.J., Gesch, R.W., Lascano, R.J., 1994. Soil and canopy energy balance in a west Texas vineyard. Agric. For. Meteorol. 71, 99-114.

Hemakumara, H.M., Chandrapala, L., Moene, A.F., 2003. Evapotranspiration fluxes over mixed vegetation areas measured from large aperture scintillometer. Agric. Water Mgt. 58, 109-122.

Heusinkveld, B.G., Jacobs, A.F.G., Holtslag A.A.M., Berkowicz S.M., 2004. Surface energy balance closure in an arid region: role of soil heat flux. Agric. For. Meteorol. 122, 21–37.

Hill, R.J., 1978. Models of the scalar spectrum for turbulent advection. J. Fluid Mechanics 88, 541-562.

Hill, R.J., 1992. Review of optical scintillation methods of measuring the refractive-index spectrum, inner scale and surface fluxes. Waves in Random Media 2, 179-201.

Hill, R.J., 1997. Algorithms for obtaining atmospheric surface-layer fluxes from scintillation measurements. J. Atmos. Oceanic Tech. 14, 456-467.

Hill, R.J., Clifford, S.F., 1978. Modified spectrum of atmospheric temperature fluctuations and its application to optical propagation. J. Optical Soc. Amer. 68, 1201-1211.

Hill, R.J., Clifford, S.F., Lawrence, R.S., 1980. Refractive index and absorption fluctuations in the infrared caused by temperature, humidity and pressure fluctuations. J. Opt. Soc. Amer. 70, 1192-1205.

Hoedjes, J.C.B., Zuurbier, R.M., Watts, C.J., 2002. Large aperture scintillometry used over a homogeneous irrigated area, partly affected by regional advection. Boundary-Layer Meteorol. 105, 99-117.

Högström, U., 1988. Nondimensional wind and temperature profiles. Boundary-Layer Meteorol. 42, 55-78.

Horst, T.W., 1999. The footprint for estimation of atmosphere-surface exchange fluxes by profile techniques. Boundary-Layer Meteorol. 90, 171-188.

Horst, T.W., Weil, J.C., 1992. Footprint estimation for scalar flux measurements in the atmospheric surface layer. Boundary-Layer Meteorol. 59, 279-296.

Horst, T.W., Weil, J.C., 1994. How far is far enough? The fetch requirements for micrometeorological measurements of surface fluxes. J. Atmos. Ocean. Technol. 11, 1018-1025.

Hsieh, C-I., Katul, G., Chi, T-W., 2000. An approximate analytical model for footprint estimation of scalar fluxes in thermally stratified atmospheric flows. Adv. Water Resour. 23, 765-772.

Kaimal, J.C., 1988. The atmospheric boundary layer: its structure and measurements. Lecture notes, 15 Jan to 28 Feb 88, Indian Institute of Tropical Meteorology, P.O. Box 913, Shivanjinager, Pune 411005.

Kaimal, J.C., Finnigan, J.J., 1994. Atmospheric boundary layer flows: Their structure and measurement. Oxford University Press, New York, USA.

Kohsiek, W., Meijninger, W.M.L., Moene, A.F., Heusinkveld, B.G., Hartogensis, O.K., Hillen, W.C.A.M., de Bruin, H.A.R., 2002. An extra large aperture scintillometer for long range applications. Boundary-Layer Meteorol. 105, 119-127.

Kolmogorov, A.N., 1940. Wienersche Spiralen und einige andere interessante Kurven im Hilbertschen Raum. Comptes Rendus (Doklady) Acad. Sci. USSR 26, 115-118.

Kolmogorov, A.N., 1941a. Dissipation of energy in the locally isotropic turbulence (English translation 1991). Proc. Roy. Soc. London A434, 15-17.

Kolmogorov, A.N., 1941b. The local structure of turbulence in incompressible viscous fluid for very large Reynolds number. Dokl. Akad. Nauk. SSSR 30, 301-305.

Kustas, W.P. Blanford, J.H., Stannard, D.I., Douglas, C.S.T., Nichols, W.D., Weltz, M.A., 1994. Local energy flux estimates for unstable conditions using variance data in semiarid rangelands. Water Resour. Res. 30, 1351-1361.

Kustas, W.P., Choudhury, B.J., Moran, M.S., Reginato, R.J., Jackson, R.D., Gay, L.W., Weaver, H.L., 1989. Determination of sensible heat flux over sparse canopy using thermal infrared data. Agric. For. Meteorol. 44, 197-216.

Lagouarde, J.P., Chehbouni, A., Bonnefond, J.M., Rodriguez, J.C., Kerr, Y.H., Watts, C., Irvine, M., 2000. Analysis of the limits of the CT2-profile method for sensible heat flux measurements in unstable conditions. Agric. For. Meteorol. 105, 195-214.

Lagouarde, J.P., Bonnefond, J.M., Kerr, Y.H., McAneney, K.J., Irvine, M., 2002a. Integrated sensible heat flux measurements of a two-surface composite landscape using scintillometry. Boundary-Layer Meteorol. 105, 5-35.

Lagouarde, J.P., Jacob, J., Gu, X.F., Olioso, A., Bonnefond, J.M., Kerr, Y., McAneney, K.J., Irvine, M., 2002b. Spatialization of sensible heat flux over a heterogeneous landscape. Agronomie 22, 627-633.

Lawrence, R.S., Strohbehn, J.W., 1970: A survey of clear-air propagation effects relevant to optical communications. Proc. IEEE 58, 1523-1545.

Leclerc, M.Y., Thurtell, G.W., 1990. Footprint prediction of scalar fluxes using a Markovian analysis. Boundary-Layer Meteorol. 52, 247-258.

Liu, S.M., Huang, M.F., Han, L.J., Zhu, Q.J., 2003. A study of surface sensible heat fluxes with large aperture scintillometers. IEEE International Geoscience and Remote Sensing Symposium, Vol I to VII, Proceedings - Learning From Earth's Shapes and Sizes. July 21 to 25, 2003, Toulouse, France (Abstract).

Mahrt, L., 1996. The bulk aerodynamic formulation over heterogeneous surfaces. Boundary-Layer Meteorol. 78, 87-119.

Mauder, M., Liebethal, C., Göckede, M., Foken, T., 2004. On the quality assurance of surface energy flux measurements. 26th Conference on Agricultural and Forest Meteorology, Vancouver BC, Canada.

McAneney, K.J. Green, A.E., Astill, M.S., 1995. Large aperture scintillometry: the homogenous case. Agric. For. Meteorol. 76, 149-162.

Meijninger, W.M.L., de Bruin, H.A.R., 2000. The sensible heat fluxes over irrigated areas in western Turkey determined with a large aperture scintillometer. J. Hydrol. 229, 42-49.

Meijninger, W.M.L., Green, A.E., Hartogensis, O.K., Kohsiek, W., Hoedjes, J.C.B., Zuurbier, R.M., de Bruin, H.A.R., 2002a. Determination of area averaged water vapour fluxes with a large aperture and radio wave scintillometer over a heterogeneous surface - Flevoland field experiment. Boundary-Layer Meteorol. 105, 63-83.

Meijninger, W.M.L., Hartogensis, O.K., Kohsiek, W., Hoedjes, J.C.B., Zuurbier, R.M., de Bruin, H.A.R., 2002b. Determination of area-averaged sensible heat fluxes with a large aperture scintillometer over a heterogeneous surface - Flevoland field experiment. Boundary-Layer Meteorol. 105, 37-62.

Mengistu, M.G., 2003. The use of infrared thermometry for irrigation scheduling of cereal rye (Secale cereale L.) and annual ryegrass (lolium multiflorum Lam.). M.Sc.Agric. thesis, University of Natal. Pp109.

Min, W.B., Chen, Z.M., Sun, L.S., Gao, W.L., Luo, X.L., Yang, T.R., Pu, J., Huang, C.L., Yang, X.R., 2004. A scheme for pixel-scale aerodynamic surface temperature over hilly land. Adv. Atmos. Sciences 21, 125-131.

Moene, A.F., 2003. Effects of water vapour on the structure parameter of the refractive index for near-infrared radiation. Boundary-Layer Meteorol. 107, 635-653.

Monin, A.S., Obukhov, A.M., 1954. Basic laws of turbulent mixing in the ground layer of the atmosphere. Tr. Goefiz. Instit. Akad. Nauk. SSSR. 24(151), 163-187.

Monnik, K.A., M.J. Savage, Everson, C.S., 1995. Comparison of eddy correlation estimates of evaporation with Bowen ratio and equilibrium evaporation. Proc. S. Afr. Irrig. Symp., 167-171.

Monteith, J.L., Unsworth, M.H., 1990. Principles of Environmental Physics. Butterworth-Heinemann, Oxford, UK.

Moran, M.S., Kustas, W.P., Vidal, A., Stannard, D.I., Blanford, J.H., Nichols, W.D., 1994. Use of ground-based remotely sensed data for surface energy balance evaluation of a semi-arid rangeland. Water Resour. Res. 30, 1339-1349.

Munro, D.S., Oke, T.R., 1975. Aerodynamic boundary layer adjustment over a crop in neutral stability. Boundary-Layer Meteorol. 9, 53-61.

Oke, T.R., 1987. Boundary Layer Climates. 2 nd ed. Routledge, London, UK.

Pasquill, F., 1972. Some aspects of boundary layer description. Q. J. R. Meteorol. Soc. 98, 469-475.

Pasquill, F., Smith, F.B., 1983. Atmospheric Diffusion, 3rd Edition. Wiley, New York, USA. 437 pp.

Paw U, K.T., 1992. Development of models for thermal infrared radiation above and within plant canopies. J. Photogrammetry Remote Sens. 47, 189-203.

Paw U, K.T., Brunet, Y., Collineau, S., Shaw, R.H., Maitani, T., Qiu, J., Hipps, L., 1992. On coherent structures in turbulence within and above agricultural plant canopies. Agric. For. Meteorol. 61, 55-68.

Paw U, K.T., Qiu, J., Su, H.B., Watanabe, T., Brunet, Y., 1995. Surface renewal analysis: a new method to obtain scalar fluxes without velocity data. Agric. For. Meteorol. 74, 119-137.

Poggio, L.P., Furger, M., Prévôt, A.S.H., Werner, K.G., 2000. Scintillometer wind measurements over complex terrain. J. Atmos. Oceanic Technol. 17, 17-26.

Priestley, C.H.B., Taylor, R.J., 1972. On the assessment of surface heat flux and evaporation using large scale parameters. Mon. Weather Rev. 100, 81-92.

Qiu, J., Paw U, K.T., Shaw, R.H., 1995. Pseudo-wavelet analysis of turbulence patterns in three vegetation layers. Boundary-Layer Meteorol. 72, 177-204.

Raupach, M.R., Legg, B.J., 1984. The uses and limitations of flux gradient relationships in micrometeorology. In Sharma, M.L. (Ed.) Evapotranspiration from Plant Communities. Elsevier, Amsterdam.

Republic of South Africa, 1998. National Water Act. Act No 36 of 1998. South African Government Printer. 90 pp.

Richardson, L.F., 1922. Weather Prediction by Numerical Process. The University Press, Cambridge.

Rosenberg, N.J., 1974. Microclimate: the Biological Environment (Second edition). Wiley and Sons, New York, USA.

Rosenberg, N.J., Blad, B.L., Verma, S.B., 1983. Microclimate: The Biological Environment, 2nd ed. Wiley, New York, USA.

Savage, M.J., Everson, C.S., Metelerkamp, B.R., 1997. Evaporation measurement above vegetated surfaces using micrometeorological techniques. Water Research Commission Report No. 349/1/97, p248, ISBN No: 1 86845 363 4.

Savage, M.J., Graham, A.D.N., Lightbody, K.E., 1993. Use of a stem steady state heat energy balance technique for the in situ measurement of transpiration in Eucalyptus grandis: Theory and errors. J. S. Afr. Soc. Hort. Sciences 3, 46-51.

Savage, M.J., Graham A.D.N., Lightbody, K.E., 2000. An investigation of the stem steady state heat energy balance technique in determining water use by trees. Water Research Commission Report No. 348/1/00, p181, ISBN No: 1 86845 617 X.

Savage, M.J., Heilman, J.L., McInnes, K.J., Gesch, R.W., 1995b. Placement height of eddy correlation sensors above a short grassland surface. Agric. For. Meteorol. 74, 195-204.

Savage, M.J., Everson, C.S., Metelerkamp, B.R., 1995a. Evaporation measurement comparisons and advective influences using Bowen ratio, lysimetric and eddy correlation methods. Proc. S. Afr. Irrig. Symp. 160-166.

Savage, M.J., Leclerc, M.Y., Karipot, A., Prabha, T.V., 2000. Underestimation of eddy covariance sensible heat flux? 24 th Agricultural and Forest Meteorology Conference, Davis, California, USA. Pp 46-47.

Savage, M.J., McInnes, K.J., Heilman, J.L., 1996. The "footprints" of eddy correlation sensible heat flux density, and other micrometeorological measurements. S. Afr. J. Science 92, 137-142.

Schmid, H.P., Lloyd, C.R., 1999. Location bias of flux measurements over inhomogeneous areas. Agric. For. Meteorol. 93, 195-209.

Schmid, H.P., Oke, T.R., 1990. A model to estimate the source area contributing to turbulent exchange in the surface layer over patchy terrain. Q. J. R. Meteorol. Soc. 116, 965-988.

Scientific Programming Enterprises, 1999. Plotit for Windows 95/NT, Version 3.20k. Haslett, Michigan, USA.

Scintec, 2000. Surface Layer Scintillometer SLS20 / SLS40 SLS20-A / SLS40-A including OEBMS1 and stand-alone options. User's Manual. Scintec Atmosphärenmesstechnik AG, Tübingen, Germany. 102 pp.

Sharma, M.L., 1987. Estimating evapotranspiration. Adv. Irrig. 4, 213-281.

Shaw, R.H., undated. Unpublished lecture notes. Atmospheric Science, Boundary-layer meteorology, 106 pp; Atmospheric Science 230, Atmospheric turbulence, 97 pp. University of California, Davis, California, USA.

Snyder, R.L., Spano, D., Paw U, K.T., 1996. Surface renewal analysis for sensible and latent heat flux density. Boundary-Layer Meteorol. 77, 249-266.

Sorbjan, Z., 1989. Structure of the Atmospheric Boundary Layer. Prentice-Hall, New Jersey, USA. 316 pp.

Spano, D., Snyder, R.L. , Duce, P., Paw U, K.T., 2000. Estimating sensible and latent heat flux densities from grapevine canopies using surface renewal. Agric. For. Meteorol. 104, 171-183.

Stannard, D.I., 1997. A theoretically based determination of Bowen-ratio fetch requirements. Boundary-Layer Meteorol. 83, 375-406.

Stell, M.F., Moore, C.I., Burris, H.R., Suite, M.R., Vilcheck, M.J., Davis, M.A. Mahon, R., Oh, E., Rabinovich, W.S., Gilbreath, G.C., Scharpf, W.J., Reed, A.E., 2003. Passive optical monitor for atmospheric turbulence and wind speed. Ed. Voelz, D.G., Ricklin, J.C. Proceedings of the Society of Photo-Optical Instrumentation Engineers. Conference on Free-Space Laser Communication and Active Laser Illumination III. August 4 to 6, 2003. San Diego, California, USA. (Abstract).

Sutton, O.G., 1953. Micrometeorology: A Study of Physical Processes in the Lowest Layers of the Earth's Atmosphere. McGraw-Hill, London, UK.

Swinbank, W.C., 1951. The measurement of vertical transfer of heat and water vapor by eddies in the lower atmosphere. J. Meteorol., 8(3): 135 145.

Tanner, C.B., 1960. Energy balance approach to evapotranspiration from crops. Soil Sci. Proc. Amer. 24, 1-9.

Tanner, C.B., 1963. Basic instrumentation and measurements for plant environmental and micrometeorology. Soil Bulletin 6, 1-32.

Tanner, C.B., Pelton, W.L., 1960. Potential evapotranspiration by the approximate energy balance method of Penman. J. Geophys. Res. 65, 3391-3399.

Tatarskii, V.I., 1961. Wave Propagation in Random Media. Dover Publications, New York, USA.

Tennekes, H., Lumley, J.L., 1972. A first course in turbulence. MIT Press, Cambridge, Mass., USA.

Thiermann, V., 1992. A displaced-beam scintillometer for line-averaged measurements of surface layer turbulence. 10th Symposium on turbulence and diffusion. Portland, Oregon, USA.

Thiermann V., Grassl, H., 1992. The measurement of turbulent surface-layer fluxes by use of bichromatic scintillation. Boundary-Layer Meteorol. 58, 367-389.

Thom, A.S., 1972. Momentum, mass and heat exchange of vegetation. Q. J. R. Meteorol. Soc. 98, 124-134.

Thom, A.S., 1975. Momentum, mass and heat exchange in plant communities. In Monteith, J.L. (Ed.) Vegetation and the Atmosphere. Vol. 1. Principles. Academic Press. London, UK, pp 57-109.

Thomson, D.J., 1987. Criteria for the selection of stochastic models of particle trajectories in turbulent flows. J. Fluid Mech. 180, 529-556.

Tunick, A., 2003. CN2 model to calculate the micrometeorological influences on the refractive index structure parameter. Environmental Modelling Software 18, 165-171.

Twine, T.E., Kustas W.P., Norman, J.M., Cook, D.R., Houser, P.R., Meyers, T.P., Prueger, J.H., Starks, P.J., Wesely, M.L., 2000. Correcting eddy-covariance flux underestimates over a grassland. Agric. For. Meteorol. 103, 279-300.

Van Atta, C.W., 1997. Effect of coherent structures on structure functions of temperature in the atmospheric boundary layer. Arch. Mech. 29, 161-171.

Vilcheck, M.J., Reed, A.E., Burris, H.R., Scharpf, W.J., Moore, C., Suite, M.R., 2002. Multiple methods for measuring atmospheric turbulence. Ed. Ricklin, J.C., Voelz, D.G. Proceedings of the Society of Photo-Optical Instrumentation Engineers. Conference on Free-Space Laser Communication and Laser Imaging II. July 9 to 11, 2002, Seattle, Washington, USA. (Abstract).

Wang, J., Bras, R.L., 1998. A new method for estimation of sensible heat flux from air temperature. Water Resour. Res. 34, 2281-2288.

Water Research Commission, 2004. Research Proposals: Call for Proposals 2005/2006. Projects/Programmes to be solicited (2005/2006 Funding cycle). http://www.wrc.org.za/proposals/unsolicited/projectstobesolicited.asp Accessed 15 July 2004.

Watts, C.J., Chehbouni, A., Rodriguez, J-C., Kerr, Y.H., Hartogensis, O., de Bruin, H.A.R., 2000. Comparison of sensible heat flux estimates using AVHRR with scintillometer measurements over semi-arid grassland in northwest Mexico. Agric. For. Meteorol. 105, 81-89.

Weiss, A.I., 2002. Determination of thermal stratification and turbulence of the atmospheric surface layer over various types of terrain by optical scintillometry. Dissertation for the Doctor of Natural Sciences. Swiss Federal Institute of Technology, Zurich, Switzerland. Pp 157.

Wesely, M.L., 1976. The combined effect of temperature and humidity on the refractive index. J. Appl. Meteorol. 15, 43-49.

Wilson, K., Goldstein, A., Falge, E., Aubinet, M., Baldocchi, D., Berbigier, P., Bernhofer, C., Ceulemans, R., Dolman, H., Field, C., Grelle, A., Ibrom, A., Law, B.E., Kowalski, A., Meyers, T., Moncrieff, J., Monson, R., Oechel, W., Tenhunen, J., Valentini R., and Verma, S., 2002. Energy balance closure at FLUXNET sites. Agric. For. Meteorol. 113, 223-243.

Zhang, C., Shaw, R.H., Paw U, K.T., 1992. Spatial characteristics of turbulent coherent structures within and above an orchard canopy. In Precipitation Scavenging and Atmosphere-Surface Exchange, Vol. 2, coordinators Schwartz, S.E., Slinn, W.G.N., Hemisphere Publishing Co., Washington, USA, pp 41-75.